Maciej Krychowiak

Laserinduzierte Fluoreszenz von atomaren Heliumstrahlen im Fusionsrandplasma

Laser-induced fluorescence of atomic helium beams in a fusion edge plasma

Laser-induced fluorescence of atomic helium beams in a fusion edge plasma

vorgelegt von

Maciej Krychowiak
geboren am 29.03.1975
in Trzcianka

Dekan: Prof. Dr. Klaus Fesser

1. Gutachter: Prof. Dr. Thomas Klinger

2. Gutachter: Prof. Dr. Frederick Skiff

Tag der Promotion: 15.10.2007

Abstract

Thermal helium beams are well-established fusion plasma diagnostics for measuring radial profiles of electron density and temperature in the plasma edge with high spatial and time resolution ($\Delta r \approx 1\,\mathrm{mm}$ and $\Delta t \approx 1\,\mathrm{ms}$). The method is based on measurements of three spectral lines of atomic helium. Electron density and temperature are obtained by comparing two line intensity ratios, with main dependence on either n_e or T_e, with those calculated using a collisional-radiative (CR) model for helium. The accuracy of the derived plasma parameters strongly depends on the reliability of the model. However, most of the rate coefficients used in the model are known only from calculations which, to some extent, provide different results. Deviations between calculated and measured line intensities as well as the penetration depth of a helium beam are observed. Therefore, it is the aim of this work to validate experimentally the CR model at those points, which are accessible with the laser-induced fluorescence (LIF) spectroscopy.

A LIF system was set up in connection with a thermal helium beam on the tokamak TEXTOR in Jülich. The laser system comprises an excimer-laser pumped dye laser. It provides narrow-band pulsed high-power laser radiation in the near UV and visible spectral range. Several laser pumping schemes starting from the $n = 2$ levels of atomic helium have been tried, since these are the states from which the population distribution is determined by plasma excitation in the course of beam penetration. The fluorescence signals, measured perpendicularly at three radial positions simultaneously, provide absolute population densities of the pumped (lower) levels (measurements at the laser wavelength) as well as rate coefficients for collisional transfer between excited levels (measurements at different wavelengths). Deviations of the measured population densities from the model calculation were observed and possible explanations discussed. A number of experiments allowing the derivation of rate coefficients from the collision-induced fluorescence signals were performed, which suggest new values of those rate coefficients in some cases. The beam attenuation in the course of plasma penetration was quantified by use of helium line emission recorded with a 2D camera. It is compared to model results and reasons of the resulting deviations are discussed. A possible n_e measurement scheme is indicated, based on the time trace of decaying collision-induced fluorescence following a laser pulse at $\lambda = 388.9\,\mathrm{nm}$.
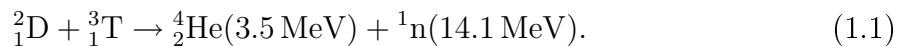
Contents

Chapter 1

Introduction

One of the future alternatives to cover the growing energy demand on earth can be provided by nuclear fusion, which relies on the synthesis of light nuclei to heavier ones. It features not only nearly inexhaustible fuel reserves and their equal distribution on earth but also emits no CO_2, which is supposed to cause the global warming. The energy gain of this reaction is due to the mass difference between the sum of the reaction partners and the resulting particles. In order for the reaction to take place, the Coulomb repulsion between the positively charged nuclei must be overcome. This can be achieved in an ionised gas of sufficient high temperature, called a plasma. In the stars which are driven by fusion processes the plasma is confined by the gravitation. For a future thermonuclear reactor magnetic confinement in toroidal geometry is the most promising method. Here the interaction of charged particles with a magnetic field is used. The synthesis of deuterium and tritium is the most probable reaction in a future reactor since it provides the highest reaction rate at realistic plasma temperatures of $T \simeq 10 \, \mathrm{keV}$[1]

$$^2_1\mathrm{D} + {}^3_1\mathrm{T} \rightarrow {}^4_2\mathrm{He}(3.5 \, \mathrm{MeV}) + {}^1\mathrm{n}(14.1 \, \mathrm{MeV}). \tag{1.1}$$

The released energy is shared between the reaction products according to their inverse mass. The energy carried by the α particle is supposed to heat the plasma by momentum transfer collisions. The fast neutrons releasing the plasma can be used to breed tritium from lithium and their energy converted to electric energy. However, the high temperature is not the only criterion to achieve a self-sustaining plasma, i.e. a plasma which can burn without external heating. The triple product of the plasma density n, temperature and the energy confinement time τ_E must exceed [Wesson, 1997]

$$nT\tau_\mathrm{E} > 4.5 \times 10^{21} \, \mathrm{m}^{-3} \, \mathrm{keVs}. \tag{1.2}$$

The energy confinement time is the measure of the thermal insulation of the plasma and the plasma-wall interaction plays a very important role in this context. On the one hand the inner wall of the vacuum vessel and the in-vessel components are exposed to high particle and heat loads. Thus impurities released in this way enter the plasma and cause the dilution of the fuel and cooling of the plasma. On the other hand, the properties of the edge plasma can considerably influence the bulk plasma. For this reason the understanding of the edge plasma behaviour is of high importance on the way to a

---

[1] $1 \, \mathrm{eV} \hat{=} 11600 \, \mathrm{K}$

working fusion reactor.

Appropriate methods of diagnosing the electron density and temperature in the plasma edge are necessary for the investigation of the plasma-wall interaction. The insertion of Langmuir probes into the plasma providing n_e and T_e values is limited due to the heat load to the probe tips. It can also cause a serious disturbance to the plasma. Passive spectroscopic method are the simplest concerning the experimental effort, they provide however line-of-sight integrated signals. Local values of n_e and T_e can be obtained by use of the laser light scattering (Thomson scattering) on electrons. Such diagnostics require a relatively high experimental effort and their time resolution is limited by the repetition frequency of the laser.

The use of atomic beams provides local measurements at good temporal resolution [Hintz and Schweer, 1995]. While the emission of lithium gives access to radial profiles of electron density, helium atoms with their singlet and triplet spectroscopic systems allow the determination of both the electron density and temperature with a resolution of $\Delta r \approx 1\,\mathrm{mm}$ and $\Delta t \approx 1\,\mathrm{ms}$. The method relies on the measurement of relative intensities of two line pairs of atomic helium, which is puffed radially into the edge plasma in the form of thermal or supersonic beams. Each of the line ratios is a function of one of the two plasma parameters, the electron density or the electron temperature and only weakly dependent on the other parameter. The values of n_e and T_e are derived by comparing the line ratios with calculated values. The electron densities of interest are too high to use a corona population distribution and too low to assume a local thermodynamic equilibrium. Instead, collisional-radiative model calculations are required. The accuracy of the plasma parameters derived by comparison with calculated line ratios strongly depends on the accuracy of the model constructed, i.e. consideration of all processes having an impact on the excited population distribution. On the other hand, the parameters of atomic helium, which quantify its interaction with the surrounding plasma of given parameters, e.g. the electron impact excitation rate coefficients, must be known with sufficient accuracy. These parameters – at least for higher temperatures as diagnosed with helium beams in fusion edge plasmas – are known in most cases only from calculations which, depending on the approximation used, differ considerably in many cases. This introduces some level of incertitude in the result of the model calculation and hence in the derived plasma parameters. In fact, comparison of intensities of some spectral lines of atomic helium calculated by the CR model and measured in the TEXTOR plasma edge show discrepancies [Brix, 1998]. The same is true when comparing the penetration depth of the beam into the plasma: the model calculations predict a deeper penetration than follows from measurements. Comparisons of n_e and T_e values with other diagnostics such as Langmuir probes or Thomson scattering systems indicate the accuracy of the helium beam method to around 10% for the n_e and 30% for the T_e derivation. For these reasons, investigation effort is still required in order to improve the model calculations.

Excitation of helium atoms according to selected transitions between bounded electronic quantum levels by use of resonant pulsed laser radiation (LIF) allows to measure the population density of the excited level as well as some rate coefficients for collisional

transitions between excited levels [Burakov et al., 1991]. It is the aim of this thesis to validate experimentally – by use of the LIF method for as many points as possible – the CR model used in connection with the helium beam diagnostics. Analysis of the sensitivity of the model prediction to the measurement results should provide those points of the model, which could explain measured deviations from the model calculations.

The structure of the thesis is as follows. After theoretical considerations connected to the LIF method and the line emission of the plasma (Chapter 2) the CR model used for our calculations is described in detail. Atomic data of the most important processes – the electron impact excitation and ionisation – available in the literature are reviewed and additional processes are quantitatively discussed, which can play a role in the modelling of a helium beam. The numerical treatment of the time dependent and of the steady state model solution is presented. In Chapter 4 the main features of the TEXTOR tokamak are depicted, followed by a detailed description of the constituents of the prepared LIF set-up: the laser system, the helium inlet and the observation system. Chapter 5 deals with the methods of experimental data analysis, which are necessary to obtain relative population densities from absolute measurements, which are compared with relative populations resulting from the model calculation. Additionally, the incorporation of the laser impact in the CR model calculation is explained. The results of the measurements and comparisons with model calculations are presented and discussed in Chapter 6 followed by a summary of the thesis.

Chapter 2

Theoretical background

2.1 Laser-induced fluorescence

Spectroscopy of laboratory plasmas can be divided in two types: passive and active spectroscopy. In the first case the measurement set-up consists of solely an observation system, mainly utilising imaging optics. This implicates that the plasma radiation is collected along a line of sight, which is defined by the whole intersection region of the plasma and the observation line. Since laboratory plasmas typically feature pronounced spatial variations of their parameters, local values of measured quantities cannot be provided by passive measurements but rather values averaged over the line of sight.

To circumvent this problem methods of local profile reconstruction can be applied. These use arrangements consisting of several simultaneously recorded lines of sight. They can cross (e.g. tomographic reconstruction to obtain local intensity profiles of VUV (vacuum ultraviolet) or soft X-rays [Zoletnik and Kálvin, 1993]). In other arrangements all lines of sight start from one point in space (various inversion methods requiring additional information about symmetry of the radiation source, for example in deriving local Z_{eff} values from the near IR (infrared) bremsstrahlung [Meister et al., 2003]). In some cases it is possible to spatially resolve passive plasma radiation by making use of a change of the magnetic field strength along the line of sight, which often has a pronounced impact on the radiation. One well known example from microwave spectroscopy is the use of the ECE (electron cyclotron emission) for the measurement of spatial electron temperature profiles. Another example is the use of Zeeman splitting of spectral lines (Sec. 2.4.2), which allows one the identification of the point in space of the line emission [Goto and Morita, 2002]. The great advantage of passive measurement arrangements is that, compared to active diagnostics, their spatial adjustment is much easier and not crucial for the proper interpretation of the measured signals.

In active spectroscopy a variety of atomic [Hintz and Schweer, 1995, Schweer et al., 1999] or laser beams [Arecchi and Schulz-Dubois, 1972, Sacchi and Svelto, 1978] are used. Here, the additional probe beam is introduced into the plasma and overlaps, to a certain extent, with the observation line (Fig. 2.1). The region of intersection of both lines defines the observation volume, which can be optimised to reach the required spatial resolution. Typically the probe beam is observed simultaneously at different points (e.g. atomic beams or Thomson scattering diagnostics [van der Meiden et al., 2005]), which enables the direct measurement of spatial profiles of the local plasma parameter values.
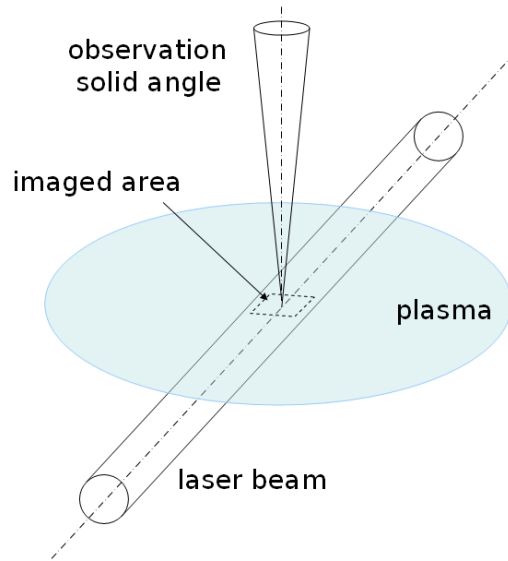
Figure 2.1: Active plasma spectroscopy: intersection of the probing beam and the line of sight in the plasma allows to spatially reduce the measurement volume.

Another possibility is to scan the inclination angle of one [Mertens et al., 1993] or both lines.

Laser-induced fluorescence (LIF) is an active spectroscopic method utilising narrow-band lasers as the probe beam. In terms of particle-photon scattering, LIF can be considered as an inelastic scattering process since the fluorescence light typically consists of photons with wavelength different to the laser light. Rayleigh scattering by atoms, Thomson scattering by electrons and Mie scattering by larger particles are examples of elastic scattering processes [Muraoka and Maeda, 1993].

Parameters of selected plasma components (atoms, ions or molecules) are measured by using the interaction between electromagnetic radiation and the atom that is considered as a quantum-mechanical system with discrete energy levels. The diagnostic method is based on selective excitation from a certain energy level and thus can provide information about population densities of the level that was excited by the laser light. For that absolute measurements of the fluorescence signal is required. Also velocity distribution of the species along the laser beam direction, in particular the temperature and drift velocities, can be measured. The analysis of e that follow laser excitation yields important informations about collision processes in the plasma and related quantities e.g. electron density or collision rate coefficients [Chall et al., 1985]. Furthermore, LIF allows the measurement of those physical values in the observation volume, which influence the shape of the spectral profiles of absorption lines such as magnetic field (Zeeman effect [Mertens et al., 1993]), electric field (Stark effect [Czarnetzki et al., 1999]), plasma pressure or the effective ionic charge Z_{eff} (pressure broadening [Bychkov et al., 1987]).

Laser radiation is typically used as the light source owing to the outstanding performance of modern lasers concerning all important parameters such as output power, pulse
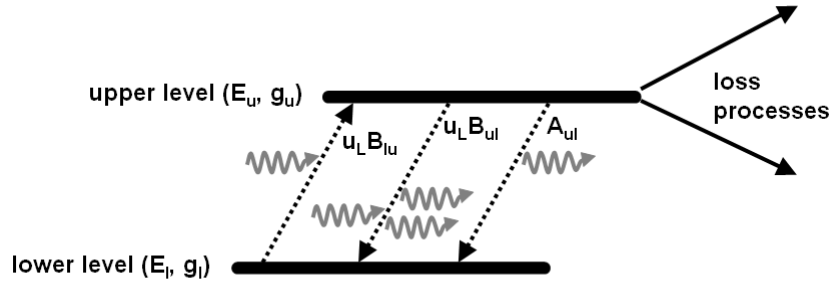
Figure 2.2: Scheme of a two-level-system for LIF with the corresponding Einstein coefficients. The model can be extended by additional loss processes from the upper level, such as radiative decay to energetically lower lying levels or collisional transitions to other levels and into continuum (ionisation).

lengths, spectral width and wavelength tuning range. Before the invention of lasers, spectral lamps were used as a source of line radiation for fluorescence measurements [Pospieszczyk et al., 1980, Demtröder, 2000], however with much less resolution and sensitivity. Laser sources also provide good beam collimation and the beam is guided over large distances by use of mirrors or even coupled into glass fibres, which makes the adjustment of mirrors superfluous. Further features of laser sources, which are important for some applications are the light polarisation and coherence. Active plasma spectroscopy with lasers brings several advantages such as a very high spectral, spatial and temporal resolution as well as high accuracy and sensitivity. Laser measurements are not perturbing to the plasma itself and, under some conditions, the signals do not depend on the plasma parameters [Meng and Kunze, 1979]. Ground or other non-radiative state (metastables) populations can be measured directly. Moreover, measurements can be performed even from large distances [Muraoka and Maeda, 2001].

For better understanding of the resonant laser-atom interaction it is useful to consider it at first in the so-called two-level-system. The spectral width of the laser is assumed to be chosen in a way as to cover the entire absorption profile of only one spectral transition between two discrete electronic quantum levels with different energies $E_u > E_l$ (u: upper level, l: lower level, Fig. 2.2). Collisional or radiative population exchange with other levels is neglected. The wavelength of the laser and the energies of the level u and l are related by the radiative transition between the levels

$$\lambda = \frac{hc}{E_u - E_l} \qquad (2.1)$$

where h denotes the Planck constant and c the velocity of light. The spontaneous release of a photon (see Sec. 2.2) with the corresponding wavelength and Einstein coefficient A_{ul} is only one of three possible radiative transitions between both levels. The other ones are connected with additional electromagnetic field. The probability for the absorption of a photon by the atom in the presence of a laser field with the spectral energy density

$u_\omega = \frac{\mathrm{d}E}{\mathrm{d}V \mathrm{d}\omega}$ is given by

$$P_{\text{abs}} = u_\omega \mathrm{B_{lu}}, \tag{2.2}$$

where $\mathrm{B_{lu}}$ is the Einstein coefficient of absorption. In an analogue way, the probability for an induced photon emission is equal to $u_\omega \mathrm{B_{ul}}$ with the Einstein coefficient for induced emission

$$\mathrm{B_{ul}} = \frac{\mathrm{g_l}}{\mathrm{g_u}} \mathrm{B_{lu}} \tag{2.3}$$

($\mathrm{g_l}$ and $\mathrm{g_u}$ are the statistical weights of the lower and the upper level).

The laser light of a wavelength resonant with the considered atomic transition will have an impact on the population of the corresponding levels (optical pumping). This process can be described with the following differential equations:

$$\frac{\mathrm{d}n_{\mathrm{u}}}{\mathrm{d}t} = -\frac{\mathrm{d}n_{\mathrm{l}}}{\mathrm{d}t} = (\mathrm{B_{lu}} n_{\mathrm{l}} - \mathrm{B_{ul}} n_{\mathrm{u}})u_\omega - \mathrm{A_{ul}} n_{\mathrm{u}},$$

where n_{u} and n_{l} are the population densities of the upper and the lower level. The equations can be solved analytically and the result for the temporal evolution of the upper level population, when assuming the laser pulse to be a square function of time with the pulse length $\mathrm{T_L}$, is

$$n_{\mathrm{u}}(t) = \begin{cases} \mathrm{n}\frac{\mathrm{g_u}}{\mathrm{g_l} + \mathrm{g_u}} \frac{S}{S+1}\left(1 - \mathrm{e}^{-(S+1)\mathrm{A_{ul}}t}\right) & \text{for } 0 \leq t \leq \mathrm{T_L} \\[2mm] n_u(\mathrm{T_L})e^{-\mathrm{A_{ul}}(t-\mathrm{T_L})} & \text{for } t > \mathrm{T_L} \end{cases}, \tag{2.4}$$

where n denotes the total population of both levels (being constant in time) and S is the so-called saturation parameter, defined by

$$S = \frac{\mathrm{g_l} + \mathrm{g_u}}{\mathrm{g_l}} \frac{\mathrm{B_{ul}} u_\omega}{\mathrm{A_{ul}}}. \tag{2.5}$$

The saturation parameter essentially reflects the ratio of the laser-induced and spontaneous emission rate. It can also be expressed as a ratio of the laser spectral energy density to the so-called saturation spectral energy density (here the energy density per wavelength interval $u_\lambda = -\frac{2\pi c}{\lambda^2} u_\omega$ is used). With Eq. (2.23) we obtain:

$$S = \frac{u_\lambda}{u_\lambda^s} \quad \text{with} \quad u_\lambda^s = \frac{\mathrm{g_l}}{\mathrm{g_l} + \mathrm{g_u}} \frac{8\pi \mathrm{hc}^2}{\lambda^5}. \tag{2.6}$$

The saturation laser energy decreases with the fifth power of the laser wavelength. This has consequences for LIF measurements in the UV-VUV spectral range. Pulsed dye lasers, as typically used in plasma applications [Burakov et al., 1991], are able to radiate at wavelengths down to the near UV range. Further reduction of the wavelength is realised by frequency up-conversion (doubling and tripling through harmonic generation) or frequency mixing methods [Demtröder, 2000]. However, these non-linear processes result in considerable losses of the laser power. With modern methods e.g. at $\lambda = 121\,\mathrm{nm}$

that corresponds to the Lyman-alpha transition of hydrogen saturation parameter of ~ 0.1 is achieved [Mertens and Bogen, 1987].

The value of the saturation parameter has a strong impact on the temporal behaviour of the upper level population during the laser pulse, as can be seen from Eq. (2.4). The laser pulse width of at least

$$T_L^s = \frac{1}{(S+1)\mathrm{A_{ul}}} \tag{2.7}$$

is needed to establish stationary population. For low laser energy ($S \ll 1$) this time constant is simply given by the inverse spontaneous transition probability. For high laser energy ($S \gg 1$), T_L^s reduces by the factor of S. Another conclusion can be drawn from Eq. (2.4) concerning the stationary situation: for low laser energy the fluorescence response to the laser pulse, being proportional to the upper level population (Eq. (2.15)), is proportional to S and hereby to the laser energy itself. In the case of strong laser energy the upper population is not sensitive anymore to the laser energy since the pumping process is already saturated. Spontaneous decay does not play a role anymore in the depopulation of the upper level since the laser-induced photon release is – according to Eq. (2.5) – much stronger. Hence, increasing the laser energy enhances both the transition rates from the lower to the upper level and in the opposite direction in the same way which has no effect on the population distribution. In other words, the system becomes a transparent medium (the absorption coefficient, according to Eq. (2.55), becomes zero) for light at the resonant wavelength. The population ratio of both levels only depends on their statistical weights:

$$\mathrm{n_u^s/n_l^s = g_u/g_l}. \tag{2.8}$$

Calculated temporal behaviour of the upper level population in a two-level-system for different saturation parameters is shown in Fig. 2.3. Laser pulse length of 15 ns and saturation parameter of $S = 0.1 - 100$ according to our laser system (Sec. 4.2) as well as spontaneous decay probability of $\mathrm{A_{ul}} = 10^7 \mathrm{s^{-1}}$ and statistical weights $\mathrm{g_l}{=}1$ and $\mathrm{g_u}{=}3$ according to the atomic helium transition $2^1\mathrm{S}{\rightarrow}3^1\mathrm{P^o}$ have been assumed. The solid lines represent the case of a laser pulse lasting between $t = 0\,\mathrm{ns}$ and $t > 100\,\mathrm{ns}$ while the dashed lines result from the assumption of a laser pulse which ends at $t = 15\,\mathrm{ns}$. In the case of a long laser pulse all curves reach the saturation after a time period of $t < \mathrm{A^{-1}} \simeq 70\,\mathrm{ns}$. This means that for a laser pulse width of $t = 15\,\mathrm{ns}$ the maximum fluorescence signal is not reached and the end of the pulse as long as the saturation parameter lies considerably below $S = 100$. The choice of the saturation parameter above this value by according adjusting the laser energy will be desirable in applications with low signal-to-noise ratios as in our case. Another advantage of a strongly saturating laser energy for measurements of level population is the fact that fluorescence signal does not depend on the laser energy fluctuations. Then the derivation of population densities from the fluorescence signals does not require precise information about the laser energy distribution throughout the observation volume [Daily, 1978].

In many realistic cases other processes must be taken into account, e.g. electron-
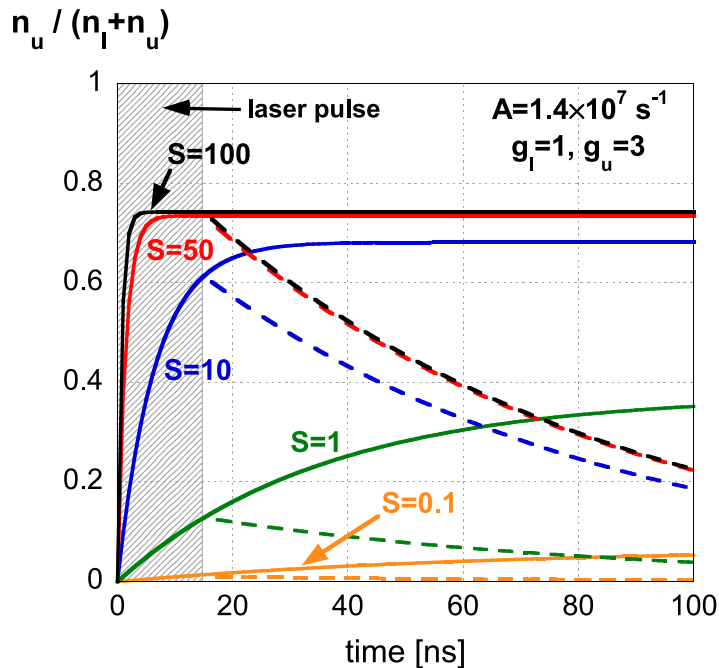
Figure 2.3: Calculated time dependence of the upper level population pumped by a laser for a two-level system. Different values of the saturation parameters have been chosen. For the dashed lines it has been assumed that the laser pulse ends at $t = 15$ ns (grey-hatched box).

collision population transfer between excited states. In general, the time dependent differential equations of the collisional-radiative model, which include the terms representing the laser interaction with the atom must be solved (Sec. 3.3). However, in a simplified case if only the population of both of these levels changes considerably during the laser pulse, which are optically involved in the pumping process, the saturation parameter can be written in a generalised form as [Dullni, 1984, Bogen and Hintz, 1986, van Lessen et al., 1998]:

$$S = \frac{\mathrm{g_l} + \mathrm{g_u}}{\mathrm{g_l}} \tau_u \mathrm{B_{ul}} u_\omega, \tag{2.9}$$

where τ_u is the effective lifetime of the upper level, which depends on the plasma parameters and is derived from the inverse of the sum of all population loss rates:

$$\tau_u = \left(\left(\sum_{i \neq u} \langle \sigma_{ui} v \rangle + \langle \sigma_{u-ion} v \rangle \right) n_e + \sum_{i < u} \mathrm{A_{ui}} \right)^{-1}. \tag{2.10}$$

It means that to reach a certain level of saturation, higher laser power is needed since the induced emission rate has to counteract the enhanced loss rate from the upper level. The advantage of laser saturation here is that the fluorescence response will have only a small dependence on the quenching (collisional deexcitation from the upper to the lower level) rate [Piepmeier, 1972, Kramer, 1990].

The flux of fluorescence photons per unit observation volume emitted from the upper level into the full solid angle 4π is proportional to the upper level population during or after the laser pulse and is given simply by the product of the population and the corresponding transition probability. In a two-level-system, during a laser pulse and after enough time for reaching a steady population distribution (Eq. (2.7)) it would, accordingly to Eq. (2.4), amount to

$$\int\limits_{spectral\,line} \int\limits_{\Omega=0}^{4\pi} \Phi \, \mathrm{d}\Omega \, \mathrm{d}\lambda = \frac{\mathrm{g_u}}{\mathrm{g_l} + g_u} \frac{S}{S+1} \mathrm{nA_{ul}}. \tag{2.11}$$

However, the shapes of absorption profiles of spectral lines undergo numerous changing processes (Sec. 2.3). At low densities the inhomogeneous broadening mechanism caused by the Doppler effect will be usually dominant [Unsöld, 1968]. Different parts of a Doppler-broadened absorption profile $g^D(\lambda)$ correspond to atoms having different velocity components v_L along the laser beam direction (Fig. 2.4). Atoms moving away from the laser need resonant laser light at higher frequency for the absorption to take place. That is at a wavelength, which is blue-shifted by the value of

Figure 2.4: Doppler-broadened absorption line: the coloured areas indicate the resonance parts of the velocity distribution for different velocity vectors of the excited atoms.

$$\Delta\lambda = \frac{v_L}{\mathrm{c}}\lambda. \tag{2.12}$$

Resonance wavelength of atoms with a velocity v_L opposite to the laser beam direction will be red-shifted by the same value.

In the case of a Doppler-broadened line profile, the easy way of calculating the fluorescence photon flux as given in Eq. (2.11) holds only if an approximately constant value of the saturation parameter sustains over the whole absorption profile. In this case of the so-called broadband laser excitation atoms corresponding to all parts of the absorption line profile, i.e. independent of their velocity, are excited in a similar way. For this reason broadband lasers are preferably used for measurements of level populations.

A different situation is given, if the width of the laser profile is considerably smaller than that of the absorption line ($\Delta\lambda_L < \Delta\lambda_D$, Fig. 2.5). In this case only a fraction of the lower level population is resonant with the laser light and therefore can be excited (if 'velocity changing' collisions are not too fast [Sobelman, 1957]). This provides a possibility to measure the shape of the velocity distribution function by scanning the laser wavelength over the whole absorption profile. Assuming a Gaussian shape u_λ^G (see
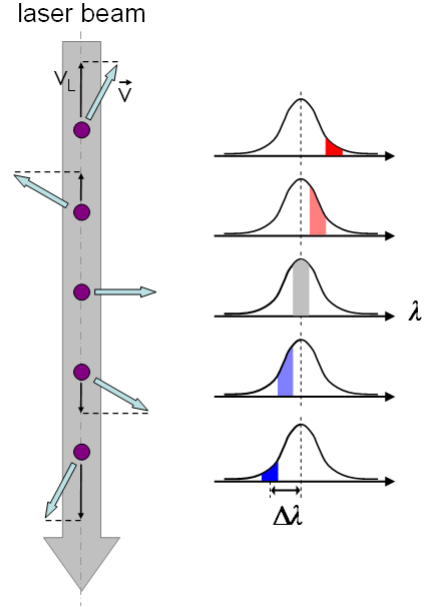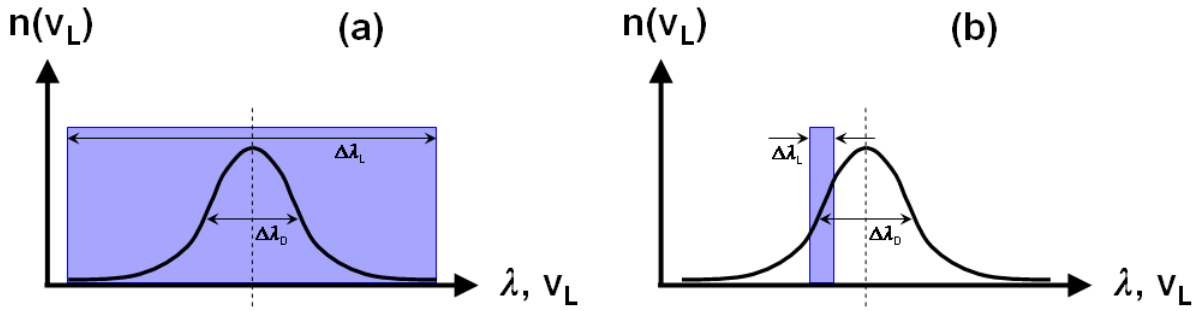
Figure 2.5: Laser excitation of a species with Doppler-broadened absorption profile by using a) a broad-band laser, b) a narrow-band laser.

Eq. (2.49)) of the spectral profile of the laser energy density in the non-saturating regime the measured profile shape $I(\lambda)$, being a convolution of the laser and the absorption profile

$$I(\lambda) = \int g^{\mathrm{D}}(\lambda)\, u^{\mathrm{G}}_{\lambda}\, \mathrm{d}\lambda, \qquad (2.13)$$

is again given by a Gaussian profile but with a larger full with at half maximum (FWHM) of

$$\Delta\lambda_{\mathrm{I}} = \sqrt{(\Delta\lambda_{\mathrm{D}})^2 + (\Delta\lambda_{\mathrm{L}})^2}. \qquad (2.14)$$

From the measured width, the Doppler width $\Delta\lambda_{\mathrm{D}}$ can be extracted and from that the temperature T of the species can be derived by use of Eq. (2.50). On the other hand, provided the gas temperature is known, the laser spectral width can be measured in this way (for uncertainty minimisation, species with larger atomic mass and hence smaller Doppler width will preferably be chosen [Omenetto et al., 1980]). Shifts of the maximum in the measured profile give information about drift velocities of the species according to Eq. (2.12). Population of the lower level can be in principle also derived in this case by using the unfolding procedure provided the laser spectral width is known with a sufficient precision. For measurement of level population, however, a broadband laser will be much more preferable due to larger signal-to-noise ratios and due to insensitivity to the laser width.

2.2 Line emission of plasmas

The line radiation of plasma particles has its origin in spontaneous transitions of electrons from a quantum level with the binding energy of E_{u} to another level with a lower energy E_{l}. The energy difference is radiated in form of electromagnetic waves, and the wavelength can be specified on the basis of the quantum nature of light by using the photon energy $E_{\mathrm{ph}} = \mathrm{h}\nu$ and assuming that one photon is released by one decay process of an electron: $\lambda = \mathrm{c}/\nu = \mathrm{hc}/(E_{\mathrm{u}} - E_{\mathrm{l}})$. To predict the intensity of the line radiation,

two additional physical values must be known: the average rate of spontaneous photon emission between the levels u and l (Einstein coefficient A_{ul}, also misleadingly referred to as the transition probability) as well as the population density of the radiating level n_{u}. The spectral power emitted from a unit volume into a unit solid angle, called the spontaneous line emission coefficient, is then simply given by:

$$\epsilon_{\mathrm{ul}} = \frac{1}{4\pi} n_{\mathrm{u}} \mathrm{h} \nu_{\mathrm{ul}} A_{\mathrm{ul}} L(\nu). \tag{2.15}$$

The line profile $L(\nu)$, normalised to $\int L(\nu) = 1$, is introduced due to the fact that no strictly monochromatic line emission exists. Different line broadening and splitting mechanisms, as typically occurring in plasmas, are discussed in sections 2.3-2.4.2. The Einstein coefficients A_{ul} are calculated using quantum mechanics and are known with sufficient precision, at least for atomic helium transitions of interest in this thesis. Finally, the population distribution of radiating levels is strongly dependent on the surrounding plasma parameters. For some parameter ranges relatively simple dependences concerning the population distribution among excited levels (and different ionisation stages) can be written (e.g. the corona equilibrium), for others, complicated rate equation systems balancing the population and depopulation processes of different levels must be set up and solved. These problems are addressed in Sec. 2.2.1. Finally, in Sec. 2.2.2 a situation is discussed in which the plasma particle density is high enough to cause reabsorption of its own line radiation (optically thick plasma).

2.2.1 Models for excitation population distribution

Line radiation from plasma particles is a result of spontaneous radiative decay of excited levels, which are formed due to interactions of the particles with each other. There are several possible processes and the main (with the inverse ones) are:

- collisional excitation and deexcitation,

- collisional ionisation and three body recombination,

- excitation due to photon absorption and spontaneous (as well as induced) photon emission,

- photoionisation and radiative recombination,

- autoionisation and dielectronic recombination.

The transition rates of radiative processes are specified with Einstein coefficients for spontaneous A_{ul} and induced emission B_{ul} as well as photon absorption

$$B_{\mathrm{lu}} = \frac{\mathrm{g_u}}{\mathrm{g_l}} B_{\mathrm{ul}}. \tag{2.16}$$

Collisional processes can be quantified by use of rate coefficients

$$\langle \sigma_{\mathrm{lu}} v \rangle = \int\limits_{0}^{\infty} \sigma_{\mathrm{lu}}(E) v f(E) \, \mathrm{d}E, \tag{2.17}$$

which are given by the product of the relative velocity v of the collision partners and the cross section σ_{lu} of the corresponding process or, generalised, by averaging of this product over the energy distribution $f(E)$ of the collision partner. In many cases, for the calculation of electron collisional rate coefficients the Maxwell distribution can be assumed for the energy distribution of the free electrons [Sobelman et al., 1995]:

$$f_{\mathrm{M}}(E) = \frac{2\sqrt{2m}}{\sqrt{\pi (\mathrm{k_B} T)^3}} E \mathrm{e}^{-\frac{E}{T}}, \tag{2.18}$$

where T denotes the temperature of the perturber species and, m, their mass.

Depending on the electron density in the plasma, three different cases regarding the calculation of the population distribution among excited levels can be distinguished: the thermodynamic equilibrium, the corona model and the intermediate case of the collisional-radiative model. For sufficiently high electron densities the plasma reaches the thermodynamic equilibrium. Here, all collisional and radiative interactions are compensated by the inverse processes and the following distributions are valid:

- The velocity distribution of plasma particles is given by the Maxwellian distribution,

- The population ratio of two levels of the same ionisation stage is given by the Boltzmann distribution

$$\frac{n_{\mathrm{u}}}{n_{\mathrm{l}}} = \frac{\mathrm{g_u}}{\mathrm{g_l}} \mathrm{e}^{-\frac{E_{\mathrm{u}} - E_{\mathrm{l}}}{\mathrm{k_B} T}}, \tag{2.19}$$

  where $\mathrm{g_l}$ and $\mathrm{g_u}$ are the statistical weights of both levels and $E_{\mathrm{u}} - E_{\mathrm{l}}$ is the energy gap between them. Interestingly, the spectral line ratios originating from different excited levels $I_{\mathrm{u}}/I_{\mathrm{l}} \propto n_{\mathrm{u}}/n_{\mathrm{l}}$ do only depend on plasma temperature, and cannot be used for electron density measurement.

- In contrast, the population distribution between different ionisation stages, given by the Saha equation

$$\frac{n_{Z+1}}{n_Z} = \frac{\mathrm{g}_{Z+1}}{\mathrm{g}_Z} 2 \left(\frac{\mathrm{m_e k_B} T}{2\pi \hbar^2} \right)^{\frac{3}{2}} \frac{1}{n_{\mathrm{e}}} \mathrm{e}^{-\frac{\Delta E_{Z,Z+1}}{\mathrm{k_B} T}}, \tag{2.20}$$

  shows both the temperature and the density dependence (Z is the ionisation degree and $\Delta E_{\mathrm{Z,Z+1}}$ the ionisation energy).

- Finally, the spectral energy density of the radiation field can be easily derived from the Planck radiation formula

$$u_\omega = \hbar \omega \frac{2\omega^2}{\pi \mathrm{c}^3} \frac{1}{\mathrm{e}^{\hbar \omega / \mathrm{k} T} - 1}. \tag{2.21}$$

By using the above distributions characterising the thermodynamic equilibrium, one can derive substantial dependencies between atomic (or ionic) constants, which are independent of the surrounding plasma conditions [Hutchinson, 2002]. For example, from the equilibrium condition for the radiation

$$(A_{ul} + B_{ul}u_{\omega})n_u = B_{lu}u_{\omega}n_l, \tag{2.22}$$

the relation between the coefficients for spontaneous, A_{ul}, and for induced emission B_{ul} can easily by derived. With the Planck radiation formula (2.16) and Eq. (2.21) we obtain:

$$B_{ul} = \frac{2\pi^3 c^3}{h\omega^3} A_{ul}. \tag{2.23}$$

On the other hand, because all collisional processes are compensated by the inverse processes, we can write:

$$n_u n_e \langle \sigma_{ul} v \rangle = n_l n_e \langle \sigma_{lu} v \rangle \tag{2.24}$$

and by using the Boltzmann distribution (2.19) obtain the ratio of rate coefficients for inverse processes:

$$\frac{\langle \sigma_{ul} v \rangle}{\langle \sigma_{lu} v \rangle} = \frac{g_l}{g_u} e^{-\frac{E_l - E_u}{k_B T}}. \tag{2.25}$$

For somewhat lower electron densities, the plasma becomes optically thin and as a consequence the Planck radiation formula does not describe the radiation field anymore. However, if the electron density is not too low [McWhirter, 1965]:

$$n_e \geq 1.6 \times 10^{12} T_e^{\frac{1}{2}} (E_u - E_l)^3, \tag{2.26}$$

where T_e and $(E_u - E_l)$ are to be inserted in K and eV, respectively, and n_e is obtained in cm^{-3}, the local thermodynamic equilibrium is valid, in which the remaining three distribution functions (Eqs. (2.18), (2.19) and (2.20)) hold. Unfortunately, the low densities of fusion plasmas do not allow the use of these simple distribution functions.

On the other hand, for very low electron densities

$$\sum_{l \neq u} n_e \langle \sigma_{ul} v \rangle \ll \sum_{l < u} A_{ul} \tag{2.27}$$

the deexcitation processes are mainly governed by radiative decay and the electronic transitions between excited levels can be neglected. Since cascade excitation from excited levels is negligible, all levels are populated mainly by collisional excitation from the ground state. This situation is referred to as the corona equilibrium. Here, level populations relative to the ground state population in the steady state, provided no metastable levels exist, are simply given by:

$$\frac{n_{\mathrm{u}}}{n_1} = n_{\mathrm{e}} \frac{\langle \sigma_{1\mathrm{u}} v \rangle}{\sum\limits_{\mathrm{l<u}} A_{\mathrm{ul}}}. \tag{2.28}$$

Similarly to the thermodynamic equilibrium case line intensity ratios are not sensitive to electron density and the electron temperature can be derived by utilising different T_{e} dependence of some excitation rate coefficients.

For moderate densities, as typically found in fusion plasmas, neither the thermodynamic equilibrium nor the corona limit hold. Under these conditions the level population depends on the balance of all processes of excitation, radiation and others. The general solution is very difficult because one has to consider a large set of equations describing all processes for all levels. Though, in many cases, the Maxwellian distribution of electron energy still holds so that the rate coefficients for collisional processes can be derived by cross section averaging over this distribution. The reverse processes are obtained just by considering the statistical weights and the Boltzmann factor (Eq. (2.25)) [Sobelman et al., 1995]. An example of a balance equation for a single level u, considering electron collisional excitation and deexcitation, spontaneous radiative transitions and electron collisional ionisation is written as:

$$\frac{\mathrm{d}n_{\mathrm{u}}}{\mathrm{d}t} = \sum_{i \neq \mathrm{u}} \langle \sigma_{i \to \mathrm{u}} v \rangle n_{\mathrm{e}} n_i - \sum_{i \neq \mathrm{u}} \langle \sigma_{\mathrm{u} \to i} v \rangle n_{\mathrm{e}} n_i + \sum_{i > \mathrm{u}} A_{i \to \mathrm{u}} n_i - \sum_{i < \mathrm{u}} A_{\mathrm{u} \to i} n_i - \langle \sigma_{\mathrm{u} \to \mathrm{ion}} v \rangle n_{\mathrm{e}} n_{\mathrm{u}}. \tag{2.29}$$

The stationary population distribution is derived by solving a system of rate equations set to zero. On the other hand, solving the time dependent equations allows the study of the time evolution of non-steady state situations, for example if short-pulse laser radiation perturbs a steady state distribution (see Sec. 5.3). In the low or high electron density limit collisional-radiative models turn into the corona model or the thermodynamic equilibrium, respectively.

2.2.2 Radiation transport

If the density of the line radiating species in the plasma is not too high, the self-absorption of the radiation can be neglected. Such a plasma is said to be optically thin. In this case a passive line intensity measurement corresponds to the sum of the line emission coefficients along the line of sight. In the opposite case the effect of the radiation trapping must be taken into account. The reabsorption of line radiation has two consequences for plasma spectroscopy. On the one hand, the relation between the emission coefficients in the bulk plasma and the radiation leaving the plasma surface are non-linearly coupled. On the other hand, the re-absorption processes influence the population distribution of excited levels.

Provided $I_\nu(x)$ is the intensity profile of line radiation incident on a plasma layer of the thickness $\mathrm{d}x$, the intensity profile after having passed the layer is equal to

$$I_\nu(x + \mathrm{d}x) = I_\nu(x) - \kappa_\nu I_\nu(x)\mathrm{d}x + \eta_\nu \mathrm{d}x. \tag{2.30}$$

The attenuation of the intensity is due to the resonant self-absorption of radiation by atoms in the lower level l, to be quantified with the spectral profile of the absorption coefficient

$$\kappa_\nu = \frac{\mathrm{h}\nu}{4\pi} \left(n_\mathrm{l} B_\mathrm{lu} - n_\mathrm{u} B_\mathrm{ul} \right) P_\nu, \tag{2.31}$$

where n_i is the population density of the level i, B_lu and B_ul are the Einstein coefficients of absorption and induced emission (related according to Eq. (2.16)) and P_ν is the absorption spectral profile normalised to 1. As one can see, the absorption is counteracted by the induced emission and by line emission of the plasma at the point x with the line emission profile

$$\eta_\nu = \frac{\mathrm{h}\nu}{4\pi} n_\mathrm{u} A_\mathrm{ul} P'_\nu, \tag{2.32}$$

where P'_ν is the spectral emission profile, which can be assumed to be the same as the absorption profile P_ν.

If assuming a uniform plasma with zero incident radiation, Eq. (2.30) is easily solved:

$$I_\nu(x) = \frac{\eta_\nu}{\kappa_\nu} \left(1 - \mathrm{e}^{-\kappa_\nu x} \right). \tag{2.33}$$

By using Eqs. (2.16), (2.23) and the Boltzmann distribution (2.19) we obtain for the ratio of the emission and the absorption profile (the so-called source function S_ν):

$$S_\nu \equiv \frac{\eta_\nu}{\kappa_\nu} = \frac{2\mathrm{h}\nu^3}{\mathrm{c}^3} \frac{1}{\mathrm{e}^{\mathrm{h}\nu/\mathrm{k_B}T} - 1} \tag{2.34}$$

which corresponds to the black-body radiation function (Eq. (2.21)). For an optically thick plasma (optical depth $\tau_\nu \equiv \kappa_\nu x \gg 1$) the line intensity approaches the black-body radiation level. If the re-absorption is not strongly pronounced, Eq. (2.33) reduces to

$$I_\nu(x) = \eta_\nu x, \tag{2.35}$$

which means that the line intensity is just given by the line integrated emission coefficient.

Considering these both extreme cases for a real laboratory plasma with a temperature gradient (lower temperatures at the edge), one can explain the often observed drop of line intensities in the centres of optically thick resonance lines. The absorption is highest in the line centre and therefore, the radiation at these central frequencies from the plasma centre is reabsorbed and mainly the lower-temperature radiation from the plasma edge reaches the detector. On the other hand, the radiation at the remaining frequencies (outside the line centre) suffers lower absorption and the detector "sees" an apparent higher average temperature (Figure 2.6).

The influence of the radiation trapping on the population density of an excited level
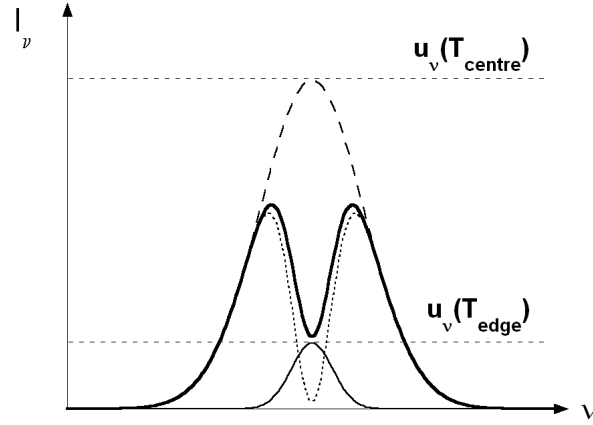
Figure 2.6: Radiation trapping in inhomogeneous optically thick plasmas. The dashed line is the emission coefficient profile of an optically thick line in the bulk plasma. The dotted line is the same profile after re-absorption by the plasma. The thin solid line is the emission profile of an optically thick line in the plasma edge and finally the thick solid line is the profile as seen from outside of the plasma.

n_{u} can be investigated by considering its time development at location x [Holstein, 1947, 1951]:

$$\frac{\mathrm{d}}{\mathrm{d}t} n_{\mathrm{u}}(x) = -A_{\mathrm{ul}} n_{\mathrm{u}}(x) + A_{\mathrm{ul}} \int n(x') G(x', x)\, \mathrm{d}x'. \qquad (2.36)$$

The second term allows for the excitation due to reabsorption of the line radiation from elsewhere in the plasma where $G(x', x)\mathrm{d}x$ is the probability that a photon emitted at x' is absorbed at x. Because of $n_{\mathrm{u}} \ll n_{\mathrm{l}}$, the induced emission is very ineffective and can be neglected. (A different situation is encountered when dealing with high power resonant laser radiation: the strongly increased upper level density can even cause dropping the absorption coefficient to zero, making the medium transparent - see Sec. 2.1). The function $G(x', x)$ is calculated using

$$G(x', x) = -\frac{1}{4\pi(x' - x)^2} \frac{\partial T}{\partial (x' - x)}, \qquad (2.37)$$

where $T(x' - x)$ is the probability for a photon not to be absorbed after passing the distance $(x' - x)$

$$T(x' - x) = \int\limits_{\mathrm{line}} P(\nu) \mathrm{e}^{-\kappa_\nu (x' - x)} \mathrm{d}\nu. \qquad (2.38)$$

The solution $n_{\mathrm{u}}(x)$ of the Eq. (2.36) can be represented with an infinite sum of eigenfunctions $n_{\mathrm{u},i}(x)$, which exponentially decay with the corresponding decay time $A_{\mathrm{ul}} g_i$:

$$n_{\mathrm{u}}(x) = \sum_{i=0}^{\infty} n_{\mathrm{u},i}(x)\mathrm{e}^{-A_{\mathrm{ul}}g_i t}. \tag{2.39}$$

g_i are the corresponding eigenvalues arranged with $g_0 < g_1 < g_2...$ This means that after a long enough time the initial profile consists only of the fundamental mode since the higher modes are distinct and this mode decays with the time constant $g_0 A_{\mathrm{ul}}$. Its eigenvalue g_0 is called the escape factor. It turns out that for a large range of optical depths of 10^{-1} to 10^4, transition probabilities modified with the escape factor can be used in collisional-radiative models without producing considerable errors in the level populations [McWhirter, 1965].

The calculation of the escape factor is not straight forward and depends on the absorption coefficient at the line centre, the line shape and the geometry of the plasma. For a Gaussian line profile, an infinite cylinder with radius R and an optical depth of $\tau_\nu < 10^2$ Fujimoto [2004] provides the following formula to calculate the escape factor

$$g_0 \simeq \frac{1.92 - 1.3/(1 + (\kappa_0 R)^{6/5})}{(\kappa_0 R + 0.62)[\pi \ln(1.357 + \kappa_0 R)]^{1/2}} \tag{2.40}$$

with the absorption coefficient in the line centre

$$\kappa_0 = \frac{\mathrm{e}^2}{4\mathrm{m_e}c\epsilon_0 \Delta\omega_{\mathrm{G}}\sqrt{\pi}} n_{\mathrm{l}} f_{\mathrm{lu}}, \tag{2.41}$$

where $\Delta\omega_{\mathrm{G}}$ is the width of the Gaussian line profile and f_{lu} is the oscillator strength of the transition. Additional calculation results can be found in [Irons, 1979, Behringer, 1998].

2.3 Shapes of spectral lines

Any emitted line radiation is not strictly monochromatic. The radiation is always emitted within a certain frequency interval $\mathrm{d}\omega$ and the minimum line width is called the natural line width, which is due to the finite lifetime of the upper (radiating) level. Moreover, there are several other mechanisms which change the shape or even the maximum frequency of spectral lines in plasmas. They will be described in the following beginning with a distinction between the homogeneous and inhomogeneous broadening mechanisms, which are of importance for the laser-induced fluorescence spectroscopy.

2.3.1 Homogeneous and inhomogeneous broadening mechanisms

There are two different kinds of processes that lead to spectral line broadening. In the case of a homogeneously broadened line the emission or absorption probability of a photon with the frequency ω along a transition between two bounded levels u and l is the same for all considered atoms [Demtröder, 2000]. This means that all atoms are characterised by the same emission/absorption line profile. Line broadening due to finite

or reduced lifetimes of the upper level are examples of homogeneous broadening. The shape of those lines is given by the Lorentzian profile. On the other hand, atoms with an inhomogeneous line profile will have a different emission/absorption profile depending on their velocity component v_z in the observation or the laser beam direction. Doppler broadening in plasmas or line profiles of impurities in solids (influence of the lattice environment) [Stenholm, 2006] are examples of inhomogeneous line broadening. A Gaussian shape of such lines is then given unless the frequency of velocity changing collisions in the plasmas is too high [Sobelman, 1957]. The difference between both kinds of broadening has a consequence for resonant laser pumping: in the case of a homogeneously broadened line strictly monochromatic laser light is resonant with all atoms in the lower level. If the transition is Doppler broadened, the laser can pump only a fraction of the atoms whose relevant velocity component v_z lies in the range of $\Delta v_z = \Delta \omega_h \lambda / 2\pi$ from the resonant velocity $v = v_{max} - c(\lambda - \lambda_0)/\lambda_0$ (λ_0 denotes the centre of the Doppler absorption profile, v_{max} the corresponding velocity, $\Delta \omega_h$ the homogeneous line width and λ the laser wavelength; the laser beam propagates from negative to positive z values). To maximise the pumping rate in case of inhomogeneously broadened transitions it is thus desirable to use lasers with a spectral width of at least the Doppler width.

2.3.2 Natural line width

The appearance of a finite line width can be understood in the frame of a classical treatment of an excited atom as a damped oscillator with a non-zero damping constant γ. The oscillation amplitude in the case of weak damping is given by

$$x(t) = x(t{=}0)e^{-(\gamma/2)t} \cos \omega_0 t \tag{2.42}$$

where ω_0 is the undamped oscillator frequency. While the Fourier transform of a pure sinusoidal oscillation returns a single frequency ω_0 of the sine function the transformation of an oscillation with an exponential amplitude decay

$$A(\omega) = \frac{1}{2\pi} \int\limits_{-\infty}^{\infty} x(t)e^{-i\omega t} dt \tag{2.43}$$

(i denotes the imaginary unit) provides the following frequency distribution

$$I(\omega) = \frac{\gamma/2\pi}{(\omega - \omega_0)^2 + (\gamma/2)^2}. \tag{2.44}$$

This is the so-called Lorentz profile (Figure 2.7). Its full width at half maximum of $\delta\omega = \gamma$ is the natural line width. Lorentz profiles determine the shape of those spectral lines for which the dominant broadening mechanism is due to the finite lifetime of the upper level.

On the other hand it can be shown that the intensity emitted by a damped oscillator falls exponentially with a time constant γ [Demtröder, 2000]. In this way a relation is found between the lifetime τ_u of the excited level, the transition probability (the Einstein
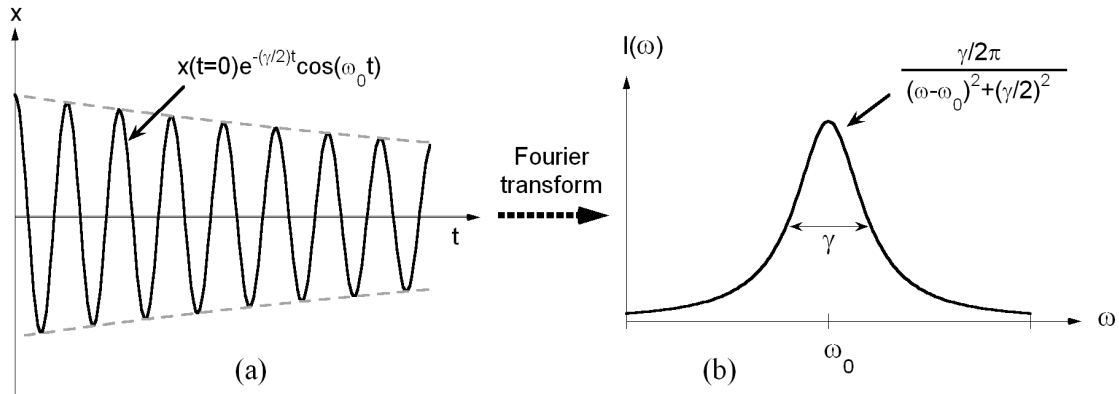
Figure 2.7: The Fourier transform of a weakly damped oscillating amplitude (a) results in a Lorentzian line shape (b).

coefficient) for spontaneous decay $A_{ul} = 1/\tau_u$ and the natural line width $\delta\omega$:

$$\delta\omega = \gamma = \frac{1}{\tau_u} = A_{ul}. \tag{2.45}$$

Interestingly, the above relation between the natural (minimal) line width and the lifetime of a radiating level can be derived from the Heisenberg uncertainty principle. Giving a lifetime τ_i of a level its energy can be determined with the minimum uncertainty of $\Delta E_u = \hbar/\tau_u$. Assuming an infinite lifetime for the ground state (lower level), with $\delta\omega = \Delta E/\hbar$ one obtains:

$$\delta\omega = \frac{\Delta E_u}{\hbar} = \frac{1}{\tau_u}. \tag{2.46}$$

The transition probabilities of atomic dipole transitions in the visible spectrum typically lie in the range of $A_{ul} \sim 10^7\,\mathrm{s}^{-1}$. The natural line width then is $\delta\omega \approx 10\,\mathrm{MHz}$ and hence several orders of magnitude lower than the frequency of the emitted wave of $\omega \approx 2\pi c/600\,\mathrm{nm} \approx 3 \times 10^{15}\,\mathrm{Hz}$, which legitimates the above assumption of a weakly damped oscillator. Therefore, in a plasma in most cases line widths are dominated by additional broadening mechanisms.

2.3.3 Doppler broadening

A system in thermal equilibrium can be characterised by a temperature T, which is always larger than zero. The temperature is a measure of the kinetic energy of the
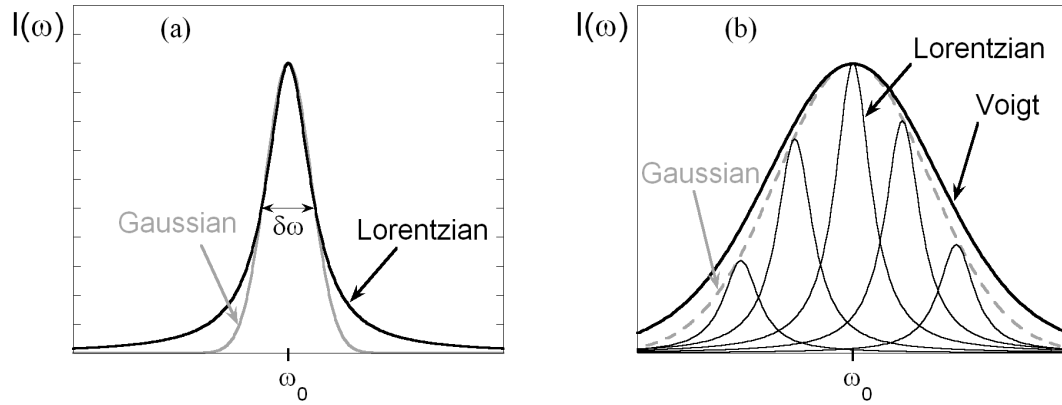
Figure 2.8: (a) Comparison of a Gaussian and a Lorentzian line shape of the same width and normalised to the same maximum amplitude. (b) Convolution of a Gaussian and Lorentzian results in a Voigt profile.

atoms. Thus, all atoms move with a non-zero velocity and the fraction of the atoms with a mass m and a velocity component v_z (the z axis should denote the direction of the laser beam propagation) lying in the interval $\mathrm{d}v_z$ is given by the Maxwellian distribution function:

$$n(v_z)\mathrm{d}v_z = \frac{N}{v_{\max}\sqrt{\pi}}\,\mathrm{e}^{-(v_z/v_{\max})^2}\mathrm{d}v_z, \tag{2.47}$$

where N is the total number of atoms and $v_{\max} = \sqrt{2kT/m}$ the most probable velocity. Given ω_0 to be the centre of an absorption line with a (homogeneous) line width $\delta\omega_h$ an atom moving with a velocity component $v_z \ll$ c along the laser beam propagation direction will experience in its frame of reference the laser frequency ω_L to be shifted due to the Doppler effect by the value $\Delta\omega = \omega_L v_z/\mathrm{c}$, which is equivalent to a shift of the absorption frequency ω_0 by the value

$$\Delta\omega = \omega_0\frac{v_z}{\mathrm{c}}. \tag{2.48}$$

By inserting the above Doppler shift relation into the Maxwell distribution function (2.47) and considering that the absorbed intensity linearly depends on the particle density one can see that the absorption profile of a Doppler broadened line has the same shape as the Maxwell distribution, which is called the Gaussian profile:

$$I(\omega) = I(\omega_0)\mathrm{e}^{-\left(\frac{\omega-\omega_0}{\omega_0 v_{\max}/\mathrm{c}}\right)^2} \tag{2.49}$$

The Doppler width of such a profile is given by

$$\Delta\omega_D = 2\sqrt{\ln2}\,\frac{v_{\max}}{\mathrm{c}}\omega_0 = \sqrt{\frac{8\ln2\,kT}{m}}\frac{\omega_0}{\mathrm{c}}. \tag{2.50}$$

The Doppler widths of visible lines of helium gas at room temperature ($T = 300\,\mathrm{K}$) is

lying in the range of $\Delta\omega_{\mathrm{D}} \sim 2 \times 10^{10}$ Hz. This is around three orders of magnitude larger than the corresponding natural line widths (see Sec. 2.3.2). However, the exponential decrease of a Gauss profile is much stronger in the line wings than that of a Lorentzian (Figure 2.8). Therefore, it is sometimes possible to derive information on the homogeneous line width by investigation of the far wing regions of Gaussian profiles. If the homogeneous line width is not very much smaller than the Doppler width the absorption profile deviates from the Gaussian shape. This is because the absorption profile must be then considered as a convolution of Lorentz profiles over the whole velocity distribution function being a Gaussian. This convolution

$$I(\omega) = C \int\limits_{0}^{\infty} \frac{\mathrm{e}^{-\left(\frac{\omega-\omega_0}{\omega_0 v_{\mathrm{max}}/c}\right)^2}}{(\omega-\omega_0)^2 + (\gamma/2)^2} \mathrm{d}\omega_0 \tag{2.51}$$

results in the Voigt profile. Different approximations for calculation of the Voigt profile are used since there is no analytic solution of the convolution integral [Traving, 1968].

At low plasma densities the Doppler broadening typically dominates over other broadening mechanisms [Unsöld, 1968]. This holds also for thermal and supersonic helium beams in the plasma edge of fusion experiments.

2.3.4 Pressure broadening

The energies of radiating or absorbing atomic levels are affected by the collisions of atoms with other plasma particles. One can distinguish between elastic and inelastic collisions, which are also called quenching collisions because the excited atom transfers its excitation energy to the perturber without light emission.

The frequency shift $\Delta\nu$ depends amongst others on the distance between the collision partners. In a plasma that is in thermal equilibrium these distances are statistically distributed and hence, if the density of collision partners is large enough, the line profile experiences an additional broadening and in some cases also a shift of the line centre. The former is called pressure broadening since it typically depends linearly on the perturber density (for high densities deviation from the linear dependence has been observed for an atomic helium line by Büscher et al. [1995]).

Inelastic collisions can be treated as processes reducing the lifetime of the excited level. With the quenching collision frequency S_{ul}, the lifetime τ_{u} reduction of the upper level (according to Eq. (2.45))

$$\tau_{\mathrm{u}} = \frac{1}{\mathrm{A}_{\mathrm{u}} + S_{\mathrm{ul}}} \tag{2.52}$$

is the reason for the homogeneous line broadening while a shift of the line profile cannot be caused by those collisions. Elastic collisions are, in contrast, generally responsible for both, the line broadening and the shift. If the radiative transition from the upper to the lower level occurs during an elastic collision, the frequency of the emitted photon can be shifted to both lower or higher values depending on the interaction with the collision

partner. Hence, the broadened line profile can additionally experience a shift.

For both elastic and inelastic collisions it can be shown, again by using the classical oscillator model, that they result in homogeneous line broadening. When considering inelastic collisions, the same line of arguments can be followed, as in the case of the natural line width (Sec. 2.3.2), by adding an additional damping constant to the description of the oscillator, which affects its amplitude. Elastic collisions affect only the oscillator phase owing to the emission frequency shift during a collision. In this case one also obtains a Lorentzian shaped line profiles [Traving, 1960].

In plasmas with a sufficient degree of ionisation (electron concentration of more than 1%), the most important process leading to pressure broadening will be due to collisions with charged particles owing to the long-distance Coulomb forces [Wiese, 1965]. If a charged particle (perturber) collides with an atom in which the L-degeneracy is removed (like in helium) the electric field of the perturber interacts with the dipole moment of the atom induced by the perturber itself (quadratic Stark effect) as well as with its permanent quadrupole moment (for L$\neq$0) [Traving, 1968]. For electron densities $n_e < 10^{15}$cm^{-3} the helium lines in the visible spectral range can be treated as isolated lines, i.e. as lines whose Stark widths are much smaller than the zero-field separations between the interacting levels (e.g. the 3S, P and D levels). For isolated lines the Stark broadening due to electron impact will be dominant [Griem, 1974]. The weakly temperature dependent half widths have been calculated and tabulated by Griem [1974] for this case by using the classical impact approximation (fast moving perturbers cut the emitted wave train into a number of smaller independent ones). For electron densities of $n_e = 10^{13}$cm^{-3} the widths are less than $\Delta\lambda_{S,e} < 0.1$ pm, further decreasing for even lower densities ($\Delta\lambda_{S,e} \propto n_e$) and therefore are negligible compared to the Doppler broadening.

Resonance broadening, or self broadening, plays a role if the considered atoms collide with atoms of the same kind and if one of the levels interacts with the ground state (only possible in singlet helium). Typically a very low broadening contribution for not very high pressures can be estimated by [Sobelman et al., 1995]

$$\delta\omega = 9 \times 10^{15} \frac{e^2}{m_e \omega_0} f N, \tag{2.53}$$

where f is the oscillator strength and N the perturber density in cm^{-3}.

The Van der Waals broadening is due to collisions with a different gas or with the same gas if no resonant transfer of excitation energy, as in the case of the self broadening, is possible. This mechanism has even weaker impact on the overall line broadening. In this case the line width can be calculated with [Sobelman et al., 1995]

$$\delta\omega = 8 \times 10^{-12} n^{*8/5} v^{3/5} N, \tag{2.54}$$

where n^* is the effective principal quantum number and v the atom velocity in cm/s. For $v = 10^5$ cm/s, $\omega_0 = 10^{15}$ s^{-1}, $f_{lu} = 1$ and $N_{He} = 10^{13}$ cm^{-3} we get for the line width due to resonance broadening $\delta\omega \approx 2.5$ MHz and due to Van der Waals broadening $\delta\omega \approx 500$ kHz i.e. values comparable to the natural line widths (see Sec. 2.3.2).

Shapes of lines which are broadened by both the collisional and Doppler mechanism

are described by the Voigt profile if both processes are statistically independent [Griem, 1974].

2.3.5 Saturation broadening

Saturation line broadening is important in laser spectroscopy due to the very high laser powers being available nowadays. We assume a system of two non-degenerated levels with lower level l, the upper level u and with a homogeneously broadened absorption line profile $\alpha(\omega)$. This profile has, for weak laser powers, which do not considerably change neither the population of the lower (N_l) nor the upper level (N_u), the same Lorentzian shape as the profile of the absorption cross section $\sigma_{lu}(\omega)$:

$$\alpha_{lu}(\omega) = \frac{\gamma/2\pi}{(\omega - \omega_0)^2 + (\gamma/2)^2} = \sigma_{lu}(\omega)(N_l - N_u) \tag{2.55}$$

with the line width γ, the line centre at $\omega = \omega_0$ and the normalisation $\int_0^\infty \alpha_{lu}(\omega)\,d\omega = 1$. The absorption coefficient is proportional to the difference of the lower and the upper level population because the laser is absorbed by atoms in both levels in the same way (see Eq. (2.3)). However, strong laser powers have impact on the difference in population and in this way change the shape of the absorption coefficient profile. According to the first case $t \leq T_L$ of Eq. (2.4), keeping in mind that the upper level population is initially zero, we derive the dependence between the population differences with (ΔN) or without (ΔN_0) laser and the saturation parameter S

$$\Delta N = \frac{\Delta N_0}{1 + S} \tag{2.56}$$

and thus the saturation parameter dependence of the laser absorption coefficient profile $\alpha_{lu}^L(\omega)$ becomes:

$$\alpha_{lu}^L(\omega) = \frac{\alpha_{lu}(\omega)}{1 + S} \tag{2.57}$$

(for high saturation parameters the medium becomes transparent for additional radiation!). Finally we need the spectral dependence of the saturation parameter of the monochromatic laser radiation. Being proportional to the pumping rate (Eq. (2.5)), it also has a Lorentzian shape, which can be written as

$$S(\omega) = S_0 \frac{(\gamma/2)^2}{(\omega - \omega_0)^2 + (\gamma/2)^2}\,, \tag{2.58}$$

where S_0 is the value of the saturation parameter in the line centre. Inserting Eqs. (2.55) and (2.58) into Eq. (2.57) we obtain

$$\alpha_{lu}^L(\omega) = \frac{C}{(\omega - \omega_0)^2 + (\gamma/2)^2(1 + S_0)} \tag{2.59}$$
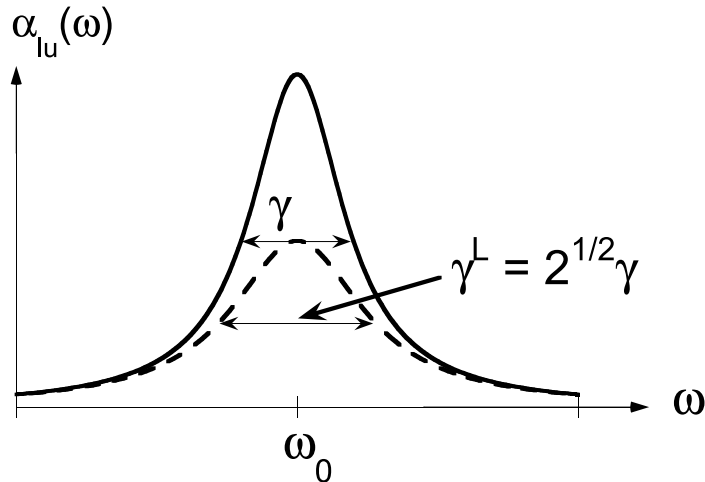
Figure 2.9: Lorentz absorption coefficient profile of a homogeneously broadened line (solid line) and the same profile broadened by laser radiation with the central saturation parameter $S_0 = 1$ (dashed line).

with a constant C. This is again a Lorentzian profile, however, with a larger width γ^{L} depending on the saturation parameter in the line centre as follows:

$$\gamma^{\mathrm{L}} = \gamma\sqrt{1 + S_0}. \tag{2.60}$$

The saturation line broadening is a result of a stronger squeezing of the absorption coefficient in the line centre than on the wings due to a stronger laser absorption in the line centre. A comparison between a Lorentz profile with $S_0 = 1$ and without is shown in Figure 2.9. The absorption in the line centre drops by a factor of two while the line width increases by $\sqrt{2}$.

Saturation broadening of inhomogeneously broadened lines results in Voigt-Profil [Demtröder, 2000].

2.3.6 Instrumental broadening

Assuming an ideal monochromatic light source to be resolved with a spectrometer, one will always observe a finite line width. Similarly, when pumping a spectral transition with an idealised monochromatic absorption profile, by use of a narrow-band laser will provide a fluorescence spectral profile with a finite width. This is because there are no ideal measuring instruments and each of them can be characterised with the so-called instrumental function, which can be measured by using a (nearly) monochromatic light source or absorption profile or calculated by using convolution techniques [Jannson, 1997]. A measured profile from an arbitrary experiment is then a convolution of the instrumental function and the actual profile under investigation. It can be obtained by appropriate correction of the measured profile.

2.4 Line splitting

2.4.1 Fine structure

The emission of electric dipole radiation is a result of an electronic transition between two quantum levels designated with sets of quantum numbers. Selection rule for the orbital angular momentum quantum number l of the optical electron for this kind of radiation, as derived from quantum mechanics, is:

$$\Delta l = \pm 1. \tag{2.61}$$

In general, doublet, triplet, or lines of higher multiplicity are observed, on the basis of the so-called fine structure of the atomic energy levels. Fine structure arises from the combination of two types of angular momentum in determining the magnetic moment of an atomic system: orbital angular momentum ($\boldsymbol{L}$) and spin angular momentum ($\boldsymbol{S}$). Provided that only one electron (the so-called 'optical electron') is involved in a particular atomic transition, we need only consider the angular momenta relevant to that electron: $\boldsymbol{l}$, $\boldsymbol{s}$. In order to understand the relative contributions of the two types of angular momenta to the atomic magnetic moment, a relativistic treatment of the electron motion in the atom is required. This is provided by the Dirac equation, which yields a value of exactly $g_{\mathrm{s}} = 2$ for the so-called gyromagnetic ratio [Bransden and Joachain, 1983] of the electron. The modern theory of quantum electrodynamics has shown that the true value of g_{s} is larger by about 0.2% [Bethe and Salpeter, 1977]. From the process of spin-orbit coupling, one can deduce the number of sublevels into which a particular atomic level is split, on the basis of the orbital and spin quantum numbers. The quantum-mechanical theory of the coupling of angular momenta yields a resultant angular momentum $\boldsymbol{J}$, with corresponding values for the angular momentum quantum number:

$$|L - S| \leq J \leq L + S \tag{2.62}$$

in steps of unity. The units of the vector operator $\boldsymbol{J}$ are $\hbar = \mathrm{h}/(2\pi)$. In the case of a single electron, we have $s = 1/2$, and therefore at most two values for the quantum number J (now denoted as j) are possible:

$$j = l - s, \text{ or } j = l + s. \tag{2.63}$$

In the case of vanishing orbital angular momentum (the so-called s-states), we have simply $j = s$ and the levels do not show any fine structure. For single-electron atoms, levels with $l \geq 1$ split into two sublevels (doublet structure) such as it is e.g. visible in the case of the sodium (which has only one valence electron in the second shell and can therefore be treated approximately in this way) D-line $(3^2\mathrm{P}_{1/2,3/2} {\rightarrow} 3^2\mathrm{S}_{1/2})$. Additional selection rules for electric dipole transitions between levels due to the new quantum number J are:

$$\begin{aligned} \Delta J &= 0, \pm 1, \text{ with the case} \\ J &= 0 \rightarrow J' = 0 \end{aligned} \tag{2.64}$$

strictly forbidden for all single-photon transitions. For the single optical electron, the corresponding selection rule, which should be applied together with (2.61), is

$$
\begin{aligned}
\Delta j &= \pm 1 \\
\Delta j &= 0 \text{ except if } j = 0
\end{aligned}
\qquad . \tag{2.65}
$$

The energy splitting between the sublevels of the hydrogen atom without including the Lamb shift (a quantum electrodynamic process arising from the emission and absorption of virtual photons by the electrons) is given by [Sobelman, 1979]:

$$
\Delta E_{\text{FS}} = \frac{Z^4 \alpha^2}{n^3 l(l+1)} \text{Ry}, \tag{2.66}
$$

where Z is the nuclear charge, Ry the Rydberg energy

$$
\text{Ry} = \frac{1}{2} \text{m}_{\text{e}} \text{c}^2 \alpha^2 \approx 13.6 \,\text{eV}, \tag{2.67}
$$

and α the fine-structure constant

$$
\alpha = \frac{1}{4\pi\epsilon_0} \frac{\text{e}^2}{\hbar \text{c}} \approx \frac{1}{137} \,. \tag{2.68}
$$

The fine-structure splitting is of the order of α^4, and is thus some α^2 smaller than the level spacing (e.g. $\Delta E_{\text{FS}} \approx 5 \times 10^{-5}\,\text{eV}$ for the L_α line of the hydrogen atom). Moreover, it scales as n^{-3} and therefore is much lower for highly excited levels.

In atoms with more than one electron the interaction between orbital and spin angular momenta of all electrons not belonging to a filled shell must be considered. The total angular momentum of the filled shells is equal to zero. The use of quantum mechanical rules again provides the quantum number J (in capital letter as for the whole electron system) of the total angular momentum. If the coupling between the orbital $\boldsymbol{l}_i \cdot \boldsymbol{l}_j$ or spin $\boldsymbol{s}_i \cdot \boldsymbol{s}_j$ momenta of the electrons (electrostatic interaction) is stronger than the coupling between the momenta of the single electrons $\boldsymbol{l}_i \cdot \boldsymbol{s}_i$ (spin-orbit interaction), the total orbital momentum $\boldsymbol{L}$ and total spin $\boldsymbol{S}$ are constructed first, and thereafter form together the total angular momentum $\boldsymbol{J}$ (LS or Russel-Saunders coupling). In the opposite case, the total angular momenta $\boldsymbol{j}_i$ of the individual electrons interact with each other, and form the total angular momentum $\boldsymbol{J}$ of the system (jj coupling). As a rule, the general level structure of atoms at the beginning and middle of the periodic system of elements corresponding to lower excited states are well explained in the LS coupling approximation [Sobelman, 1979]. This also holds for the helium atom (however, with some exceptions, e.g. of the 4Fᵒ levels, [Parish and Mires, 1971]). jj coupling, on the other hand, is of interest for heavy elements as well as for multiply charged ions since the spin-orbit interaction strongly increases with nuclear charge ($\propto Z^4$) whereas the electrostatic interaction is approximately proportional to Z. There are also some other coupling schemes, such as jl coupling (also referred to as jK coupling [Cowan and Andrew, 1965]), which is used in systems with the optical electron being far away from the core (noble gases). Here, the total orbital angular momentum of the core $\boldsymbol{L}$

couples with its total spin momentum $\boldsymbol{S}$ building the momentum vector $\boldsymbol{j}$ which further couples to the orbital angular momentum $\boldsymbol{l}$ of the optical electron since the spin-orbit interaction of the optical electron is very weak. Finally, the resulting angular momentum $\boldsymbol{K}$ couples to the spin of this electron. Independently of the coupling type, the number of sublevels is the same for a given momentum $\boldsymbol{J}$ [Shevelko and Vainshtein, 1993]. In many cases, the use of such coupling schemes is not possible and intermediate coupling mechanisms must be used. In the following, only the LS coupling, taking atomic helium as an example, is explained in some more detail.

In the ground state both electrons of atomic helium are in the $1^1\mathrm{S}_0$ level with $l_1 = l_2 = 0$. If one of the electrons is in a higher energy level, the total angular momentum quantum number L, constructed along to the rule

$$L = l_1 + l_2,\, l_1 + l_2 - 1,\, ...,\, l_1 - l_2,\ \text{with } l_1 \geq l_2, \tag{2.69}$$

can take only one value of $L = l_1$ because $l_2 = 0$. In all other levels than the ground state, the spin of both electrons can be oriented parallel or antiparallel with the respective total spin quantum numbers of $S = 0$ (singlet helium) or $S = 1$ (triplet helium). In the first case the total angular momentum quantum number J has only one possible value of $J = L$ (no fine structure) while $S = 1$ results in three possible values of $J = L + 1, L, L - 1$ but only for $L \geq 1$. This means that all triplet levels except the $n^3\mathrm{S}$ levels split up into three sublevels. The selection rules for electric dipole transitions of light atoms, besides those in (2.64), are:

$$\begin{aligned} \Delta L &= \pm 1 \\ \Delta S &= 0 \end{aligned} \quad . \tag{2.70}$$

The constancy of the total spin means that there are no dipole transitions between singlet and triplet levels (intercombination lines) in helium, at least in the visible spectral range (in fact, some levels of the higher n shells do not obey the pure LS coupling). This criterion is used as a proof for the validity of the LS coupling.

The fine structure splitting of $n^3\mathrm{P^o}$ and $n^3\mathrm{D}$ levels of atomic helium and helium-like ions can be calculated, respectively, from [Bethe and Salpeter, 1977]:

$$\Delta E = \tfrac{1}{12} \mathrm{m_e c}^2 \alpha^4 \frac{(Z-1)^3}{n^3} \begin{cases} 6 - (Z - 3) & \text{for } j = 0 \rightarrow 1 \\ -\tfrac{2}{5} - 2(Z - 2) & \text{for } j = 1 \rightarrow 2 \end{cases}$$

$$\Delta E = \tfrac{1}{60} \mathrm{m_e c}^2 \alpha^4 \frac{(Z-1)^3}{n^3} \begin{cases} 4 - 2(Z - 3) & \text{for } j = 1 \rightarrow 2 \\ -\tfrac{3}{7} - 3(Z - 2) & \text{for } j = 2 \rightarrow 3 \end{cases} \tag{2.71}$$

(these equations take the relativistic corrections into account, and also the spin-orbit and spin-spin interactions). In Figure 2.10 (a) it can be seen how two triplet levels $2^3\mathrm{P^o}$ and $3^3\mathrm{D}$ each split into three sublevels (note the inverse energy shifts, i.e. $\Delta E_{J-1} > \Delta E_J$, which is typical for helium [Heckmann and Träbert, 1980]). Therefore, triplet transitions which are not connected to the $n^3\mathrm{S}$ levels split into more than 3 lines: in this case six. The spectral distances of five of them are in the range of $\pm 2\,\mathrm{pm}$ (Figure 2.10 (b)) while
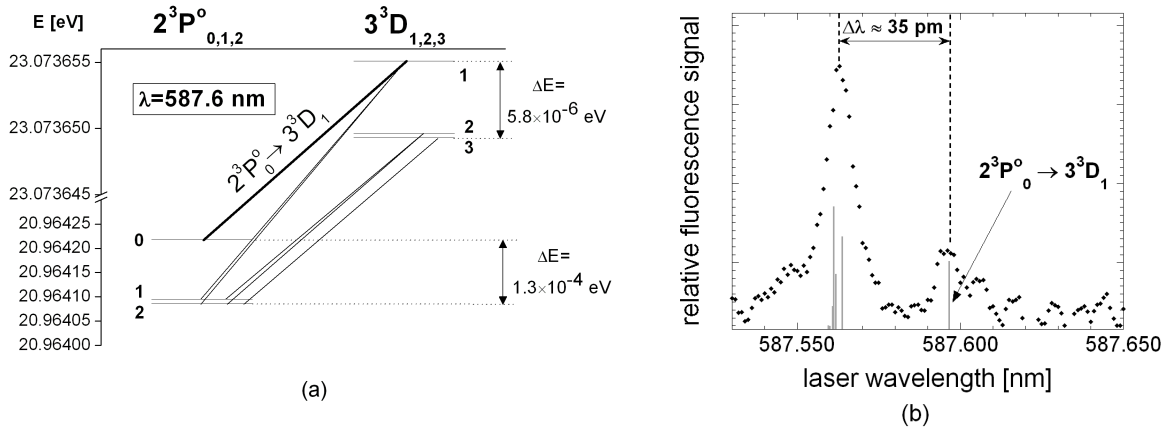
Figure 2.10: Fine structure splitting of two triplet levels of atomic helium: 2^3Po and 3^3D; a) Part of the Grotrian diagram including both levels; b) LIF measurement at a glow discharge resolving two main structures of the split line at $\lambda = 587.6$ nm (all six components are superimposed with their relative Einstein coefficients A_{ki}).

one line $(3^3\mathrm{D}_1 \rightarrow 2^3\mathrm{P}_0^o)$ is separated by ~ 35 pm from the others because of the much larger energy separation between the $2^3\mathrm{P}_J^o$ sublevels. The larger separation has been observed by a LIF experiment in a glow discharge, which we use for the calibration of the laser (Figure 2.10 (b), see also Sec. 4.2). The higher peak at lower wavelength consists of five lines which could not be resolved because of their Doppler broadening (for $T_{\mathrm{He}} = 300$ K: $\Delta\lambda_{\mathrm{D}} \approx 3.6$ pm) combined with the laser spectral width ($\Delta\lambda_{\mathrm{L}} \approx 2$ pm) and the saturation broadening. Another example of the fine structure of atomic helium is given in Figure 4.6 rhs.

2.4.2 Zeeman splitting

The energies of electronic levels in atoms, since they are connected to the orbital and spin magnetic moments of the electrons, are sensitive to external magnetic fields. This corresponding alteration of the unperturbed atomic spectra by an external magnetic field is known as the Zeeman effect, and, in stronger fields, is also referred to as the Paschen-Back effect. In a weak magnetic field, the Zeeman effect is classified as 'normal' or 'anomalous', this classification being made purely on historical grounds, since the so-called 'anomalous' effect is far more common. The term 'normal' applies if the atom has a zero total spin angular momentum (singlets) and the latter in the case of nonzero total spin (multiplets). If the coupling of the atomic magnetic moments to the external fields is comparable to, or exceeds, the spin-orbit coupling, one deals with the Paschen-Back effect. Magnetic fields, as they typically occur in fusion experiments, result in considerable changes in level structures and therefore are explained in more detail below.
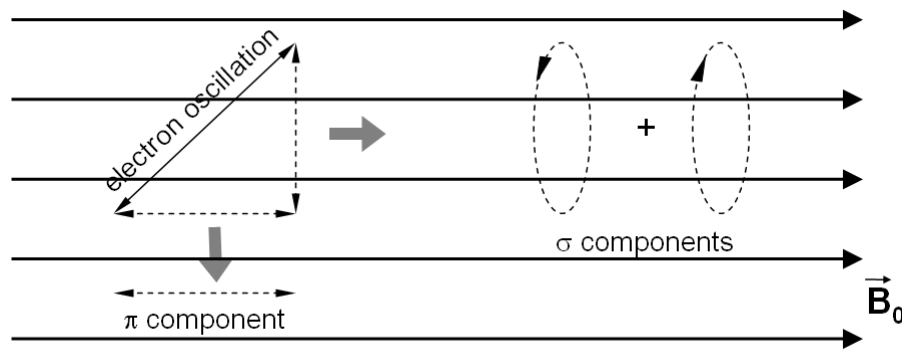
Figure 2.11: Classical oscillator model for explanation of the normal Zeeman effect.

2.4.2.1 Normal Zeeman effect

The normal Zeeman effect describes the splitting of levels with pure orbital momentum ($\boldsymbol{S}{=}0$, $\boldsymbol{J}{=}\boldsymbol{L}$), i.e. singlet levels, for example of atomic helium. This splitting can be depicted by using the classical model of an oscillating electron emitting light at a frequency ω at a transition between two levels under consideration (see Figure 2.11) [Haken and Wolf, 1990]. An oscillation along an arbitrary axis can be represented as a superposition of a linear oscillation along the magnetic field lines and two opposite circular oscillations, which add up to the perpendicular linear oscillation.[1] No interaction between the magnetic field and the dipole moment parallel to $\boldsymbol{B}_0$ ($\boldsymbol{v}{\times}\boldsymbol{B}_0{=}\boldsymbol{0}$) takes place. The Lorentz force due to the circular oscillation results in a positive and a negative frequency shift (depending on the oscillation direction) of

$$\delta\omega_\pm = \pm\frac{\mu_\mathrm{B}}{\hbar}B_0 = \frac{\mathrm{e}B_0}{2\mathrm{m_e}}, \qquad (2.72)$$

Moreover, we infer also the polarisation of all components:

- π line: linear polarised light is emitted at the non-shifted frequency perpendicular to $\boldsymbol{B}_0$ (no dipole radiation along the dipole axis); the electric field vector $\boldsymbol{E}$ of the radiation is parallel to the magnetic field line.

- σ^+ and σ^- lines: circularly polarised light is emitted along $\boldsymbol{B}_0$ and linearly polarised (with $\boldsymbol{E} \perp \boldsymbol{B}_0$) perpendicular to $\boldsymbol{B}_0$. The parallel radiation has twice the intensity of the perpendicular one. The σ^+ light has a higher frequency and is right-hand circularly polarised (with respect to the direction of $\boldsymbol{B}_0$) while the opposite holds for σ^- light.

---

[1]This is the classical analysis of Lorentz and therefore the triplet of lines appearing in the normal Zeeman effect is referred to as a Lorentz triplet.
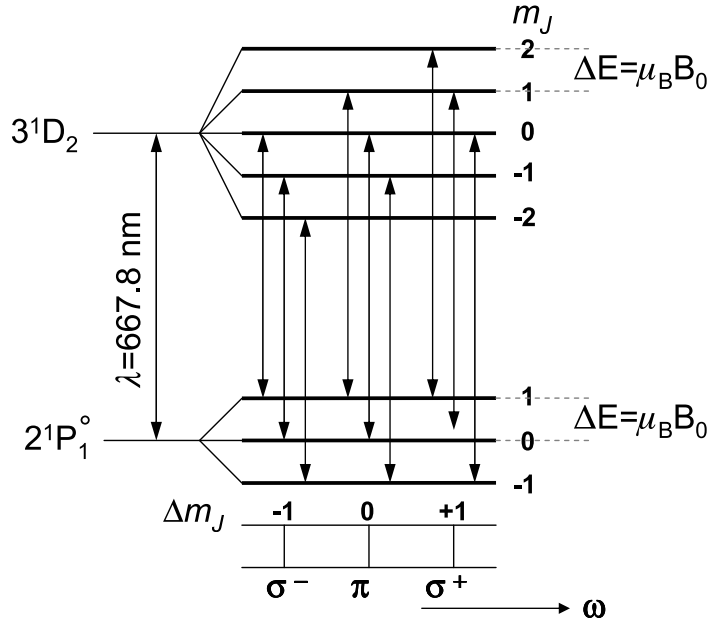
Figure 2.12: Splitting of a neutral helium line (normal Zeeman effect).

Under perpendicular observation (with respect to $\boldsymbol{B}_0$), the unshifted π component has twice the intensity of either σ component. The intensities are distributed spatially according to:

$$P_\pi(\Theta) = \tfrac{3}{8\pi}\sin^2\Theta$$

$$P_{\sigma_\pm}(\Theta) = \tfrac{3}{16\pi}(1 + \cos^2\Theta),$$

(2.73)

where Θ denotes the angle between the direction of observation and that of the external magnetic field.

Quantum mechanical calculations of the interaction energy between the magnetic field and the total angular momentum $\boldsymbol{J}$ yield for both, the normal and the anomalous Zeeman effect, the expression

$$\Delta E_{mj} = -m_J g_J \mu_{\mathrm{B}} B_0.$$

(2.74)

g_J is the Landé factor

$$g_J = 1 + \frac{J(J+1) + S(S+1) - L(L+1)}{2J(J+1)},$$

(2.75)

which is equal to one for pure orbital and 2.0023 for pure spin magnetism (the deviation from the exact value of two is due to quantum electrodynamic interactions of the electron with its own radiation field). The energy shift for a given J depends only on the magnetic field strength and on the magnetic quantum number m_J and thus a level splits into $2J{+}1$

sublevels ($m_J = -J$, $(-J+1)$, ..., $(J-1)$, J). For singlet levels ($g_J = 1$) we obtain the energy difference between two adjacent sublevels ($\Delta m_J = 1$) of $\Delta E = \mu_B B_0$, which coincides with the classical treatment (Eq. (2.72)). Dipole transitions are only allowed if

$$\begin{aligned} \Delta m_J = 0 \, (\pi \text{ lines) or} \\ \Delta m_J = \pm 1 \, (\sigma \text{ lines}). \end{aligned} \quad (2.76)$$

Since the level splitting in the normal Zeeman case depends neither on n nor on J ($g_J = 1$ for $S = 0$, see Eq. (2.75)), the emission into the whole solid angle of singlet transitions is always subject to splitting into three lines: one unshifted π line and two equidistantly shifted σ lines. The angular dependence is as described above. This situation is shown in Figure 2.12 for the example of the singlet helium transition $3^1\mathrm{D}_2 \rightarrow 2^1\mathrm{P}_1^{\mathrm{o}}$. The frequency shift between the σ components for $B_0 = 1\,\mathrm{T}$ is $\Delta\omega = 2\mu_B/\hbar = 1.8 \times 10^{11}\,\mathrm{Hz} \,\hat{=}\, 5.8 \times 10^{-5}\,\mathrm{eV}$ and easily exceeds the Doppler broadening of this line at room temperature (see Sec. 2.3.3). It lies in the range of the fine structure splitting (compare Figure 2.10 (a) for the $\lambda = 587.6\,\mathrm{nm}$ line). This means that the splitting of, e.g. the triplet line at $\lambda = 587.6\,\mathrm{nm}$, at a magnetic field strength of $B_0 = 1\,\mathrm{T}$ already needs to be described by the Paschen-Back rather than the Zeeman effect.

2.4.2.2 Anomalous Zeeman effect

If the total angular momentum of at least one level involved in the radiation process is to be described by the orbital and spin angular momenta ($L_i \neq 0$ and $S_i \neq 0$) the level splitting in weak magnetic fields is called the anomalous Zeeman effect, which is actually more often encountered than the normal Zeeman effect. Because the total magnetic moment is not parallel to the total angular momentum vector (different g factors for $\boldsymbol{L}$ and $\boldsymbol{S}$) the calculation of the level splitting is more complicated. The energy shift of a level in the presence of a magnetic field, which is weak in comparison to the internal magnetic field of the atomic system, is given by Eq. (2.74). The selection rules of Eq. (2.76) must be obeyed. In general, both levels of electric dipole-allowed transitions have different energy shifts because of different g_J values (Eq. (2.75)). The number of sublevels is the same as in the case of the normal Zeeman effect: $2J + 1$, corresponding to the possible values of m_J. The relative intensities of Zeeman components under transverse observation are given in Table 2.2. The rules for the longitudinal observation have been mentioned in the previous section: no π radiation and double σ intensities.

2.4.2.3 Paschen-Back effect

If the magnetic field is strong enough to lead to a breakdown of the spin-orbit interaction (this can be estimated by comparing the amount of the fine structure and the Zeeman splitting, as above) the anomalous Zeeman effect does not describe correctly the multiplet level splitting and the Paschen-Back calculation needs to be used. Since the fine structure coupling strongly increases with nuclear charge, for the Paschen-Back effect in light atoms a much weaker magnetic field is needed than for heavy ones.

	Transverse observation		
Transition	I_π	$I_{\sigma_+}(M_J \to M_J - 1)$	$I_{\sigma_-}(M_J \to M_J + 1)$
$J \to J$	M_J^2	$\frac{1}{4}(J + M_J)(J + 1 - M_J)$	$\frac{1}{4}(J - M_J)(J + 1 + M_J)$
$J \to J - 1$	$J^2 - M_J^2$	$\frac{1}{4}(J + M_J)(J - 1 + M_J)$	$\frac{1}{4}(J - M_J)(J - 1 - M_J)$
$J \to J + 1$	$(J + 1)^2 - M_J^2$	$\frac{1}{4}(J + 1 - M_J)(J + 2 - M_J)$	$\frac{1}{4}(J + 1 + M_J)(J + 2 + M_J)$

Table 2.2: Relative intensities (in a given row) of Zeeman components for transverse observation [Condon and Shortley, 1991]. At longitudinal observation π components are not observed and σ lines are twice as intense (see Eqs. (2.73) for the spatial distribution).

The orbital and spin angular momentum of the considered system do not interact with each other in the case of the Paschen-Back effect. Instead, both momenta couple separately with the magnetic field. Therefore, the total angular momentum $\boldsymbol{J}$ is no longer defined ($\boldsymbol{J}$ is not a constant of the motion and hence J no longer a 'good quantum number'). The levels split into $(2L + 1)(2S + 1)$ sublevels with $m_L = -L, (-L + 1), ..., (L - 1), L$ and $m_S = -S, (-S + 1), ..., (S - 1), S$. For allowed dipole transitions again the following rules must be obeyed:

$$\begin{aligned}
\Delta m_L &= 0 \text{ or } \pm 1 \, (\pi \, \text{and} \, \sigma \, \text{components}) \\
\Delta m_S &= 0
\end{aligned} \tag{2.77}$$

and thus, complicated multiplet (anomalous) Zeeman line patterns become simple Lorentz triples. The energy shift is given by

$$\Delta E_{m_L, m_S} = (\Delta m_L + 2\Delta m_S)\mu_B B_0.$$

An example calculation is shown in Figure 2.13. As one can see, owing to the breakdown of LS coupling in the Paschen-Back calculation, nine resulting allowed transitions appear at only three different equidistant wavelengths.

The Zeeman calculation assumes the LS coupling as not disturbed by the magnetic field. In contrast, the Paschen-Back theory assumes the coupling to be fully removed. Actually, both assumptions are extreme cases. Often, foremost when dealing with light atoms in fusion plasmas, the magnetic field strength lies in between both extrema (magnetic perturbation comparable with spin-orbit coupling). When enhancing the magnetic field strength starting from the weak field regime, the quantum number J begins more and more to deviate from the correct description of the system and the ordinary selection rule on J (Eq. (2.70)) is violated, which results in the appearance of forbidden lines which do not obey the rules on J [Condon and Shortley, 1991].
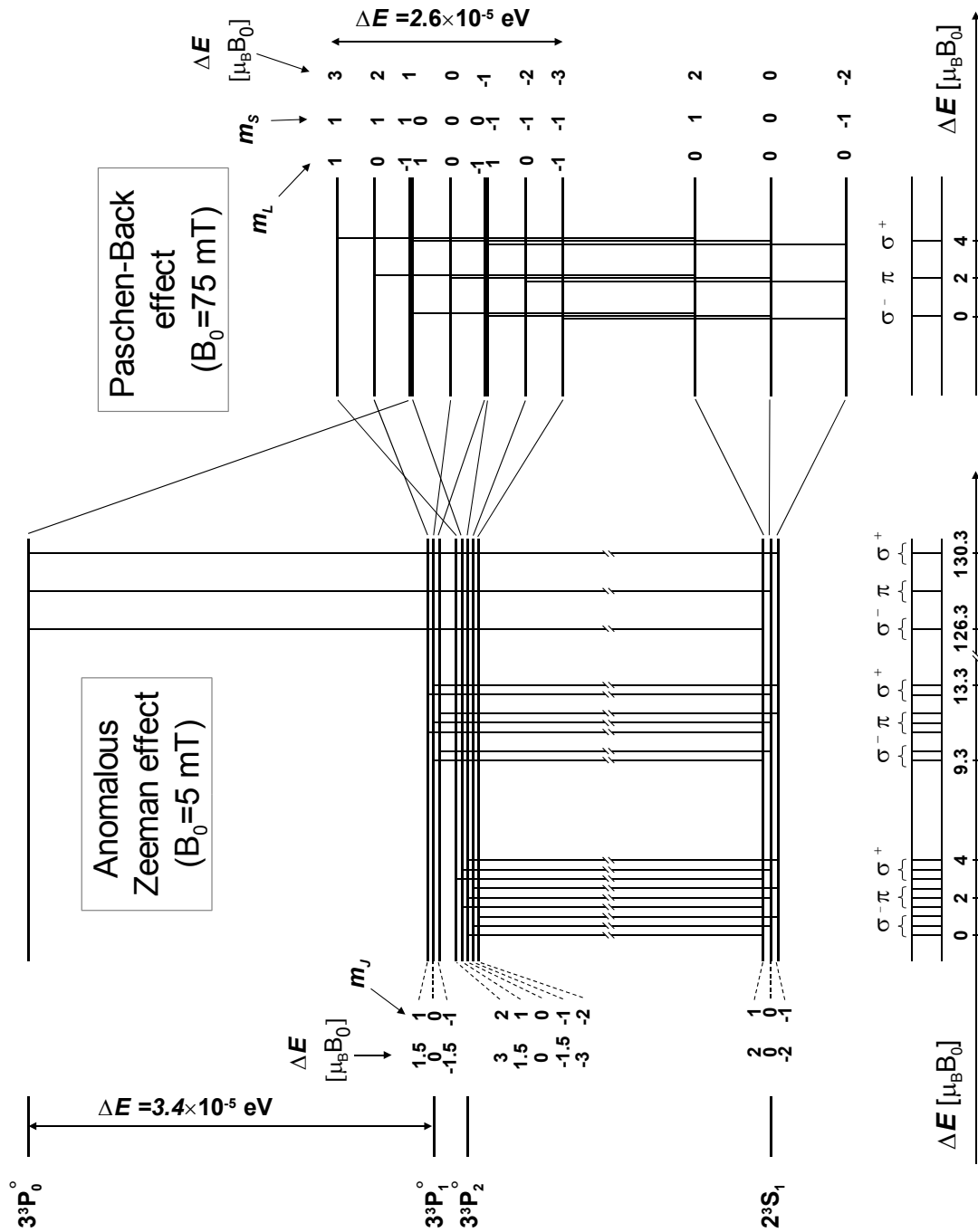
Figure 2.13: Calculation of anomalous Zeeman and Paschen-Back splitting (hyperfine structural effects have been ignored) of the atomic helium transition $3^3P^o \rightarrow 2^3S$ ($\lambda = 388.9\,\mathrm{nm}$). Magnetic field strength of 75 mT, as chosen for the Paschen-Back calculation, is actually too small for the assumption of a pure Paschen-Back splitting (energy splitting of $\Delta E_{\mathrm{PB}} = 2.6 \times 10^{-5}\,\mathrm{eV}$ is not greater than the fine structure splitting of $\Delta E_{\mathrm{FS}} = 3.4 \times 10^{-5}\,\mathrm{eV}$). It was taken in order to retain the relative energy scaling of both parts of the splitting diagram. Energy gaps are indicated by axis breaks.

2.5 Calculation of cross sections

In Sec. 2.2.1 the rate coefficient $\langle v\sigma(v)\rangle$ has been introduced as a quantity describing collisional processes in plasmas. To calculate a rate coefficient for a given process, the perturber temperature or, if this cannot be defined, its energy distribution must be known. The basic atomic property that is independent of the surrounding plasma parameters is the cross section $\sigma(v)$. It is the fundamental quantity for deriving rate coefficients and depends only on the relative velocity of the perturber and the atom. The cross section has the dimension of an area. It can be regarded as the interaction area surrounding the atom for the given process and projectile velocity. The flux of mono-energetic projectiles, i.e. of particles with the same velocity vector $\boldsymbol{v}$ and density n, $\Gamma = nv$, represents the impact rate of the projectiles on a unit area. By multiplying the flux with the active area one obtains the rate of the interaction between the projectile and the atom $nv\sigma(v)$. The rate constant is obtained by expressing the interaction rate per unit projectile density and, for non-mono-energetic projectiles, by appropriate averaging over the energy distribution (Eq. (2.17)).

In the following, a short overview based on [Shevelko and Vainshtein, 1993, Sobelman et al., 1995] will be given of the calculation methods and the approximations used on the example of electron-impact excitation.

Born approximation
Quantum mechanical calculations of cross sections are mostly performed by solving the time independent non-relativistic Schrödinger equation

$$H(Z_n, N+1)\Psi = E\Psi, \tag{2.78}$$

where Z_n is the nuclear charge, N is the number of electrons in the atom, E the total system energy (the atom energy in a given quantum level and the kinetic energy of the incident electron), Ψ is the wave function of the system and H is the Hamiltonian of the whole system:

$$H(Z_n, N+1) = -\sum_{i=1}^{N+1}\left(\nabla_i^2 + \frac{2Z_n}{r_i}\right) + \sum_{j=i+1}^{N+1}\sum_{i=1}^{N}\frac{2}{r_{ij}}. \tag{2.79}$$

In theoretical treatments of cross sections for electron impact excitation, the projectile electron velocity compared to the velocity of the optical electron is very important [Kim, 1983]. For high perturbing electron velocities, first-order perturbation theory can be applied, simplifying the calculations significantly. In this so-called Born approximation, the resulting cross sections can be given in closed analytical form being only dependent on atomic constants and the relative velocity. Here, it is assumed that the wave function distortion of the perturbing electron due to the (weak) interaction with the atom is small. In this case, the relative motion of the projectile and the target can be described by a plane wave

$$\boldsymbol{\Phi_k}(\boldsymbol{r}) = \mathrm{e}^{-i\boldsymbol{kr}}, \tag{2.80}$$

where $\boldsymbol{k}$ is the momentum of the projectile. Assigning with $a_0 M_0$, $a_1 M_1$ the sets of quantum numbers for the initial and final state of the atom, respectively (M denoting the magnetic quantum number), the differential cross section writes

$$\mathrm{d}\sigma^{\mathrm{B}}_{a_0 M_0, aM} = \frac{\mu^2}{16\pi^2} \frac{k}{k_0} \left| \int \mathrm{e}^{-i(\boldsymbol{k}_0 - \boldsymbol{k})\boldsymbol{r}} U_{a_0 M_0, aM}(\boldsymbol{r}) \mathrm{d}\boldsymbol{r} \right|^2 \mathrm{d}\Omega, \tag{2.81}$$

where μ is the reduced mass (approximately equal to the electron mass in electron-impact processes) and

$$U_{a_0 M_0, aM}(\boldsymbol{r}) = \langle a_0 M_0 | \sum_i \frac{2}{|\boldsymbol{r} - \boldsymbol{r}_i|} - \frac{2Z_n}{r} |aM\rangle. \tag{2.82}$$

Then, by using the Bethe integral

$$\int \frac{\mathrm{e}^{-i\boldsymbol{qr}}}{|\boldsymbol{r} - \boldsymbol{r}_i|} \mathrm{d}\boldsymbol{r} = \frac{4\pi}{q^2} \mathrm{e}^{-i\boldsymbol{qr}_i} \tag{2.83}$$

Eq. (2.81) with plane waves (Eq. (2.80)) can be written in the so-called $\boldsymbol{q}$ representation, where $\boldsymbol{q} = (\boldsymbol{k}_0 - \boldsymbol{k})$ is the momentum transfer. This reduces the partial wave representation to only one expansion of the function $\mathrm{e}^{i\boldsymbol{qr}}$ over interaction multipoles of the multiplicity κ. The expansion is done in such a way as to provide a separation of the radial and angular variables. For dipole allowed transitions ($\kappa = 1$, $\Delta l = \pm 1$, $\Delta S = 0$) a simple approximation can be obtained, called the Bethe formula:

$$\sigma^{\mathrm{B}}_{a_0 a} = \pi \mathrm{r}_{\mathrm{B}}^2 \frac{8}{k_0^2 \Delta E} f_{a_0 a} \ln \frac{2qk_0}{\Delta E}, \tag{2.84}$$

where $\mathrm{r}_{\mathrm{B}} = 5.292 \times 10^{-11}\,\mathrm{m}$ is the Bohr radius.

Atom-excitation cross sections calculated in the Born approximation have some general properties. For high perturber energies $E_{\mathrm{p}} \gg \Delta E$ the cross section scales as

$$\sigma^{\mathrm{B}} \propto \frac{\ln E_{\mathrm{p}}}{E_{\mathrm{p}}} \tag{2.85}$$

for dipole allowed transitions and as

$$\sigma^{\mathrm{B}} \propto \frac{1}{E_{\mathrm{p}}} \tag{2.86}$$

for parity forbidden ones (for spin forbidden transitions $\sigma^{\mathrm{B}} \propto 1/E_{\mathrm{p}}^3$). Moreover, for transitions with $\Delta n \geq 1$ the maximum cross section $\sigma^{\mathrm{B}}_{\mathrm{m}}$ scales as ΔE^{-2} and cross sections for transitions with $\Delta n \gg 1$ are proportional to n^{-3}. In the literature the cross sections are often expressed in the form of the collision strength

$$\Omega_{ij} = g_i \frac{E_{\mathrm{p}}}{E_{\mathrm{Ry}} \pi \mathrm{r}_{\mathrm{B}}^2} \sigma_{ij}, \tag{2.87}$$

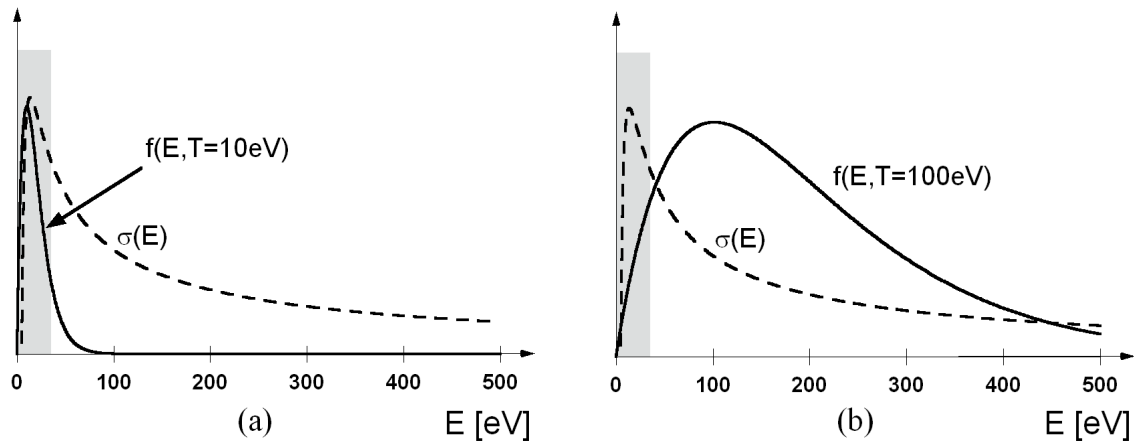with a weaker projectile energy dependence at $E_{\mathrm{p}} \gg \Delta E$.

Figure 2.14: Influence of the Born cross sections near the threshold energy (grey) on the rate coefficient calculation for different values of the reduced temperature $k_B T_e / \Delta E$; f: projectile energy distribution function.

Since cross sections calculated in the Born approximation are reliable only for high perturber energies, rate coefficients based on such cross sections have much better accuracy at high reduced temperatures $k_B T_e / \Delta E$. This can be seen in Figure 2.14. An example excitation cross section with the threshold energy of $\Delta E \sim 5\,\mathrm{eV}$ is sketched, overlaid by Maxwellian electron energy distribution of $T_e = 10\,\mathrm{eV}$ (a) and $T_e = 100\,\mathrm{eV}$ (b). In the latter case, the folding of the cross section and the energy distribution is only weakly sensitive to the cross section values near the threshold energy (indicated in grey).

Generalised Born approximation

In general, due to several simplifications made in the derivation of Born cross sections, these are used, except at high perturber energies, mostly for a rough estimation of the cross sections. In their maxima (i.e. at lower energies), cross sections calculated by use of the Born approximation are typically overestimated by a factor of two and their maximum energies are shifted towards the threshold energy. This is because the repulsive interaction between the perturber and the optical electron (atom polarisation) is neglected and therefore the average distance between the free and the optical electron is taken too low [Sobelman et al., 1995]. Transitions with $\Delta S \neq 0$ induced by electron impact can be described in the framework of the Born approximation only by including the electron exchange effect. If the Born approximation is extended accordingly it gains more accurate results in some cases.

The (first-order) distorted-wave approximation (such as the Coulomb-Born approximation) allows for the distortion of the incident and scattered wave by the long-range Coulomb field of the ion. This is important for the calculation of the electron-impact excitation of ions near the threshold energy. It can easily be seen when considering the case of an electron with exactly the threshold energy ($E_e = E_{th}$): the electron attraction due to the Coulomb-field of the ion causes an energy increase of the electron and a jump
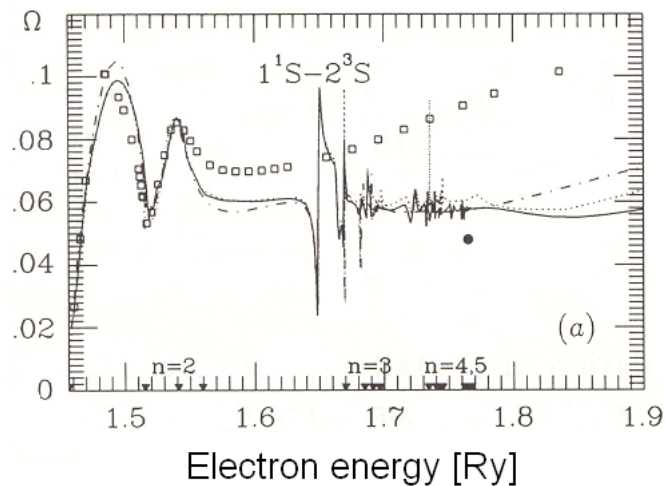
Figure 2.15: R-matrix calculation of the electron impact excitation of the ground state of helium to the 2^3S state (figure taken from [Sawey et al., 1990]): —— 29 states, $\cdots\cdots$ 19 states, $-\cdot-$ 11 states, $\square$ 5 states and $\bullet$ experiment [Brongersma et al., 1972].

of the calculated cross section from zero to relatively large values.

To obtain non-zero electron-excitation cross sections for intercombination transitions ($\Delta S \neq 0$), taking exchange-interaction terms into account is essential (Born-Oppenheimer approximation, or Coulomb-Born-Oppenheimer for ions). For an accuracy comparable to that of the Born-approximation in the case of transitions with $\Delta S = 0$, the orthogonalisation of the initial and final wave functions must be ensured. Another approach for atoms (the Ochkur approximation), with limited range but much easier in application, relies on taking only the first non-vanishing term of the $1/\boldsymbol{k}$-expansion of the exchange-scattering amplitude. The simple $\boldsymbol{q}$-representation is then possible, as in the Born-approximation. Finally, normalisation procedures for cross sections are additionally considered for transitions with small energy difference. Inclusion of those three refinements is referred to as the generalised Born approximation.

More accurate methods

In some cases the Born approximation does not provide sufficient accuracy. Then, higher terms of the perturbation theory can be additionally considered. This is e.g. done for quadrupole transitions $ns - n'd$ for which the Born approximation provides underestimated cross sections. In the second-order terms excitation through an additional channel, the virtual level np, is added.

Higher accuracy for lower perturber energies is obtained by including the complete coupling between several transition channels (also to energetically inaccessible levels) if this coupling is stronger than the one between the initial and the final level, as it is done in the close-coupling method. This is necessary in the case of slow collisions. In the R-matrix method the interaction region is additionally divided into two parts. The inner region is described in the same way as in the close-coupling approximation: electron exchange and correlation between the scattered electron and the N-electron target atom

are important and the $(N+1)$-electron collision complex behaves in a similar way to a bound state [Burke and Berrington, 1993]. In the outer range the scattered electron just moves in the long-range multipole potential of the target. R-matrix calculations provide reasonable results for lower energies below the ionisation threshold and for transitions into levels up to $n-1$ if the levels of the nth shell were included [Bartschat et al., 1995].

In Figure 2.15 an example R-matrix cross section calculation for the electron excitation of the helium ground state to the triplet metastable level 2^3S is shown in form of the collision strength with different number of target states ($n \leq 2$ up to $n \leq 5$) included in the calculation. The threshold energy is $E_{th} = 1.46$ Ry (19.8 eV). The resonances connected to the levels of different n values are visible at different degrees of accuracy.

A further accuracy increase in calculation of excitation and ionisation cross sections was reached by making use of two new methods for helium developed in the nineties of the last century, the convergent close coupling (CCC) by Fursa and Bray [1995] and the R-matrix method with pseudo states (RMPS) by Bartschat et al. [1996a]. The basic idea of these approaches lies in the inclusion of additional states in the close coupling expansion or in the R-matrix calculation, which are chosen such as to represent in an average way the infinite number of higher-lying Rydberg and continuum states of the target. This increases the accuracy of the calculations, and allows excitation calculations for high electron energies [Bray et al., 2000] as well as of ionisation cross sections [Bartschat et al., 1995].

2.6 Helium beam diagnostics

Passive plasma observation is intrinsically connected with the line-of-sight integration of the detected light. To overcome this limitation, the use of probe beams, such as atomic beams, provides a means to make local measurements perpendicularly to the beam. A widely used application in plasma diagnostics consists of a radial puff of helium atoms into the plasma. Atomic helium is very well suited to this purpose because its very stable electronic configuration makes it inert to chemical reactions. With a very high ionisation energy of $E_{ion} = 24.6$ eV helium atoms can penetrate relatively deep into the plasma with a fairly high probability of the beam atoms getting excited before being ionised.

Helium atoms are being excited while penetrating into the plasma. A certain population distribution among excited levels establishes depending on the surrounding plasma parameters: the electron density n_e and electron temperature T_e. Via the measurement of line radiation the population density of the excited levels can be determined, which in turn provides a measure of the local plasma parameters. Helium atoms contain two electrons and quantum mechanically this gives rise to two sub-systems: parallel and antiparallel orientation of the electron spins. In the latter case the total spin quantum number is $S = 0$ and no multiplicity of spectral transitions is observed. This is the singlet helium system (Figure 2.16). On the other hand, the parallel spin orientation with $S = 1$ results in tripling of quantum levels and multiple splitting of the corresponding spectral lines (see Sec. 2.4.1). Because helium atoms show pure LS-coupling for most
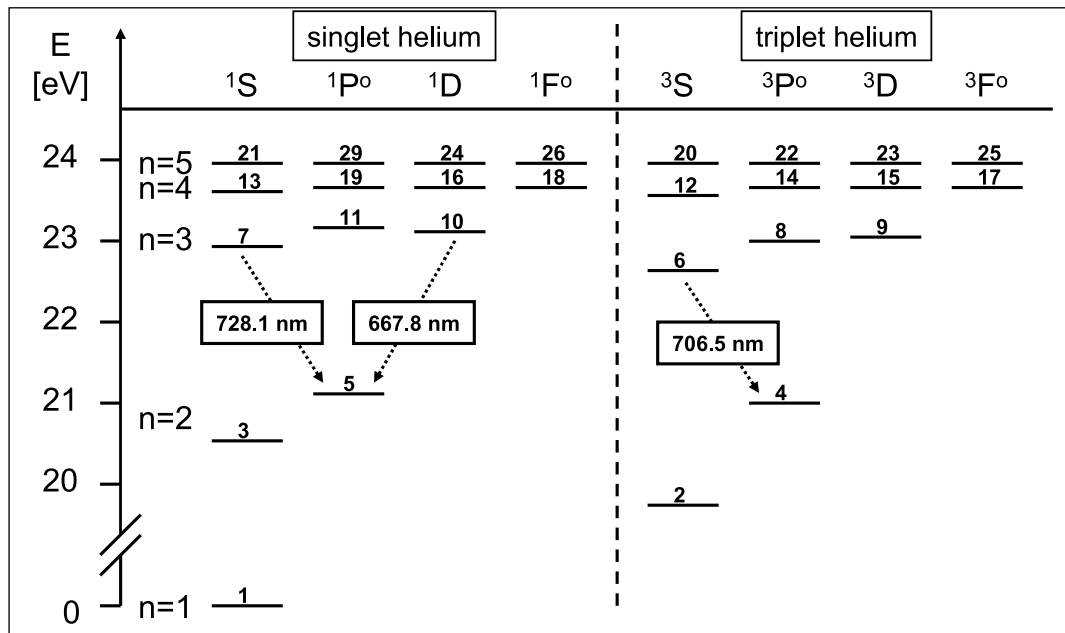
Figure 2.16: Part of the Grotrian diagram of the singlet and triplet system of atomic helium. Three transitions as used for n_e and T_e derivation on TEXTOR are indicated. For numerical treatment the levels are numbered with falling ionisation energy.
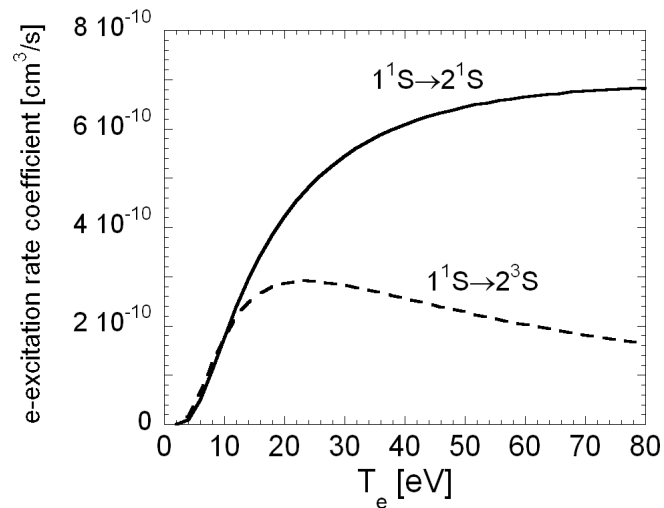

Figure 2.17: Electron temperature dependence of the rate coefficients for electron-impact excitation of the ground state of atomic helium to the singlet and triplet metastable levels.

levels, no radiative intercombination transitions ($\Delta S \neq 0$) in the visible are observed. This means that the triplet system cannot effectively be populated by radiative transitions from the singlet levels but only by collisional processes, in many cases mainly by electron excitation from the ground state. However, the cross sections for electron impact excitation from the ground state into the singlet and triplet system reveal different asymptotic behaviour at high energies. While those for dipole allowed transitions scale as $\sigma \propto \frac{\ln E_{\mathrm{p}}}{E_{\mathrm{p}}}$, the cross sections for excitation into the triplet system, which is connected with an electron exchange, show a resonance character with a maximum at the perturber energy near the excitation energy and with strong decrease for higher energies $\sigma \propto E_{\mathrm{p}}^{-3}$ (Figure 2.17).
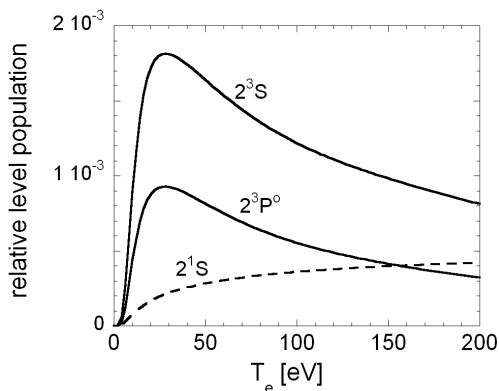

Figure 2.18: T_{e} dependence of the populations of three selected helium levels relative to the ground state population (calculated for $n_{\mathrm{e}} = 5 \times 10^{18}\,\mathrm{m}^{-3}$).

This difference in the energy dependence can be used for diagnosing the electron temperature in the plasma: the triplet population relative to the singlet is sensitive to this quantity. As an example calculated populations of both metastables and the $2^3\mathrm{P}^{\mathrm{o}}$ level as a function of electron temperature for $n_{\mathrm{e}} = 5 \times 10^{18}\,\mathrm{m}^{-3}$ are plotted in Figure 2.18. The maximum triplet level population occurs at $T_{\mathrm{e}} \approx 25\,\mathrm{eV}$ while the singlet level is still increasing at $T_{\mathrm{e}} = 200\,\mathrm{eV}$. The intensity ratios of triplet and singlet lines can therefore be used as a measure for T_{e}. The lines with the wavelength $\lambda = 728.1\,\mathrm{nm}$ ($3^1\mathrm{S}{\rightarrow}2^1\mathrm{P}^{\mathrm{o}}$) and $\lambda = 706.5\,\mathrm{nm}$ ($3^3\mathrm{S}{\rightarrow}2^3\mathrm{P}^{\mathrm{o}}$) are usually taken for this purpose.

In fusion edge plasmas diagnosed by helium beams where the typical electron density range is $n_{\mathrm{e}} = 10^{18} - 10^{19}\,\mathrm{m}^{-3}$ the corona model to the population distribution cannot be applied (see Sec. 2.2.1) because the population losses are in some cases mainly influenced by electron collisions. The depopulation rates then strongly depend on electron density. On the other hand, some levels are mainly depopulated by spontaneous light emission even at higher electron densities. Hence, ratios of line emission from both these kinds of levels provide a measure for the electron density. Usually the lines $\lambda = 728.1\,\mathrm{nm}$ ($3^1\mathrm{S}{\rightarrow}2^1\mathrm{P}^{\mathrm{o}}$) and $\lambda = 667.8\,\mathrm{nm}$ ($3^1\mathrm{D}{\rightarrow}2^1\mathrm{P}^{\mathrm{o}}$) are used, requiring the measurement of one additional line to the line pair needed for the temperature derivation.

For a reliable determination of the plasma parameters from the line intensity ratios, the above effects need to be quantified. This is done by use of a collisional-radiative model, in which the population and depopulation processes of the levels are arranged in the form of rate equations (Sec. 3.3). With the assumption of the relaxation of the helium atoms in the beam, the time independent solution of the equation system provides the dependence of the line intensity ratios on the plasma parameters. This solution can be clearly depicted as in Figure 2.19. It shows lines of constant line intensity ratios for the n_{e} and T_{e} determination. The lines are not perpendicular to the axes (mostly for higher
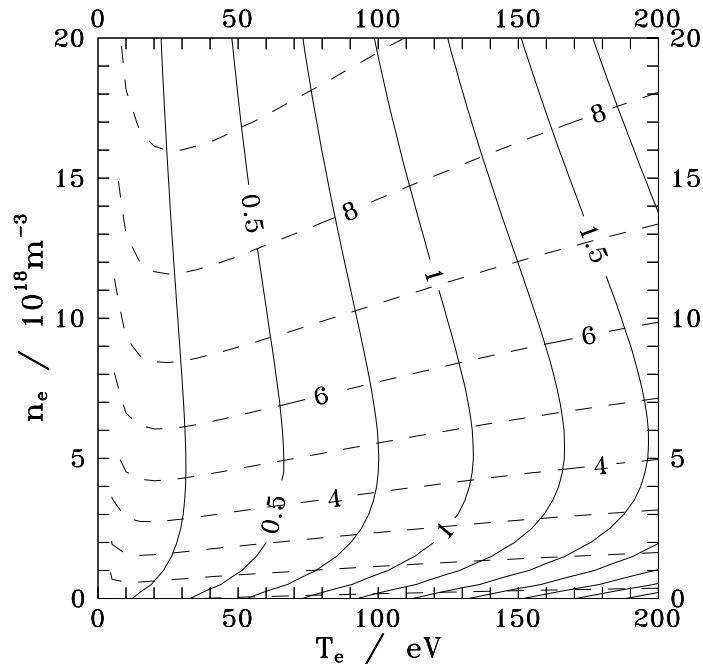
Figure 2.19: n_{e} and T_{e} dependence of the line intensity ratios for the derivation of T_{e} ($I_{728.1}/I_{706.5}$, solid lines) and n_{e} ($I_{667.8}/I_{728.1}$, dashed lines) calculated with the stationary solution of the collisional-radiative model (figure taken from [Brix, 1998]).

n_{e} and T_{e} values), which means that the line ratios reveal also a slight dependence on the other plasma parameter. In this sense only the simultaneous measurement of both line intensity ratios provides a self-consistence picture of both plasma parameters. Moreover, for low n_{e} and T_{e} values the lines are not orthogonal to each other posing the application limit of this measurement method. In these ranges small measurement uncertainties cause a relatively large confidence interval of the evaluated plasma parameters.

The atoms in the beam penetrate the plasma with a velocity of around 1.5 km/s (see Sec. 4.3.2). Since the plasma parameters are not constant along the penetration path of the beam, the population distribution always strives to reach stationary values for the local plasma parameters on a time scale depending on the plasma parameters themselves. If this time constant is small enough to prevent significant change of the plasma parameters as encountered by the beam particles on their way through the plasma, the beam is said to be relaxed. Generally, the relaxation time shows a strong inverse dependence on the electron density. For this reason the relaxation of the population distribution is not always insured at the very edge of the plasma. A more detailed analysis of this problem follows in Sec. 3.2.3.

The penetration depth of a neutral helium beam into a plasma is restricted by the electron-impact ionisation losses from the ground state. Ionised particles move away from the beam as a result of elastic collisions with the background plasma ions before the recombination can take place [Kornejew, 1996]. Figure 2.20 shows radial profiles of the three mentioned helium lines measured on TEXTOR in front of a carbon limiter
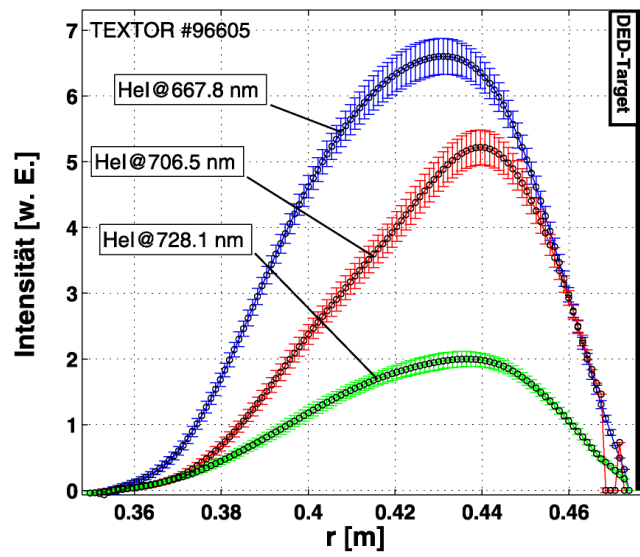
Figure 2.20: Radial profiles of intensity of the three lines used for n_e and T_e derivation on TEXTOR in front of a carbon limiter surface (figure taken from [Schmitz, 2006]).

surface (DED limiter). The beam radiation is detected along a radial range of ~ 10 cm allowing n_e and T_e measurements well inside the last closed flux surface.

Chapter 3

Collisional-radiative model for atomic helium beam

The accuracy of atomic data included in the collisional-radiative model used for electron density and temperature derivation from helium line intensity ratios is of highest importance for the quality of the obtained plasma parameters. Nevertheless, there are also additional effects, which need to be taken into account in some cases.

As we will see later in this section, for the application of helium beam diagnostics in fusion plasmas electron-impact excitation from the ground state and excited levels are very important and critical processes. The very complicated theoretical treatment as well as difficulties in experimental verification lead to considerable uncertainties in some cases. In contrast, the level energies and radiative transition probabilities are known with sufficient accuracy [Wiese et al., 1966, Martin, 1973, 1984a,b, Theodosiou, 1987].

In this section, first an overview will be given on the electron-impact excitation and ionisation data available from calculations and measurements along with their expected accuracy and the agreement between different calculation methods and measurement results. In addition, other collisional processes will be considered in terms of their relevance for the modelling of the helium population distribution in fusion edge plasmas, followed by a quantitative discussion of radiation trapping in the beam, beam relaxation as well as photoionisation due to the laser radiation. Finally, the numerical approach for the solution of the population distribution will be presented.

3.1 Existing data on electron impact excitation and ionisation

The quality of atomic data for helium excitation and ionisation by electron impact strongly depends on the considered transition. Thus, the following overview on the existing calculated and measured data will distinguish between the different transitions.

Due to the large abundance of helium in astrophysical space and due to many laboratory applications a lot of calculations on helium have been performed over the years resulting in increasing accuracy owing to new methods and more powerful computer hardware. However, most of this work was devoted to low temperature plasmas and hence provides electron-impact excitation cross sections for electron energies below 10

eV. Also experimental verification of selected excitation rates coefficients found in the literature is limited to low electron energies.

The first set of semi-empirical data for excitation from the ground state to the metastables, based on calculations and measurements available at the time, to be used for modelling of a glow discharge plasma [Fujimoto, 1979], was 1978 provided by Fujimoto [1978]. Janev et al. [1987] provided fit formulas for these data. The uncertainties, estimated from the disagreements between the calculations and measurements found in the literature, are for many cases at least a factor of two (except for the excitation of singlet levels from the ground state).

Abramov et al. [1987] calculated in 1987 a complete set of data for the excitation between the levels with $n \leq 4$ by use of the Born approximation. However, the recommended fit functions for the rate coefficients distort their temperature dependence in some cases [Brix, 1998]. This data set was employed by Brosda [1993] to model the line radiation of helium in a thermal beam at TEXTOR.

An almost complete set of excitation data for the transitions between the levels with $n \leq 4$, however only for low temperatures, was calculated by Sawey et al. [1990] and Sawey and Berrington [1993]. The R-matrix method was used, with inclusion of 29-state (all states with $n \leq 5$) as an improvement of former calculations with inclusion of 5, 11 and 19 states, which were reported in [Berrington et al., 1975, Freitas et al., 1984, Berrington and Kingston, 1987], respectively. Kornejew [1996] used these rate coefficients for temperatures $T_e < 3\,\text{eV}$ and combined it with the Abramov data at high temperatures to obtain a full set of rate coefficients covering all transitions between levels with $n \leq 4$. Severe discrepancies in the rate coefficients (up to two orders of magnitude) were found for some dipole forbidden transitions from the ground state as well as for transitions between the excited states.

Another compilation of the same R-matrix calculations by Sawey and Berrington and several experimental results was published by de Heer et al. [1992] (the parametric representation of the data is given in [Kato and Janev, 1992]), however, only the excitation from the ground state into levels with $n \leq 4$ is treated. Experimental data, based mainly on photon emission cross section measurements, are used to fill the gap for moderate energies near the ionisation energy since the R-matrix method used by Sawey and Berrington is not supposed to provide correct results in this energy range. The data for energies above the ionisation threshold, in particular for excitation of levels with $n \geq 3$ are supposed to be overestimated by up to a factor two [de Heer et al., 1992]. The assessed accuracy of the experimental data is dependent on the kind of the transition. The smallest uncertainties of $<10\%$ are reached for the singlet transitions at higher energies above 40 eV (for lower energies the error is larger and reaches 30%). However, two exceptions exist: for the excitation of the $n^1\text{D}$ levels and of the 2^1S level for all energies the errors are typically $\leq 30\%$. The triplet states excitation data are less accurate due to experimental difficulties. Below 100 eV the error is estimated with 30% and it increases for higher energies.

The recently developed calculation methods (see Sec. 2.5) were applied by Fursa and Bray [1995] (CCC) for helium excitation from the ground state to the levels with

$n \leq 3$ and energies up to 500 eV as well as by Bartschat et al. [1996b] (RMPS with inclusion of 41 terms) for the excitation from the ground state to the $2^{1,3}$S levels and from for the 2^3S→2^1S transition and energies up to 80 eV. Both methods provided very similar results for the excitation from the ground state to the $n = 2$ levels and agreed well with experimental data [Bartschat, 1998]. However, some discrepancies of the CCC calculations were observed for transitions involving the $n = 3$ levels and for excitation and ionisation from the metastable 2^3S level. An updated compilation of the excitation data from the ground state relating to CCC and RMPS calculations was provided 1998 by de Heer [1998]. For the singlet transitions from the ground state to the levels with $n \leq 4$ an accuracy of 10% for most cases is claimed as well as for the $n = 2$ triplet levels, however, for not too high energies. The errors decrease with increasing n and L.

Bray et al. [2000] extended the CCC calculation to the excitation from the $n = 1 - 2$ states (except for 2^1P°) to levels with $n \leq 5$ and provided thermally averaged collision strengths up to $T_e = 50$ eV. The main discrepancies to the R-matrix calculation of Sawey and Berrington are found for the excitation to the levels with $n = 4$ and 5. Similar results are reported by Ballance et al. [2006] who recently calculated rate coefficients with the RMPS method for all 171 transitions between levels with $n = 1 - 4$ for low energies ($T_e < 47$ eV). They also compare the calculated rate coefficients for some $\Delta n = 0$ transitions with LIF measurements (for T_e below 10 eV) by Denkelmann et al. [1999] and find a good agreement.

Ralchenko et al. [2000] provide a number of new CCC calculations with increased accuracy for transitions between the levels with $n = 1$ to 4. The results for the excitation from the $n > 1$ levels were preferred over older data [Kato et al., 1992, de Heer et al., 1995, Beigman et al., 2000] and included into a complete recommended data set compiled together with fit formulas for the transitions $n = 1$ to 4 (these data make up also the recommended ADAS [Summers and O'Mullane, 2005] dataset 2000 [Paton, 2005]). For higher n levels suitable scaling relations are given. Ralchenko et al. find good agreement with new differential cross section measurements of the transitions from the ground state to the $n = 2$ levels by Cubric et al. [1999]. The uncertainty estimation of the data is close to the one presented by de Heer [1998]: a minimum error of 30% is given for spin forbidden transitions from the ground state and of 50% for transitions between excited levels. The maximum deviation between the fit curves and the data is 10%.

Merabet et al. [2001] further extended the CCC model to obtain better accuracy for excitation from the ground state into the $n = 4$ and 5 levels. They performed both the CCC and RMPS calculations for electron as well as H^+, H_2^+ and H_3^+ impact excitation from the ground state to the n^1P° levels with $n = 2$ to 5 for large energy ranges. The agreement for electron excitation between the calculations and their own measurements at intermediate energies as well as former measurements for lower energies is very good. In contrast, there are severe discrepancies for proton excitation at low energies.

A detailed discussion of the excitation data from the metastables is provided by de Heer et al. [1995]. They estimate the overall accuracy of the data to 10%.

Calculation results of the CCC and RMPS methods for excitation from the metastable levels coincide well for low energies and with high energy Born data. However, they are

not supported by some low energy measurements in the case of excitation from the 2^3S level [Bartschat, 1998]. Excitation measurements from the same metastable level into the levels 3^3S, 3^3D and 4^3D do not reveal the proper asymptotic behaviour for large energies [Boffard et al., 1999]. Boffard et al. estimate the uncertainties of the cross sections for excitation from the 2^3S metastable level with up to 40%, similar to those for the excitation from the ground state.

The available theoretical electron impact excitation data, despite their abundance and the use of different calculation methods, still reveal uncertainties for some transitions, mainly between excited levels, which are manifested in different calculation results or deviations from measurements. For the most of the data no experimental verification exists. Therefore, each experimental effort is of interest in this context.

Measurements on electron impact ionisation are given only for the ground and the triplet metastable levels [Long and Geballe, 1970, Dixon et al., 1976]. Fujimoto [1978] provided semi-empirical formulas for these data as well as formulas based on scaling laws for higher excited levels (also the photoionisation is considered). Comprehensive new CCC calculations made by Ralchenko et al. [2000] agree well with measurement for excitation from the ground state, but not from the metastable state (this issue is discussed in more detail in Sec. 3.2.1.1). Moreover, ionisation cross sections with fit formulas for all levels with $n \leq 4$ are provided. The accuracy of these data is believed not to exceed 15%.

3.2 Model for an atomic helium beam in the edge of a fusion plasma

In this section the CR model used for the data analysis in this work will be described in some detail. Several processes which can play a significant role in helium beam modelling in fusion plasmas, with emphasis put on the modelling of our LIF experiments, will be discussed.

Helium atoms injected into a plasma in form of a directed beam penetrate the plasma for a certain distance. Collisions with plasma particles encountered on the way through the plasma result in excitation and ionisation of the atoms, the last process being equivalent to the final loss of an atom from the beam volume. As already noted, electron collisions and spontaneous radiative decay are those processes, which have the strongest influence on the excitation population distribution of the atoms in the beam and hence on the measured line radiation. However, for some helium plasma conditions as well as sometimes for helium beams in fusion plasmas, collisions with other parties can be important and therefore must also be considered. These are heavy particles like the background plasma ions and neutrals, impurity ions and helium atoms themselves.

Some additional effects can influence the population distribution as well and will be therefore discussed in the following sections. One of them is connected with the directed propagation of the atoms through plasma regions of increasing electron density and temperature. Depending on n_e and T_e, the time scales for the population relaxation of

the beam atoms in some levels can be too large to justify the assumption of a quasi-steady state population distribution. This assumption is typically made because it considerably reduces the computational effort needed for the derivation of n_e and T_e (see Sec. 3.3). However, at the very edge of the plasma, where the electron density is relatively low, the relaxation effects can cause the triplet levels to be weaker populated than what follows from the steady state modelling, thereby having an effect on the electron temperature derivation. The beam relaxation effect is also important for the evaluation of our LIF measurements since some of them have been made at plasma conditions at which relaxation cannot be assumed.

Additional processes to be discussed are volume and the wall recombination, the inclusion of higher n shells into the model, photoionisation by the strong laser radiation, radiation trapping by the helium atoms themselves, deviation of the electron energy distribution from a Maxwellian as well as the mixing of some singlet and triplet levels, e.g. 4^1F^o and 4^3F^o, due to the breakdown of the LS coupling scheme. The impact of the magnetic field on the trajectories of the perturbing electrons as well as ions is negligible [Hey et al., 2000].

One of the aims of this thesis is to compare modelled populations of selected levels with results of LIF measurements. Accordingly, the model to be used is supposed to appropriately predict those level populations which are compared with measurement. From the analysis of the absolute measured fluorescence photon flux at the laser wavelength the absolute population of the pumped level can be derived. Hence, the model must predict absolute $n = 2$ level populations. On the other hand, temporal behaviour of collision-induced fluorescence signals provides a possibility to obtain the value of the rate coefficients for collisional population redistribution between the upper level and the level from which the observed fluorescence light originates. Since no analysis of absolute passive radiation from higher levels is performed, there is no need to optimise the model to provide a proper description also of the high n levels. The arising simplifications of the model are discussed in the following sections.

3.2.1 Survey on collisional processes and their importance for the modelling of LIF signals

3.2.1.1 Electron collisions

The electron temperatures at which our measurements were performed lie in the range of several tens of eV. Hence, the excitation from the ground state will be dominated by electron collisions, since the minimum threshold energy for the excitation into the $n = 2$ shell is 19.8 eV and slightly larger for higher n shells. The same holds for the collisional ionisation from the ground state. Concerning the excitation and ionisation from excited levels, electron collisions play also a very important role. (However, due to considerably smaller threshold energies, heavy particles can influence these processes as well.)

A reliable dataset on electron collisions from the ground and excited states is therefore needed. For first comparisons with measurements, the last complete set of data for

excitation between all levels with $n = 1 - 4$ recommended by Ralchenko et al. [2000] is used (the ADAS2000 dataset is based on the same data).

The electron impact ionisation data recommended by Ralchenko et al. [2000] rely to a large extent on their own CCC calculations and fit well experimental results for the ionisation from the ground state. On the contrary, the calculation provides ionisation cross sections for the 2^3S metastable state, which are smaller by up to a factor of two than results of two independent, partially overlapping experimental works [Long and Geballe, 1970, Dixon et al., 1976]. These experimental data were supplied by Kato and Janev [1992] by a fit formula. They recommended also cross sections for the ionisation from the 2^1S metastable state based on calculations by Briggs and Kim [1971], which provided a correct prediction for the measured ionisation from the 2^3S metastable. The ionisation data for 2^1S is also larger than that of Ralchenko et al. [2000] by up to a factor of three. The cross sections for the ionisation from both metastables as well as from the ground state recommended by Ralchenko et al. [2000] and Kato and Janev [1992] are shown in Figure 3.1. It is noted that the data for the ionisation from the ground state recommended in both works are the same and coincide with measurements.

In the CR model proposed by Brix [1998] the data provided by Kato and Janev for the ionisation from both metastables were used. For the ionisation out of the higher excited levels with $n = 2 - 4$ semi-empirical cross sections provided by Fujimoto [1978] were used. All ionisation rate coefficients based on those Fujimoto's cross sections at $T_e = 50\,\text{eV}$ are typically twice as large as the ones calculated by Ralchenko et al. [2000]. For our calculations we use the set of larger rate coefficients. This is because the measurements performed within this thesis also support stronger ionisation losses than given by the Ralchenko data (see Sec. 6.1.1).

Electron excitation and ionisation data for transitions including levels of the $n = 5$ and higher shells were treated differently in CR models of different authors. Kornejew [1996] included the shells $n = 5 - 6$ in the model and assumed the level population of both shells as statistically distributed, i.e. in accordance to their statistical weights. Brix [1998] compiled a partial set of excitation and ionisation data for the $n = 5$ shell using a scaling formula of Kato and Janev [1992], ATOM calculations based on Born approximations [Beigman et al., 1997] and the van Regemorter formula for dipole allowed transitions

$$Y_{ij} = \frac{8\pi}{\sqrt{3}} \frac{1\,\text{Ry}}{\Delta E_{ij}} \text{f}_{\text{ij}} \text{g}_{\text{i}} P_{ij}, \tag{3.1}$$

where ΔE_{ij} is the excitation energy, f_{ij} the oscillator strength of the dipole transition and P_{ij} is a tabulated correction based on the Gaunt factor [van Regemorter, 1962]. The rate parameter Y_{ij} is related to the rate coefficient $\langle \sigma_{ij} v \rangle$ as follows [Bray et al., 2000]:

$$\langle \sigma_{ij} v \rangle = \frac{2\sqrt{\pi}\alpha \text{c} \text{a}_0^2}{\text{g}_{\text{i}}} \text{e}^{-\frac{\Delta E_{ij}}{\text{k}_\text{B} T_\text{e}}} \sqrt{\frac{1\,\text{Ry}}{\text{k}_\text{B} T_\text{e}}} Y_{ij}. \tag{3.2}$$

Fujimoto [1979] considered the shells $n = 1 - 20$ with some simplifications and Ballance et al. [2006] included the higher shells $n = 5 - 500$ by using so-called projection matrices,
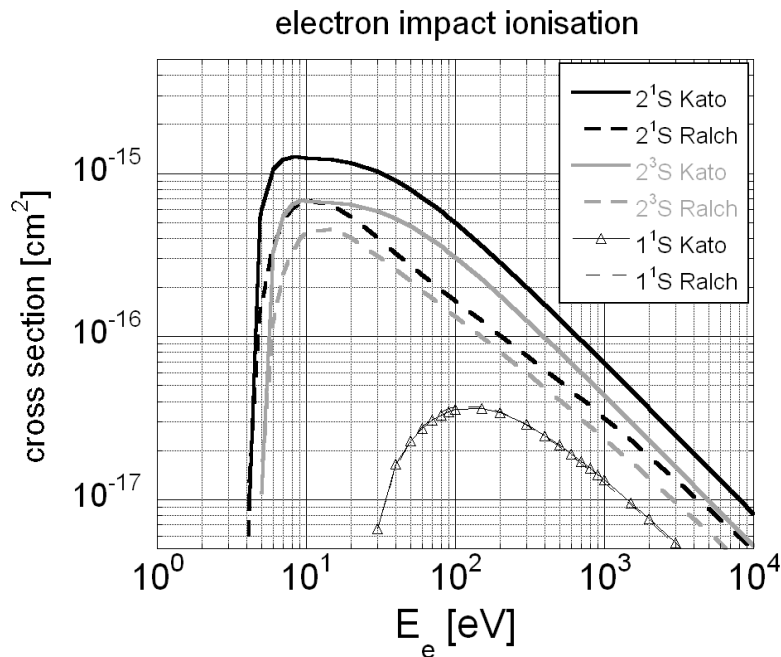
electron impact ionisation

Figure 3.1: Cross sections for the electron impact ionisation from the metastable states as recommended by Ralchenko et al. [2000] and by Kato and Janev [1992]. The coinciding data for the ionisation from the ground state are added for comparison.

which are calculated by an appropriate ADAS code [ADA, 2007].

The inclusion of the higher shells is for the purpose of our population calculations of the levels with $n = 2$ not so important as for the modelling of line intensity ratios used for n_e and T_e derivation. This is because of a higher impact of such a model extension on population of levels of higher n shells [Kornejew, 1996]. Moreover, the uncertainties of our absolute level population measurements by LIF of around a factor of two (see Sec. 6.2) is much poorer than the accuracy of the n_e and T_e derivation of 10-30%. In order to estimate the impact of such a model extension the population of the $n = 2$ levels as a function of electron density and for several values of electron temperature have been calculated based on the model including only the levels with $n \leq 4$ as well as by extending the model with the data for the shell $n = 5$ and finally $n = 6$ compiled by Brix [1998, 2007]. Figures 3.2 and 3.3 show the results in form of relative population change of the four considered levels due to the inclusion of one higher shell. There is barely an impact on the singlet levels for both calculations. In contrast, the triplet levels experience a population decrease of up to 18% upon inclusion of the $n = 5$ shell data being mostly pronounced at higher densities of $n_e \gtrsim 3 \times 10^{12}\,\mathrm{cm}^{-3}$ and does only weakly depend on T_e. Further extension of the data set to the $n = 6$ shell results in a positive or a negative change of the triplet population of up to 10%. The change direction depends on T_e. However, for moderate temperatures of interest, $40\,\mathrm{eV} < T_e < 80\,\mathrm{eV}$, the change is at most 6% and can be neglected in view of the accuracy of our LIF measurements of the level population. Consequently, the data up to the $n = 5$ shell are used for our data
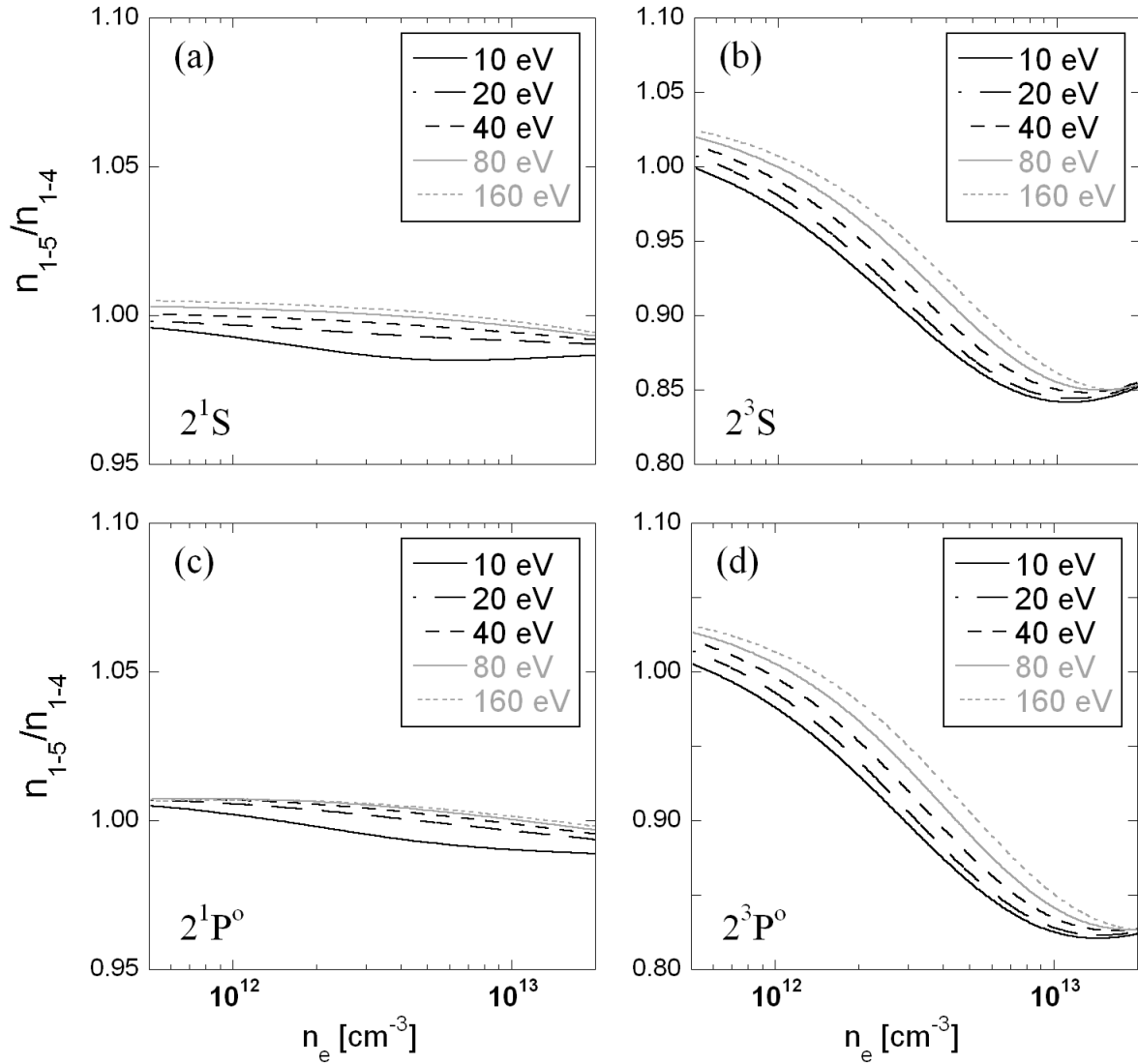
Figure 3.2: Comparison of the $n = 2$ level populations (relative to the ground state) calculated with the model including levels with $n \leq 4$ and by extending the model with the $n = 5$ states. The population ratio of the latter to the former calculation is shown as a function of the electron density for various values of the electron temperature.
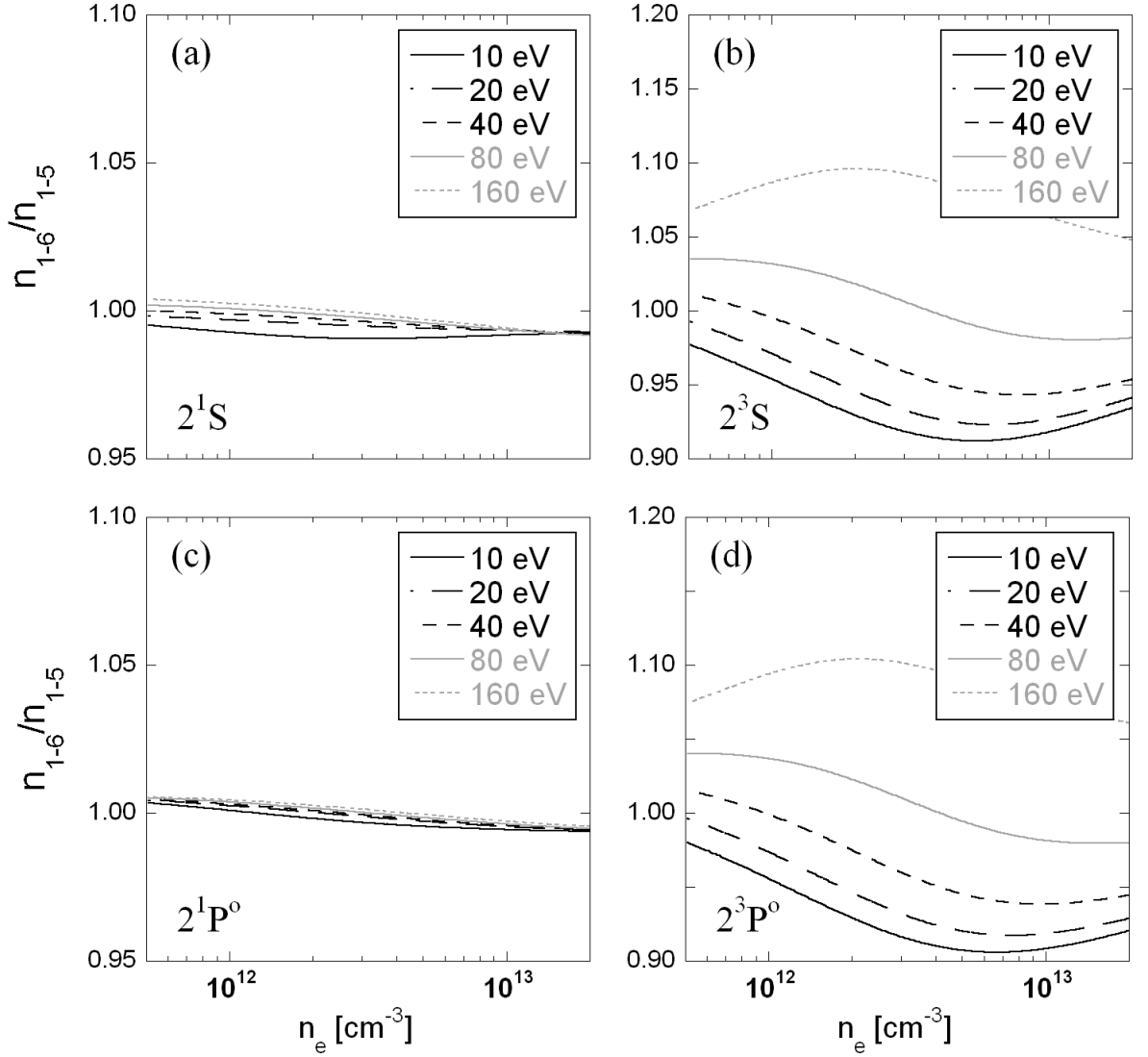
Figure 3.3: Comparison of the $n = 2$ level populations (relative to the ground state) calculated with the model including levels with $n \leq 5$ and by extending the model with the $n = 6$ states. The population ratio of the latter to the former calculation is shown as a function of the electron density for various values of the electron temperature.

analysis.

The rate coefficients used in this work have been calculated from the corresponding cross sections with the assumption of the thermalisation of the plasma electrons. In some situations, e.g. in low density plasmas or when heating magnetised plasmas with resonant electromagnetic waves, deviations from the Maxwellian electron energy distribution function can be expected. Brix performed test calculations for an energy distribution of a given temperature followed by a calculation in which an electron fraction of 10% was assumed to have a five time larger temperature than the remaining 90% of the electrons [Brix, 1998]. In this example, the impact of the two-temperature energy distribution on the level populations was investigated. At $T_e = 20\,\mathrm{eV}$ and $n_e = 5 \times 10^{12}\,\mathrm{cm}^{-3}$ the largest deviation of 40% was observed in the case of the level $3^1\mathrm{P}^\mathrm{o}$. They decrease for higher temperatures. Negligible deviations were observed in the triplet levels.
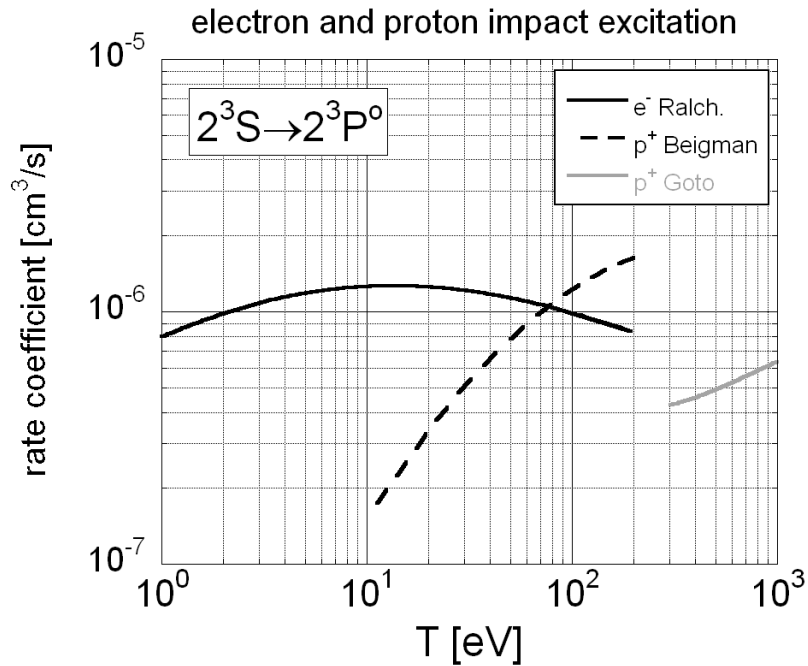

Figure 3.4: Rate coefficients for electron and proton excitation between the levels $2^3\mathrm{S}$ and $2^3\mathrm{P}^\mathrm{o}$. The electron excitation data is based on [Ralchenko et al., 2000]. Proton excitation data are based on calculation of Beigman et al. [2003] and on the use of the mass scaling procedure along to [Goto and Fujimoto, 1997].

3.2.1.2 Proton collisions

Inelastic collisions of protons with thermal helium atoms in the ground state[1] are much less probable at plasma temperatures of $T \approx 100\,\mathrm{eV}$ than helium excitation and ionisa-

---

[1]The discussion is qualitatively valid also for collisions with deuterons. Correction factors for cross sections of deuterons are given by considering the mass scaling [Janev, 1995].

tion by electrons because the energy transfer between a proton and an electron is very ineffective due to the large mass difference. The maximum cross sections for proton excitation from the ground state to the n^1P^o levels lie at the proton energy of $\sim 100\,\text{keV}$ [Hippler and Schartner, 1974, Fritsch, 1992]. Hence, proton excitation from the ground state plays a dominant role only for high energy helium beams.

A different situation is given for population redistribution between excited levels, mainly within the same n shell. Here, the energies to be transferred to the electron in the range of 1 eV brings the proton collisional excitation in competition with the electron ones, at least at higher temperatures. However, as long as the LS coupling can be assumed, only proton impact transitions without changing the total spin of the atom have to be considered because, in contrast to electron impact processes, no electron exchange can take place.

For a proper prediction of the population of the $n = 2$ levels the total transition rates between those levels, containing the electron and proton impact processes, must be considered. Therefore, the ratio of both rate coefficients $\langle v\sigma\rangle_p / \langle v\sigma\rangle_e$ is of interest. The ratio of the transition rates, yielding the correction factor to the pure electronic transition rate, is approximately equal to the ratio of the rate coefficients. This is because of the assumption of the quasi neutrality of the plasma resulting in $n_e \approx n_p$ for a hydrogen plasma with a not too high content of impurity ions.

Cross section calculations of proton impact excitation between the $n = 2$ levels of helium based on the Born approximation with normalisation at low energies are provided by Beigman et al. [2003]. The resulting rate coefficient for the triplet case is plotted in Figure 3.4. For comparison the electron excitation rate coefficient according to [Ralchenko et al., 2000] for the same transition is also shown. Both curves cross at $T \simeq 80\,\text{eV}$ which means that at this plasma temperature, being assumed to be valid for both electrons and protons, the excitation rate due to electron collisions must be doubled in order to additionally account for the proton collisions. For higher temperatures the proton collision impact is even higher. In Figure 3.5 calculation results are shown for the relative change of both $n = 2$ triplet levels when including the proton collisions accordingly to the rate coefficient provided by Beigman (Figure 3.4). The calculation is made for a range of electron density and five different electron temperature values. The largest impact is clearly seen at higher temperatures since the proton collision excitation is dominant there. As expected, the metastable state population always decreases in favour of the 2^3P^o level (the much higher relative 2^3P^o level population increase than the decrease of the 2^3S level population at low densities and the opposite situation at high densities is due to the increasing population ratio $n_{2^3P^o}/n_{2^3S}$ with increasing electron density). In the temperature range of $40\,\text{eV} < T_e < 80\,\text{eV}$ and for the densities $1 \times 10^{12}\,\text{cm}^{-3} < n_e < 1 \times 10^{13}\,\text{cm}^{-3}$ the population change reaches 20% for the metastable and even 60% for the 2^3P^o level. However, the cross sections for proton impact excitation calculated within the Born approximation at these low proton velocities pose even with normalisation procedures an upper limit and are expected, at least for the excitation between the $n = 2$ levels, to be considerably overestimated so that for the temperature range of our interest electron collisions should be still dominant

[Beigman, 2007]. The negligibility of proton collisions here is also supported by estimating the proton impact cross section from the electron impact ones by applying a simple mass scaling in accordance to [Goto and Fujimoto, 1997]. The resulting rate coefficient is also plotted in Figure 3.4. It is shifted to higher temperatures by more than a factor of ten compared to the Born calculation. Hence, the impact of proton collisions on the population redistribution between the $n = 2$ levels is neglected in our calculations.
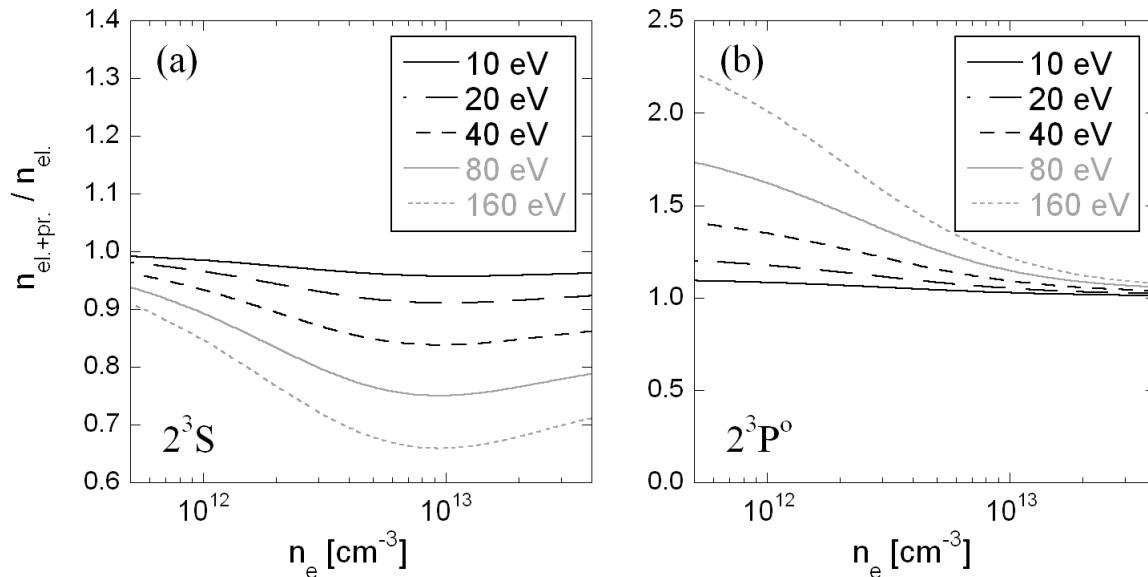

Figure 3.5: Impact of the extending of electron collisions by the proton excitation rate between the levels 2^3S and 2^3P° on the triplet $n = 2$ levels.

Rate coefficients calculated by Beigman et al. [2003] in the Born approximation are available for almost all fine structure resolved $\Delta n = 0$ proton excitation processes within the shells $n = 2 - 4$. Borodin et al. [2006] provide calculations for the $n = 3$ levels using the close coupling method. Two examples of rate coefficients for the $n = 3$ shell are shown in Figure 3.6. Results of the Born approximation without and with normalisation, the close coupling method and the mass scaling by Goto are shown. They are compared to the electron impact excitation by Ralchenko. In the case of the transition 3^3P° $\rightarrow 3^3$D the proton collisions are more pronounced in comparison to the electron ones. While the rate coefficient in the Born approximation without normalisation is up to ten times higher the result by applying the normalisation procedure is much lower and exceeds the rate coefficient for the electron impact excitation only at higher temperatures of $T \gtrsim 150\,\mathrm{eV}$ (these results for both transitions seem to coincide with the application of the mass scaling to the electron rate coefficients). The close coupling method provides the smallest values, which – comparing to electron collision rates – leads to a negligibly

small proton collision rates at temperatures below 100 eV (for deuterons it is 200 eV due to the mass scaling of cross sections). However, whereas the Born approximation results are to be treated as an upper limit for the proton impact rate coefficients the close coupling method used by Borodin et al. [2006] provides a lower limit. Thus, the true value is expected to lie in between and the proton collisions impact could be comparable to the electron ones for larger temperatures.

The impact of even such large rate coefficient for the transition $3^3P^o \rightarrow 3^3D$, as it follows from the Born calculation, is negligible on the population of the $n = 2$ levels (below 2%) and hence it is neglected in the model. The question of the rate coefficients (due to electron and proton collisions) for the population transfer between levels of the shell $n = 3$ and $n = 4$ is raised in chapter 6 when discussing the measurement results.
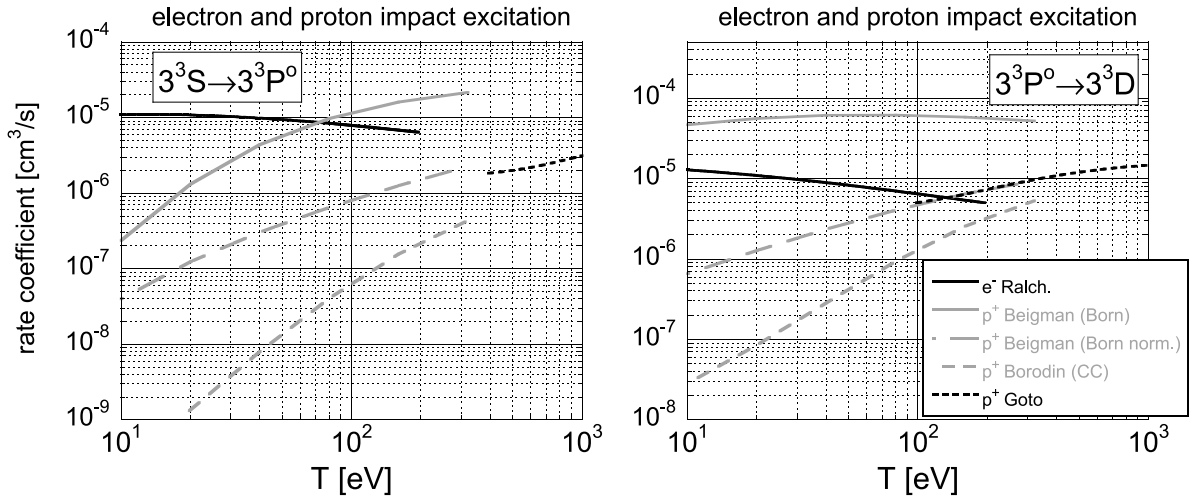

Figure 3.6: Rate coefficients for electron and proton impact excitation for two transitions: $3^3S \rightarrow 3^3P^o$ and $3^3P^o \rightarrow 3^3D$. The electron excitation data is based on [Ralchenko et al., 2000]. Proton excitation data are based on the Born approximation without and with normalisation [Beigman et al., 2003], the close coupling (CC) method [Borodin et al., 2006] as well as on the use of the mass scaling procedure according to [Goto and Fujimoto, 1997].

3.2.1.3 Other processes

Excitation collisions with impurity ions should play, at least for the modelling of our experiments, an even less important role than collisions with protons, for two reasons. Because of the larger mass and hence lower velocities of those ions, higher impurity ion temperatures are needed for the rate coefficients to be as large as those of proton collisions (the measured ion energies at the maximum cross section for ground state helium excitation by different ions scale with the ion mass and charge [Anton et al., 1992]). Moreover, typical densities of impurity ions in fusion edge plasmas lie below

10% of the electron density. At the value of effective ionic charge of $Z_{\text{eff}} = 2$ which is due to hydrogen-like carbon CVI being assumed to be the only impurity species in a hydrogen plasma, its density would amount to $1/20$ of the electron density.

The cross sections for collisions of helium atoms with each other are much smaller than those of atomic helium with ionised particles because of the lack of the long-range Coulomb interaction. Hence, high neutral gas density is needed for helium-helium collisions to play a role. Similarly to the case of proton collisions, first the transitions between the levels of the same n shell are affected. Measurements of rate coefficients for helium-helium excitation collisions between the $n = 3$ levels in a glow discharge showed that they are five to six orders of magnitude lower than those for electron-helium excitation [Denkelmann et al., 2000]. Hence, they should be also negligible in our case.

Charge exchange reactions in particular of excited helium atoms with plasma ions can play a role as loss processes for helium atoms out of the beam. For the estimation of the relative importance of those processes induced by proton and impurity ion collisions, the same argumentation line can be applied as for the helium excitation collisions with protons and impurities. As no reaction parameters are available for charge exchange collisions of helium with protons, those for hydrogen-like ions can be used for estimations. Research on this topic is currently in progress [Brix, 2007].

Helium atoms, once being ionised, are in our model considered as lost beam particles. This is justified as can be shown by comparing of the time scales for the recombination and for collisions of helium ions with protons. The three body recombination is negligible for low electron densities as in the fusion edge plasmas [Sobelman et al., 1995]. The time constant for radiative recombination lies in the range of 1 second [Fujimoto, 1978]. In contrast, the time constant for elastic proton collisions with helium atoms, according to [Hinton, 1983]

$$\nu_{\text{ab}} = \frac{16\sqrt{\pi}}{3} \frac{1}{m_{\text{a}}} \left(\frac{1}{m_{\text{a}}} + \frac{1}{m_{\text{b}}} \right) \frac{q_{\text{a}}^2 q_{\text{b}}^2 \ln\Lambda}{(4\pi\epsilon_0)^2 (v_{\text{a}}^2 + v_{\text{b}}^2)^{3/2}} n_{\text{b}}, \tag{3.3}$$

(m_i, q_i and v_i are the particle masses, charges and velocities, respectively, $\ln\Lambda$ is the Coulomb logarithm being a weak function of temperature and density, to be approximated by the value of 10 [Chen, 1984] and n_{b} the proton density) is of the order of $10^{-4}\,\text{s}^{-1}$ and hence much shorter than the recombination time scale. Thus, helium ions are spread around the plasma volume in the torus and their recombination in the observation volume does not play a role. The background density of ionised helium in the hole plasma can be neglected as a source for volume recombined helium atoms as well as a source for fluxes of recycled neutral helium in the ground or the metastable states resulting from the wall recombination processes.

Atomic helium levels with $L \geq 3$ are subject to a partial or complete breakdown of the LS coupling scheme [Parish and Mires, 1971] with the wave function mixing of the corresponging n^1L and n^3L levels. This results in an enhanced population distribution between the singlet and triplet side, which can be simulated by enhanced collisional rate coefficients between the mixed levels [Goto, 2003]. In an extreme case, the population

ratios of the mixing levels $n(n^3L)/n(n^1L)$ will be equal to three, as the corresponding ratio of the statistical weights. A calculation assuming this extreme condition showed no impact of the level mixing on the population of the $n = 2$ singlet levels and a population increase of below 10% for the triplet levels of this shell. Thus, this effect is neglected in our model.

3.2.2 Radiation trapping

Radiation transport must be considered in collisional-radiative modelling of the population distribution among excited levels of an atom if the density of the radiating species in the lower level of the considered transition is high enough to considerably reabsorb its own line radiation from an adjacent point in space. In many cases, only radiation of the resonance lines, i.e. transitions ending in the ground state, will be affected, owing to the much larger population of the ground state compared to the excited levels.

Absorption of line radiation, similarly to the situation when pumping with resonant laser light, results in an enhancement of the population of the radiating level to the detriment of the lower level. In general, the radiation transport equation (2.30) must be solved, which is very complicated for a three dimensional case. However, if the optical depth of the plasma is not too high ($\tau \sim 1$ as in our case fulfils this criterion), the concept of the escape factor can be applied to quantify the radiation trapping impact on the level population (see Sec. 2.2.2). This is a correction factor lowering the Einstein coefficient for spontaneous radiation A_{ki}, which results in a higher calculated excitation degree of the considered species. Its calculation depends on the geometry of the plasma and the line shape.

For the estimation of the impact of radiation trapping on the prediction of the level population in the $n = 2 - 3$ shells of atomic helium, the formula (2.40) provided by Fujimoto [2004] for a cylindrical plasma with a parabolic radial density profile of the emitting species and with a Gaussian emission line profile is used. In the calculation (Figure 3.7) a typical reservoir pressure of $p = 6$ mbar, with resulting helium flow of $\Gamma_{\text{He}} = 3.2 \times 10^{18} \text{s}^{-1}$, was assumed as well as an electron temperature of $T_{\text{e}} = 50$ eV. In case (a) the situation of our outermost observation point at the minor plasma radius of $r = 47$ cm is considered (see Figure 5.5). The radius of the helium density profile around the beam axis is 1 cm (see Figure 5.8) and the central line helium density amounts to $n_{\text{He}} = 1.6 \times 10^{13} \text{cm}^{-3}$. Since the formula 2.40 is calculated under the assumption of a constant absorber (ground state helium) density we use as an approximation half the central line value of $n_{\text{He}} = 0.8 \times 10^{13} \text{cm}^{-3}$. The resulting escape factors for the four strongest resonance transitions between the ground state and the levels 2^1P°, 3^1P°, 4^1P° and 5^1P° are listed in Table 3.1. In Figure 3.7 (a) the calculated relative population changes of the levels in shells $n = 2 - 3$ resulting from the inclusion of the radiation trapping are shown as a function of electron density. The reabsorption of light by the ground state atoms increases the excited level population. The most affected levels are the n^1P° with a population increase by a factor of 2.15 for 2^1P°. The singlet metastable level population only slightly increases by up to 7% at higher density. On the contrary,
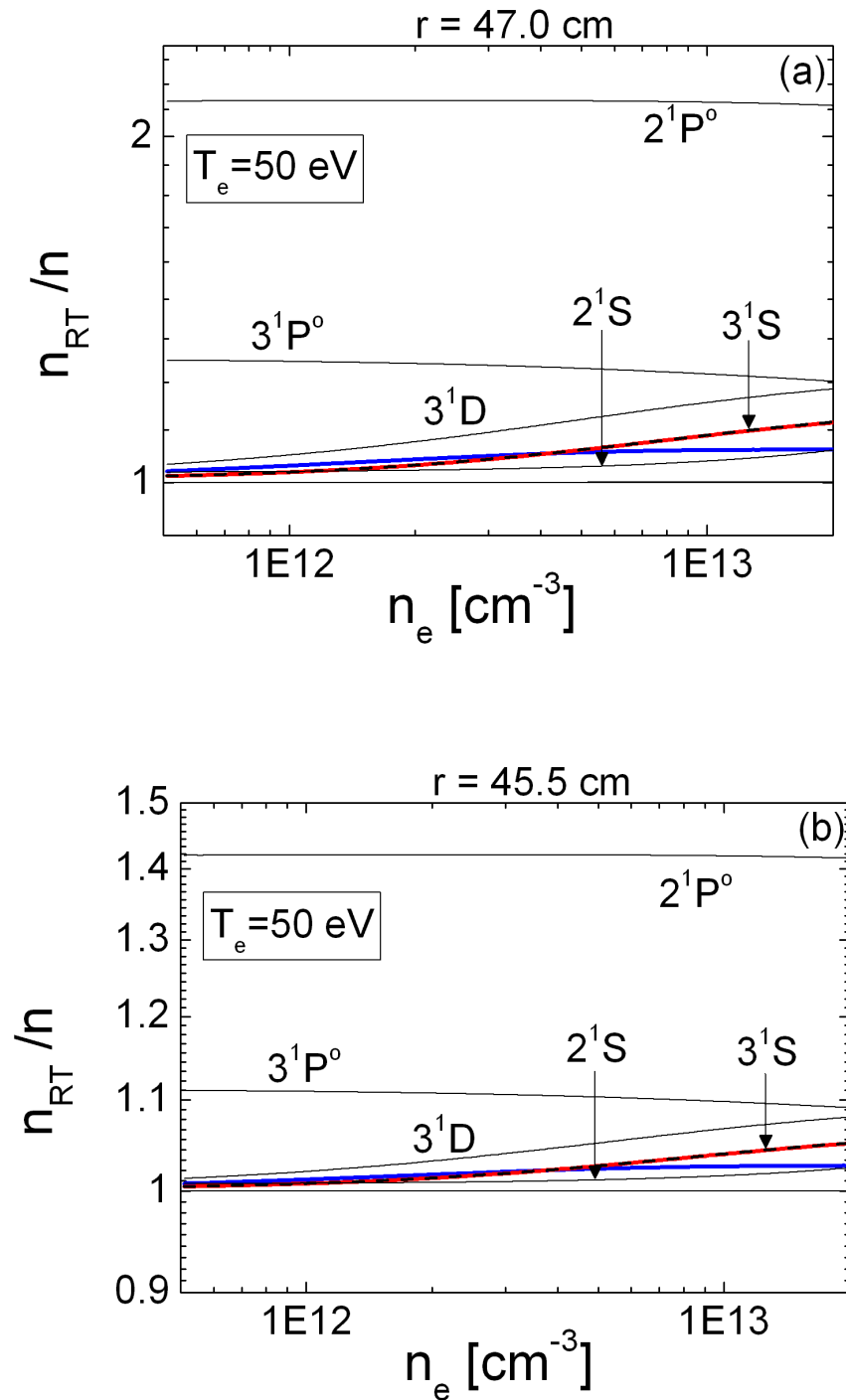
Figure 3.7: Relative enhancement of the modelled population of the $n = 2 - 3$ shells levels due to radiation trapping by the beam particles for $T_e = 50\,\text{eV}$. The levels which are not explicitly marked experience a change below 1%. The red and blue dashed lines indicate the change of the T_e sensitive line ratio $I_{728.1}/I_{706.5}$ and the n_e sensitive ratio $I_{667.8}/I_{728.1}$, respectively. (a) minor plasma radius $r = 47\,\text{cm}$ (b) $r = 45.5\,\text{cm}$.

	$r = 45.5\,\text{cm}$	$r = 47\,\text{cm}$
2^1P^o	0.70	0.47
3^1P^o	0.90	0.78
4^1P^o	0.96	0.89
5^1P^o	0.99	0.94

Table 3.1: Escape factors for four strongest resonance transitions used for the calculation shown in Figure 3.7 for two radial positions in the plasma.

the influence on the triplet levels is negligible. Thus, for our absolute population measurements of the $n = 2$ levels only the influence of radiation trapping on the level 2^1P^o is of importance.

The increased 3^1P^o population spreads to the adjacent levels 3^1S and 3^1D, which is more pronounced at higher densities due to the stronger collisional population transfer. This leads to an enhancement of the n_e sensitive line ratio $I_{667.8}/I_{728.1}$ by up to 7% and the T_e sensitive ratio $I_{728.1}/I_{706.5}$ by up to 13% (shown with a blue and red line in Figure 3.7 (a)). For a lower electron density of $n_\text{e} = 1 - 2 \times 10^{12}\,\text{cm}^{-3}$, which is typical at the considered radial position, the effect is smaller, respectively 4.8% and 3.6% for the n_e and the T_e sensitive intensity ratio (this is approximately equivalent to an overestimation of n_e by 9% and of T_e by 4.5%). A calculation for $T_\text{e} = 20\,\text{eV}$ showed a further slight decrease of the impact of the radiation trapping.

However, this calculation provides a rather overestimated impact of the radiation trapping for the case of helium beams at TEXTOR. This is because gas nozzles are positioned typically in a radial distance of several centimetres from the point, where the measured intensity profiles start to be visible, in order to avoid their overheating due to the contact with the plasma. (In contrast, the radial position of the nozzle during our experiments was $r = 48\,\text{cm}$ and thus only 1 cm away from the outermost observation point). Hence, at a given flux of helium atoms its on-axis density when entering the plasma will be considerably smaller due to the beam divergence and with further decrease due to ionisation losses.

Figure 3.7 (b) shows for comparison the calculation result for our middle observation point at the plasma radius of $r = 45.5\,\text{cm}$. Owing to the beam attenuation (Figure 5.6) and divergence the centre line helium density drops here to $n_\text{He} = 3.9 \times 10^{12}\,\text{cm}^{-3}$ and for the calculation of the escape factor again the half ot this value is taken. The radius of the parabolic helium density profile is estimated to 1.5 cm (see Figure 5.8). The lower values of the resulting escape factors are also listed in Table 3.1. The enhancement of the 2^1P^o population is still considerable (42%) but that of the 3^1P^o falls below 11%, which means that the line intensity ratios of interest are weaker affected (below 2.7% and 4% for the n_e and T_e sensitive ratio at higher densities of $n_\text{e} \leq 1 \times 10^{13}\,\text{cm}^{-3}$, respectively).

3.2.3 Beam relaxation in the course of the plasma penetration

Provided a probe ensemble of helium atoms in the ground state would be introduced instantly into a plasma of constant parameters, a certain time interval would be needed to establish a steady state distribution between the different excited levels with respect to the ground state population. This time constant depends on the excitation transition rates and hence, mainly on the electron density in the case of helium beams used for the diagnosing of edge fusion plasmas.
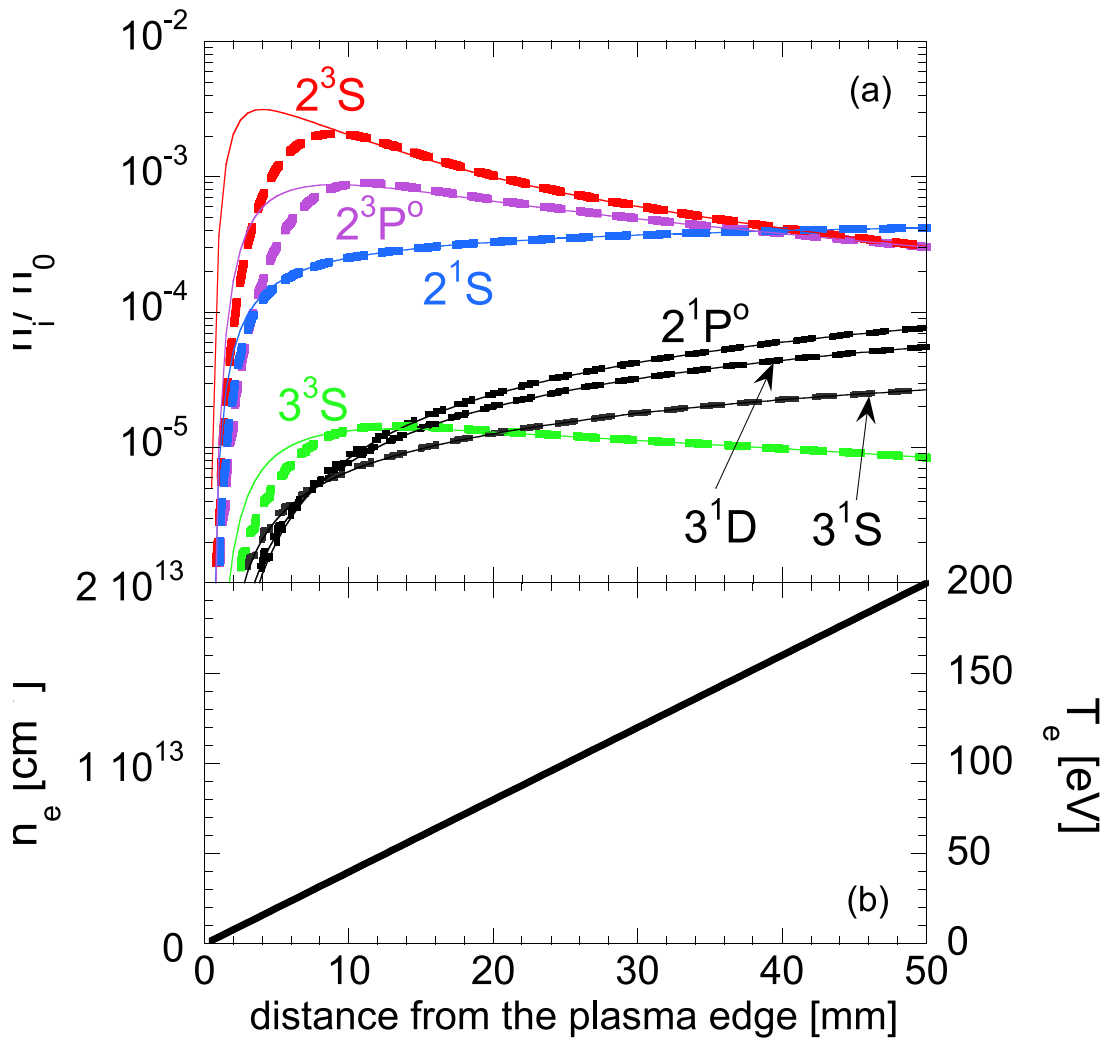

Figure 3.8: (a) Impact of the lack of the beam relaxation on the population of the $n = 2$ and some of the $n = 3$ levels along the beam path through the plasma. Solid lines represent the quasi-steady state solution for each radial position while the dashed lines are calculated with the time dependent solution accountig for the beam relaxation effect. (b) Linear n_e and T_e profiles assumed in the calculation.

Helium atoms injected radially into a fusion plasma experience – based on their directed movement towards the plasma centre – increasing electron density and temperature on their penetration path due to the edge gradients of n_e and T_e. If the time constant related to the steady state population distribution is shorter than the time scale of the change of n_e and T_e, the population distribution can be treated as quasi-stationary with the corresponding local plasma parameters. This situation is referred to as beam relaxation. In the opposite case, the level populations deviate from the steady state distribution and, in order to calculate them, it is necessary to track back the path of the particles through the plasma (the numerical approach used for both the time dependent and the quasi-steady state solution are described in Sec. 3.3). The profiles of the plasma parameters from the considered radial position to the plasma edge as well as the beam velocity are needed for such calculations.

In Figure 3.8 radial profiles of steady-state populations of selected $n = 2 - 3$ levels are shown with solid lines. Dashed lines represent the time dependent solution which takes the radial movement of the beam into account. Considerable deviations are visible in the plasma edge being mostly due to the low electron density, linearly coupled to the excitation transition rates. However, only triplet levels are here affected, their populations being strongly influenced by the triplet metastable level 2^3S. Its relaxation time constant of $\tau \gtrsim 1\,\mu$s in the edge, corresponding to the beam propagation of $\Delta r \gtrsim 1.5\,$mm, is too large to establish steady-state population of the triplet levels. Typically, the relaxation times of the triplet levels are an order of magnitude larger than those of the singlet levels [Brix, 1998]. This results in an overestimation of the electron temperature at low electron densities of $n_e \lesssim 2 \times 10^{12}\,$cm^{-3} if the steady-state solution of the rate equation system is used for comparison with the measured line ratios.

3.2.4 Photoionisation

The photoionisation is a special issue, which must be considered because of the use of high laser powers in our LIF experiments. The laser light, used for resonant excitation between two selected levels of helium atoms in the beam by accurate wavelength adjustment, can simultaneously lead to ionisation from excited levels. If photoionisation takes place from the observed level, the measured fluorescence flux is lowered. Since the laser always pumped the levels of the $n = 2$ shell, its photon energy was only sufficient for the photoionisation from the levels with $n > 2$.

The photoionisation cross sections obtained from different measurements and calculations coincide well with each other [Stebbings et al., 1973, Fujimoto, 1979]. For the 3^{2S+1}P^o levels and a photon wavelength of $\lambda \approx 600\,$nm they lie in the range of $\sigma_{\mathrm{ph.ion}} \approx 10^{-17}\,$cm^2 and decrease with increasing frequency ($\sigma_{\mathrm{ph.ion}} \propto \nu^{-2}$) and principal quantum number n. With the laser pulse energy of 1 mJ, the pulse duration of $\Delta \mathrm{T_L} = 15\,$ns and the cross sectional area of the laser beam of 3 cm^2 we obtain a photon flux density of $\Gamma_{\mathrm{ph}} = 10^{-3}\,J/3.3 \times 10^{-19}\,\frac{\mathrm{J}}{\mathrm{ph}}/15 \times 10^{-9}\,s/3\,cm^2 = 6.7 \times 10^{22}\frac{\mathrm{ph}}{\mathrm{cm^2 s}}$. The photoionisation rate then amounts to $\Gamma_{\mathrm{ph}}\sigma_{\mathrm{ph.ion}} \approx 7 \times 10^5\,$s^{-1} and the relative photoionisation losses during a laser pulse $(\Delta n/n)_{\mathrm{ph.ion}} = \Gamma_{\mathrm{ph}}\sigma_{\mathrm{ph.ion}}\Delta \mathrm{T_L}$ do not exceed 1%.

Hence, a photoionisation should neither influence the fluorescence radiation nor lead to considerable losses of helium atoms in the beam.

3.3 Numerical approach for the calculation of the population distribution by using the CR model

The population density $n_i = n_i(r, t)$ of the ith quantum level of helium atoms in the beam is in general a function of the minor plasma radius r and of the time t. The total derivative of this function with respect to the time is

$$\frac{\mathrm{d} n_i(r, t)}{\mathrm{d} t} = \frac{\partial n_i(r, t)}{\partial t} + v_{\mathrm{He}} \frac{\partial n_i(r, t)}{\partial r} = S_i(r, t), \tag{3.4}$$

where v_{He} is the velocity of the beam, here, oriented along the minor radius of the plasma. The gas injection system used in our experiments delivers long gas pulses, the total gas flux of which can be assumed as constant on the relaxation time scale of the levels ($\tau_{\mathrm{relax}} < 10^{-3}\,\mathrm{s}$ for the ground state; see also Figure 5.2). Thus, the radial profiles of the population densities can be assumed as stationary, i.e. $\frac{\partial n_i(r,t)}{\partial t} = 0$ which means that the source term $S_i(r)$ of the ith level (for example in the steady state (relaxed) condition this term for the ground state will be mainly expressed by the overall ionisation losses) is counterbalanced by the transport term $(v_{\mathrm{He}} \frac{\partial n_i(r)}{\partial r})$, different from zero for a finite gradient of the population density.

The source term is accounted for by considering all population and depopulation processes of the level i:

$$S_i(r) = \sum_{j \neq i} \langle \sigma_{j \to i} v_{\mathrm{e}} \rangle n_{\mathrm{e}} n_j - \sum_{j \neq i} \langle \sigma_{i \to j} v_{\mathrm{e}} \rangle n_{\mathrm{e}} n_i + \sum_{j > i} \mathrm{A}_{j \to i} n_j - \sum_{j < i} \mathrm{A}_{i \to j} n_i - \langle \sigma_{i \to \mathrm{ion}} v_{\mathrm{e}} \rangle n_{\mathrm{e}} n_i. \tag{3.5}$$

Here, the electron collisions (excitation and deexcitation; heavy particle collisions can be treated in the same way), spontaneous decay and the population losses caused by ionisation are included. The transport term of Eq. (3.4) can be incorporated in the solution by considering a given spatial fraction of the beam in a moving coordinate system such as to trace the same beam particles on their way through a plasma with pronounced gradients of n_{e} and T_{e}. This is equivalent to the treatment of the set of the rate coefficients (depending on T_{e}) and of the electron density in Eq. (3.5) as functions of time. The transformation between the radial and the time variable is given simply by the beam velocity $v_{\mathrm{He}} = \frac{\mathrm{d} r}{\mathrm{d} t}$, which is assumed constant along the penetration path of the beam. In addition, the radial profiles of $n_{\mathrm{e}}(r)$ and $T_{\mathrm{e}}(r)$ are needed.

The differential equations of type (3.5) are written for all levels of interest (29 levels of the shells with the principal quantum number $n = 1 - 5$ in our case). The equation system is solved numerically by using the step width controlled Runge-Kutta method [Press et al., 2002]. The initial populations are set to one for the ground state and zero

for all excited levels.

For not too low electron densities ($n_\mathrm{e} \gtrsim 2 \times 10^{12}\,\mathrm{cm}^{-3}$) an additional assumption to the beam stationarity ($\frac{\partial n_i(r,t)}{\partial t} = 0$) can be made, significantly simplifying the model calculation. The relaxation times of all excited levels then become sufficiently short as to justify the neglecting of the transport of excited atoms. Consider the equation for the total time derivative of the population density $n_i^\mathrm{rel}(r,t) = \frac{n_i}{n_1}(r,t)$ of an excited level i relative to the ground state population

$$\frac{\mathrm{d}n_i^\mathrm{rel}(r,t)}{\mathrm{d}t} = \frac{\partial n_i^\mathrm{rel}(r,t)}{\partial t} + v_\mathrm{He}\frac{\partial n_i^\mathrm{rel}(r,t)}{\partial r} = S_i^\mathrm{rel}(r,t). \qquad (3.6)$$

If the source and loss terms (due to collisions and radiation) in S_i^rel for a given excited level are much larger than the population gain or loss due to the beam movement, neglecting the transport term is justified for the calculation of the level populations. This can be shown for example for the triplet metastable $2^3\mathrm{S}$ population in a plasma at $n_\mathrm{e} = 10^{13}\,\mathrm{cm}^{-3}$ and $T_\mathrm{e} = 100\,\mathrm{eV}$ (see Figure 3.8). The main loss process is the electron collision excitation to the level $2^3\mathrm{P}^\mathrm{o}$. The excitation transfer is given with $n_{2^3\mathrm{S}}^\mathrm{rel} n_\mathrm{e} \langle \sigma v_\mathrm{e} \rangle_{2^3\mathrm{S} \to 2^3\mathrm{P}^\mathrm{o}} \approx n_{2^3\mathrm{S}}^\mathrm{rel} 10^{13}\,\mathrm{cm}^{-3}\, 10^{-6}\,\mathrm{cm}^3\mathrm{s}^{-1} = n_{2^3\mathrm{S}}^\mathrm{rel} 10^7\,\mathrm{s}^{-1}$ (the main population process is the spontaneous emission from the level $2^3\mathrm{P}^\mathrm{o}$ with $\mathrm{A}_{2^3\mathrm{P}^\mathrm{o} \to 2^3\mathrm{S}} = 10^7\,\mathrm{s}^{-1}$ and $n_{2^3\mathrm{P}^\mathrm{o}}^\mathrm{rel} \approx n_{2^3\mathrm{S}}^\mathrm{rel}$). For the transport term we write $10^5\,\frac{\mathrm{cm}}{\mathrm{s}}\, n_{2^3\mathrm{S}}^\mathrm{rel} \frac{50\%}{1\,\mathrm{cm}} = n_{2^3\mathrm{S}}^\mathrm{rel} 0.5 \times 10^5\,\mathrm{s}^{-1}$ (the gradient of the $2^3\mathrm{S}$ population density is taken from Figure 3.8). As one can see, the transport term is more than two orders of magnitude lower than the excitation transfer (this is not the case for lower electron density at the plasma edge). Neglecting this term is called the quasi-steady state approximation. A steady state situation is given for a vanishing population gradient.

In the quasi-steady state approximation we obtain $\frac{\mathrm{d}n_i^\mathrm{rel}(r)}{\mathrm{d}t} = S_i^\mathrm{rel}(r) = 0$, which means that the relative excited level populations for any given radial position have a steady state distribution, i.e. a distribution which is established after a sufficiently long time interval (relaxation time) under steady state conditions of electron density and temperature. On the other hand, the total time derivative of the relative population is given with

$$\frac{\mathrm{d}}{\mathrm{d}t}\frac{n_i(r)}{n_1(r)} = \frac{1}{n_1(r)}\frac{\mathrm{d}}{\mathrm{d}t}n_i(r) - \frac{n_i(r)}{n_1^2(r)}\frac{\mathrm{d}}{\mathrm{d}t}n_1(r) \equiv 0. \qquad (3.7)$$

The expression in the first term is given by the system of Eqs. (3.5) divided by the ground state population n_1. The second term – if not neglected – improves the accuracy of the quasi-steady state solution to $\sim 0.3\%$ [Brix, 1998]. It is sufficiently well approximated with the ionisation losses from the ground state:

$$n_i^\mathrm{rel}(r)\frac{\frac{\mathrm{d}}{\mathrm{d}t}n_1(r)}{n_1(r)} \approx -n_i^\mathrm{rel}(r) \langle \sigma_{1 \to \mathrm{ion}} v_\mathrm{e} \rangle n_\mathrm{e}(r). \qquad (3.8)$$

Finally, for a given radial position r with constant n_e and T_e the problem is described by a linear inhomogeneous equation system and the solution is given simply by multiplication of the inhomogeneous vector with the inverted coefficient matrix prepared accordingly to Eq. (3.7)

The quasi-steady state solution is supposed of course to coincide with the time dependent calculation for sufficiently high electron densities. This comparison was routinely used in our calculations to ensure that no mistakes were made in the setting up and the numerical treatment of the problem. An example calculation result of both methods is shown in Figure 3.8.

The extension of the CR model calculation to include the influence of resonant laser radiation on the excited levels population distribution is described in Sec. 5.3.

Chapter 4

Experiment

In this chapter, the experimental system is described. First, an overview will be given, followed by a detailed description of the sub-systems the experiment consists of. Emphasis is put on an exact characterisation of the components in terms of its suitability for providing absolute population densities.

The main measurements presented in this thesis were carried out on the tokamak TEXTOR (Sec. 4.1) located in the Forschungszentrum Jülich (Germany). Additionally, a glow discharge chamber suitable for LIF measurements in the laser laboratory was used for calibration of the laser system. It is described in Sec. 4.2 together with the laser system, consisting of an excimer pumped dye laser, which was used for the excitation of helium atoms in the TEXTOR edge plasma. Helium gas was puffed into the plasma in the form of a thermal beam by using a nozzle mounted in the vacuum lock system (Sec. 4.3). Finally, the detection of fluorescence light was performed by use of an absolutely calibrated observation system consisting of imaging optics, interference filters and light guides transporting the photons to photomultiplier tubes (Sec. 4.4).

The laser beam is guided from the laboratory to the top of the tokamak by folding mirrors to the toroidal position of the limiter lock 1 system (Figure 4.1). It is then directed down under an angle of $7°$ to the vertical direction (see Figure 4.8) and adjusted onto the gas nozzle mounted in a vacuum lock system. For our measurements at TEXTOR we utilised the limiter lock 1 system, which is typically used for investigations of plasma-wall interactions. This was done for several reasons:

- The lock system provides a very flexible tool for such a gas injection system. The nozzle can be moved radially between discharges or even exchanged and replaced by another nozzle type within a few hours without breaking the TEXTOR vacuum. Alternatively, light sources for absolute calibration and spatial adjustment of the observation system can be inserted into the observation volume on the same time scale. This proves to be of high importance in the latter case, since a fine readjustment of the optical path was always necessary prior to each measurement day. Also remote operation of the lock system was possible from both the TEXTOR control room and the place in the TEXTOR bunker where the corresponding observation system was arranged. A detailed description of the functionality of the lock systems at TEXTOR is provided by Schweer et al. [2005].

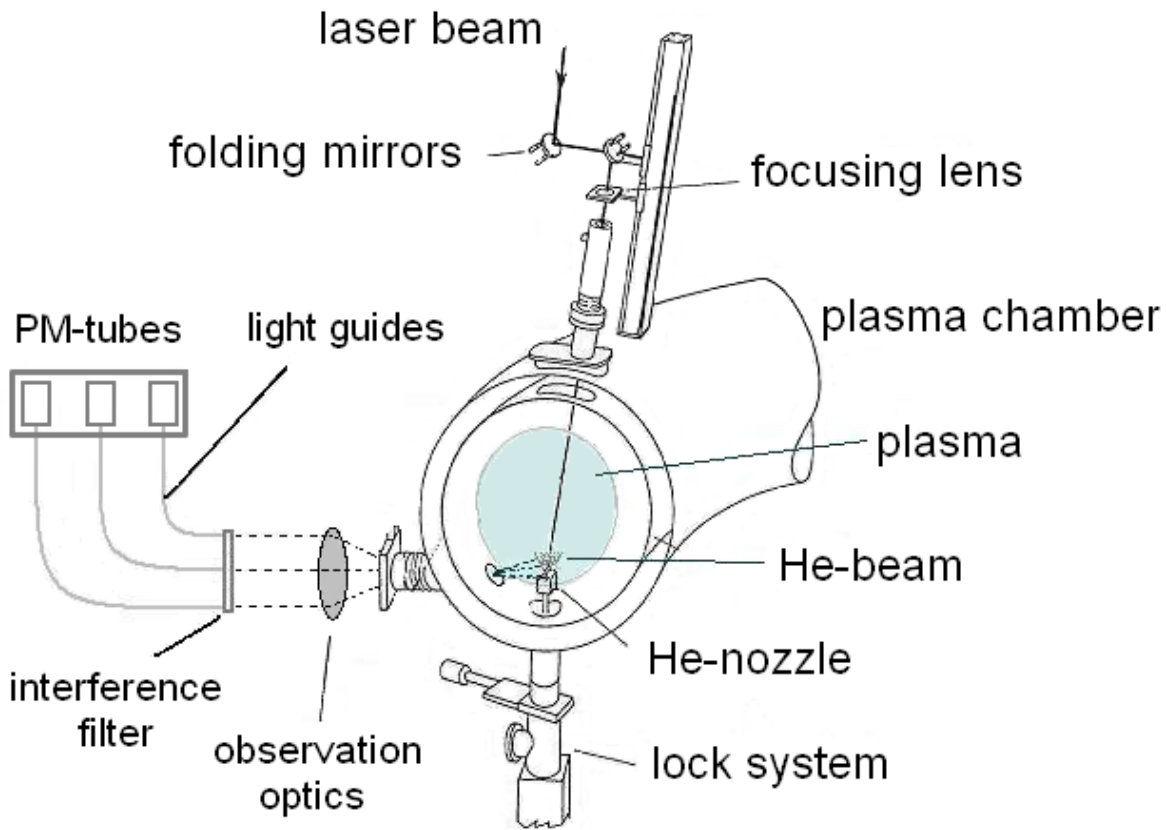- A free port above the lock system was available and has been used for the laser

Figure 4.1: Experimental set-up of the LIF measurements on TEXTOR.

beam entrance. The large port diameter of 150 mm allowed a visual adjustment of a diaphragm system by directing a helium-neon laser onto the nozzle. Adjusting the dye laser beam to pass through the diaphragm system provided a rough adjustment of the laser beam on the nozzle.

- A third port at the height of the nozzle position was available, which is used for spectroscopic investigation of probes exposed to the plasma by use of the lock system. This port has been used for three different applications: collection of fluorescence photons, performed by use of part of the optical path installed at this port. A 2D-camera with an image intensifier recorded the line radiation of helium puffed through our nozzle. These images were analysed and provided quantitative information about the beam divergence and its ionisation in the course of plasma penetration (see Sec. 5.1). Furthermore, the live image transmitted by this camera was very helpful for the fine adjustment of the dye laser beam on the nozzle.

An additional diaphragm was used to let through the middle part of the laser beam only. An image of the diaphragm was created at the nozzle position by a lens. Remote control of the lens position allowed the fine adjustment of the laser beam on the nozzle.
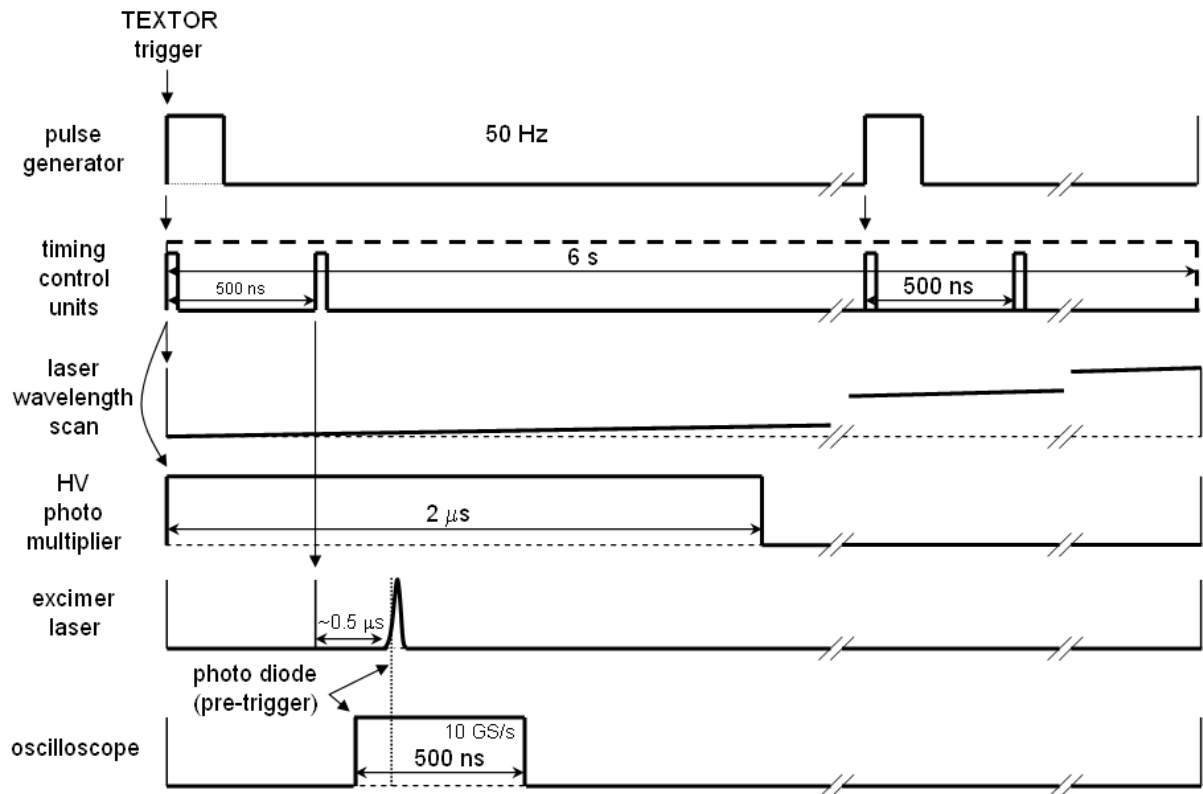
Figure 4.2: Schematic of the trigger system for LIF measurements on TEXTOR.

The observation of the fluorescence photons was performed perpendicularly to the torus and in the horizontal plane, simultaneously at three radial positions in the plasma. Observation volumes of 8 mm diameter are imaged 1:1 by a lens onto the entrance surface of liquid light guides, which further transport the photons to the photomultiplier tubes (Hamamatsu, type R3896). The electric signals are recorded by a digital storage oscilloscope of 1 GHz analogue bandwidth (LeCroy, type WaveRunner 6100A).

The system is started with a TEXTOR trigger pulse at $t = 0\,\mathrm{s}$ of a discharge which initialises a series of 300 pulses with frequency 50 Hz coming from a pulse generator. These define the measurement points (Figure 4.2). The first trigger pulse also starts the constant speed wavelength scan of the dye laser taking 6 seconds. Each generator pulse first triggers a 2 μs gate for the photomultiplier tubes. After 0.5 μs the excimer laser is triggered. Because of its internal delay with a jitter of $\pm 0.4\,\mu$s the storage oscilloscope is triggered by a photo diode signal detecting the excimer laser pulse in order to synchronise it with the acquisition. The data acquisition, beginning $\sim 100\,\mathrm{ns}$ before the laser pulses are seen by the photomultipliers, allows the measurement of helium background radiation from the beam and the plasma.
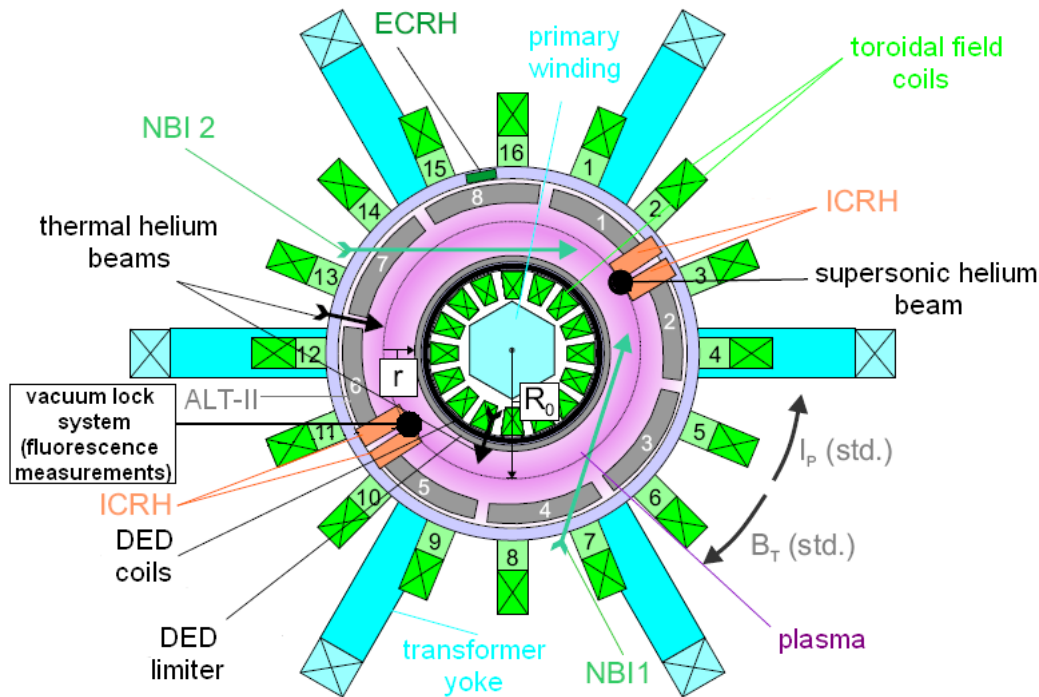
Figure 4.3: Top view on TEXTOR in the mid plane.

4.1 The TEXTOR tokamak

The TEXTOR tokamak (**T**orus **Ex**periment for **T**echnology **O**riented **R**esearch) [Solt-wisch et al., 1984, Neubauer et al., 2005] has been taken into operation in 1981. In 1994 the magnetic flux of the transformer has been enhanced (TEXTOR-94) which allowed longer discharges of up to 12 seconds. The upgrade was most of all important for the investigation of wall materials in reactor-like conditions, which is the main objective of the machine. Special care was taken in the design phase of the machine to allow the possibility of good conditions and flexibility to facilitate the edge plasma investigation, such as various ports for diagnosing and controlling the edge plasma or the possibility of heating the liner (first wall).

The toroidal magnetic field in TEXTOR is created by a set of 16 symmetrically arranged coils, which provide a field strength on the magnetic axis of $B_\phi = 1.8 - 2.8 \, \text{T}$ (see Figure 4.3). The plasma current of $I_\text{p} = 200 - 800 \, \text{kA}$ is driven inductively by a transformer, which comprises the primary winding in the torus centre and the yokes. The liner, made of Inconel 625, is placed at the minor radius of $r = 55 \, \text{cm}$ and is heated routinely up to 300°C. This helps to release water particles from the surface as well as facilitates the density control of the plasma due to the smaller hydrogen/deuterium content in the liner material.

TEXTOR is a medium sized tokamak with a circular poloidal cross section. The major plasma radius, i.e. the distance between the centre of the solenoid and the centre of the liner, is $R_0 = 1.75$ m. The minor plasma radius of typically $a = 46$ cm is defined by the position of the plasma limiting components (limiters). The toroidal pump limiter ALT-II (Advanced Limiter Test) [Finken et al., 2005a] is placed on the low-field side, in a distance $\vartheta = 45°$ below the equatorial plane. It consists of 8 toroidally arranged blades, with graphite tiles on the plasma-facing side, mounted to the liner to form a full toroidal belt (poloidal extent is 28 cm). Its radial position can be varied between 46 and 48 cm. Plasma particles neutralised on graphite plates in the Srape Off Layer (SOL) are pumped through channels on the back side with turbomolecular pumps. Two poloidal graphite limiters, mounted to the yoke, are placed on the top and the bottom at the same toroidal position and can be radially adjusted in the range of 40 to 49 cm. Finally, on the high-field side a graphite bumper limiter is mounted to the liner at $r = 49.3$ cm serving currently as a protection for the DED (Dynamic Ergodic Divertor) coils [Finken et al., 2005b].

The plasma is primarily heated by Ohmic resistance due to the electrical current in the plasma driven by the transformer. With a typical loop voltage of 1 V and a plasma current of $I_\mathrm{p} = 350$ kA the Ohmic heating power amounts to about 350 kW. Additional heating facilities at TEXTOR are: two neutral beam injection (NBI) systems injecting fast hydrogen or deuterium neutrals (acceleration potential of up to 55 kV) tangentially into the plasma (in opposite direction to each other) with a heating power of 4 MW in total, two pairs of ion cyclotron resonance heating (ICRH) antennas at a frequency around 30 MHz with a total power of 4 MW as well as electron cyclotron resonance heating (ECRH) gyrotrons at the frequencies 110 GHz (300 kW) and 140 GHz (800 kW). A more detailed description of TEXTOR features is provided by Neubauer et al. [2005].

Experiments presented in this thesis were mainly performed in deuterium Ohmic heated discharges with a plasma current of $I_\mathrm{p} = 350$ kA and a nominal magnetic field of $B_\phi = 2.25$ T. So-called plasma plateaus, i.e. time windows of constant plasma parameters, of around 5 seconds were possible. During this time, the laser wavelength is scanned over the expected spectral range of the excited transition (e.g. $\Delta\lambda \approx 70$ pm for the triplet transition at $\lambda = 587.6$ nm, see Figure 5.9), which is subject to Zeeman splitting owing to the presence of the local magnetic field. The last closed flux surface, defined by the radial position of the toroidal pump limiter, was at $r = 47$ cm. The central line-averaged electron densities lay in the range $\bar{n}_\mathrm{e} = 2 - 4 \times 10^{19}$ m^{-3} and the electron density and temperature in the edge region in which fluorescence light has been measured were $n_\mathrm{e} = 1.5 - 6 \times 10^{18}$ m^{-3} and $T_\mathrm{e} = 30 - 70$ eV.

4.2 Laser system

To obtain measurable signals, laser-induced fluorescence in the visible spectral range often depends on high spectral power densities. Let us make an estimation of the saturating laser power for a laser with a spectral width of $\Delta\lambda = 10$ pm (covering a set of π
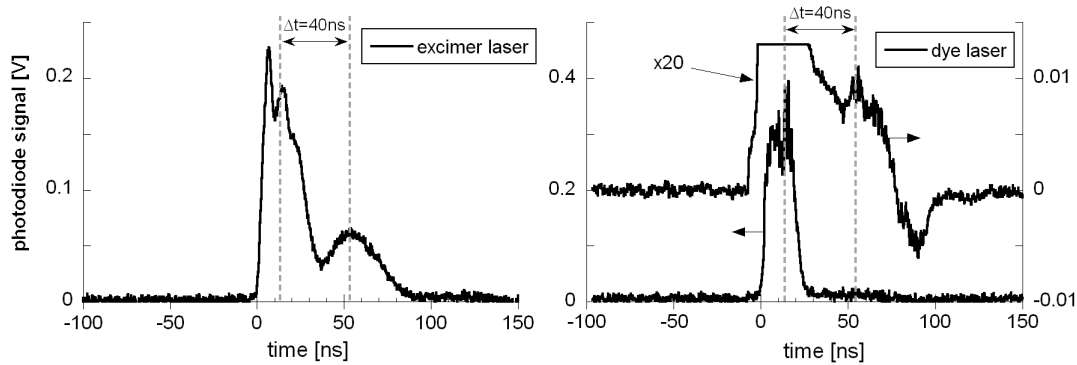
Figure 4.4: Time traces of the excimer and the dye laser ($\lambda = 388.9\,\text{nm}$) pulses measured with a fast vacuum photodiode.

components of the $2^3\text{P}^\circ \rightarrow 3^3\text{D}$ transition of thermal helium in a fusion plasma (see Figure 5.10). According to Eq. (2.9), in order to obtain a unity saturation parameter over an irradiated area of 10 cm^2, one needs for $g_l = g_u = 1$ and $\lambda = 400\,\text{nm}$ a power of 730 W. To reach stronger saturation levels in which fluorescence response does not depend on the laser power anymore, which is favourable for absolute population measurements, correspondingly higher laser powers are needed. These, in addition to spectral tunability, are achievable only in pulsed lasers, this is not necessarily a drawback because enhanced upper level populations due to the laser pumping are in many cases quickly deteriorated by collisional or radiative processes. Then, a laser pulse ending at the point in time of the maximum population facilitates the detection of fluorescence light owing to the absence of the laser stray light. Also the investigation of the fluorescence decay after the laser pulse brings additional insights in the collisional processes [Burrell and Kunze, 1978]. For this reason, the laser system that has been used in our measurements provides several advantageous features to be presented in this section. For absolute population measurement it is crucial to characterise the laser radiation from several points of view: the spatial energy distribution, the temporal laser profile evolution as well as pulse energy stability and finally, the spectral energy distribution plays a very important role for the data evaluation. These characteristics are described in this section.

The laser radiation source that we used for our experiments consists of two stages: a pump and a dye laser producing a narrow-band laser light at the desired wavelength. A pulsed excimer laser (Lambda Physik, type: LPX 315i) serves as the pump laser. It is a gas laser based on the principle of dimers stable only in an excited level and dissociating on a short time scale after radiative decay to the ground state. This establishes the population inversion, as needed for the onset of the lasing process. Laser pulses at $\lambda = 308\,\text{nm}$ are produced in pulsed gas discharges with xenon chloride molecules and neon as buffer gas. Depending on the high voltage of the discharge of 15-20 kV, the excimer laser provided energies of 500-600 mJ within a typical pulse length of 25 ns resulting in peak powers of $\sim 30\,\text{MW}$. Maximum repetition frequencies of 150 Hz are achievable with the laser. However, for TEXTOR measurements 50 Hz were chosen

because of the large data amount to be saved and analysed in the short time between the discharges. A time trace of an excimer laser pulse measured with a high speed vacuum diode is shown in Figure 4.4. A second peak, visible around 40 ns after the main one, is caused by the buffer gas and is actually not converted by the dye laser. The laser has a rectangular spatial cross section of $3 \times 1\,\mathrm{cm}^2$ and a divergence of $1° \times 3°$. To counteract this, a correction lens with a focal length of $f = 2\,\mathrm{m}$ was used at the entrance aperture of the dye laser.

The dye laser converts the broadband laser light of the excimer laser into narrowband laser pulses with a length of nearly 20 ns. The optical setup of this laser is shown in Figure 4.5 (the laser comprises of one more amplifier stage, as shown in the figure, which was not used in our experiments). The energy of the pump laser is divided by beam splitters into three parts, each of them being focused in vertical direction by cylindrical lenses into quartz cuvettes for the excitation of the dye particles. The oscillator consists of the first cuvette, a beam expander, a set of two gratings and the output coupler. The oscillator beam after passing three Brewster plates is shifted in height by around 1 cm and directed back into the same cuvette.
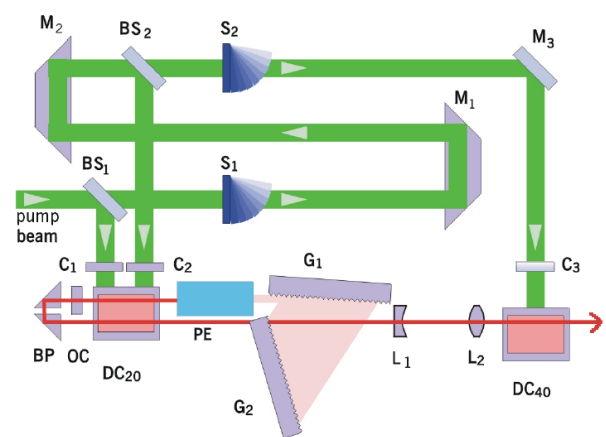

Figure 4.5: Optical setup of the dye laser: M-mirrors, BS-beam splitters, S-shutters, C-cylindrical lenses, DC-dye cuvettes, PE-prism beam expander, G-gratings, OC-output coupler, BP-Brewster plates with 180° turning prism.

At a different vertical position it is preamplified by the second fraction of the pump laser. This is a special feature of this laser allowing higher output energies but connected with a considerably difficult oscillator/preamplifier adjustment procedure. The laser beam escaping the first cuvette is expanded by a telescope and amplified in the following dye cuvette by the third fraction of the pump laser energy.

The optical configuration of the dye laser was initially designed for measurements at the hydrogen L_α line in the vacuum UV spectral range at $\lambda = 121.6\,\mathrm{nm}$ [Brezinsek, 2002, Brezinsek et al., 2002]. Laser radiation at this wavelength is achieved by frequency tripling in a Kr/Ar-gas mixture of a laser radiation at $\lambda = 364.7\,\mathrm{nm}$, which is produced by the dye laser (near UV). This non-linear frequency conversion process requires preferably very small spectral widths of the laser, which is provided by the use of the double grating arrangement of 90 mm gratings with 3000 lines/mm. However, this restricts spectrally the lasing range of the oscillator to $\lambda < 582\,\mathrm{nm}$. It was possible to shift up the upper wavelength limit by $\Delta\lambda \approx 15\,\mathrm{nm}$ by the use of the wavelength tuning grating G_2 in the zero-order as a mirror. This slightly deteriorated the spectral bandwidth of the oscillator but allowed to reach a very important triplet helium line at $\lambda = 587.6\,\mathrm{nm}$. For a further increase of the maximum wavelength another grating would have to be used.

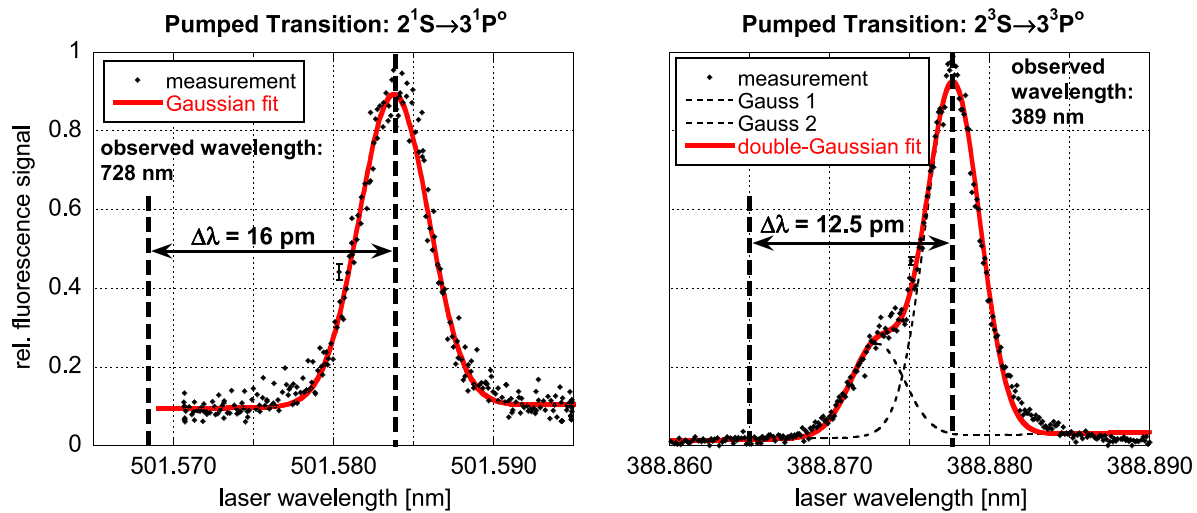The wavelength tuning of the oscillator is performed by turning the grating G_1. It

Figure 4.6: Fluorescence signals of two HeI transitions as measured for wavelength calibration purposes on a glow discharge set-up in the laboratory. Left: excitation of the singlet transition $2^1S \rightarrow 3^1P^o$ at $\lambda = 501.6\,nm$ (fluorescence signal observed at $\lambda = 728.1\,nm$, $3^1S \rightarrow 2^1P^o$). Right: excitation of the triplet transition $2^3S \rightarrow 3^3P^o$ at $\lambda = 388.9\,nm$ (fluorescence signal observed at the same wavelength). $\Delta\lambda$ indicates a typical 'day-to-day' wavelength shift of the laser for experimental reasons.

is mechanically coupled to a stepper motor providing a smallest wavelength increment of $\Delta\lambda \approx 0.1\,pm$. Automatic wavelength scans are possible in two modes. In the trigger mode, the laser waits for a trigger pulse to increment the wavelength whereas in the constant speed mode, which was used, one trigger pulse starts a scan over a pre-defined wavelength range and time interval. An analogue signal output from the laser – proportional to the wavelength – is used to monitor the wavelength scan.

The dye laser used may be affected by a certain wavelength shift which is not necessarily constant. To avoid a mismatch between the scanned wavelength range and the wavelength of the transition to be excited during relatively short TEXTOR plasma pulses of few seconds, a wavelength calibration of the laser system is carried out before each experimental unit (half a day).

For this purpose a similar laser-induced fluorescence set-up on a glow discharge chamber has been prepared in the laboratory. The laser is spectrally fine-tuned to provide a fluorescence signal at any helium transition of interest in the glow discharge chamber. Sample measurements are shown in Figure 4.6. In the case of the singlet transition $2^1S \rightarrow 3^1P^o$ a single Gaussian profile fits the data, whereas when dealing with the triplet transitions, one has to consider their fine structure. The excited transition $2^3S \rightarrow 3^3P^o$ consists of three components, two of them lying close together (these cannot be resolved) and in a distance of $\Delta\lambda = 4.4\,pm$ from the third component, which is enough to enable resolution with our laser. Two overlaid Gaussians fit the data very well, reflecting within

10% the separation of the components and their intensity ratio of $S_2/S_1 \approx 2.9$, which results from the statistical weights of the single sublevels of this multiplet and the fact of using strong, i.e. saturating laser radiation ($S_2/S_1 \approx (8/11)/(1/4)$). Finally, these measurements provide the wavelength offset of the dye laser, lying in the range of 10-30 pm and not being constant in the time, as well as the laser spectral width.

Dye	Wavelength range [nm]	Peak wave-length [nm]	Helium lines	Efficiency [%]	Solvent	Concentration [g/l]
QUI	368-402	390	389.6 396.5	11	dioxane	0.2
Coumarin 47	440-484	456	471.3	18	methanol	1.6
Coumarin 307	479-553	500	492.2 501.6 504.8	16	methanol	3.4
Rhodamine 6G	569-608	581	587.6	16	methanol	1.2

Table 4.1: Laser dyes with their concentrations and the solvents used in TEXTOR experiments (from [Brackmann, 1997]).

The pulses of the dye laser are ~ 18 ns long (see Figure 4.4). The energy of the excimer laser in the second peak is mostly not converted by the dye laser (one exception is shown in Figure 6.8). Only a small peak in the dye laser energy is visible at the same time delay of 40 ns to the main peak when zooming in the energy scaling.

Atomic helium lines of interest lie in the whole visible spectral range. Unfortunately, laser dyes provide the lasing process typically in a spectral range of $\Delta\lambda = 50$ nm and for this reason several dyes had to be used in our experiment. Table 4.1 lists them with their wavelength ranges, peak ef-ficiencies, concentrations and solvents as well as

Figure 4.7: Energy of 300 laser pulses fired with 50 Hz repetition rate during a discharge.

helium lines that can be pumped. The use of different dyes considerably hampers the experiments because of the need for a dye laser readjustment at each change of the dye.

The maximum pulse energy depends on the dye used and can reach up to 100 mJ. However, to reach saturation levels of $S = 100 - 1000$ for our measurements, in most cases pulse energies of $E_L = 0.1 - 1$ mJ were used. The ASE (Amplified Spontaneous Emission) fraction amounts to $< 0.5\%$ [Sirah Laser- und Plasmatechnik GmbH, 1999]. The energy stability from pulse to pulse, relying on the pump laser energy as well as on the dye laser conversion, lies at most at $\pm 5\%$ (see Figure 4.7). The laser has, at least at lower energy levels, approximately a circular spatial cross section with a diameter $d \approx 3$ mm. It expands to 15 mm on the approximately 15 metre long way to the observation point. A 5 mm iris is used to select only the central part of the laser beam. A focusing lens with
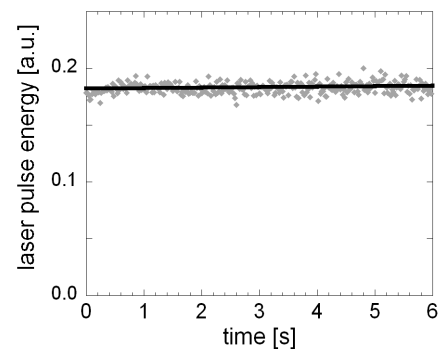
the focal length $f = 60\,\text{cm}$ images the iris at the observation volume to produce a sharp circular shape of the laser beam with diameter of 20 mm. The reason of using only the central part of the beam is to provide a low energy deviation on the laser cross section. Indeed, measurements of the spatial profile energy distribution with a small pyrometric energy detector (diameter 3.8 mm) have shown an energy drop by a factor of 2 between the centre and the edge of the beam image. Neglecting this energy gradient should not result in a considerable error due to the saturation regime of our measurements and due to the fact that fluorescence photons guided by our detectors come mainly from the volume close to the laser beam axis, which coincide with the helium beam axis, where the helium density is higher than at the edge of the laser beam (see Figure 5.8).

The dye laser light is linearly polarised. A $\lambda/2$ delay plate is used to turn the polarisation direction by $70° - 90°$ to align it approximately with the direction of the magnetic field in the torus to concentrate the most laser energy on the pumping of the π components of the Zeeman split transitions. The polarisation alignment was checked by pulse energy measurement with a polariser (analyser) in front of a pyrometric detector. No effort was made to exactly adjust the polarisation direction in the torus because the laser entrance port and therewith the laser beam is not exactly vertical but hits the nozzle at an angle of $\beta = 7°$ (see Figure 4.8). Since the magnetic field is not purely toroidal but has also a poloidal component (γ is assigned to the angle between the toroidal direction and the magnetic field; $\gamma \sim 5°$), the laser will, independently on its polarisation direction, always have a non-vanishing polarisation component perpendicular to the field lines pumping σ components of the Zeeman split lines. On the opposite, there is a laser polarisation direction at which its component parallel to $\boldsymbol{B}$ vanishes. Both components can be easily calculated by performing an axes transformation twice (two rotations around the observation point are needed). The $(E_{x'}, E_{y'}, E_{z'})$ components of the polarisation vector $\boldsymbol{E}$ ($x' \| \boldsymbol{B}$, y' shows in vertical direction, z' is perpendicular to x' and y') are calculated with the transformation matrix $\boldsymbol{P}$:

$$
\begin{pmatrix} E_{x'} \\ E_{y'} \\ E_{z'} \end{pmatrix} = \begin{pmatrix} \cos\gamma & 0 & \sin\gamma \\ 0 & 1 & 0 \\ -\sin\gamma & 0 & \cos\gamma \end{pmatrix} \begin{pmatrix} 1 & 0 & 0 \\ 0 & \cos\beta & \sin\beta \\ 0 & -\sin\beta & \cos\beta \end{pmatrix} \begin{pmatrix} E_x \\ E_y \\ E_z \end{pmatrix} =
$$
$$
= \begin{pmatrix} \cos\gamma & -\sin\gamma\sin\beta & \sin\gamma\cos\beta \\ 0 & \cos\beta & \sin\beta \\ -\sin\gamma & -\cos\gamma\sin\beta & \cos\gamma\cos\beta \end{pmatrix} \begin{pmatrix} E_x \\ E_y \\ E_z \end{pmatrix} \equiv \boldsymbol{P} \begin{pmatrix} E_x \\ E_y \\ E_z \end{pmatrix} \quad . \quad (4.1)
$$

For $E_y = 0$ (transverse wave propagation), $E_x = \boldsymbol{E}\cos\alpha$ and $E_z = \boldsymbol{E}\sin\alpha$ (α is the polarisation angle vector, $\alpha = 0°$ if $\boldsymbol{E}$ parallel to the toroidal direction) we obtain for the laser intensity parallel and perpendicular to the magnetic field line:

$$
I_{\|} = (\cos\alpha\cos\gamma + \sin\alpha\cos\beta\sin\gamma)^2
$$
$$
I_{\perp} = \sin^2\alpha\sin^2\beta + (-\cos\alpha\sin\gamma + \sin\alpha\cos\beta\cos\gamma)^2 \quad . \quad (4.2)
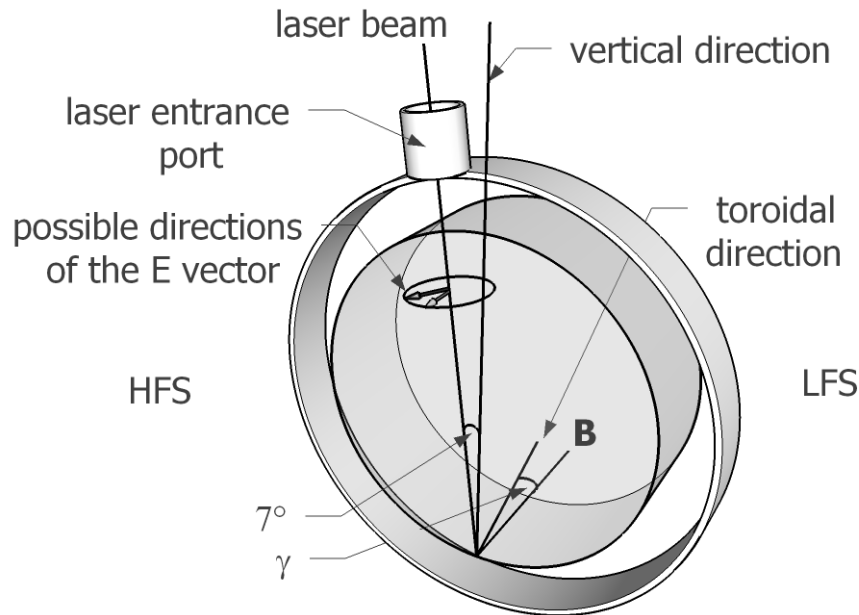$$

Figure 4.8: Poloidal cross section of the plasma at the observation point. HFS and LFS respectively designate the high (magnetic) field side and the low field side of the tokamak.

A general solution for $I_\parallel = 0$ of the first equation, $\alpha = \text{tg}^{-1}(-\frac{1}{\text{tg}\gamma\cos\beta})$, exists for all values of β and γ ($\alpha = \pm90°$ for $\beta = \pm90°$). This means that for an arbitrary pair of (β, γ) there is an angle α of the laser polarisation vector for which no excitation of π lines occurs. In contrast, no solution for $I_\perp = 0$ of the second equation exists if both angles, β and γ, are different from $0°$ and $180°$, as in our geometry, ensuring the excitation of σ lines in any case. The minimum value of $I_\parallel/(I_\parallel + I_\perp)$ for $\beta = 7°$ and $\gamma = 5°$ is very small ($\approx 1.13 \times 10^{-4}$ and lies at $\alpha \approx 4.96°$). However, for high laser powers it can result in considerable fluorescence signals. A calculation of relative fluorescence signal intensity of a π and a σ line as a function of α for the saturation parameter $S = 4000$ is shown in Figure 4.9 (a). A simple model $I^{\text{F}} \propto \frac{S}{S+1}$ was assumed (Eq. (2.11)). While the π intensity drops to zero at the minimum, the minimum signal of the σ line amounts to $\sim 1/3$ of the maximum due to the non-linear dependence of the signal intensity on S. In Figure (b) a more realistic logarithmic saturation response for high S values was assumed [Salmon and Laurendeau, 1985]; in this case the signal changes around the minima are not so drastic. Figures (c) and (d) show two TEXTOR measurements. In (c), the laser was tuned to the wavelength $\lambda_{\text{L}} = 587.570\,\text{nm}$ (the set of π components, see Figure 5.10). During the discharge time $t = 3 - 5.5$ seconds the polarisation angle was scanned in the range $\alpha = 85° - 155°$ by turning of the retardation plate. A clear fluorescence signal drop to zero was observed at the corresponding discharge time point. In contrast, a nearly constant signal sustains over another discharge in which the laser wavelength was tuned to the set of σ^+ lines at $\lambda_{\text{L}} = 587.530\,\text{nm}$ and the polarisation angle scan was the same (Figure (d)). Unfortunately, the polarisation angle scan does not cover the minimum of the σ^+ line. However, these considerations and especially
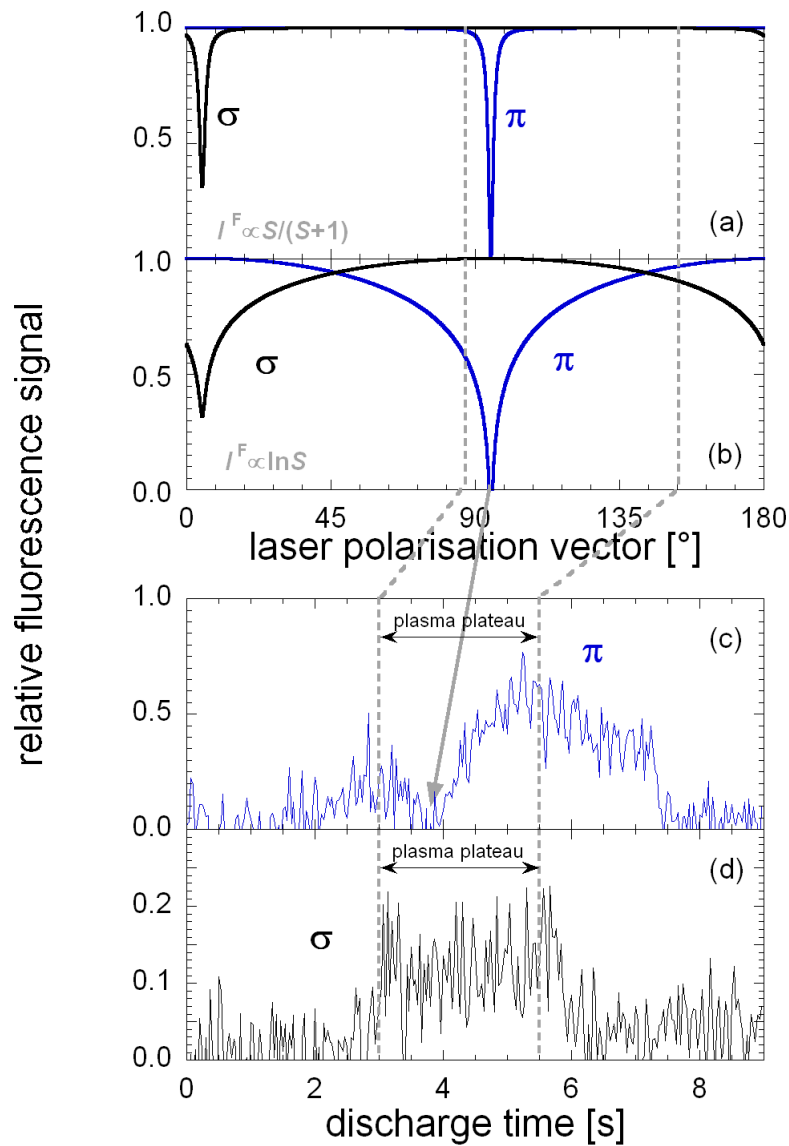
Figure 4.9: Fluorescence signals of a π and σ^+ transition as a function of the laser polarisation direction for non-symmetric geometric conditions (see Figure 4.8); (a,b) - calculation, (c,d) - TEXTOR measurement around $\lambda = 587\,\mathrm{nm}$. See the text for a detailed explanation.
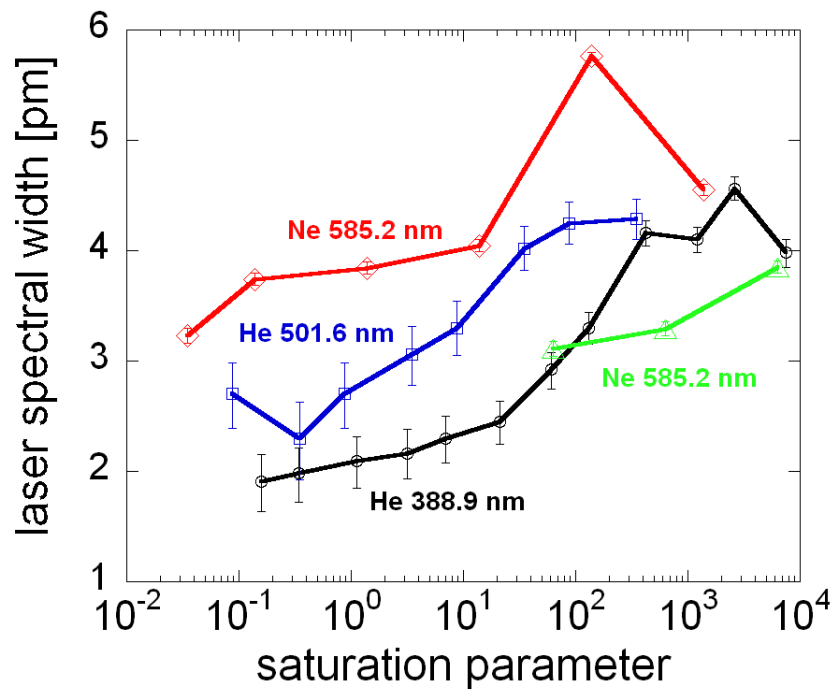
Figure 4.10: Saturation parameter dependence of the laser spectral width measured on different days in a helium and neon glow discharge.

the measurement in Figure (c) show that it is not crucial to exactly adjust the laser polarisation parallel to the magnetic field lines if attempting to pump π components.

The spectral width of the used dye laser specified by the vendor lies slightly below 1 pm for the whole spectral range. However, the measured widths were always larger than the specification. Figure 4.10 shows the observed laser spectral widths as a function of the saturation parameter S measured at two helium and one neon line on different days in the helium and neon glow discharge. The non-saturated laser widths are obtained from the observed ones at low values of S. They lie in the range 2-3.5 pm. Two different neon measurements do not coincide. Moreover, a measurement with an etalon at $\lambda_{\mathrm{L}} = 388.9\,\mathrm{nm}$ on a different day (after laser readjustment due to measurements with a different dye) provided a width of 2.6 pm. Thus, the conclusion is drawn that the spectral width is rather sensitive to the exact adjustment of the oscillator/preamplifier line.

4.3 Helium inlet

4.3.1 General considerations

For the purpose of plasma diagnostics it is preferable to use a well collimated atomic beam. It is clear that if one compares two beams of different divergence but with the same total particle flux (Figure 4.11), a low-divergence beam will provide a higher spatial resolution along the line of sight. This is important if the plasma parameters to be measured are not constant along the observation line on the length scale of the beam radius. A spatial resolution below the correlation length of the fluctuating structures is required in fluctuation measurements. Moreover, in the case of a low-divergence beam significantly more probe particles are present in the observation volume for a given particle flux enhancing the signal-to-noise ratio.
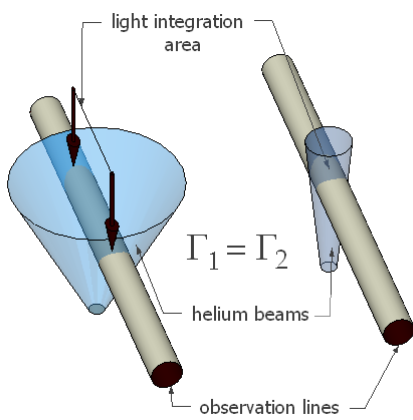

Figure 4.11: Observation line across helium beams of different divergence.

This is one of the reasons why supersonic helium beams have been developed for plasma diagnostics and their use is increasing [Brix, 1998, Hidalgo et al., 2004, Andruczyk et al., 2006, Kruezi, 2007]. Owing to the supersonic gas expansion in connection with a nozzle-skimmer arrangement they provide very good beam parameters such as a divergence of around $\pm 1°$ and the centre line helium density of up to 10^{19} m^{-3}. These beams are also fairly monoenergetic. In order to keep the good beam properties, gas pressure in the nozzle-skimmer chamber must not be too high. Otherwise the interaction between the supersonic beam and the background gas deteriorates the beam quality. Therefore supersonic beams require separate pumping stations and are often pulsed. Three kinds of valves are commonly used: current loop, solenoid and piezo-electric [Gentry, 1988]. The last example is of particular interest for fusion devices since the piezo crystal is not sensitive to the high magnetic fields present. They can operate with frequencies of several hundred Hertz, opening and closing times in submillisecond range and at pressures of several ten bar.

If there is no need for low divergence of the beam, simple tubes can be used as gas injection elements into the vacuum. The properties of such beams can be understood in terms of the theory of gas effusion. Effusive escape of gas particles is given if the Knudsen number $K = \bar{l}/d$, $\bar{l}$ being the mean free path and d the representative physical length scale, is larger than one [Wutz et al., 2000] (see Table 4.2). This is the case of the molecular flow in which collisions of gas particles with the wall are dominant over collisions between the particles. Let us consider effusive particle flow from a reservoir with a density n into another reservoir with negligibly small density through a hole of diameter d in a thin wall separating both reservoirs. The angular dependence of the outcoming flow into a unit solid angle is given by

viscous flow	$K < 10^{-2}$
Knudsen flow	$10^{-2} < K < 0.5$
molecular flow	$K > 0.5$

Table 4.2: Flow types dependent on the Knudsen number K.

$$\frac{\mathrm{d}\dot{N}}{\mathrm{d}\Omega} = \frac{1}{4\pi} n\bar{v} A \cos\vartheta, \tag{4.3}$$

where $\bar{v}$ is the mean particle velocity, A the hole cross section and ϑ the angle to the normal. The integration over the solid angle $\mathrm{d}\Omega = 2\pi\sin\vartheta\mathrm{d}\vartheta$ yields the total flow

$$\dot{N} = \frac{1}{4} n\bar{v} A. \tag{4.4}$$

The large, $\cos\vartheta$-dependent divergence of the effusive particle beams can be seen from Eq. (4.3). It can be made smaller if using a tube instead of a hole because only particles entering the tube under small angle pass the tube undisturbed. Particles with larger perpendicular velocity component will hit the tube wall and be redistributed uniformly into the half solid angle 2π (following the cosine law). This results in a decrease of the total flow through the tube being quantified in terms of a probability of passing through the tube by the particle. This probability, firstly calculated by Knudsen, is given by

$$P = \frac{8}{3}\frac{r}{l} \tag{4.5}$$

for a tube of the length l and with a circular cross section with the radius r. Later computer simulations confirmed this relation, however only for long tubes ($\frac{l}{r} > 50$), as in our case (see Sec. 4.3.2). Then, we obtain for the total flux through a long circular tube the expression

$$\dot{N}_{\mathrm{tube}} = \frac{2}{3}\frac{r}{l} n\bar{v} A. \tag{4.6}$$

The mean particle velocity is similar to the one corresponding to the Maxwellian velocity distribution (see Sec. 4.3.2). In contrast to the supersonic expansion, no monoenergetic beam can by achieved when using nozzles based on the effusive expansion, which are thus referred to as thermal beams.

According to Eq. (4.6) we expect for a circular tube with $r = 0.1\,\mathrm{mm}$ and $l = 16\,\mathrm{mm}$, a pressure of $p = 1\,\mathrm{mbar}$ and at the room temperature a helium flow of $\Gamma_{\mathrm{He}} \approx 5 \times 10^{15}\,\mathrm{s}^{-1}$. In order to increase the flow, one can use several capillary tubes in a parallel arrangement as a nozzle. Typical gas pressures allowing reasonable helium flows through such multi-tube nozzles used on TEXTOR lie in the range of $p > 1\,\mathrm{mbar}$. As one can see from Table 4.3, the mean free path of helium atoms at these pressures are $\bar{l} < 0.1\,\mathrm{mm}$ and thus smaller than the tube inner diameter of $d_{\mathrm{tube}} = 0.2\,\mathrm{mm}$. The flow cannot be considered as purely effusive anymore requiring some corrections of the above formulas.

Divergence measurements of such a beam have been made by use of a pumped tube with a small orifice traced perpendicularly to the beam at a certain distance [Brix, 1998]. The beam intensity profiles fitted well with the function $\cos^{10}\vartheta$ and a divergence of $\pm 21°$ was obtained.

p_{He} [mbar]	$\bar{l}$
10^{-3}	0.1 m
1	0.1 mm
1000	0.1 μm

Table 4.3: Mean free path $\bar{l}$ for helium at $T = 300$ K.

4.3.2 Realisation and properties

For LIF experiments on TEXTOR high beam collimation of supersonic beam technique was not of high priority and thus did not justify construction of such a source. The use of a supersonic helium beam system, which has been recently constructed and installed on TEXTOR [Kruezi, 2007], was not possible because of the lack of appropriate entrance port for the laser beam on the side opposite to the gas injection system. Therefore, we used a different gas injection system based on a simple multi-tube nozzle. It consists of around 300 capillary tubes made of stainless still with an inner diameter of 0.2 mm, an outer diameter of 0.4 mm and the length of 20 mm. The nozzle of total width of 1 cm is con-

Figure 4.12: Poloidal cross section of the plasma with indication of our thermal helium beam and one observation line (all in same scale).

nected by a pipe of 6 mm inner diameter and 6 m length to a gas reservoir, which is filled with helium to the desired pressure prior to a plasma discharge. This gas reservoir is in turn connected by another line to the helium high-pressure cylinder. After depletion of the pressure below the preset value, automatic refilling of the gas reservoir to the preset pressure is possible. Alternatively, manual operation of the gas valve from the TEXTOR control room can be chosen. Another valve is placed between the gas reservoir and the nozzle and is opened during a discharge within a desired time window. The pressure in the reservoir is recorded by CAMAC data loggers for each discharge. This data is used for a quick check whether the gas inlet system works properly. The total amount of helium puffed in during a discharge is also obtained from the pressure drop (see Sec. 5.1). Due to the length of the pipe between the gas reservoir and the nozzle we have a delay of around half a second between the valve opening and the gas flow onset.
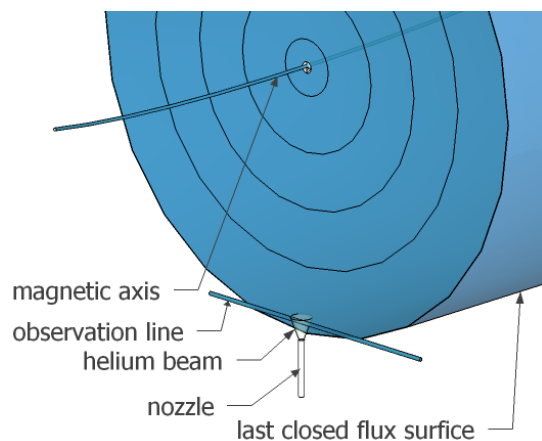
Helium gas was puffed radially into the plasma from the bottom side at the major plasma radius $R_0 = 1.75\,\mathrm{m}$ coinciding with the magnetic axis. The nozzle was placed typically at a distance of around 1 cm below the last closed flux surface. The useful penetration depth of the beam, i.e. the radial distance from the nozzle at which signals were strong enough to be measured, is around 4 cm (see Figure 5.5). Assuming a beam divergence of around $\pm 20°$ and taking into account the nozzle width we obtain the maximum beam diameter of around 4 cm. At the minor plasma radius r (on the beam axis) of our measurements of $r \approx 45\,\mathrm{cm}$ the corresponding maximum increase of r on the signal integration line (± 2cm from the beam axis) is $\Delta r = 0.5\,\mathrm{mm}$ (Figure 4.12). Moreover, in most experiments a laser beam diameter of 2 cm was chosen, additionally limiting the observation volume. Bearing in mind that the signal integration along the observation line is weighted with the helium density, which is highest at the beam axis, one can see that variation of plasma parameters along the signal integration line can be neglected if assumed that they are constant at a given plasma radius.

At a typical pressure in the gas reservoir of $p_0 = 8\,\mathrm{mbar}$ the pressure drop caused by the gas puff during a discharge amounts to $\Delta p \approx 0.5\,\mathrm{mbar}$. With the volume of the reservoir of $V = 2\,\mathrm{dm}^3$ and room temperature, we obtain by using the ideal gas law

$$\Delta N = \frac{\Delta p V}{k_{\mathrm{B}} T} \tag{4.7}$$

a total amount of helium puffed into the plasma of $\Delta N \approx 2.5 \times 10^{19}$. With a puff time of 5 second the average helium flow is $\Gamma_{\mathrm{He}} \approx 5 \times 10^{18}\,\mathrm{s}^{-1}$. Helium atoms which are introduced into the edge plasma certainly have an influence on the local and global plasma parameters. The local influence can be estimated by comparing the energy sink due to the existence of neutral helium at the considered point with the heat flow parallel to the magnetic field. The energy losses are given by the line emission of helium and its ionisation (ionised helium escapes from the beam along magnetic field lines before recombining). From the global point of view, the number of electrons introduced to the plasma with the helium atoms relative to the total electron content of the plasma is important. In both cases it can be shown that helium puffing with flows as they are typical for our thermal beam has no considerable influence on the local and the global plasma parameters. Also the neutral density of helium recycled in front of the toroidal limiter is much lower than the electron density and hence negligible [Schmitz, 2006, Lehnen, 2000].

By using the LIF method it is possible to measure local particle drift velocities (see Sec. 2.1). The most probable velocity component in the laser beam direction of helium atoms puffed through our nozzle into TEXTOR edge plasma has been measured by this method at the beam axis. From several measurements, two have been picked out with the best signal-to-noise ratio. In one measurement the laser was spectrally scanned over the triplet transition $2^3\mathrm{P}^\mathrm{o} \rightarrow 3^3\mathrm{D}$ at $\lambda = 587.6\,\mathrm{nm}$ and the fluorescence observed at the plasma radius $r = 47\,\mathrm{cm}$ (Figure 4.13 (b)). A reference fluorescence spectrum in the helium glow discharge in the laboratory was recorded shortly before (Figure (a)). This measurement is supposed to provide the unshifted maximum wavelength since no drifts of helium atoms
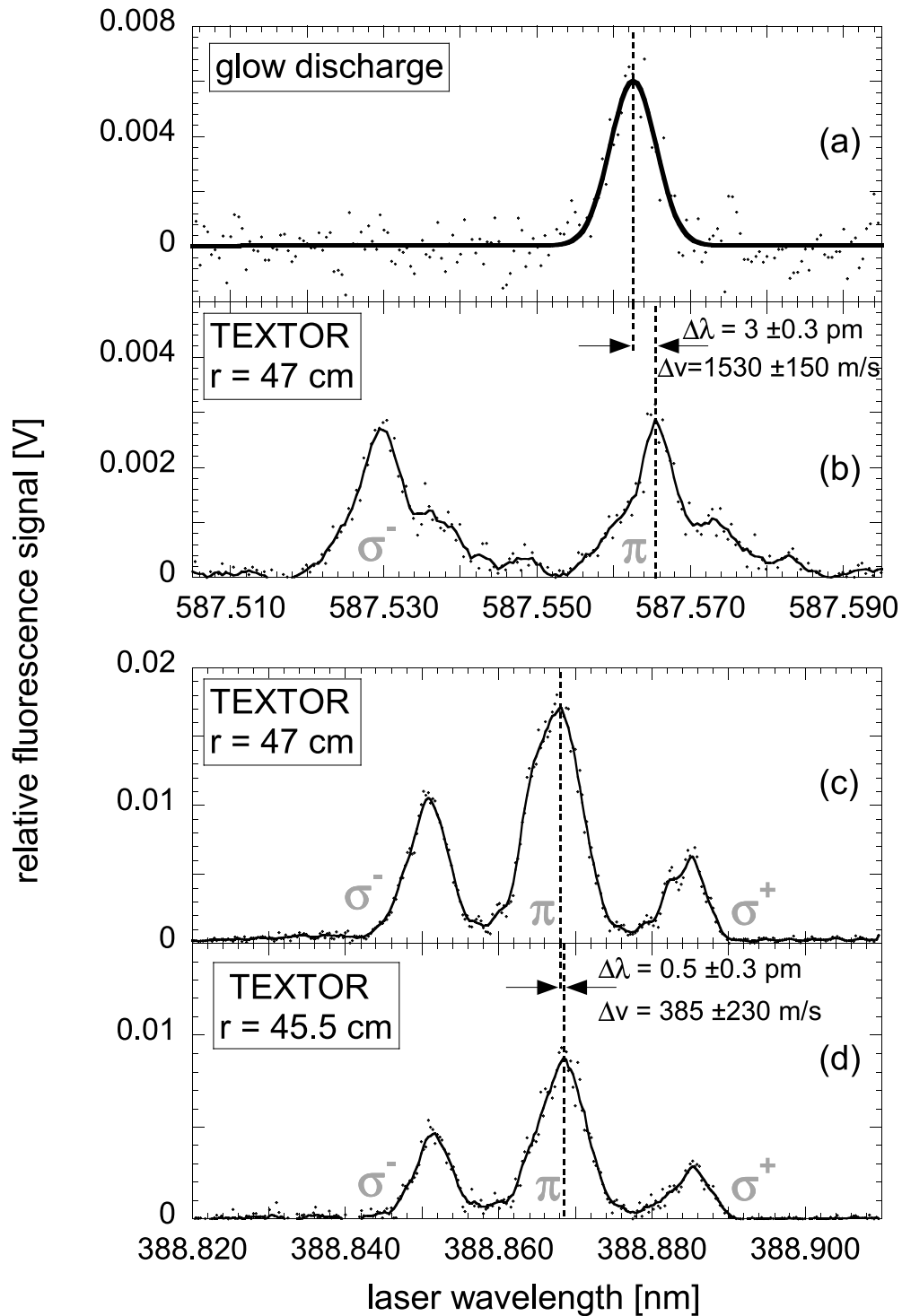
Figure 4.13: LIF-based measurements of the most probable velocity component along the laser beam direction of helium atoms in the helium beam at two radial positions in the TEXTOR plasma (b-d). A measurement in a helium glow provides the unshifted wavelength (a).

are expected. From the wavelength shift of the maximum signal $\Delta\lambda_{\max} = 3 \pm 0.3\,\text{pm}$ the initial beam velocity at the very plasma edge $v_{\text{beam}} = \frac{3\times10^{-12}\,\text{m}}{587.6\times10^{-9}\,\text{m}}\text{c} = 1530 \pm 150\,\text{m/s}$ is obtained. It is only slightly higher than the corresponding velocity of a thermal distribution $v_{\text{th}} = \sqrt{\frac{2k_B T_{\text{He}}}{m_{\text{He}}}} = 1370\,\text{m/s}$ (the liner temperature $T = 180°\text{C}$ is assumed). From another measurement a comparison of the velocity at two different radial positions $r = 47\,\text{cm}$ and $r = 45.5\,\text{cm}$ was possible. The laser was scanned here over another triplet transition $2^3\text{S}{\rightarrow}3^3\text{P}°$ at $\lambda = 388.9\,\text{nm}$ and the fluorescence recorded simultaneously at these both radial positions (Figure 4.13 (c) and (d)). The difference in the maximum fluorescence wavelength of both spectra $\Delta\lambda_{\max} = 0.5 \pm 0.3\,\text{pm}$ yields a velocity increase of $\Delta v_{\text{beam}} = 385 \pm 230\,\text{m/s}$. The increase of the beam velocity in course of the plasma penetration is explained with the fact that helium atoms with higher velocity penetrate deeper into the plasma than the slow atoms. This is because the ionisation of helium atoms, which is the reason for the beam attenuation depends mostly on the residence time of the atoms in the plasma.

4.4 Observation system

The observation system consists of a lens imaging the observation volumes via three mirrors (one of them in the vacuum) onto the liquid light guides (see Figure 4.1). Three radial positions under a solid angle of $\Delta\Omega \approx 1\,\text{mrad}$ are observed, the circular cross sections with the diameter $d = 8\,\text{mm}$ being defined by the 1:1 image and by the inner diameter of the light guides. Interference filters with a bandwidth of $\Delta\lambda = 1 - 2\,\text{nm}$ in front of the light guides remove the plasma radiation from the signal to be recorded. The light guides with the length of 5 metres lead the fluorescence photons to photomultiplier tubes being placed in a box made of soft iron. The wall thickness of 5 mm provides the necessary shielding of the magnetic field. Comparison of the laser stray light signal between and during discharges provided the proof of no influence of magnetic field on the detector sensitivity.

The spatial adjustment of the optical components is facilitated by the fact that the we use the vacuum lock system for the nozzle positioning. Prior to all experiment campaigns, before arranging the gas nozzle, we introduced a specially shaped light source in the place of the observation volume and performed the adjustment of the optical path by using its radiation.

In the following, the features and limitations of the observation system will be described in more detail, with main emphasis on its absolute sensitivity being of large importance for our measurements.

4.4.1 Absolute calibration of the LIF system

If a LIF measurement set-up is intended to provide number densities of level populations the absolute sensitivity of the system must be known, i.e. a calibration factor transforming, in accordance to Eq. (2.11), the measured signal I_F (usually the anode current of a photomultiplier tube) into a photon flux $\Phi_V^{4\pi}$ released into the full solid angle 4π per unit observation volume:

$$k = \Delta V \frac{\Delta \Omega}{4\pi} T(\lambda_F) QE(\lambda_F) \mu q_e \tag{4.8}$$

(ΔV: fluorescence volume, $T(\lambda_F)$: spectral transmission of the optical path, $QE(\lambda_F)$: quantum efficiency of the detector, μ: detector gain, q_e: electron charge). The photon flux is then given by $\Phi_V^{4\pi} = I_F / k$.

There are two approaches to obtain the value of k. The direct method relies on individual characterisation of each single component which influence the system sensitivity. However, this straightforward method is connected with some practical difficulties, e.g. if using light guides in the optical path. The quantum efficiency and the detector gain are typically provided by the manufacturer, nevertheless they should be measured for each single detector, which can be done by using an absolute calibrated light source.

A more intuitive way of calibration is to keep all optical and electrical components of the observation system as used during experiment and to provide a light source of known photon flux in the place of the fluorescence observation volume. This can be done by utilising the Rayleigh scattering of photons on uncharged particles. For this purpose the vacuum chamber is filled with a known pressure of a working gas, e.g. nitrogen. The laser illuminates the gas in the observation volume with the same energy and geometric properties as during experiment. Since the Rayleigh scattering is a non-resonant process it can be used at an arbitrary laser wavelength.

This calibration procedure has several advantages. Since both the calibration and the LIF measurements use the same optical path the observation solid angle does not have to be known. During calibration the scattered laser radiation is used as the calibrated light source and for this reason the observation volume is the same as during the LIF experiments and does not have to be known either. Further, during one calibration measurement the total transmission of the optical path and the detector characteristics are allowed for and the value of k as one quantity is derived.

The Rayleigh scattering is in particular useful for calibrating of LIF measurements in a 2-level-system because the elastically scattered laser photons appear at unchanged wavelength as in the case of the LIF scheme. The cross sections for the Rayleigh scattering are usually known with sufficient accuracy [Muraoka and Maeda, 1993]. They can by calculated from

$$\sigma_R = \frac{8\pi^3}{3n_R^2} \frac{(N^2 - 1)^2}{\lambda^4} \tag{4.9}$$

where N denotes the index of refraction and n_R is the gas density. The calibration signal from the Rayleigh scattering is given by

$$I_R = k n_R \sigma_R p_R P_L \frac{1}{E_{ph}}. \tag{4.10}$$

k is the factor describing the experimental conditions and is defined in Eq. (4.8) and is the same for LIF and calibration measurements, p_R is the polarisation factor depending on the laser polarisation and the observation angle, P_L is the laser power density (given

in W/m^2) and $E_{ph} = h\nu$ is the photon energy. Signals originating from fluorescence experiments can be described in an analogue way:

$$I_{\mathrm{F}} = k n_{\mathrm{F}} \sigma_{\mathrm{F}} p_{\mathrm{F}} P_{\mathrm{L}} \frac{1}{E_{ph}} \qquad (4.11)$$

with p_{F} being a factor accounting for the angular dependence of spontaneous emission in the presence of a magnetic field and the absorption cross section of

$$\sigma_{\mathrm{F}} = \mathrm{r_e} \pi \lambda_0^2 \mathrm{f_{lu}} \mathrm{L}(\lambda - \lambda_0) \qquad (4.12)$$

($\mathrm{r_e}$: the classical electron radius, λ_0: the centre of the absorption line profile, $\mathrm{f_{lu}}$: the oscillator strength, $\mathrm{L}(\lambda - \lambda_0)$: line shape with the normalisation $\int \mathrm{L}(\lambda - \lambda_0)\,\mathrm{d}\lambda = 1$). It is clear that for the derivation of the particle density

$$n_{\mathrm{F}} = n_{\mathrm{R}} \frac{\sigma_{\mathrm{R}} p_{\mathrm{R}}}{\sigma_{\mathrm{F}} p_{\mathrm{F}}} \frac{I_{\mathrm{F}}}{I_{\mathrm{R}}} \qquad (4.13)$$

the knowledge of k as well as of the laser power is not at all necessary. n_{F} is just derived from the gas density during the calibration as well as from the signal intensities, cross sections and polarisation factors of the LIF and calibration measurement. Only the laser power needs to be kept constant during both measurements.
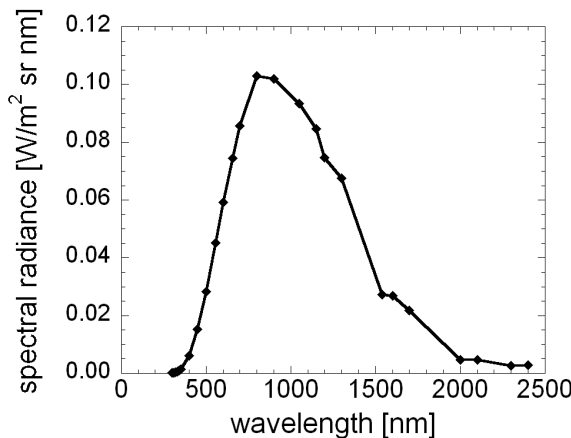

Figure 4.14: Spectral radiance of the Ulbricht sphere used for the absolute calibration of the observation system.

These considerations are valid only for laser powers, which are not too high to cause the onset of the nonlinear response of the fluorescence signal to the laser power. For saturating laser powers Eq. (4.11) does not hold anymore because the laser radiation (P_{L}) itself considerably contributes to the depletion of the upper level population and is a competitive process to the spontaneous radiative decay (the linear dependence of I_{F} on the lower level population n_{F} modifies to the dependence on the excess of the lower level over the upper level population). For such conditions the Rayleigh-scattered light can still serve as a calibrated light source at the laser wavelength. However, if observation of the fluorescence radiation is to be performed at several different wavelengths a calibration source with continuous spectrum is much more useful since the laser wavelength can not in all cases be easily tuned to those wavelengths at which the observation is going to be performed. An Ulbricht sphere is an example of such a source (see Figure 4.14) with the advantage of a relatively large calibrated area of several square centimetres. Attention must be paid when placing the sphere at the observation volume so that the part of the radiating surface, which is imaged by the optics on the detector is homogeneously illuminated. Also the solid angle

of the observation system must lie within the solid angle of the sphere for which the calibration is provided.

For a known spectral radiance $\Phi_C(\lambda_F)\,[\mathrm{W/m^2 sr\,nm}]$ of the calibrated light source the calibration factor is just given by

$$k = \frac{1}{4\pi}\frac{I_C}{\Phi_C}\frac{T_{IF}(\lambda_F)}{\int T_{IF}(\lambda)\,\mathrm{d}\lambda}L E_{ph}. \tag{4.14}$$

I_C denotes the calibration signal, $T_{IF}(\lambda)$ the spectral transmission profile of that part of the optical path, which defines the spectral transmission of the system (usually an interference filter or a monochromator) and L is the dimension of the fluorescence volume along the line of sight. In the case of the particle density not being uniform throughout the observation volume (our helium beam provides such a situation), one will be rather interested in the total number of investigated particles in the observation volume. The calibration factor k' transforming the measured signal into the fluorescence photon flux into the full solid angle is defined by $\Phi^{4\pi} = I_F/k'$ and given with:

$$k' = \frac{1}{4\pi}\frac{I_C}{\Phi_C}\frac{T_{IF}(\lambda_F)}{\int T_{IF}(\lambda)\mathrm{d}\lambda}\frac{1}{S}E_{ph}, \tag{4.15}$$

where S is the cross section of the observation volume in the plane perpendicular to the line of sight. Finally, one has to keep in mind, that the calibration factor as derived by means of Eq. (4.15) is one average value derived for the whole observation area S. If the spectral radiance under investigation is not uniform throughout the cross section S (the opposite case of a uniform light source provides the Ulbricht sphere), the sensitivity distribution of the observation system throughout S must be checked. A correction factor to k' must be introduced if the sensitivity varies over the area S.

Our observation system has been calibrated for absolute photon flux sensitivity at several wavelengths of helium lines to be observed by using of an Ulbricht sphere (VSS600 by LabSphere). This light source provides calibrated radiation in the wavelength range of 300-2400 nm (Figure 4.14), though the calibration for the wavelengths below 400 nm (in our case at $\lambda = 318.7$, 388.9 and 396.5 nm, however only fluorescence light at the middle wavelength was successfully detected) suffers from low signals and special care must be taken concerning a proper subtraction of background light. During the calibration exactly the same optical as well as electrical set-up (including the high voltage on the photomultiplier tubes) is applied as during experiments to keep the uncertainty of the calibration procedure as low as possible. The absolute calibration has been repeated a few times after a time period of typically several months to account for possible changes of the system sensitivity caused e.g. by the coating of the in-vessel optical components.

4.4.2 Interference filters

As can be seen from Eq. (4.15), the quantities needed to derive the calibration factor are, besides the calibration signal and the spectral radiance of the light source, the observation cross section S as well as the spectral properties of the wavelength selecting
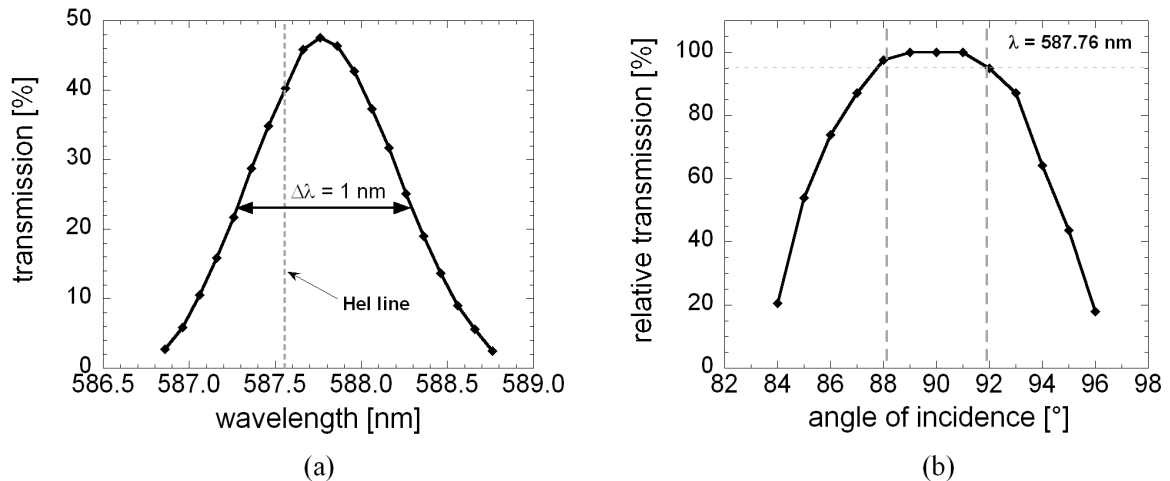
Figure 4.15: (a) Measured transmission profile of the interference filter (010FC36-50/587.6 AM-38009 S/N-02) by Andover Corporation. The wavelength of the relevant helium line is indicated. (b) Dependence of the filter transmission at $\lambda = 587.76\,\mathrm{nm}$ on the light incidence angle (same filter as in (a)) .

optical parts, in our case interference filters. We have to handle the derivation of the latter with special care since we used narrow-band interference filters with a spectral bandwidth of $\Delta\lambda = 1 - 2\,\mathrm{nm}$. The spectral transmission profile of the filters has been measured with an arrangement comprising, among other things, a continuous light source and a monochromator with a spectral resolving power, which was high enough to not considerably affect our measured profiles. One example of a measured transmission profile of an interference filter by the Andover Corporation is shown in Fig. 4.15 (a). Also the wavelength of the helium line under investigation is indicated. It is clear that a miscalibration of the wavelength scale by 0.3 nm, which can happen e.g. because of a spectral misalignment of the monochromator, results in an error in the calibration factor k' by a factor of two if the misalignment shifts the measured profile towards larger wavelengths in this case (in Eq. (4.15) $T_{\mathrm{IF}}(\lambda_{\mathrm{F}})$ changes by this factor whereas the integral transmission remains constant). To ensure a proper wavelength calibration of those measurements a helium spectral lamp has been used as a reference for unshifted wavelengths of helium lines.

Interference filters reveal a strong dependence of the transmission properties on the incidence angle θ of the incoming light: the transmission profile shifts to shorter wavelengths if the filter is shifted. The shifted maximum wavelength λ_{s} can be estimated with [Kruezi, 2007]:

$$\lambda_{\mathrm{s}} = \lambda_0 \left(1 - \left[\frac{n_{\mathrm{a}}}{n_{\mathrm{f}}} \sin\theta \right]^2 \right)^{\frac{1}{2}} ,$$

where λ_0 is the unshifted maximum wavelength, n_{a} is the refractive index of the air and n_{f} is the effective refractive index of the filter material. The measured dependence of

the incident angle θ on the relative transmission at the wavelength of maximum filter transmission for $\theta = 90°$ is shown in Fig. 4.15 (b). An angle mismatch of just $3°$ results in a transmission drop of $\sim 13\%$. This means that cautious placement of the filters into the optical path, vital for sustaining the absolute sensitivity of the system, is required. Moreover, the angular dependence of the filter transmission must be also taken into consideration because the light rays coming from the imaged object to the detector have a certain angular distribution. Accordingly to the geometric properties of our optical path the maximum incident angle is $\theta = 1.9°$ and has no noticeable influence on the overall system sensitivity.

4.4.3 Photomultiplier

Photomultipliers are light detectors converting radiant energy into electrical current. The sensor is a photocathode which is located in a vacuum envelope. The photons impinging on the photocathode release photoelectrons from its surface due to the photoelectric effect. Since this effect is based on the quantum nature of light, the photoelectric current is linearly depending on the photon flux, at least within a certain working parameters range. Released photoelectrons are then accelerated by a static electric field through a structure of several dynodes, each of which multiplies the number of photoelectrons by secondary electron emission by a factor of $\delta = aE^k$ depending on the potential difference between two dynodes E (a and k are constants depending on the dynode material and surface condition as well as the incident angle of the electrons [Zwicker, 1977]; k has a typical value of 0.7-0.8 [Hamamatsu, 1999]). The current through the final stage, the anode, is larger than the photocathode current by the factor of

$$\mu = \frac{a^n}{(n+1)^{kn}} V^{kn} \tag{4.16}$$

which is called the gain of the photomultiplier. V is the supply voltage of the tube which is here supposed to be equally distributed between all acceleration stages and n is the number of dynodes. For example with 10 dynodes the gain is proportional to around the 8th power of the supply voltage, which typically is 1 kV. Thus the gain is very sensitive to its variations (doubling the supply voltage in our case increases the gain by around factor 500, see Figure 4.17).

Photomultipliers are commonly used in laser-induced fluorescence applications with pulsed lasers because of their several outstanding properties:

- high quantum efficiency of up to 30% (approximately three photons are needed for the release of one photoelectron),

- high gain of the photoelectron current of up to 10^9, conveniently controlled by the supply voltage,

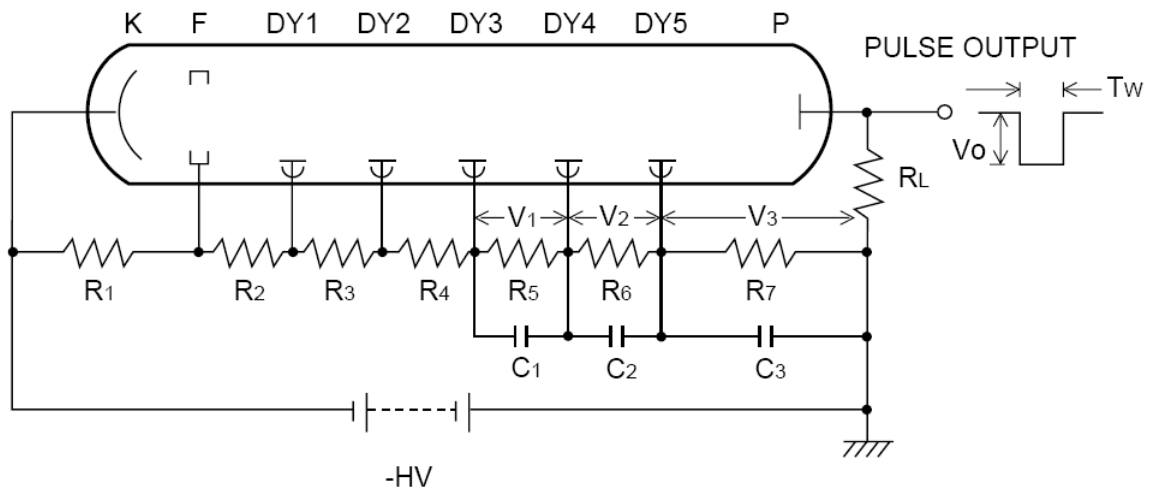- low signal-to-noise level for very low light levels,

Figure 4.16: Voltage divider for a photomultiplier tube consisting of the photocathode (K), focusing electrode (F), five dynodes and the anode (P).

- spectral range sensitivity over several 100 nm, with available ranges from vacuum ultraviolet to near infrared,

- very short time response (rise times below 1 ns),

- linear response of the output current to the incoming photon flux,

- large photocathode area of up to several ten square centimetres.

The supply voltage is usually provided to the dynode stages by use of voltage dividers with a grounded anode and negative high voltage connected to the cathode. An example electrical circuit is shown in Figure 4.16. The anode current can be then fed through a load resistor R_L to the ground and the output signal measured as a voltage drop on this resistor.

For many applications the use of a standard voltage divider consisting solely of equal resistors is sufficient. Though if linear detector response is of concern, the anode current cannot be too large: for continuous signals it should not exceed one percent of the voltage divider current in order not to deteriorate the linearity by more than one percent [Kunze, 1986] (too large currents result in a voltage drop on the last dynode).

The linearity range can be extended by enhancing the divider current (choice of smaller resistor values) or by keeping low the load resistance current (choice of large resistor value). However, the limitation for the former measure is given among others by resistors overheating and the latter measure causes problems in detection of very short signal pulses. This is because of parasitic capacitance between the anode and ground of the order of $C_p \sim 10\,\mathrm{pF}$ acting together with the load resistor as an electric low pass filter. To keep undistorted time shapes of signal pulses in the order of length of 1 ns the load resistor cannot be larger than $R_L = 1\,\mathrm{ns}/10\,\mathrm{pF} = 100\,\Omega$. Due to the need of the

impedance match between the load resistor, the coaxial cable and the waveform recorder we have chosen the value of $R_\mathrm{L} = 50\,\Omega$. Though this low load resistance results in a severe limitation of the photomultiplier linearity range. This was espacially problematic in our measurements because of large portions of the laser stray light in experiments in which the fluorescence light has been observed at the laser wavelength. Therefore, additional measures had to be undertaken in order to extend the linearity range.
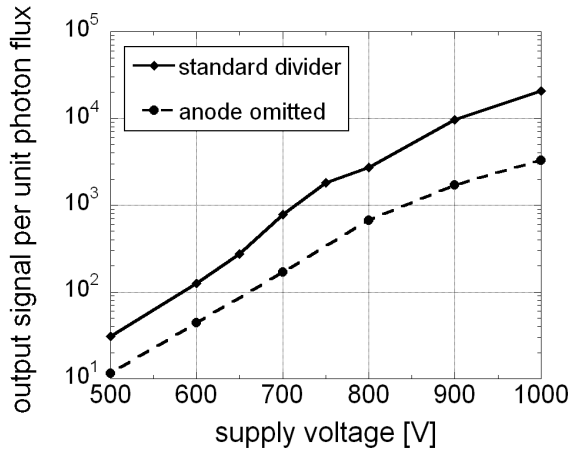
Figure 4.17: Gain curves measured for a photomultiplier tube for the standard voltage divider circuit (see Figure 4.16) and with the last dynode serving as the anode (see text for explanation).

A burning plasma will provide a certain level of background radiation along the line of sight at the observed wavelength. To avoid unnecessary exposure of the detector to this background radiation we drove the photomultipliers in the so-called gated mode in which the high voltage to one of the first dynodes is connected shortly before the laser pulse and disconnected after the pulse. We opened our photomultipliers around 1 μs prior to the laser pulse and closed them 1 μs after the pulse (see the trigger chain in Figure 4.2).

Another way to improve the linearity range is to enhance the maximum current of the last dynodes by supplying them with capacitances, which serve as additional charge sources during short pulsed signals (Figure 4.16). Since in some cases this was still not enough to keep the laser stray light signals within the linear range of the photomultipliers we utilised an additional method, which relies on enhancing the potential difference between the last two dynodes and omitting the anode (stronger electric field more effectively avoids creating of space charges disturbing the linear response [Sauerbrey, 1972]). By disconnecting the last dynode from the voltage divider and connecting it to the anode we doubled the voltage drop between the last but one dynode and the last one, which served as from now as the anode. This had one additional advantage: the output current has been lowered since one amplification stage has been omitted (this can be seen on the Figure 4.17: both curves have been measured at the same photon flux). A comparison of the linearity behaviour for these two cases are shown in Figure 4.18. The solid black curves show the measured output current as a function of the incident light intensity, the dashed lines are the linear extrapolation of the points for low signal levels and the blue curves are the ratio of the measured to the extrapolated signals in percent. One can see that e.g. for the linearity level of 80% the allowed light intensity increased by nearly a factor of ten. Nevertheless in some cases the laser stray light caused detector saturation.

The shortest light pulses in our experiments are expected to lie in the range below 10 ns. However, the absolute calibration as performed with a continuous light source

(Ulbricht sphere) provides the system sensitivity only for dc signals. Therefore, it should be checked for high frequency signals separately. For this purpose a fast fibre-optic transmitter with a transmission rate of 155 MBaud ($\lambda = 600\,\text{nm}$) has been driven with a square voltage pulse with a rise time of 6 ns. No flattening of the photomultiplier current pulse has been observed in comparison to the driver pulse, which confirms the high frequency capability of the system.
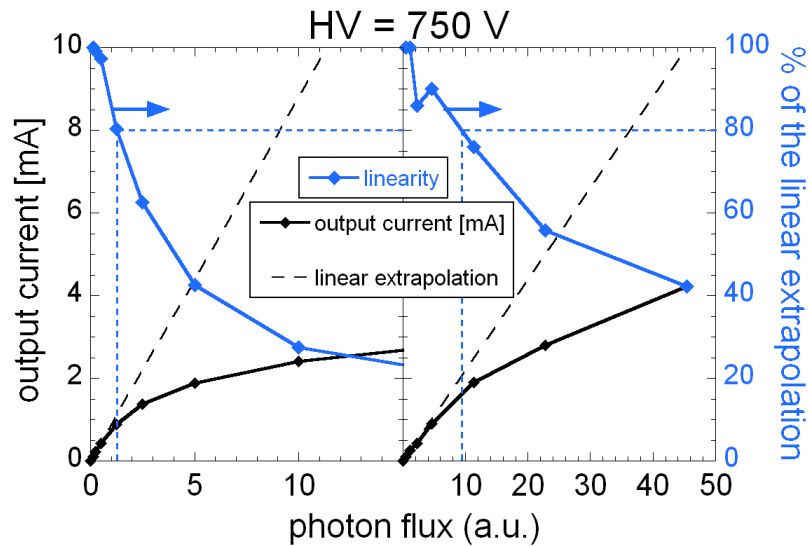

Figure 4.18: Check of the linear range of a photomultiplier for the standard voltage divider circuit (left, see Figure 4.16) and with the last dynode serving as the anode (right, see text for explanation).

Chapter 5

Additional data analysis steps

One of the objectives of this work was to measure the absolute populations of levels excited by laser light and – after setting them in relation to the ground state population density – to compare them with model predictions. This requires some additional steps in terms of data analysis, which are described in this section.

The first section deals with the experimental derivation of the number of ground state helium atoms in the observed fluorescence volume, which is determined by the ionisation and divergence of the beam in the course of plasma penetration. In the second section a method is described, which allows the calculation of the fraction of the lower level population, which is excited to the upper level by the laser radiation. Complicated level splitting due to the magnetic field as well as the fact that our laser does not cover spectrally the whole transition makes the use of a computer-aided simulation necessary. Finally, inclusion of the influence of the resonant laser light on the population distribution in the time dependent solution of the CR model is presented in the last section. This is necessary for the analysis of the time traces of measured collision-induced fluorescence signals from which e.g. the rate coefficients for population transfer between excited levels are inferred.

5.1 Helium distribution in the beam

The number of ground state helium atoms in the observation volume must be known in order to derive relative population densities from absolute ones, which can be compared with model calculations. The total helium flow (integrated flow rate) through the nozzle into the plasma is thus required. This holds also for the time dependence of the flow through the nozzle being not necessarily constant. Both values are determined by test gas puffs into the torus in the absence of plasma. In a second step, one has to consider the divergence of the beam in the course of penetration into the plasma and its atten-uation owing to ionisation losses. Since the theoretical description of these processes is difficult e.g. in view of the uncertainty on the ionisation cross-sections, an experimental determination is a better method. Finally, by appropriate integration of the local helium density with respect to the volume overlap between laser beam and observation line, the absolute number of observed atoms is derived.

For the determination of the time trace of the total (integrated) helium flow through the nozzle, test gas puffs into the torus in the absence of plasma have been performed for

the same parameters as during experiments. By recording time traces of two pressures, in the gas reservoir and in the torus, the time dependence of the flow can be reconstructed.

Based on the ideal gas law, the pressure change $\mathrm{d}p/\mathrm{d}t$ in the torus during the gas test puff can be balanced by the particle flow through the nozzle (source) and the particle loss to the pumps (sink):

$$\frac{\mathrm{d}p}{\mathrm{d}t}\mathrm{V_{tor}} = \frac{\mathrm{d}N}{\mathrm{d}t}\mathrm{k_B}T - \mathrm{S}p, \tag{5.1}$$

where S is the pumping speed, commonly given in [l/s]. In the case of closed helium gas valve ($\mathrm{d}N/\mathrm{d}t = 0$), the above equation simplifies and we obtain the following time dependence of the pressure in the torus

$$p = \mathrm{e}^{-\frac{\mathrm{S}}{\mathrm{V_{tor}}}t}. \tag{5.2}$$

The pumping speed per unit volume $\mathrm{S}/\mathrm{V_{tor}}$ is then simply derived from the time constant of the exponential decay of the pressure curve (here the assumption is made that S is constant in this pressure range). Once $\mathrm{S}/\mathrm{V_{tor}}$ has been determined, the relative gas flow through the nozzle can be derived by differentiation of the pressure curve during the gas pulse

$$\Gamma_{\mathrm{He}}(t) = \frac{\mathrm{V_{tor}}}{\mathrm{k_B}T}\left(\frac{\mathrm{d}p}{\mathrm{d}t} + \frac{\mathrm{S}}{\mathrm{V_{tor}}}p\right) \ \ \text{for} \ \ t_{\mathrm{on}} < t < t_{\mathrm{off}}. \tag{5.3}$$

Figure 5.1: Pressure in the torus (black) and in the reservoir (grey) during a gas test puff (hatched area indicates the valve opening time).

The total amount of gas puffed into the torus is derived from the pressure drop in the gas reservoir, again, by use of the ideal gas law ($\Delta N = \Delta p \mathrm{V_{res}}/\mathrm{k_B}T$). With these two pressure measurements during the gas test puffs, we derive the time dependent absolute helium flow through the nozzle. Figure 5.1 shows a measured time trace of the (relative) torus pressure as well as the pressure drop in the gas reservoir. Helium flows obtained by the above method for different initial reservoir pressures are shown in Figure 5.2. The valve was open in the time window of 0.8-4.8 s. The curves show a delay in the onset and the termination of the flow, which is caused by the flow time along the approximately 6 metres long line between the reservoir and the nozzle. A relatively flat maximum sustains in the time interval 2-5 s. which we use for our LIF measurements during plasma discharges.

Other measurements are shown in Figure 5.3. In this case the valve was opened between 0.8 and 1.6 s. The four solid curves show the relative helium flow during the test puffs derived from the idel gas law, rescaled to its maximum. No flat top phase of the gas flow is established. One additional measurement is superimposed, which was
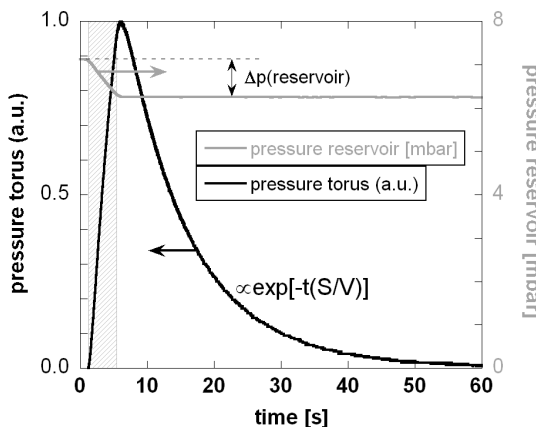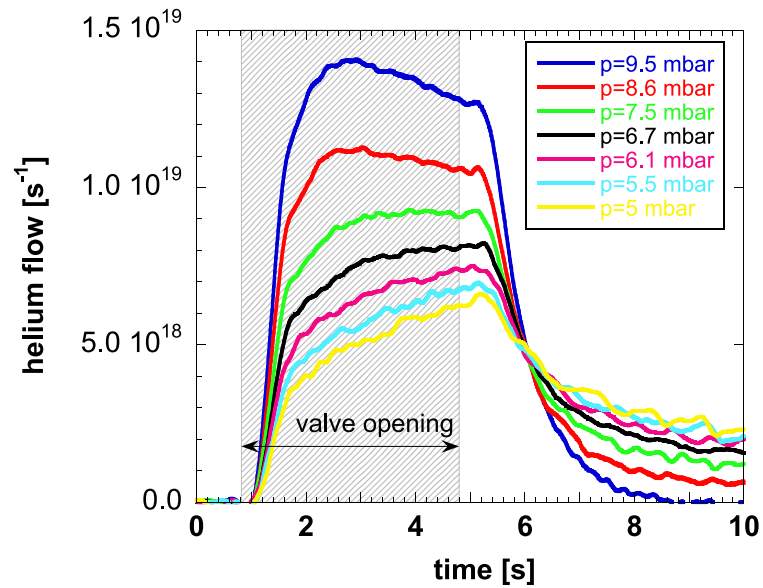
Figure 5.2: Helium flow through the nozzle as a function of time derived from the gas test puffs into the torus for different initial helium beam reservoir pressures.
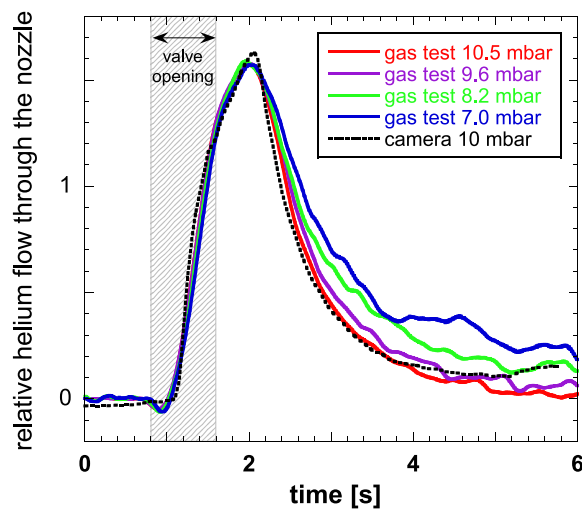

Figure 5.3: Comparison of relative helium flow through the nozzle measured with the 2D camera during a plasma discharge (black dotted line) and during gas test puffs and obtained by means of Eq. (5.3) (other lines).
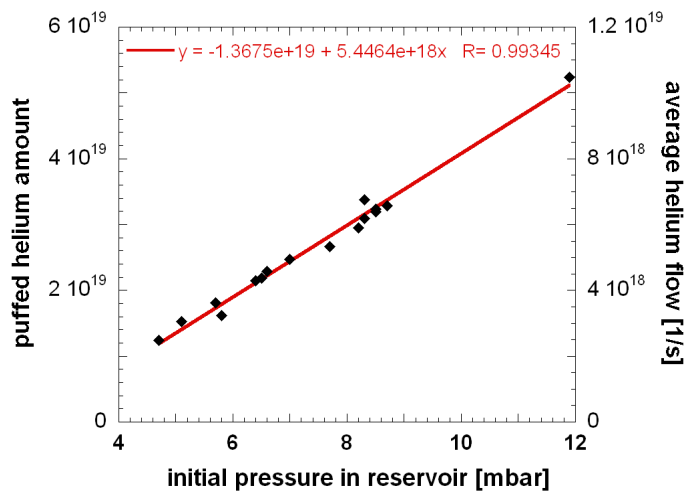
Figure 5.4: Total helium amount puffed within one gas test pulse (with a fit function formula) and average flow through the nozzle for different reservoir pressure.

made during a plasma discharge by recording helium light at $\lambda = 501.6\,\mathrm{nm}$ with a 2D camera with an image intensifier for the same valve opening time and the initial reservoir pressure of $p_{\mathrm{He}} = 10\,\mathrm{mbar}$. Its time trace very well coincides with the curve obtained from the gas tests at the similar reservoir pressure of $p_{\mathrm{He}} = 10.5\,\mathrm{mbar}$. From the gas tests shown in Figures 5.2 and 5.3 we obtain parameters of the gas puff ensuring a flat top phase of the helium gas flow through the nozzle as well as an additional check for the derivation of the relative gas flow from the pressure in the torus in form of the beam emission measured with the camera. In Figure 5.4 the total helium amount puffed during a gas pulse as well as the average helium flow through the nozzle for typical reservoir pressures as used in experiments are plotted.

The second issue to be considered on the way of the deriving the number of observed helium atoms during experiments is the beam divergence and attenuation on its way through the plasma. To tackle this problem the line emission of helium atoms in the beam at the wavelength of $\lambda = 501.6\,\mathrm{nm}$ ($3^1\mathrm{P}^\mathrm{o}{\rightarrow}2^1\mathrm{S}$) was recorded by the 2D camera by using the same observation port as for the fluorescence measurements. An example image is shown in Figure 5.5. The colour intensity in each pixel corresponds to the integral light emission along the line of sight of the camera i.e. in the poloidal direction. On integrating the signals over their extension in the toroidal direction, one obtains a radial profile $I(r)$ of the total light emission of the beam at the wavelength under consideration. In the following it will be shown that this quantity is a measure of ionisation losses from the beam [Bogen et al., 1984, Pospieszczyk and Ross, 1988].

Since we can treat the population distribution function $n_i(r,t)$ as stationary (see Sec. 3.3), setting its partial derivative with respect to the time (see Eq. (3.4)) to zero yields

$$v_{\mathrm{He}}(r)\,\frac{\partial n_i(r,t)}{\partial r} = S_i(r,t). \tag{5.4}$$

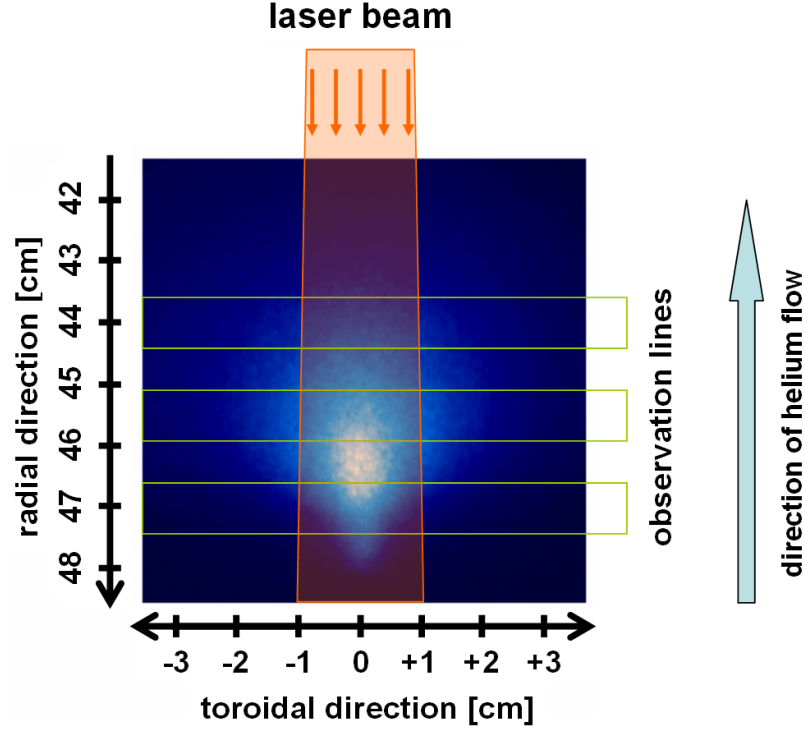Here, it is sufficient to only consider the ground state with the density n_1, since it

Figure 5.5: Beam emission at $\lambda = 501.6\,\mathrm{nm}$ $(3^1\mathrm{P^o} \rightarrow 2^1\mathrm{S})$ recorded with a 2D-camera during the flat-top phase of a discharge with $\overline{n}_e = 4 \times 10^{19}\,\mathrm{m}^{-3}$. The path of the laser beam as well as the lines of sight are indicated.

provides the main source of ionisation loss (see the discussion in Sec. 6.4 and Figure 6.21 there). For the source term we can write

$$S_1(r,t) = -n_1(r,t)n_\mathrm{e}(r) \left\langle \sigma_{1\rightarrow\mathrm{ion}} v_\mathrm{e} \right\rangle. \tag{5.5}$$

Upon insertion Eq. (5.5) in Eq. (5.4), one derives for the radial profile of the total (i.e. integrated over the poloidal and toroidal direction) ground state helium density in the beam the following expression:

$$n_1(r') = n_1(\mathrm{a}) - \int_\mathrm{a}^{r'} n_1(r)n_\mathrm{e}(r) \left\langle \sigma_{1\rightarrow\mathrm{ion}} v_\mathrm{e} \right\rangle \frac{\mathrm{d}r}{v_\mathrm{He}(r)}, \tag{5.6}$$

where a denotes the minor plasma radius. On the other hand the measured line intensity $I(r)$ from the level k can be written as

$$I(r) = \mathrm{const} \times n_1(r)n_\mathrm{e}(r) \left\langle \sigma_{1\rightarrow\mathrm{k}} v_\mathrm{e} \right\rangle, \tag{5.7}$$

assuming that the radiating level k, being in equilibrium with the ground state population, is populated mainly by electron collision-induced transitions from the ground state and its most important depopulation channel is spontaneous radiation (both assump-
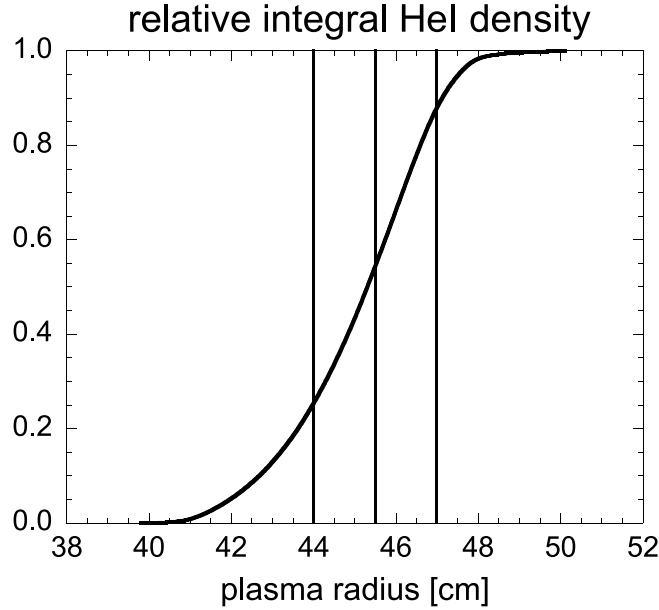
Figure 5.6: Attenuation of the helium beam in the course of the plasma penetration due to ionisation losses derived by integrating of the beam emission shown in Figure 5.5 according to Eq. (5.9). Indicated are the three radial positions of our fluorescence measurements (see also Figure 4.1).

tions are justified for the observed transition). Replacing in Eq. (5.6) the expression for $n_1 n_e$ derived from Eq. (5.7) yields:

$$n_1(\mathrm{a}) - n_1(r') \propto \int_\mathrm{a}^{r'} I(r) \frac{\langle \sigma_{1\to\mathrm{ion}} v_\mathrm{e} \rangle}{\langle \sigma_{1\to\mathrm{k}} v_\mathrm{e} \rangle} \frac{\mathrm{d}r}{v_\mathrm{He}(r)}. \tag{5.8}$$

While there is thus no direct electron density dependence in this expression, the electron temperature dependence of the rate coefficients remains. Since both collisional rate coefficients appearing in Eq. (5.8) have a similar temperature dependence in the range 10-100 eV, their ratio can be extracted from the result of the radial integration. Furthermore, if assuming a radially constant (negative) velocity $v_\mathrm{He}(r) = \mathrm{const} < 0$ of the beam, which is oriented in the direction of the minor plasma radius r, the profile of the particle losses is obtained simply by integration of the measured light intensity from the plasma edge to the considered radial point r':

$$n_1(\mathrm{a}) - n_1(r') \propto -\int_\mathrm{a}^{r'} I(r)\,\mathrm{d}r. \tag{5.9}$$

The influence of the assumption of a linear velocity profile $v_\mathrm{He}(r)$ on the derived beam attenuation curve can be seen in Figure 6.19 (a). Results of such an integration are shown in Figure 5.6. One can see that the amount of fluorescence signal at the innermost channel will be more than a factor of three smaller than at the channel at $r = 47\,\mathrm{cm}$ owing to ionisation losses alone.
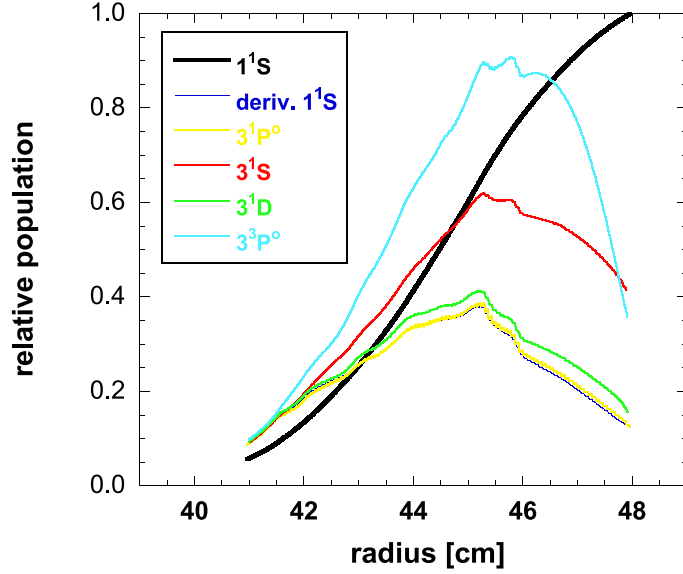
Figure 5.7: Test of the assumptions made for the derivation of Eq. (5.8). The CR model calculation of the line emission from the level $3^1\mathrm{P^o}$ (yellow line) coincides well with the time derivative (dark blue line) of the calculated ground state density (black line; ionisation losses). Emission from other levels (remaining curves) cannot be used for this purpose.

As a test of the justification of the assumptions described above allowing the use of line emission from the $3^1\mathrm{P^o}$ level as a measure of the local ionisation loss rate, the attenuation (ground state population) of a sample beam penetrating a plasma of given parameters as well as its derivative $\mathrm{d}n_{1^1\mathrm{S}}/\mathrm{d}t$ are calculated by the CR model. As we see in Figure 5.7 the time derivative curve being equivalent to the ionisation losses coincides well with the emission from the level $3^1\mathrm{P^o}$ which is not the case for the other plotted emission curves.

The second factor which also results in the reduction of the local helium density in the beam is beam divergence. It is allowed for in such a way that the local helium density profile $n_{\mathrm{He}}^{\mathrm{loc}}(\tilde{r})$ perpendicular to the beam propagation axis for a given radial position in the plasma r' is assumed to have circular symmetry ($n_{\mathrm{He}}^{\mathrm{loc}}(\tilde{r} = \mathrm{const}) = \mathrm{const}$; this is not fully true – a small asymmetry of toroidal intensity profiles is observed). Since the signals recorded by the camera are line integrated intensities in the poloidal direction, any toroidal profile of the measured intensity at a desired plasma radius r' can be easily Abel-inverted according to [Lochte-Holtgreven, 1968]

$$n_{\mathrm{He}}^{\mathrm{loc}}(\tilde{r}) = -\frac{1}{\pi} \int_{\tilde{r}}^{\tilde{R}} \frac{\mathrm{d}I(y)}{\mathrm{d}y} \frac{\mathrm{d}y}{\sqrt{y^2 - \tilde{r}^2}}, \qquad (5.10)$$

yielding the local helium density (y denotes the variable of integration, and $\tilde{R}$ the maximum distance from the beam axis to the point where the helium light was still detected). Integration is performed for all three radial positions r' of our observation channels ac-
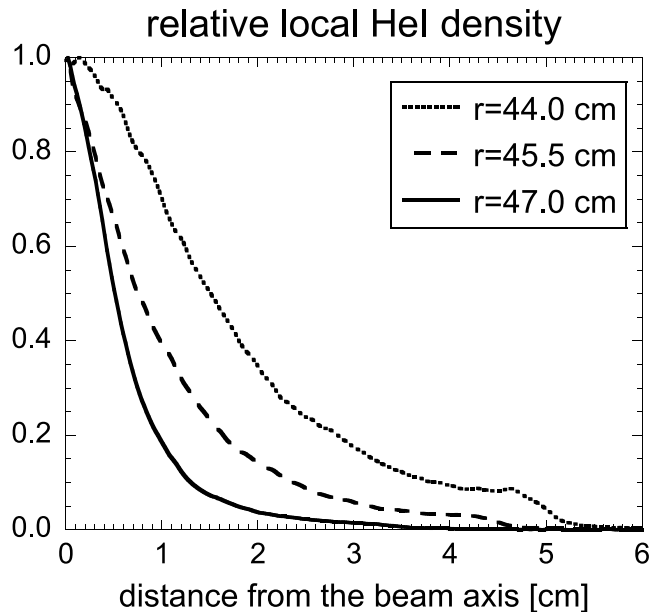
Figure 5.8: Relative local helium density $n_{\mathrm{He}}^{\mathrm{loc}}(\tilde{r})$ perpendicular to the beam propagation axis for the three radial positions of our observation system as derived by Abel inversion of the corresponding toroidal profiles from the camera measurement.

counting for their radial extension as indicated in Figure 5.5. One example is shown in Figure 5.8.

The local density profile can now be integrated over the area where the laser beam and the path of the line of sight overlap. This provides, together with the beam attenuation profile and the helium flux through the nozzle, the number of atoms which contribute to the measured fluorescence signal. It turns out that even at the outermost observation position only about 25% of the initial beam content is effectively used for the measurements.

5.2 Pumping efficiency

Pumping of a transition with a broadband laser, which is resonant with the whole fine structure or the Zeeman structure arising in a magnetic field considerably simplifies the derivation of the absolute population density of the pumped level from the fluorescence signal intensity. In our case of a narrow-band laser radiation a more complicated situation is given which is analysed in detail in this section.

Figure 5.9 shows the typical LIF measurement strategy at TEXTOR for the example of the transition $2^3\mathrm{P^o} \rightarrow 3^3\mathrm{D}$ ($\lambda = 587.6\,\mathrm{nm}$). During the plasma plateau phase of the discharge (top figure) of typically 4 seconds, the laser has been scanned over a spectral range of around 70 pm to cover the sets of σ^+ and π components of the Zeeman spectrum (bottom-right, see also Figure 5.10). In order to be able to collect the maximum possible number of fluorescence photons with the detector we measured at only
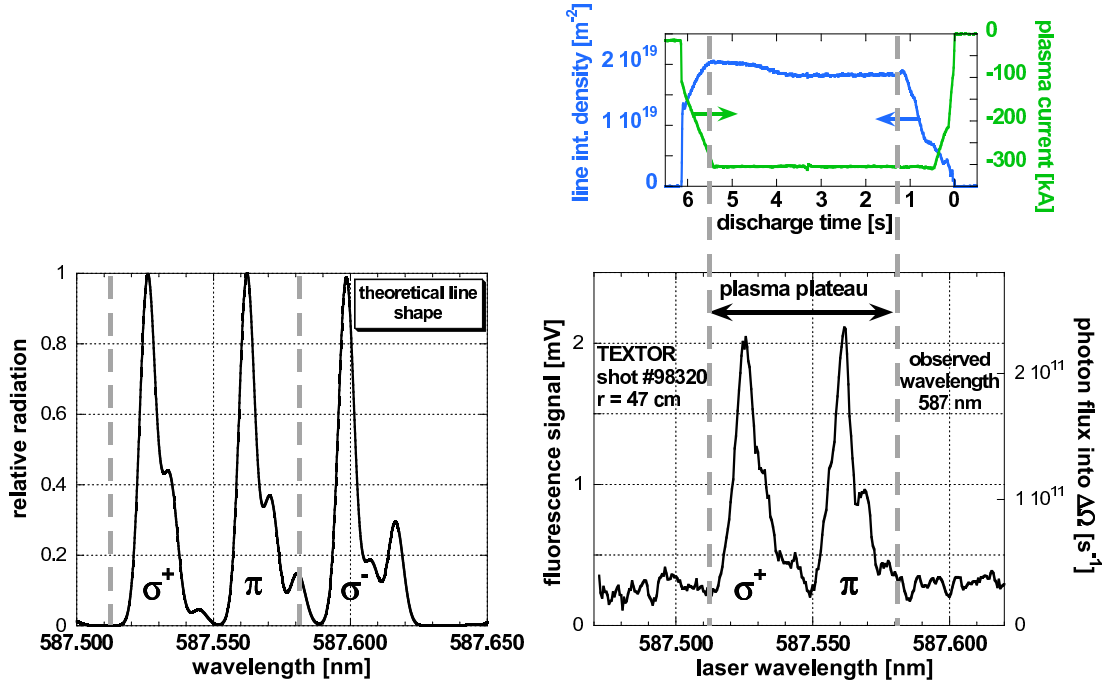
Figure 5.9: Bottom-right: fluorescence signal observed at the laser wavelength when exciting the triplet transition $2^3P^o \rightarrow 3^3D$ ($\lambda = 587.6$ nm) during a TEXTOR Ohmic discharge (σ^- missing owing to scanning range restricted on purpose); bottom-left: corresponding calculated Zeeman emission spectrum; top: plasma current and line integrated electron density during the discharge.

one wavelength during a whole discharge. A comparison with the emission spectrum (bottom-left) calculated according to [Hey et al., 1994, 2002] shows good agreement. An additional scale has been provided to the plot with the measured curve indicating the measured flux of fluorescence photons released from the observation volume into the solid angle of our observation system. Preferably from the maximum photon flux, as it ensures the maximum signal to noise ratio, the absolute population of the level pumped by the laser. Further, by employing the absolute measurement of the ground state helium in the observation volume as described in Sec. 5.1, the population of the considered level relative to the ground state population is derived and compared with the CR model prediction (Figure 6.2). The small spectral width of our dye laser does not permit coverage of all Zeeman components. This is unfortunate, since the present procedure results in a loss in intensity and makes comparison with calculated signals harder, especially in the case of triplet transitions, because of their fine structure. In fact, in the case of the triplet transition $2^3P^o \rightarrow 3^3D$ ($\lambda = 587.6$ nm), the laser cannot even cover the full set of π lines (Figure 5.10). This complicates the determination of the fraction of the 2^3P^o level population, which is being pumped to the upper level, even in the simple case of saturating laser power.

For this reason computer simulation is used to derive the pumped fraction of the lower level population. From the laser pulse energy arriving at the observation volume, as well

as the centre and the width of the laser line, the spectrum of the saturation parameter $S(\lambda)$ is being calculated under the assumption of a Gaussian laser profile. Taking the longitudinal spectral modes[1] into account is also possible but had only a negligible impact on the results. In this way it is accounted for the fact that the saturation of the pumping process is given more or less in the centre of the laser spectral profile and that the contribution of the wings to the pumping efficiency is therefore lower.

The laser energy density is assumed to be constant across the observation volume (see Sec. 4.2). A Gaussian, inhomogeneously broadened absorption line profile $f(\lambda)$ (Sec. 2.3.1) is assumed, with width depending on the gas temperature in the beam (Doppler broadening, Sec. 2.3.3). It corresponds to the population distribution of atoms in the lower level with regard to their velocity component along the laser beam direction. The fraction of pumped atoms resonant with the laser radiation at the wavelength λ at the end of the laser pulse of length T_L is given by

$$\frac{\Delta n_{\mathrm{u}}}{n}(\lambda) = \frac{g_{\mathrm{u}}}{g_{\mathrm{l}} + g_{\mathrm{u}}} \frac{S(\lambda)}{S(\lambda) + 1} \left(1 - \mathrm{e}^{-(S(\lambda)+1)A_{\mathrm{ul}}T_{\mathrm{L}}} \right) \tag{5.11}$$

(Sec. 2.1), neglecting the initial population of the upper level u (n is then the lower population density before laser irradiation). The convolution integral

$$\int_{-\infty}^{\infty} \frac{\Delta n_{\mathrm{u}}}{\mathrm{n}} f(\lambda) \mathrm{d}\lambda \tag{5.12}$$

provides the total pumped fraction for a given centre wavelength of the laser profile. The spectrum of the total pumped fraction is easily derived by performing the calculation for a whole series of laser pulses stepping across the spectrum with incremental changes of the central wavelength of the laser profile, just as in the experiment.

A more complicated situation is given if both levels of the pumped transition are split, such as by the fine structure or the Zeeman effect. In general, several separate Zeeman transitions (at slightly shifted wavelengths and differing in polarisation) will connect the different sublevels of the lower and the upper level. Moreover, the laser profile can cover, at least partially, several absorption profiles of the transitions which in turn can overlap one another. Fortunately, in our case a simplification is given, which is described in more detail in the case of the mentioned $3^3\mathrm{D} \rightarrow 2^3\mathrm{P}^{\mathrm{o}}$ ($\lambda = 587.6\,\mathrm{nm}$) transition.

This triplet transition reveals a complicated Zeeman structure in the intermediate magnetic field case. In Figure 5.10, the Einstein coefficients (A-values) of all Zeeman components are plotted against wavelength. Owing to partial overlap and because some of the A-values are very low, fewer than 71 components are apparently visible. The π and σ components have been colour-coded separately. The nine dominant π components in the wavelength range of $587.560 - 587.5807\,\mathrm{nm}$ have been listed separately in Table

---

[1]Longitudinal laser modes are due to the constraint of standing waves in the laser resonator. Their spectral separation $\Delta\frac{1}{\lambda} = \frac{1}{2n\mathrm{L}}$ is thus dependent on the resonator length L and the index of refraction n. It amounts in our laser to $\Delta\frac{1}{\lambda} = 0.018\,\mathrm{cm}^{-1}$ and their spectral profile is specified by the vendor by a Gaussian with a width of half the separation.

J_u	m_u	J_l	m_l	wavelength [nm]	A_i [10^8s^{-1}]	p_i
3	0	2	0	587.5700	0.333	1.12
3	-1	2	-1	587.5626	0.477	1.25
3	-2	2	-2	587.5615	0.358	1.12
2	2	2	2	587.5615	0.358	1.12
2	1	2	1	587.5622	0.358	1.12
2	0	1	0	587.5714	0.403	1.25
2	-1	1	-1	587.5624	0.358	1.12
1	1	1	1	587.5626	0.477	1.25
1	0	0	0	587.5807	0.316	1.12

Table 5.1: The nine dominant π components of the transition 3^3D$\rightarrow 2^3$P^o at $\lambda = 587.6$ nm (calculated for B = 2.25 T), which are taken into account for calculation of the 2^3P^o population fraction pumped to the upper level. The wavelengths, the A-values as well as the polarisation factors are shown.

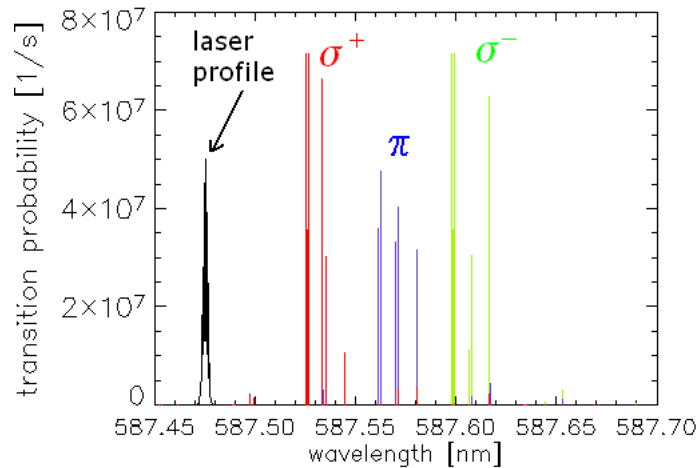5.1. These have been taken into account in the calculation.

Figure 5.10: Zeeman components of the transition 3^3D$\rightarrow 2^3$P^o at $\lambda = 587.6$ nm calculated for B = 2.25 T. π and σ components are plotted in different colours. For comparison the laser profile is superimposed.

Figure 5.11 shows the Zeeman-split transition 3^3D$\rightarrow 2^3$P^o in form of a Grotrian diagram. Only the nine dominant π components are indicated. As shown, the corresponding transitions connect all nine magnetic sublevels of the lower level with nine different sublevels of the upper level (marked with bold lines). Since there are no sublevels of the upper level from which more than one line with π polarisation starts and no sublevels of the lower level with the same feature, all nine absorption lines, even though some of them partially overlap, can be separately treated in our calculation as independent 2-level systems. Equal population distribution among the lower sublevels is assumed due to their very small energy differences.
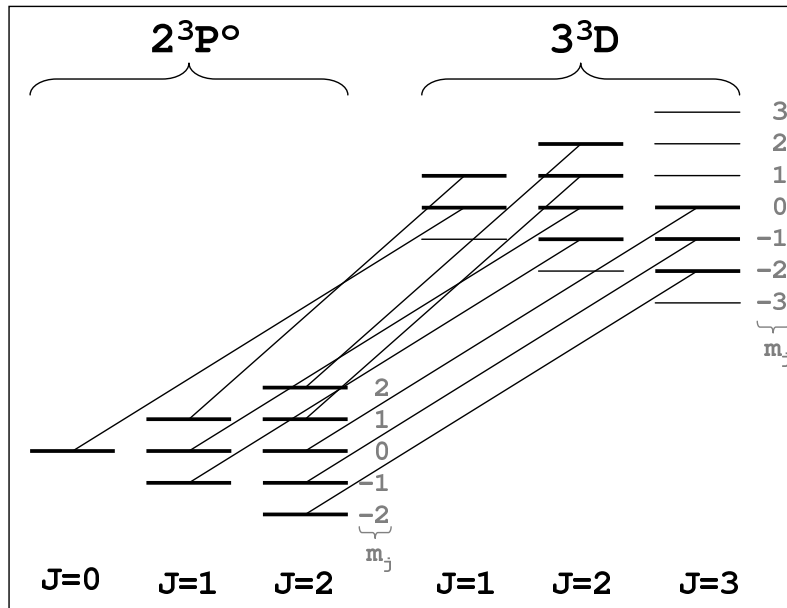
Figure 5.11: Part of the Grotrian diagram of HeI showing the Zeeman structure of the transition $3^3\mathrm{D}{\rightarrow}2^3\mathrm{P}^\mathrm{o}$ at $\lambda = 587.6\,\mathrm{nm}$. Only those transitions are indicated, which are listed in Table 5.1, and correspond to the nine dominant π components of the line.

The treatment of the overall pumping process as a sum of 2-level-system excitations, as described above, holds only approximately in the case of considerable collision-induced population transfer between the sublevels of the upper or lower level, resulting in redistribution of any non-uniform population within the time scale of the laser pulse. Let us consider this situation for the case of a strongly saturating unpolarised broadband laser spectrally covering only all the π transitions. Provided that the upper sublevels remain collisionally decoupled the laser would transfer one half of the lower population to the upper level (in the case of a laser spectrally covering all π and σ components this pumping efficiency would climb to 15/24). In contrast, an instant redistribution among the sublevels would be equivalent to the excitation along all transitions of the Zeeman structure resulting in the pumped fraction of 15/24. An increasing value of the pumped fraction will result in an increase of upper level population in the presence of laser light and hence collision-induced signals will become larger. This must be taken into account if using these signals to measure the absolute lower level population, like in the pumping scheme described in Sec. 6.1.4. However, changes in the polarisation of the fluorescence light from the upper level counteract the increasing pumped fraction so that fluorescence intensities observed perpendicularly to the magnetic field remain approximately unchanged with pumping the π transitions (see below in this section).

The effect of collisional population transfer between magnetic sublevels was observed in a hollow cathode discharge by Takiyama et al. [1994, 1997]. However, it was attributed to atom-atom collisions due to high atomic gas density in the range of $n_{\mathrm{He}} \sim 10^{16}\,\mathrm{cm}^{-3}$. In our case electron or, owing to the small energy differences of the magnetic sublevels (see Figure 2.13), more likely proton collisions could be sufficiently rapid for the redis-

tribution (calculated proton densities needed for statistical population of the hydrogen fine structure levels (n, l) with $n = 3 - 5$ for typical fusion edge plasma parameters seem to be smaller than the electron densities [Hey et al., 1996]). Since no rate coefficients for the collisional population transfer between the magnetic sublevels are known, we neglect this effect in the calculation. This question could be examined experimentally by measurement of time-resolved traces of both π and σ components of the resonant fluorescence light in the case of exciting e.g. only a π component. An attempt has been made to spectrally resolve the π and σ components of the fluorescence light by a high resolution spectrometer with an image intensifier, which can be gated on the nanosecond time scale. However, due to the short light integration times no fluorescence signal was detected.

The above considerations and assumptions permit the calculation of the approximate lower level population fraction pumped to the upper level as a function of the laser wavelength. However, this spectrum of the pumping efficiency cannot be directly compared to the measured signals. This is because the observed fluorescence light (separated from the plasma radiation by interference filters with the spectral width of $\Delta\lambda \sim 1\,\text{nm}$, Sec. 4.4.2) differs in the degree of polarisation. Its value, quantified with the polarisation factor p_i, depends on the upper sublevel i the fluorescence light originates from. We have to keep in mind that due to the finite width of the interference filter the detected fluorescence radiation consists not only of the π lines, which are excited but also of additional (mostly) sigma lines. The (polarisation dependent) factors for our observation angle of $\sim 90°$ with respect to the magnetic field, by which the (over the whole space 4π integrated) A-values have to be multiplied, are $3/2$ and $3/4$ for the π and the σ lines, respectively. The final p_i factors are obtained by weighting the factors $3/2$ and $3/4$ with the corresponding A-values for the π and σ lines. They are listed in Table 5.1.

The resulting spectrum can in principle be compared with the experimental spectrum of the fluorescence signals. The signal amplitudes provide a comparison of the absolute population density of the lower level. On the other hand, the comparison of the widths of the spectra can be utilised to cross-check the assumed spectral widths of the laser profile and absorption lines (or for derivation of one of them if unknown), which influence the width of the measured profiles as well as the pumping efficiency. In all cases the laser spectral widths derived from the analysis of spectra measured at TEXTOR were similar to those obtained from glow discharge measurements with one exception of a measurement at $\lambda_\text{L} = 587.6\,\text{nm}$ where the width $\Delta\lambda_\text{L} = 3.5\,\text{pm}$ from the glow discharge measurement, obtained on the day after the TEXTOR measurements, lay considerably above the TEXTOR result of $\Delta\lambda = 1.5\,\text{pm}$. However, an earlier measurement on the glow discharge provided the laser width of $\lambda_\text{L} = 3\,\text{pm}$ at $S = 100$ (see Figure 4.10). Since the laser spectral width is supposed to be sensitive to the exact adjustment of the laser optical path the width resulting from the fit of the TEXTOR spectrum is taken in this case and the discrepancy to the glow discharge measurement is incorporated in the uncertainty of the measured population densities.

In the case of a more complicated measured spectrum than e.g. of only a single Gaussian profile, the reconstruction of the features of the profile serves as an additional
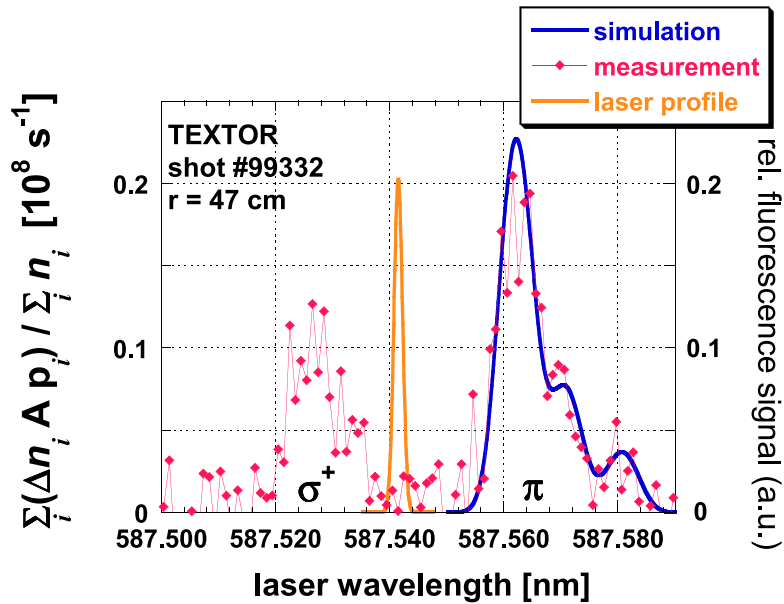
Figure 5.12: Comparison of calculated and measured fluorescence spectra at the laser wavelength $\lambda = 587.6\,\text{nm}$ for the case where the transition $2^3\text{P}^\text{o}{\rightarrow}3^3\text{D}$ is pumped. The π components alone have been fitted. For comparison the scanning laser profile is added.

check for the proper simulation procedure. This is can be seen in Figure 5.12, which shows a measured relative fluorescence spectrum with an overlaid simulated spectrum of the π components. The scaling of the y axis refers to the simulation curve. The y values are the transition probabilities for the total radiation from the upper sublevels weighted with their relative population increase Δn_i due to laser pumping and the polarisation factors p_i (n_i denotes the initial lower level population). At the maximum ($\lambda = 587.562\,\text{nm}$) the calculated pumped fraction of the lower level population amounts to around $1/2$ of the maximum which would be achievable with a broadband laser. The slight flattening at the maximum of the measured profile may be due to approaching detector saturation.

We shall now return to the problem of the collisional population redistribution between magnetic sublevels. We have seen that this effect enhances the pumped fraction by 25% in the limit of instant redistribution in the case of the transition $2^3\text{P}^\text{o}{\rightarrow}3^3\text{D}$. However, there is a mechanism, which at least partially counteracts the increase of the upper level population in terms of fluorescence intensity from this level. This is the polarisation factor, which drops from the value of $\text{p}_i = 1.16$ (average p_i over all rows in Table 5.1) to one (unpolarised light following equal distribution among sublevels) nearly balancing the enhanced upper level population.

In the case of the triplet transition $2^3\text{S}{\rightarrow}3^3\text{P}^\text{o}$ ($\lambda = 388.9\,\text{nm}$) it can easily be shown that both these effects exactly counteract independently of the collisional redistribution rate (these considerations are valid also for all singlet transitions in the presence of a magnetic field). Figure 5.13 shows the Zeeman splitting of this transition in form of a Grotrian diagram. Nine dominant out of nineteen transitions in total are indicated,
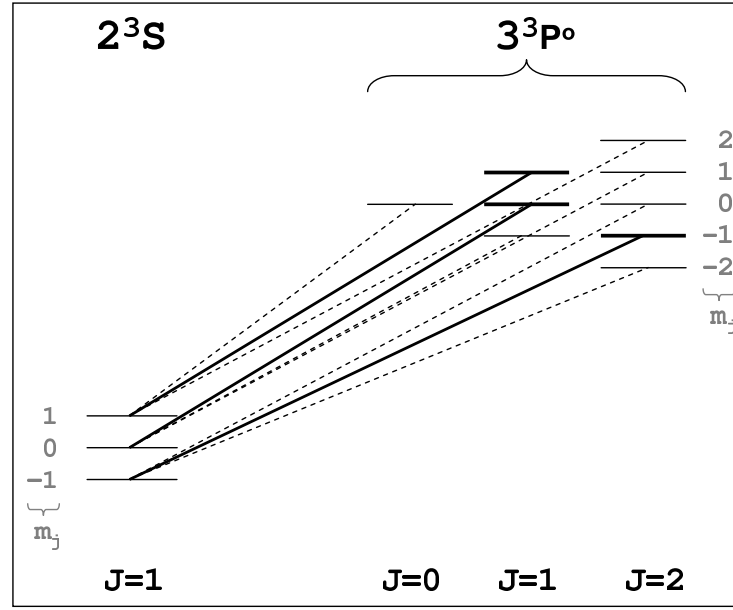
Figure 5.13: Part of the Grotrian diagram of HeI showing the Zeeman structure of the transition $3^3\mathrm{P^o} \rightarrow 2^3\mathrm{S}$ at $\lambda = 388.9\,\mathrm{nm}$. Nine dominant of nineteen transitions in total are shown (π type transitions are indicated by thick solid lines).

three of them being of the type π marked by thick solid lines (the π lines are lying at the same wavelength but separated spectrally from the σ lines). Let n_l indicate the sum of the population of all three lower sublevels, n_π the sum of three upper sublevels from which π lines are radiating (bold marked levels in Figure 5.13) and n_σ the sum of six corresponding upper sublevels for σ lines. n denotes the total population of the system, assumed to be constant. The intensity of the fluorescence light observed perpendicularly to the magnetic field lines is given by

$$I_{f\perp} \propto 1.5 n_\pi + 0.75 n_\sigma. \qquad (5.13)$$

The sum populations n_π and n_σ are weighted only by the polarisation factors (explained above) since the A-values are the same for all nine lines. The relative population at a given point in time

$$n_\sigma / n_\pi = 2 f(n_\mathrm{p}) \qquad (5.14)$$

depends on an unknown function $f(n_\mathrm{p})$ of the perturber density n_p and is equal to zero if no redistribution takes place and two at instant redistribution ($f(n_\mathrm{p}) = 1$). Thus, we obtain for the fluorescence intensity

$$I_{f\perp} \propto 1.5(1 + f(n_\mathrm{p})) n_\pi. \qquad (5.15)$$

The density n_π also depends on the redistribution rate. After inserting $n_\pi = n_\mathrm{l}$ (saturation condition) in $\mathrm{n} = n_\pi + n_\sigma + n_\mathrm{l}$ we obtain $n_\sigma = \mathrm{n} - 2 n_\pi$ and insert the result in Eq.

(5.14). This yields the dependence of n_π on $f(n_\mathrm{p})$

$$n_\pi = \frac{\mathrm{n}}{2(f(n_\mathrm{p}) + 1)}. \tag{5.16}$$

Now we use Eq. (5.15) and see that the fluorescence intensity $I_{f\perp} \propto 0.75\mathrm{n}$ does not depend on the redistribution rate but only on the total population of the system. This means that for a finite redistribution rate the effect of an increasing pumping fraction is always exactly balanced by a decreasing polarisation factor. Hence taking the redistribution into account has no effect on the predicted fluorescence intensity from the upper level pumped by the laser but only enhances collision-induced signals from other levels. This result is obtained for saturating laser powers and for the observation perpendicularly to the magnetic field lines.

5.3 Inclusion of the laser perturbation in the CR calculation

In Sec. 3.3, both solution approaches were presented which allow the calculation of the stationary, albeit not necessarily relaxed (see Sec. 3.2.3), radial profiles of the population densities of the considered levels. In the following the way is described, how the influence of the pulsed resonant laser radiation on the time dependent population distribution is incorporated into the CR model code.

The stationary solution of the CR model calculation in form of the vector $\boldsymbol{n}$ of the population density distribution for a given radial position in the plasma is used as the initial value for investigating the influence of the laser on the level populations. In principle, the instantaneous population change of the lower and the upper level due to a strongly saturating broadband laser radiation can be easily derived from the statistical weights of both levels (Eq. (2.8)). However, if rapid depopulation channels from the upper level exist (see e.g. Figure 5.15), it will be strongly depleted even on a nanosecond time scale. Moreover, valuable insights can be drawn from collision-induced fluorescence radiation from other levels. For modelling of these time dependent signals the use of the CR model code – appropriately adapted – is necessary.

At this point, the time scales of the relevant processes have once again to be considered for the proper choice of the solution method. The perturbation induced by the strong saturating laser spectrally adjusted to one of the transitions between excited levels breakes the assumption of the stationary radial profile of the population distribution. Hence, the partial time derivative in Eq. (3.4) is not zero. On the other hand, the shortness of the laser pulse of $T_\mathrm{L} \sim 20\,\mathrm{ns}$ and the short relaxation times of the excited levels of $\tau_\mathrm{relax} \sim 100\,\mathrm{ns}$ (see Figures 5.14 and 5.15) allow neglecting the transport term in Eq. (3.4). Thus, we can simply employ the Eqs. (3.5) for the source terms by appropriately incorporating the laser impact.

This is done by adding four terms to the set of equations of type (3.5) of the CR model: the stimulated transition rates (excitation and decay) as sources and sinks of the
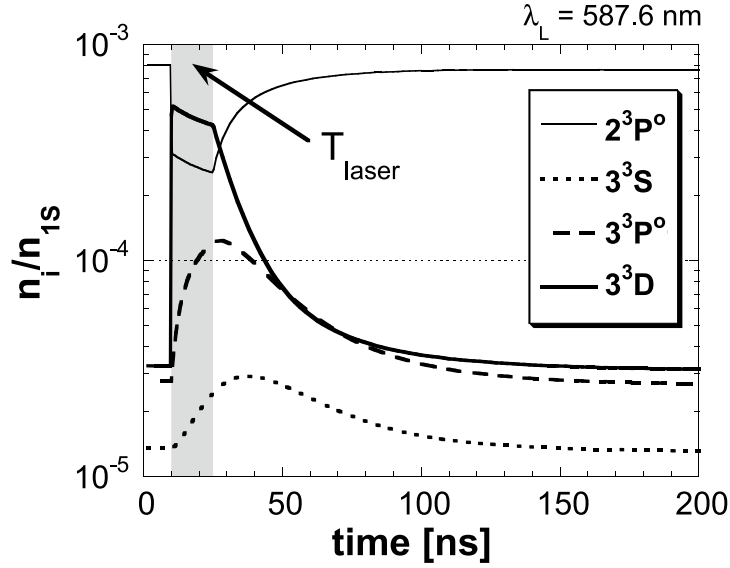
Figure 5.14: The influence of resonance laser radiation with wavelength $\lambda = 587.6$ nm on the populations of selected triplet levels (relative to the ground state). A broadband saturating laser radiation has been assumed, and the Zeeman effect neglected.

population of both levels l and u involved in the laser pumping process:

$$\frac{\mathrm{d}n_{\mathrm{u}}}{\mathrm{d}t} = \frac{\partial n_{\mathrm{u}}}{\partial t} = ... + \rho \mathrm{B}_{\mathrm{l}\rightarrow\mathrm{u}}n_{\mathrm{l}} - \rho \mathrm{B}_{\mathrm{u}\rightarrow\mathrm{l}}n_{\mathrm{u}}$$
$$, \ \rho > 0 \ \text{ for } \ \Delta t = \mathrm{T_L}. \qquad (5.17)$$
$$\frac{\mathrm{d}n_{\mathrm{l}}}{\mathrm{d}t} = \frac{\partial n_{\mathrm{l}}}{\partial t} = ... + \rho \mathrm{B}_{\mathrm{u}\rightarrow\mathrm{l}}n_{\mathrm{u}} - \rho \mathrm{B}_{\mathrm{l}\rightarrow\mathrm{u}}n_{\mathrm{l}}$$

ρ is the spectral power density of the laser radiation and B are the Einstein coefficients for absorption and induced emission (see Eq. (2.2)). We approximate the temporal profile of the laser power with a rectangular function. Similar simulations with emphasis placed on the impact of variation of rate coefficients for the collisional transfer between the $n = 3$ levels on the fluorescence signals can be found in [Hidalgo et al., 2006].

Figure 5.14 shows an example of such a calculation for $n_{\mathrm{e}} = 5 \times 10^{12}\,\mathrm{cm}^{-3}$ and $T_{\mathrm{e}} = 50\,\mathrm{eV}$. The selected laser wavelength of $\lambda = 587.6\,\mathrm{nm}$ corresponds to the triplet transition $2^3\mathrm{P^o}{\rightarrow}3^3\mathrm{D}$. The laser pulse energy of 0.2 mJ is sufficient for the saturation of the pumping process. This becomes evident through the instantaneous increase of the $3^3\mathrm{D}$ population to its maximum after switching on the laser at t = 10 ns as well as through the constant population ratio of the upper and the lower level ($3^3\mathrm{D}$ and $2^3\mathrm{P^o}$) during the laser pulse. Since for this calculation a broadband laser has been assumed this constant ratio is equal to the ratio of the statistical weights (15/9). In fact, however, the pumping process is less efficient, since the spectral width of the laser line falls below the energy spread in the lower level resulting from the Zeeman splitting. A lower population ratio is thus produced at saturation than for the example shown in Figure 5.14 (see also Sec. 5.2). Taking into account the observation geometry and helium density in the beam, one can calculate from this population the expected fluorescence response for
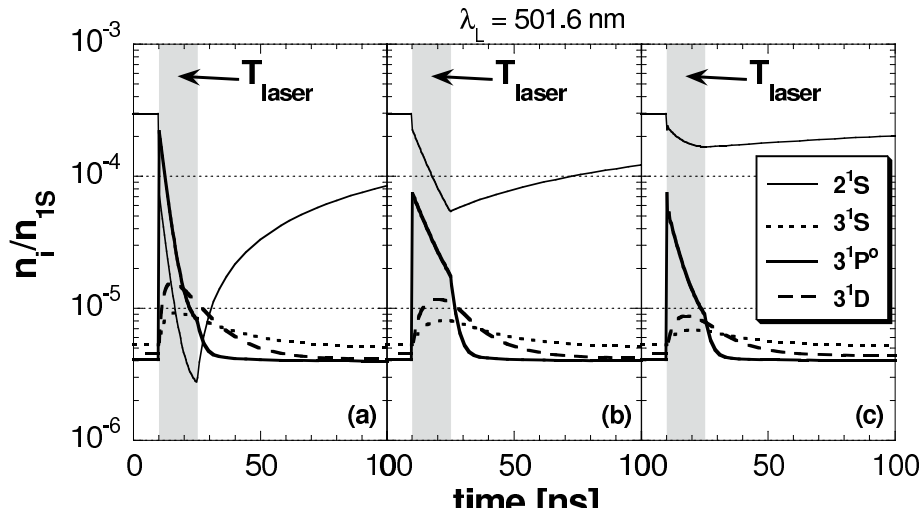
Figure 5.15: Impact of the resonant laser radiation at $\lambda = 501.6\,\text{nm}$ on the population of selected singlet levels (relative to the ground state) calculated with the code based on the CR model for atomic helium; (a): Broadband saturating laser radiation has been assumed, the Zeeman effect is neglected; (b): Real case of a narrow-band laser assumed, and the Zeeman effect is accounted for; (c): Additional correction due to strong radiative losses from the level 3^1P^o is introduced (see explanation in the text).

the experiments on TEXTOR. Its deviation from the measured signal suggests certain weaknesses of the model calculation.

Figure 5.14 also shows a decreasing population of both levels optically involved in the laser pumping process during the laser pulse as well as the increasing population of the other two $n = 3$ triplet levels with some time delay. This is due to collisional population transfer from 3^3D to 3^3P^o and from 3^3P^o to 3^3S as indicated in Figure 5.16. Fluorescence radiation in the visible or near UV spectral range from these levels could be detected as well under some conditions, enabling a check to be made via the simulation procedure of the assumed collisional rate coefficients between the $n = 3$ levels.

Another calculation example is depicted in Figure 5.15. In this case the laser light at $\lambda = 501.6\,\text{nm}$ pumps the transition $2^1\text{S}\rightarrow3^1\text{P}^\text{o}$. In all three cases the upper level population increases instantly after switching on the laser, owing to the strong laser power. The constant population ratio of the upper and the lower level during the laser pulse in case (a) is again equal to the ratio of their statistical weights ($g_\text{u}/g_\text{l} = 3/1$) since a broadband laser has been assumed and the Zeeman effect neglected. In contrast to the pumping scheme shown in Figure 5.14 the instantaneous population increase of the upper level is followed by rapid depopulation arising from the very rapid radiative channel from level 3^1P^o to the ground state. This makes the detection of the fluorescence signal at the laser wavelength very difficult, when additionally considering the spurious impact of the scattered laser light (see Sec. 6.2).

In case (b) a realistic laser spectral width of around half the width of the absorption
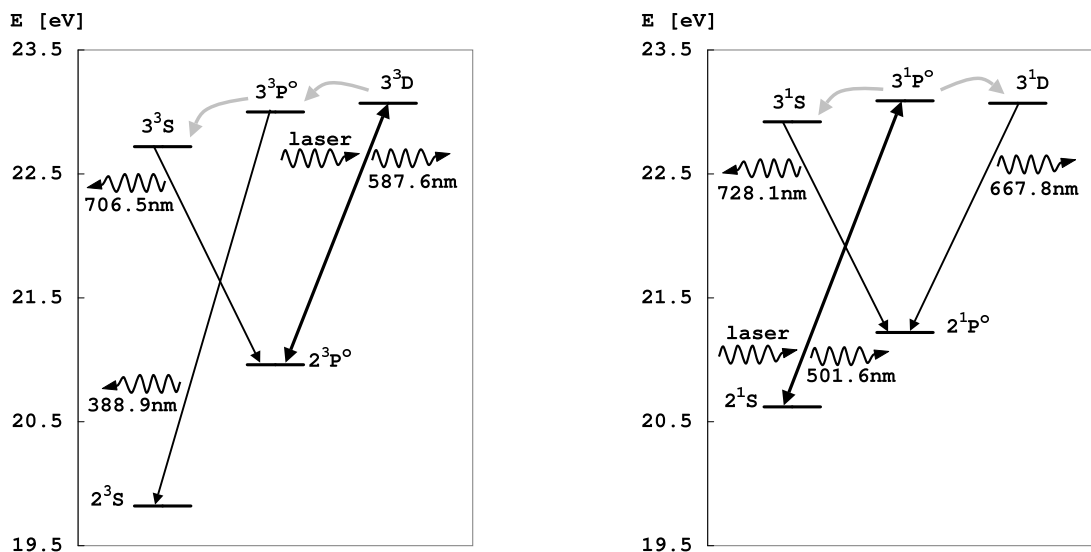
Figure 5.16: Pumping channels for the simulations shown in Figures 5.14 and 5.15. The grey arrows represent the collisional population transfer between the $n = 3$ levels.

line is assumed, which means that only half of the lower level population is subject to the laser interaction. This leads, on the assumption that $g_l = g_u = 1$ (in accordance with the Zeeman effect), to a quarter of the initial lower level population being pumped to the upper level. This can be incorporated in the simulation by introducing effective statistical weights for the upper and lower level, for the duration of the laser pulse, of $g_l = 3$ and $g_u = 1$. However, in the special case of a strong radiative decay of the upper level during the laser pulse, this treatment causes a considerable error in the calculation. Due to the strong radiative losses of the upper level and due to the constant population ratio of the upper to the lower level enforced by the saturating laser power, the lower level 2^1S serves as a population reservoir for the upper level. Its initial population drops almost to zero in case (a) and more than a factor of five in case (b). However, in case (b) only half of the lower level population experiences the laser impact (serves as reservoir) and for this reason its initial population cannot drop below the mark of 50%. This can be reconstructed in the simulation by setting the laser stimulated excitation rate proportional to the remaining reservoir population rather than to the total lower level population. The result is shown in Figure 5.15 (c): the lower level population does not fall below 50% of its initial value and as consequence the upper level is depleted even faster than in case (b), which finally adversely affects the expected fluorescence response at all three wavelengths.

Owing to the existence of the ground state in the singlet system, pumping schemes based on triplet transitions are expected to provide much stronger fluorescence signals. This was the reason why the first measurements on TEXTOR have been performed on triplet transitions.

Chapter 6

Results

In this section, first the results of the absolute measurements of the population densities of the levels from the $n = 2$ shell are presented and discussed. In addition, recorded collision-induced fluorescence signals are analysed to obtain rate coefficients for selected transitions between excited levels. The uncertainties of these LIF measurements are discussed and estimated. In the final sections the radial beam attenuation profiles derived from camera measurements and CR model calculations are compared and discussed as well as a possible method for electron density determination from amplitudes and time traces of laser- and collision-induced fluorescence signals.

6.1 LIF measurements

The time dependent solution of our CR model for given radial profiles of n_e and T_e provides the absolute population density of the considered level at the radial position of the observation if the helium flux entering the plasma is provided as input. The ionisation attenuation of the beam is included in the calculation. The helium flux is known from gas test pulses (Sec. 5.1) and hence the expected number of ground state atoms found in the observation volume. However, this number must be corrected for the divergence the beam experiences in the course of the plasma penetration. This is done by evaluating camera pictures of the beam (see Sec. 5.1).

The absolute population of any considered level can be compared to the measured one gained from the maximum fluorescence signal at the laser wavelength during a resonant laser pulse (see Figure 6.5 (b)). From this signal we obtain the increased population of the upper level due to laser pumping by use of the absolute calibration factor (Sec. 4.4.1). The result of the pumping efficiency simulation (Sec. 5.2) then provides the measured absolute population of the lower level.

The results shown in this section are given as population densities relative to the ground state population. This is because the relative populations characterise the CR model and comparisons with other models can be made more easily. The absolute population densities are strongly dependent on the ionisation of beam particles, hence on the radial position of observation but are not directly of interest unless the signal to noise ratio needs to be derived. They are, however, needed to obtain the experimental populations relative to the ground state population.
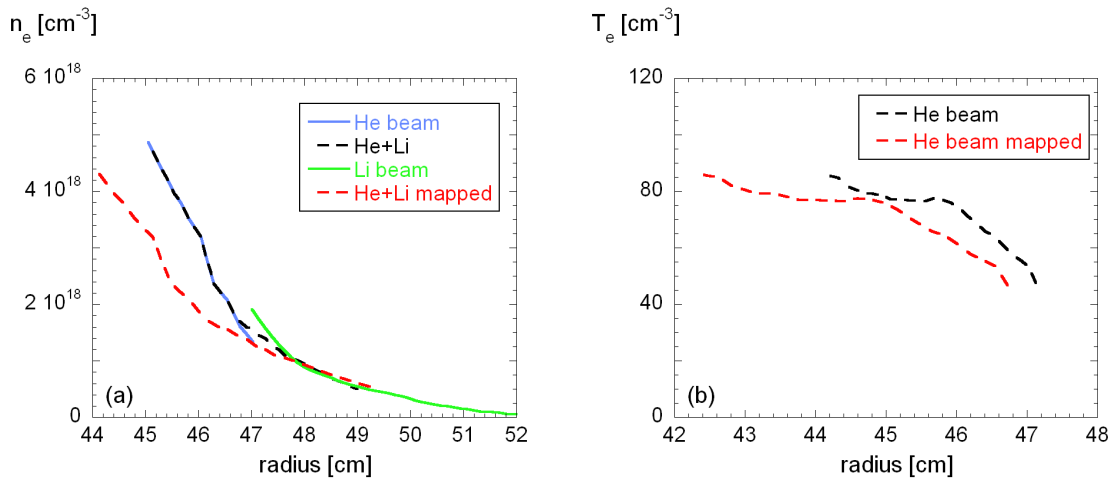
Figure 6.1: Example radial profiles of electron density (a) and temperature (b) measured with a thermal helium and lithium beam. Resulting profiles after mapping of the radial coordinate between the helium/lithium beam position (equatorial plane at the low field side) and our LIF measurement position (below the magnetic axis) are indicated with the red lines. The stretching of those profiles is due to the compression of magnetic flux surfaces at the low field side.

The beam attenuation along its path through the plasma can be quantified in two different ways: by the CR model calculation and by the evaluation of the camera pictures (Sec. 5.1). Since the latter values are based on measurement, they are used in the derivation of the measured relative populations. The measured losses of beam particles can be on the other hand used to check whether the model prediction is correct. This is done in Sec. 6.4.

The radial profiles of n_e and T_e used for the model calculation were measured with a thermal helium and lithium beam in the equatorial plane at the low field side [Schmitz, 2006]. In order to map the measured values to our poloidal position below the magnetic axis the horizontal plasma shift (Shafranov shift) due to finite plasma pressure must be considered. It results in a shift of the magnetic axis (typically $\sim 1\,\mathrm{cm}$) and of the last closed flux surface in the low field direction as well as in a compression of magnetic flux surfaces in the region where the profiles are measured (the compression factor relative to our measurement position is ~ 1.45). The Shafranov shift and the compression factor were calculated by an analytical estimate [Wesson, 1997], which allows to map the plasma parameters in the region of the closed magnetic flux surfaces. They can be also approximately applied to the outer region. This is because of similar short connection lengths along magnetic field lines of both measurement positions to the plasma-limiting component ALT-II (Sec. 4.1). Both positions belong to the downstream region and the radial changes of the plasma pressure can be assumed as being equal.

In Figure 6.1 example profiles of n_e and T_e as functions of the geometric radial coordinate at the low field side are presented. The resulting profiles mapped to our LIF measurement position are shown with the dashed red curves. Their larger radial exten-

tion is due to the compression of the magnetic flux surfaces at the low field side.

6.1.1 Absolute populations of the levels 2^{3}S and 2^{3}P°

Absolute population density of the triplet level 2^{3}S was measured by exciting helium atoms in this level to the level 3^{3}P° with the laser at the wavelength $\lambda_L = 388.9$ nm (Figure 6.6; parts of the Grotrian diagrams of singlet and triplet helium with all transitions between the levels of the shells $n = 2-4$ are provided in the appendix on the pages 158-159). To obtain the population of the level 2^{3}P° an analogue transition 2^{3}P° $\rightarrow$ 3^{3}D at the wavelength $\lambda_L = 587.6$ nm was excited (Figure 5.16 (a)). The populations of the lower levels were derived in a direct way from the maxima of the time traces of the fluorescence response (i.e. during the laser pulse) at the laser wavelength (as the example shows in Figure 6.8 (b)) upon resonant laser pulses (see also [Dinklage, 1995]). The decaying part of those fluorescence signals and signals at wavelengths other than the one of the laser light (Figure 6.8 (a)) – not suffering from the very strong laser stray light – can in principle be used as well [Kornejew, 1996]. However, their dependence on the collisional population transfer rate from the upper level makes the obtained populations sensitive to the accuracy of selected rate coefficients.

The measured populations divided by the ground state population are shown in Figure 6.2. The measurement points are obtained from signals recorded at two radial observation positions ($r = 47$ and $r = 45.5$ cm) during several discharges. The overall measurement accuracy amounts to around a factor of two (see Sec. 6.2).

Some additional transitions (also in singlet helium) were excited but no fluorescence signals at the laser wavelength were detected that would allow for determination of the absolute population of the pumped levels. The transitions are: 2^{1}S $\rightarrow$ 3^{1}P° ($\lambda = 501.6$ nm), 2^{1}S $\rightarrow$ 4^{1}P° ($\lambda = 396.5$ nm), 2^{1}P° $\rightarrow$ 4^{1}D ($\lambda = 492.2$ nm) and 2^{3}P° $\rightarrow$ 4^{3}S ($\lambda = 471.3$ nm). In view of no signal detection upon excitation of the transition 2^{1}P° $\rightarrow$ 4^{1}D no attempt was undertaken to excite another transition starting from the same singlet level 2^{1}P° $\rightarrow$ 4^{1}S ($\lambda = 504.8$ nm, the same dye, see Table 4.1) because of a much lower expected signal-to-noise ratio of this pumping scheme.

The measured populations of the triplet metastable 2^{3}S lie below the model prediction, in the range of 0.5-0.95 of that and within the error bars. A similar result of 0.4-0.7 of the model prediction is obtained for the population density of the level 2^{3}P° apart from two measurement points at $n_e = 1.5 \times 10^{12}$ cm^{-3} and $n_e = 1.95 \times 10^{12}$ cm^{-3} for which the measured population is five times smaller than the model prediction. The deviation of both these measurement points is not understood. It seems also not reasonable in view of one other measurement at very similar density of $n_e = 2 \times 10^{12}$ cm^{-3} delivering a higher 2^{3}P° population by a factor 2.5. The measurement point at $n_e = 3.55 \times 10^{12}$ cm^{-3}, providing a population of this level lying only 30% below the model prediction origins from the same discharge as one of the measurement points in question (at $n_e = 1.5 \times 10^{12}$ cm^{-3}) – they were obtained by simultaneous light detection at the two mentioned radial observation positions (the same is true for the measurement points at $n_e = 1.95 \times 10^{12}$ cm^{-3} and $n_e = 6.1 \times 10^{12}$ cm^{-3}). Thus, the remarkably low measured
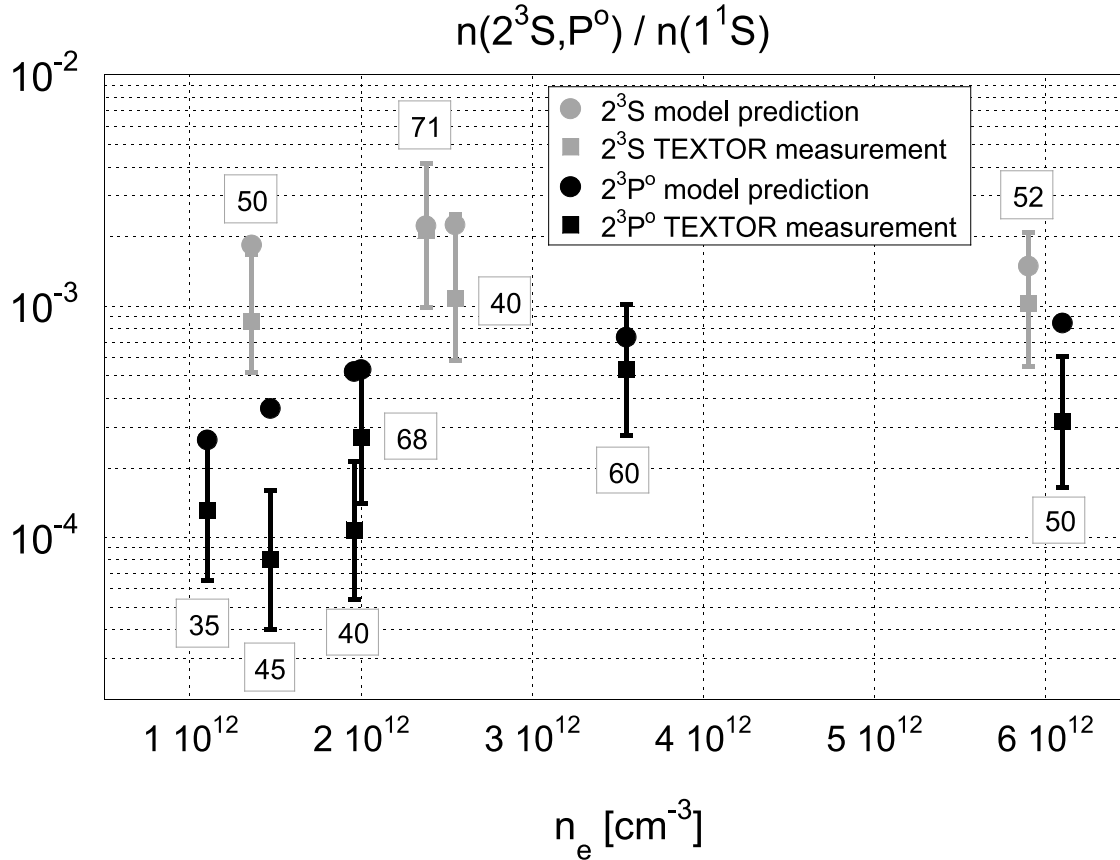
Figure 6.2: Results of the model calculation and measurements of the 2^3S and 2^3P° population (relative to the ground state population). The corresponding electron temperatures are given in boxes.

population at $n_e = 1.5 \times 10^{12}\,\text{cm}^{-3}$ cannot be explained e.g. by a failure of the gas injection, the laser or of the observation system, which would rather affect measurements at both radial points in the same manner. The only explanation, which could hold is an imprecise value of the electron densities at the observation points (this could arise due to imprecise value of the horizontal plasma shift derived from the magnetohydrodynamic equilibrium calculation or due to some errors in the n_e derivation with the helium beam diagnostic). A change of the value of n_e affects the calculated population of triplet levels in the case of our observation point at the radial position of $r = 47\,\text{cm}$ more strongly than of the one at $r = 45.5\,\text{cm}$ because of the lack of the beam relaxation at the outer observation channel. A method to avoid the uncertainty connected to the mapping of the radial positions could be a simultaneous n_e and T_e derivation from helium line intensity ratios by using the line emission of our helium beam at the same radial positions as used for the LIF measurements.

In the following we will discuss possible model corrections, which could reproduce the measured populations relative to the ground state population. In Figure 6.3 it is shown how the model prediction of the relative populations of the levels 2^3S and 2^3P° changes

after lowering of excitation rate coefficients by the factor of five. In plot (a) and (d) the influence of the excitation from the ground state is shown. Only the excitation to one of the two levels of interest causes a considerable, similar drop of their populations by 25-35%. Among the excitation from all other (excited) levels (plots (b-c) and (e-f)) we find only one rate coefficient changing the population by more than 2%. This is the one for the collisional transfer between both considered levels. However, in this case the population lost in the level 2^3P^o ($\sim 60\%$) is shifted to the metastable level such that no lowering of both populations is obtained in this way.
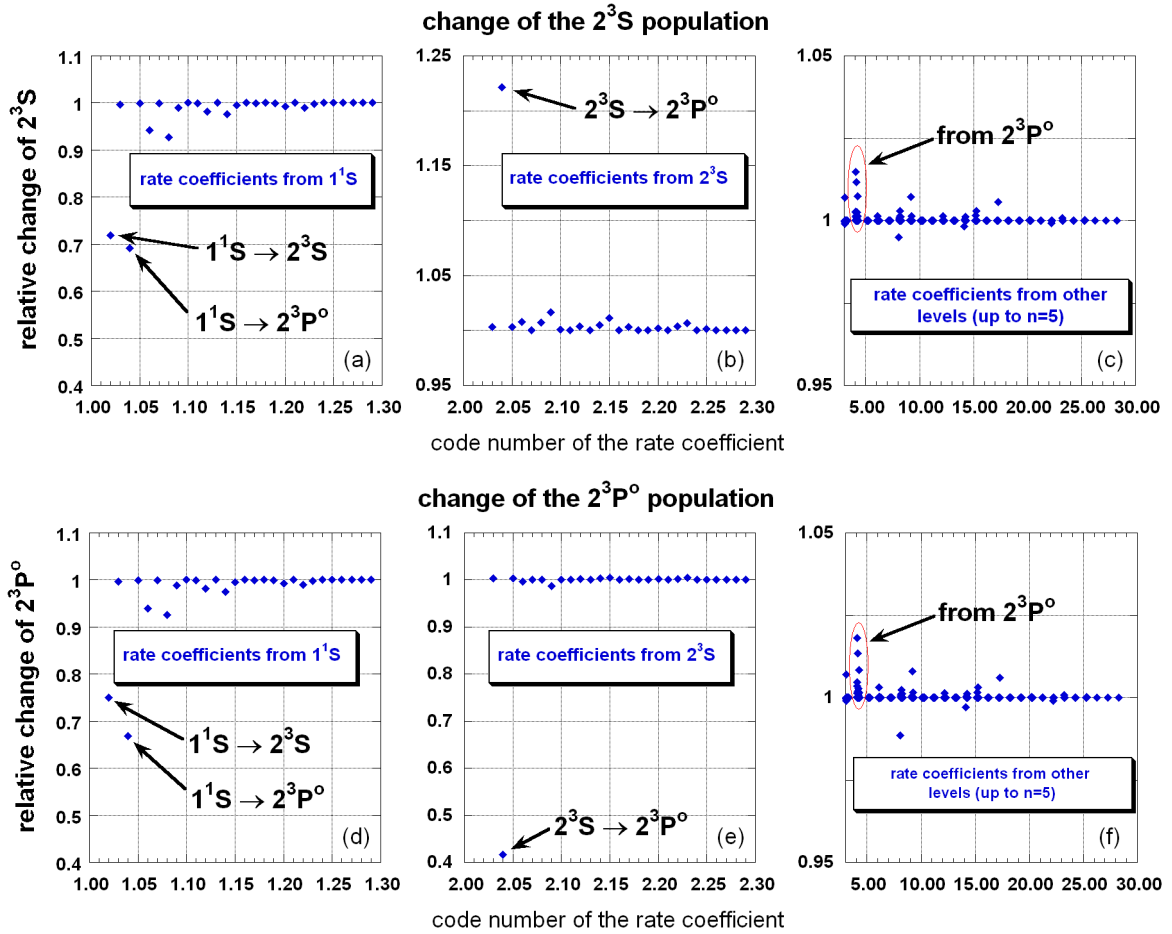

Figure 6.3: Calculated population changes of the levels 2^3S (plots (a)-(c)) and 2^3P^o (plots (d)-(e)) induced by lowering of all rate coefficients – but only one at a time – for electron impact excitation by the factor of five. In plots (a) and (d) the rate coefficients from the ground state, in plots (b) and (e) from the triplet metastable level 2^3S and in plots (c) and (f) from all other levels (up to $n = 5$) are included (the rate coefficients are coded with the number of the lower and the upper level (see Figure 2.16 and the Grotrian diagrams in the appendix, pages 158-159). The rate coefficients causing the largest changes in level populations are indicated separately. The calculation is done for $n_e = 2 \times 10^{12}\,\text{cm}^{-3}$ and $T_e = 50\,\text{eV}$.

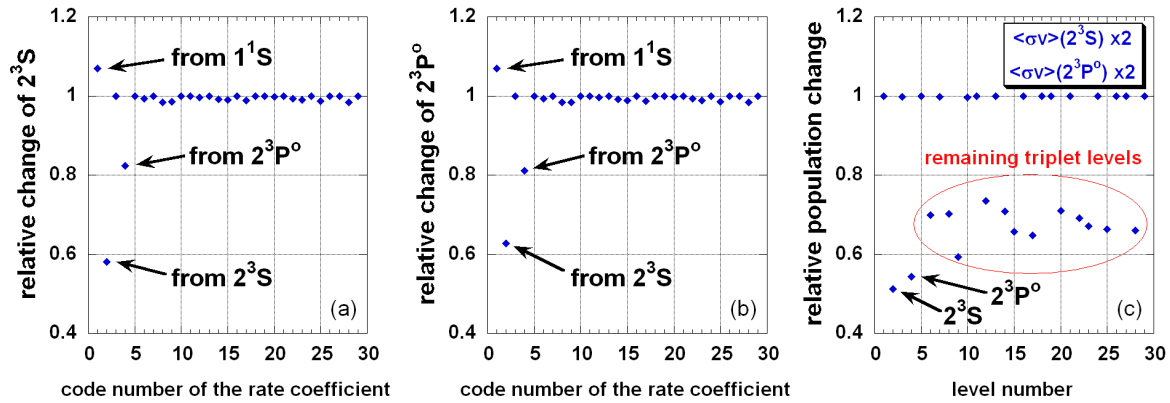Lowering the rate coefficients from all other levels by the same factor of five does not

Figure 6.4: (a-b): Calculated population changes of the levels 2^3S (a) and 2^3P° (b) induced by enhancing of all rate coefficients – but only one at a time – for electron impact ionisation (up to $n = 5$) by a factor of two. The rate coefficients are coded with the number of the level from which the ionisation takes place (see Figure 2.16 and the Grotrian diagrams in the appendix, pages 158-159). The rate coefficients causing the largest populations changes are indicated separately. (c): Calculated population changes of all levels induced by simultaneous enhancing of two ionisation rate coefficients – from the level 2^3S and 2^3P° – by a factor of two. All calculations are done for $n_e = 2 \times 10^{12}\,\mathrm{cm}^{-3}$ and $T_e = 50\,\mathrm{eV}$.

influence considerably the levels 2^3S and 2^3P°. Hence, only decreasing of the excitation rate coefficients from the ground state to both considered levels can provide a significant population drop of these levels in the model calculation (similar result were obtained for the density of $n_e = 6 \times 10^{12}\,\mathrm{cm}^{-3}$). The factor five by which the rate coefficients were lowered was chosen such as to decrease the calculated populations by up to $\sim 50\%$ which follows from the measurements. However, the available excitation data, based on calculations and measurements, are believed to have a much higher accuracy of $\sim 30\%$ [de Heer et al., 1992, Ralchenko et al., 2000] and the lowering the rate coefficients in the model by factor five seems unreasonable.

Another possibility to reduce the model prediction of the populations of the two measured levels is to increase the loss rate of the atoms from these levels, e.g. due to ionisation collisions. We use in our CR model rate coefficients for the electron impact ionisation from the metastable levels provided by Kato and Janev [1992] and from the higher excited levels by Fujimoto [1978], which are up to three times larger than the data recommended by Ralchenko et al. [2000] (see the discussion on this point in Sec. 3.2.1.1). The calculated influence of further enhanced ionisation rate coefficients by a factor of two on the relative populations of the levels 2^3S and 2^3P° is presented in Figure 6.4. The population of both levels is getting lower by similar values of around 40% upon the change of the rate coefficient from the level 2^3S and of 20% in the case of the rate coefficient from the level 2^3P°. Change of any other rate coefficient does not reduce significantly the level population. In Figure (c) the change of the relative populations of all levels is shown, introduced by doubling the values of both mentioned ionisation rate coefficients. The population drop in the case of both levels 2^3S and 2^3P° reaches 50% (all other triplet levels are affected by 20-40%) and hence is equivalent to the average deviation

between the measured populations and those calculated with our standard model (see Figure 6.2). Owing to the mentioned overall discrepancies between calculated ionisation rate coefficients from excited levels (see also the discussion in [Kato and Janev, 1992]) and the lack of measurements, the assumption of an enhanced ionisation from the level 2^3P^o seems to be justified. In contrast, the rate coefficient for the ionisation from the triplet metastable level used in our model is based on measurements of different authors providing the same results in the overlapping energy range. However, enhanced loss rates of excited helium atoms in the beam could be caused by charge exchange collisions with the background plasma ions, which is a current subject of investigation [Brix, 2007].

One could think that the result of enhanced particle losses from the $n = 2$ triplet levels is consistent with the observation of a lower penetration depth of the beam (see Sec. 6.4). However, as discussed in Sec. 6.4, in our parameter range mainly the losses from the ground state determine the beam attenuation rate.

6.1.2 Transition $2^3S \rightarrow 3^3P^o$

6.1.2.1 Signals from the $n = 3$ levels

In another experiment the triplet transition $2^3S{\rightarrow}3^3P^o$ has been pumped with a laser at $\lambda = 388.9\,\text{nm}$ and the fluorescence light as a function of time detected subsequently at three wavelengths according to the three $n = 3$ triplet levels as indicated in Figure 6.6.

Figure 6.5 shows all three signals as measured at the radial position $r = 47\,\text{cm}$ with the plasma parameters, taken from similar discharges: $n_e = 1.35{\times}10^{12}\,\text{cm}^{-3}$ and $T_e = 50\,\text{eV}$. A remarkable difference is observed in the noise level of the measurement in case (c) versus cases (a) and (b). The highest signal-to-noise ratio could be expected in the case (b) of the fluorescence at the laser wavelength. However, the strong impact of the laser stray light – being subtracted by recording the laser pulses without plasma – blinds the observation system leading to a deterioration the signal quality. The higher level of noise at $\lambda = 706.5\,\text{nm}$ (plot (a)) compared to the signal at $\lambda = 587.6\,\text{nm}$ (plot (c)) results from the lower transition rate for the collisional transfer from the level 3^3P^o to 3^3S than to 3^3D, the lower radiative decay probability from the level 3^3S than 3^3D as well as from a lower detector sensitivity at $\lambda = 706.5\,\text{nm}$ than at $\lambda = 587.6\,\text{nm}$.

The signal decay shapes of the three curves depend among other things on the well known radiative decay probabilities. Since the electron density is high enough to induce a population transfer from the level 3^3P^o to 3^3S and 3^3D all three signals will also depend on the electron density and the transfer rate coefficients. In particular the signals in cases (a) and (c) depend mainly only on one rate coefficient: the one for collisional transfer from the level 3^3P^o to 3^3S and 3^3D, respectively. This provides a possibility for the determination of both rate coefficients if the electron density is known, particularly interesting in case (c) in which the high signal purity allows the determination of the rate coefficient with relatively high precision.

First we consider the signal maxima of all three levels. The ratio of the maximum of each collision-induced signal (from the levels 3^3S and 3^3D, Figure 6.5 (a) and (c)) to the signal from the upper level 3^3P^o (Figure (b)) depends on the rate coefficient from the
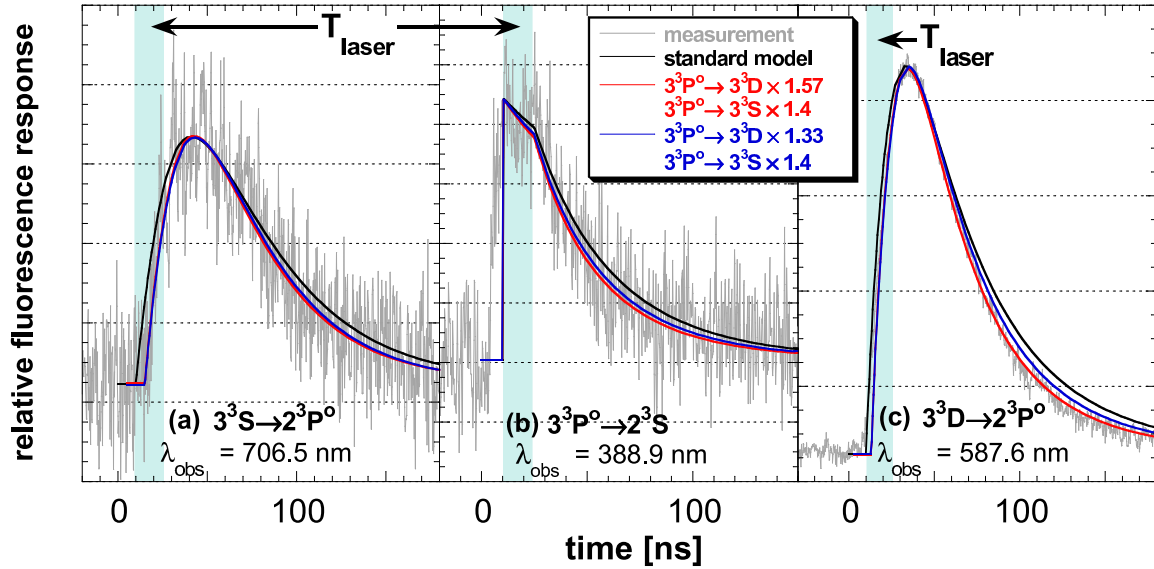
Figure 6.5: Time traces of relative fluorescence signals induced by laser pulses at $\lambda = 388.9\,\text{nm}$ measured at three different wavelengths (originating from all three $n = 3$ triplet levels, see Figure 6.6). Results of the model calculation at enhanced values of two rate coefficients are included.

upper to the considered collisionally populated level and can be also used to determine the rate coefficients in case of noisy signals. From the signal maxima the ratio of the photon fluxes can be derived with an accuracy of around 50%. Comparing the measured ratio with the one resulting from the model calculation provides information on the rate coefficients assumed in the model. The ratios of the measured and calculated signal maxima from the collisionally populated levels and the upper level are:

$$\left(I^{\text{meas}}_{3^3\text{S}} / I^{\text{meas}}_{3^3\text{P}^\text{o}}\right) / \left(I^{\text{calc}}_{3^3\text{S}} / I^{\text{calc}}_{3^3\text{P}^\text{o}}\right) = 1.09$$

$$\left(I^{\text{meas}}_{3^3\text{D}} / I^{\text{meas}}_{3^3\text{P}^\text{o}}\right) / \left(I^{\text{calc}}_{3^3\text{D}} / I^{\text{calc}}_{3^3\text{P}^\text{o}}\right) = 1.30$$

Since in both cases the measured signals originating from the collisionally populated levels exceed the calculated results both rate coefficients assumed in the model need to be increased. The factors by which they must be multiplied to make the calculated signal ratios fit the measured ones are 1.20 and 1.35, respectively.

Let us now again consider the measured time traces shown in Figure 6.5. The purest signal, Figure (c), clearly shows that the time trace calculated with the unchanged CR model (black line) decays too slowly. Two additional calculations are added to the plots. Red lines represent the best fit of the curve shown in Figure (c) in which the rate coefficient $\langle\sigma v\rangle_{3^3\text{P}^\text{o}\to 3^3\text{D}}$ is enhanced by a factor 1.57 and $\langle\sigma v\rangle_{3^3\text{P}^\text{o}\to 3^3\text{S}}$ by factor 1.4. The ratio of both factors (1.12) is chosen such as to match the rate coefficients ratio obtained from the maximum signals (1.35/1.20). Owing to the noise level of the two other measurements it can hardly be decided whether these parameters also provide a better fit to their time traces shown in Figure (a) and (b). The blue curves are a simulation result in which the rate coefficient $\langle\sigma v\rangle_{3^3\text{P}^\text{o}\to 3^3\text{D}}$ was additionally lowered just

Enhanced rate coefficient (2×)	$\frac{\Delta n_{3^3\mathrm{D}}}{\Delta n_{4^3\mathrm{D}}}$
-	5.22
$3^3\mathrm{P^o}$-$4^3\mathrm{D}$	3.5
$3^3\mathrm{P^o}$-$3^3\mathrm{D}$	8.85
$3^3\mathrm{P^o}$-$3^3\mathrm{S}$	5.22

Table 6.1: Dependence of the ratio of the maximum increased populations of the levels $3^3\mathrm{D}$ and $4^3\mathrm{D}$ on doubled rate coefficients for three transitions from the upper level. Calculation is performed for $n_\mathrm{e} = 3.5 \times 10^{12}\,\mathrm{cm}^{-3}$ and $T_\mathrm{e} = 46\,\mathrm{eV}$.

by the factor which results in an unsatisfactory fit. The factor amounts to 15% and hence this is about the accuracy of the rate coefficient, provided all other parameters are known. The change of the rate parameter $\langle \sigma v \rangle_{3^3\mathrm{P^o} \to 3^3\mathrm{S}}$ has a negligible impact on the fit curve.

6.1.2.2 Comparison of CIF signals from the levels $3^3\mathrm{D}$ and $4^3\mathrm{D}$ ($\lambda = 587.6$ and $\lambda = 447.1\,\mathrm{nm}$)

Two experiments have been performed with laser excitation according to the transition $2^3\mathrm{S} \to 3^3\mathrm{P^o}$ in which all parameters were kept constant except for the observation wavelength. The plasma parameters at the observation point ($r = 47\,\mathrm{cm}$) were $n_\mathrm{e} = 3.5 \times 10^{12}\,\mathrm{cm}^{-3}$ and $T_\mathrm{e} = 46\,\mathrm{eV}$.

In one experiment the collision-induced, time resolved signal from the level $3^3\mathrm{D}$ at the wavelength $\lambda = 587.6\,\mathrm{nm}$ and in the other one from the level $4^3\mathrm{D}$ at the wavelength $\lambda = 447.1\,\mathrm{nm}$ has been observed (Figure 6.6). The ratio of the maxima of both signals (photon fluxes) can be derived with an accuracy of about 30% mainly due to the uncertainties in the absolute calibration factors for both observation wavelengths. This ratio depends primarily on the ratio of the rate coefficients from the upper level to both observed levels, i.e. $\langle \sigma v \rangle_{3^3\mathrm{P^o} \to 3^3\mathrm{D}} / \langle \sigma v \rangle_{3^3\mathrm{P^o} \to 4^3\mathrm{D}}$ (the sensitivity of the ratio to a change of some rate coefficients is shown in Table 6.1: a strong dependence on the rate coefficients from the upper level to both observed levels is given; in contrast, the rate coefficient to the level $3^3\mathrm{S}$ has no influence). In this way this ratio assumed in the model can be experimentally validated. It turns out, that the ratio of the measured signals at the radial position of $r = 47\,\mathrm{cm}$ is larger than the calculated one by 20%. The ratio of the measured and calculated signal ratios for the same discharge but another radial position ($r = 45.5\,\mathrm{cm}$, slightly larger temperature $T_\mathrm{e} = 54\,\mathrm{eV}$) amounts to 1.55. From both results a ratio of 1.37 is obtained with uncertainty range of 30%. The ratio of rate coefficients $\langle \sigma v \rangle_{3^3\mathrm{P^o} \to 3^3\mathrm{D}} / \langle \sigma v \rangle_{3^3\mathrm{P^o} \to 4^3\mathrm{D}}$ assumed in the model must be increased by 70% in order to obtain a predicted signal ratio increase of 37%.

Figure 6.7 shows the measured time traces compared with CR model calculation for the fluorescence signals from the levels $3^3\mathrm{D}$ and $4^3\mathrm{D}$. In Figure (a) a calculation is shown

E [eV]

23.5

4³S   4³P°   4³D   4³F°

3³P°   3³D

3³S

447.1nm

22.5

706.5nm   587.6nm
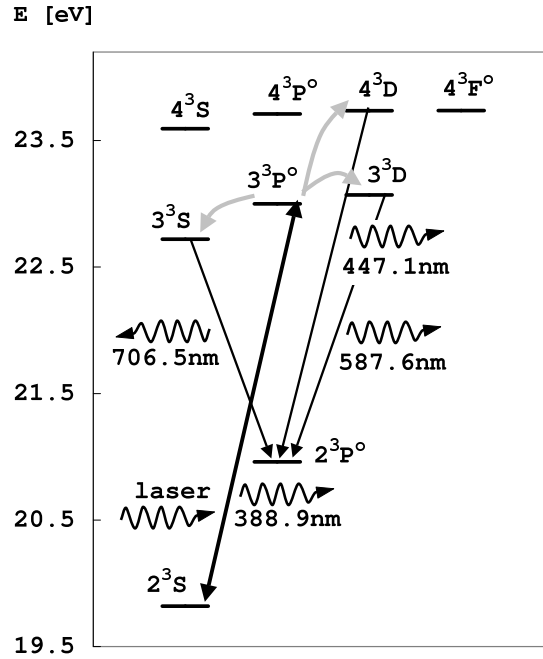
21.5

2³P°

laser   388.9nm

20.5

2³S

19.5

Figure 6.6: Pumping channels for the measurements as shown in Figure 6.7. The grey arrows represent the collisional population transfer between the excited levels.

by using the rate coefficient $\langle\sigma v\rangle_{3^3\mathrm{P}^\circ \to 3^3\mathrm{D}}$ lowered by 35%, which provides a very well fit of the measured curve (black line). Enhancing the rate coefficient from the upper level to the level $4^3\mathrm{D}$ by factor two has no impact on the calculated time trace (red line coinciding with black one). This is because the excitation to this level is a minor loss channel for the population of the upper level. No change is observed if enhancing by the same factor the rate coefficient to the level $3^3\mathrm{S}$ either. In contrast, a doubling of the rate coefficient to the level $3^3\mathrm{D}$ (from factor 0.65 to 1.3, blue line) leads to a considerably lower curve and hence to a poorer fit.

In Figure 6.7 (b) an analogue measurement and calculations are displayed for the case of the fluorescence signal from the level $4^3\mathrm{D}$. The measured curve seems to be characterised by a slightly shorter decay time than the calculation result indicated by the black line. In this case, the shape of the modelled curve shows a weak sensitivity to both rate coefficients: Increase of the rate coefficient $\langle\sigma v\rangle_{3^3\mathrm{P}^\circ \to 4^3\mathrm{D}}$ (red line) as well as $\langle\sigma v\rangle_{3^3\mathrm{P}^\circ \to 3^3\mathrm{D}}$ (blue line) by a factor of two barely alters the curve shape. In fact, a factor five increase is required to achieve a better fit (green line). Hence, no rate coefficient can be obtained from the time trace of this signal with reasonable accuracy.

Due to the insights gained from the time trace shown in Figure (a) as well as from comparison of the maximum signals from the levels $3^3\mathrm{D}$ and $4^3\mathrm{D}$ the conclusion is drawn that for the electron temperature $T_\mathrm{e} = 46\,\mathrm{eV}$ the rate coefficient for the transition $3^3\mathrm{P}^\circ \to 3^3\mathrm{D}$ should be lowered by 35% and the one for the transition to the higher lying level $4^3\mathrm{D}$ lowered by 62%. This is in agreement with an increase of $\langle\sigma v\rangle_{3^3\mathrm{P}^\circ \to 3^3\mathrm{D}} \,/\, \langle\sigma v\rangle_{3^3\mathrm{P}^\circ \to 4^3\mathrm{D}}$ by 70% as derived in the first paragraph of the present section.
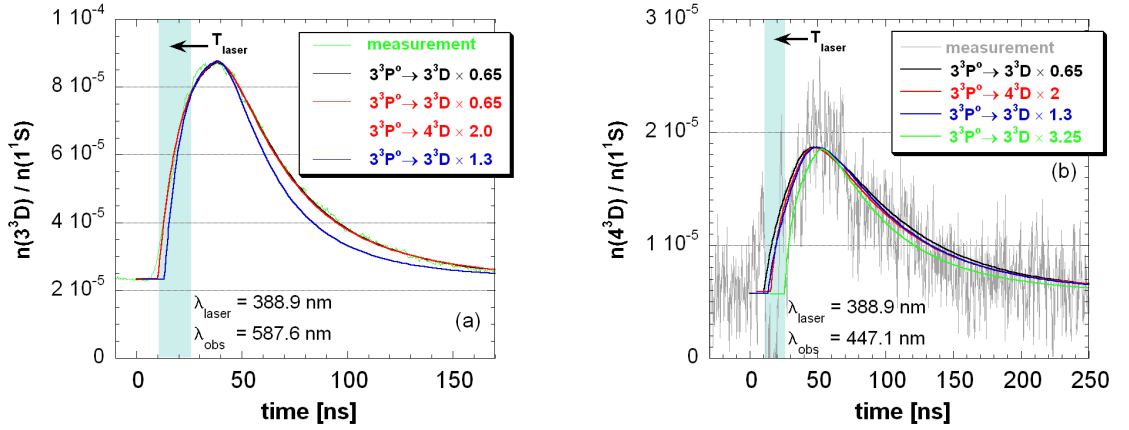
Figure 6.7: Time traces of relative fluorescence signals induced by laser pulses at $\lambda = 388.9\,\text{nm}$ (transition $2^3\text{S} \rightarrow 3^3\text{P}^\text{o}$) measured at two wavelengths: (a) $\lambda = 587.6\,\text{nm}$ (transition $3^3\text{D} \rightarrow 2^3\text{P}^\text{o}$); (b) $\lambda = 447.1\,\text{nm}$ (transition $4^3\text{D} \rightarrow 2^3\text{P}^\text{o}$). Calculation results are included for three cases: assumption of unchanged model as well as of two enhanced rate coefficients.

6.1.3 Transition $2^3\text{P}^\text{o} \rightarrow 3^3\text{D}$

The laser at the wavelength $\lambda_\text{L} = 587.6\,\text{nm}$ excited atoms from the triplet level 2^3P^o to the level 3^3D. The fluorescence was detected at the laser wavelength as well as from the level 3^3P^o at the wavelength $\lambda = 388.9\,\text{nm}$ (see Figure 5.16). Figure 6.8 shows example time traces of signals at both wavelengths. The second fluorescence peak $\sim 40\,\text{ns}$ after the main peak in the signal at the laser wavelength (Figure (b)) was characteristic for this pumping scheme. The reason is probably the stronger pronounced second peak in the power time trace of the dye laser pulses at the considered wavelength than at other wavelengths (Figure 4.4 shows a laser pulse at $\lambda_\text{L} = 388.9\,\text{nm}$).

Since the collision-induced signals at $\lambda = 388.9\,\text{nm}$ show a poor signal-to-noise ratio, their time traces cannot be used for the derivation of the rate coefficient for the transition between the upper and the observed level. However, the maximum signals can still be analysed. Their uncertainty is estimated to a factor of 1.5. In Table 6.2 the results are summarised: listed are the ratios of the maximum collisional signals (from the level 3^3P^o) and the signals from the upper level relative to the calculated ratios. The obtained factors, if larger than one, mean that the measured collision-induced signals are larger than the expected ones from the model calculation and hence the rate coefficient used in the model needs to be enhanced by a slightly larger factor.

Each signal ratio in the table (each line) is obtained from measurements during two different discharges (different observation wavelengths). Thus, the electron temperature and density differ slightly, which is taken into account in the simulation of the signal ratio. The factors obtained are to be attributed to that electron temperature at which the collision-induced signal at $\lambda = 388.9\,\text{nm}$ was measured; however, they are not expected
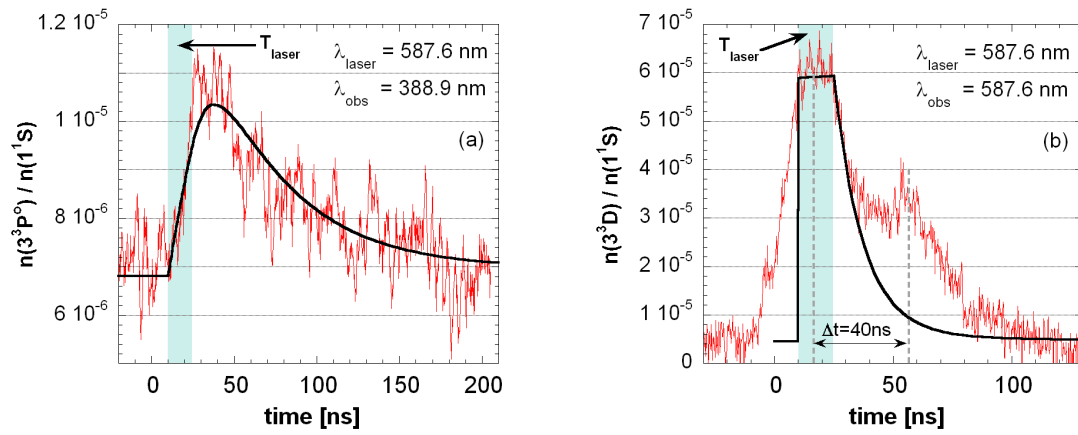
Figure 6.8: Time traces of relative fluorescence signals induced by laser pulses at $\lambda = 587.6\,\mathrm{nm}$ (transition $2^3\mathrm{P}^\mathrm{o} \to 3^3\mathrm{D}$) measured at two wavelengths: (a) $\lambda = 388.9\,\mathrm{nm}$ (transition $3^3\mathrm{P}^\mathrm{o} \to 2^3\mathrm{S}$); (b) at the laser wavelength. Simulated time traces are included.

n_e [10^{12} cm^{-3}] ($3^3\mathrm{P}^\mathrm{o}$, $3^3\mathrm{D}$)	T_e [eV] ($3^3\mathrm{P}^\mathrm{o}$, $3^3\mathrm{D}$)	$\dfrac{I^{\mathrm{meas}}_{3^3\mathrm{P}^\mathrm{o}}/I^{\mathrm{meas}}_{3^3\mathrm{D}}}{I^{\mathrm{calc}}_{3^3\mathrm{P}^\mathrm{o}}/I^{\mathrm{calc}}_{3^3\mathrm{D}}}$
1.25, 1.1	50, 35	1.6
2.2, 2.0	70, 68	1.7
1.1, 1.45	30, 45	3.3
2.55, 1.95	40, 40	0.6
5.9, 6.1	52, 50	1.7

Table 6.2: Deviations between measured and calculated ratios of the maximum fluorescence signals from the collisionally populated $3^3\mathrm{P}^\mathrm{o}$ and the upper level $3^3\mathrm{D}$. The values of n_e and T_e are given for the measurements in which the fluorescence was observed, respectively from the levels $3^3\mathrm{P}^\mathrm{o}$ and $3^3\mathrm{D}$. See text for more details.

to strongly differ for a temperature change of 50%. Hence, all factors can be treated as several measurements of the same factor for the electron temperature $T_\mathrm{e} = 28...65\,\mathrm{eV}$. The resulting factors are all lying in the range 0.6-3.3. Taking the mean value ~ 1.8 results in an enhancement of the rate coefficient $\langle \sigma v \rangle_{3^3\mathrm{P}^\mathrm{o} \to 3^3\mathrm{D}}$ by a factor of 2.15.

The measurements presented in the two last sections 6.1.2 and 6.1.3 provide the value of the rate coefficient $\langle \sigma v \rangle_{3^3\mathrm{P}^\mathrm{o} \to 3^3\mathrm{D}}$ derived in different ways. The most accurate method, relying on the analysis of the time trace of the decaying collision-induced fluorescence at $\lambda = 587.6\,\mathrm{nm}$ provides two values: 157% and 65% of the initially assumed value (taken from [Ralchenko et al., 2000]). The relatively large discrepancy of both results can be only explained by imprecise values of the electron density used in the fit of the measured time traces (the fit accuracy amounts to $\sim 15\%$). The average value from both measurements (110%) coincides well with the value assumed in the model. The rate coefficient obtained from the ratio of the collision-induced signal at $\lambda = 587.6\,\mathrm{nm}$ to the signal at the laser wavelength ($\lambda_\mathrm{L} = 388.9\,\mathrm{nm}$) amounts to 135% of the assumed
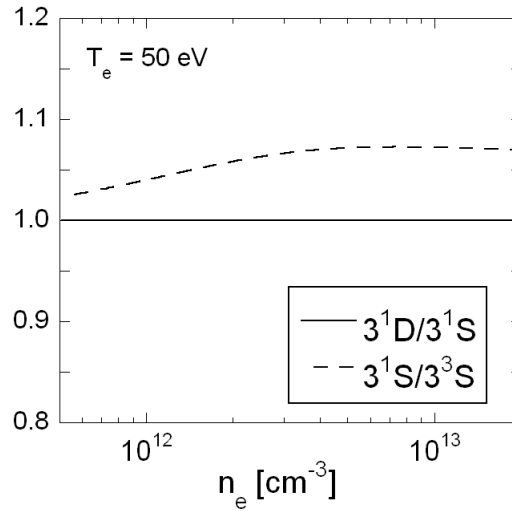
Figure 6.9: Change of the line intensity ratios used for the n_e and T_e derivation resulting from enhancing the rate coefficient $\langle\sigma v\rangle_{3^3P^o\to3^3S}$ by 30% and $\langle\sigma v\rangle_{3^3P^o\to3^3D}$ by 50%.

value. It is similar to the value of 157%, which was obtained from the same discharge series. A higher average value of 215% is, however, obtained from the ratio of the collision-induced signal at $\lambda = 388.9\,\mathrm{nm}$ to the signal at the laser wavelength ($\lambda_L = 587.6\,\mathrm{nm}$). Summarising all the measurements, due to the scattering of the measurement points an interval of 100-200% of the assumed value can be given as the result. It shows an enhanced collisional transfer rate between the levels 3^3P^o and 3^3D. This could be an indication for the contribution of proton impact excitation (the rate coefficient $\langle\sigma v\rangle_{3^3P^o\to3^3D}$ used in the model by Brix [1998] (calculation with the ATOM code using the Born approximation) is only up to 15% larger than the one recommended by Ralchenko et al. [2000] to which the comparison is made).

For the rate coefficient $\langle\sigma v\rangle_{3^3P^o\to3^3S}$ we obtain a value larger by 20-40% than the one assumed in our model calculation (taken from [Ralchenko et al., 2000]). This, again, could support the slightly larger (by up to 15%) rate coefficient used by Brix [1998] or indicate the impact of proton excitation collisions. From the comparison of the collisional signals from the levels 3^3D ($\lambda = 587.6\,\mathrm{nm}$) and 4^3D ($\lambda = 447.1\,\mathrm{nm}$) we concluded that the ratio of the rate coefficients $\langle\sigma v\rangle_{3^3P^o\to3^3D}/\langle\sigma v\rangle_{3^3P^o\to4^3D}$ assumed in our model should be enhanced by 70%. This is approximately done by enhancing the rate coefficient $\langle\sigma v\rangle_{3^3P^o\to3^3D}$ by the factor 1-2, which follows from the measurements of this rate coefficient, such that the rate coefficient $\langle\sigma v\rangle_{3^3P^o\to4^3D}$ remains unchanged. In Figure 6.9 the changes in the calculated line intensity ratios are shown, which result from the enhancing of the rate coefficient $\langle\sigma v\rangle_{3^3P^o\to3^3D}$ by the mean value of 50% and of the rate coefficient $\langle\sigma v\rangle_{3^3P^o\to3^3S}$ by 30% ($T_e = 50\,\mathrm{eV}$ was assumed). There is no effect on the ratio of the singlet lines. The intensity ratio from which the electron temperature is obtained is larger by up to 7%, which is approximately equivalent to the overestimating of the T_e value by the same factor.
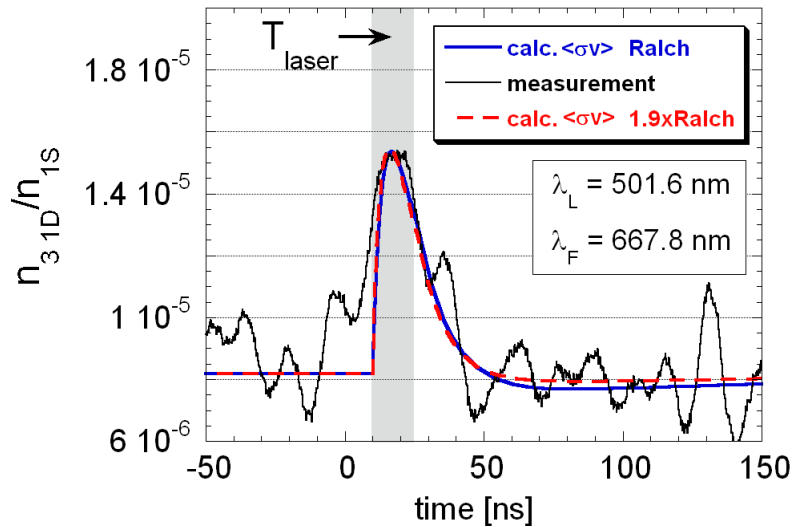
Figure 6.10: Measured and calculated relative time traces (black and blue line, respectively) of fluorescence signal at the transition $3^1D \rightarrow 2^1P°$ ($\lambda = 667.8\,\mathrm{nm}$) upon laser excitation of the transition $2^1S \rightarrow 3^1P°$ ($\lambda = 501.6\,\mathrm{nm}$; the y axis scaling refers to the calculated (blue) curve). For comparison a calculation is added resulting from enlarging the rate coefficient $\langle \sigma v \rangle_{3^1D \rightarrow 3^1P°}$ by the factor of 1.9.

6.1.4 Transition $2^1S \rightarrow 3^1P°$

In this experiment the laser excited atoms from the level 2^1S to $3^1P°$ ($\lambda_L = 501.6\,\mathrm{nm}$, see Figure 5.16 rhs). However, no fluorescence light has been detected at the laser wavelength. This is partially because of the generally lower population of the singlet states at not too high temperatures.[1] The difficulty of signal detection at $\lambda = 501.6\,\mathrm{nm}$ results also from the very rapid radiative channel from the upper level to the ground state ($A_{3^1P° \rightarrow 1^1S} = 5.66 \times 10^8\,\mathrm{s}^{-1}$) leading to a quick depletion of the upper level during the laser pulse (in fact, the population increase after the laser pulse is larger at both other $n = 3$ singlet levels than at the excited level $3^1P°$, see Figure 5.15). Additionally, the A-value of the considered transition is relatively low (nearly five times lower than the A-value of the detected transition at $\lambda = 667.8\,\mathrm{nm}$).

A low collision-induced fluorescence signal has been detected only from the level 3^1D at $\lambda = 667.8\,\mathrm{nm}$. The fluorescence radiation from the level 3^1S was below the detection limit because of a lower A-value, lower collisional transfer rate from the upper level and a lower detector sensitivity. The plasma parameters at the observation point ($r = 47\,\mathrm{cm}$) were $n_e = 3.5 \times 10^{12}\,\mathrm{cm}^{-3}$ and $T_e = 45\,\mathrm{eV}$. No signals at the other observation points were detected. The time trace of the signal averaged over a few resonant laser pulses is shown in Figure 6.10. It is reproduced well by the simulation. The measured signal amplitude is 1.65 (0.9-2.9 including the error bars) times higher than the model prediction and lies

---

[1]However, at low edge densities of $n_e \approx 1 - 2 \times 10^{12}\,\mathrm{cm}^{-3}$ the population of the initial level 2^1S lies due to the lack of the beam relaxation only slightly below the population of the triplet level $2^3P°$, see Figure 3.8.
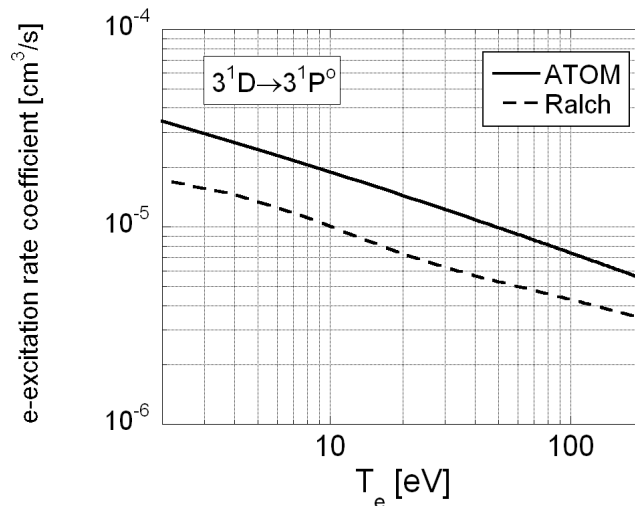
Figure 6.11: Comparison of rate coefficients for electron excitation from the level 3^1D to 3^1P° recommended by Ralchenko et al. [2000] and included in the Brix model (ATOM calculation) [Brix, 1998].

within the error bars. However, it must be emphasised that the predicted signal depends not only on the population of the lower level but also on the rate coefficient between the upper level 3^1P° and the radiating level 3^1D. We used for the calculation the value $\langle\sigma v\rangle_{3^1\mathrm{D}\rightarrow 3^1\mathrm{P}^\circ} = 5.45 \times 10^{-6}\,\mathrm{cm}^3\mathrm{s}^{-1}$ recommended by Ralchenko et al. [2000]. When inserting an almost two times higher coefficient ($\langle\sigma v\rangle_{3^1\mathrm{D}\rightarrow 3^1\mathrm{P}^\circ} = 1.04 \times 10^{-5}\,\mathrm{cm}^3\mathrm{s}^{-1}$) calculated with the ATOM code (Born approximation), as used by Brix in his CR model (Figure 6.11), the ratio of the measured and calculated 2^1S population drops to the factor 0.95 (0.55-1.7 including the error bars) and the measured signal coincides with the model prediction.

However, this single measurement does not allow to distinguish whether the model wrongly predicts the 2^1S level population or whether it includes a too small rate coefficient between the levels 3^1P° and 3^1D. Even if we assume the latter reason, the way of deriving the mentioned rate coefficient from the absolute intensity of the collision-induced fluorescence by increasing the rate coefficient, until the model prediction fits the measured signal, is imprecise due to the large uncertainties in the measured and modelled absolute fluorescence signals (see Sec. 6.2). Some rate coefficients between the levels of the same n shell can be obtained with much higher precision by analysing the time trace of the collision-induced fluorescence signals (see Sec. 6.1.2) if they are not too low. In the considered measurement scheme, however, the time trace of the signal from the level 3^1D shows a very low sensitivity to the rate coefficient for the population transfer from the level 3^1P°. This is demonstrated by additional calculation of the time trace with the rate coefficient enhanced by the factor 1.9, which causes the measured signal to fit the model calculation. The red curve in Figure 6.10 shows the resulting relative time trace. There is no possibility to distinguish which rate coefficient better fits the time trace of the signal. This is again due to the strong radiative decay constant
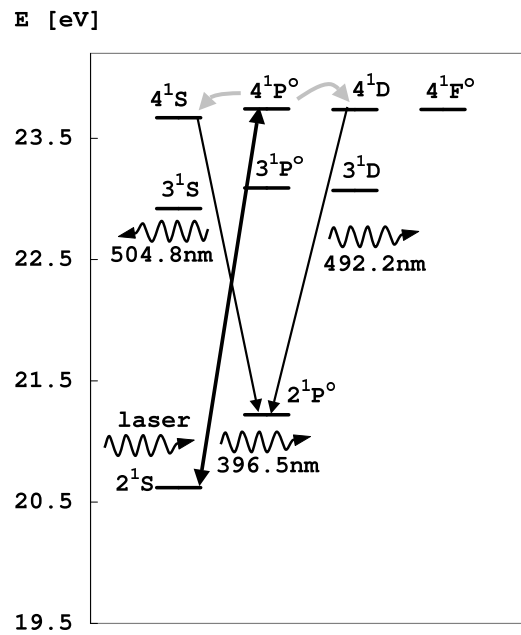
Figure 6.12: Pumping channels for the measurement shown in Figure 6.13. The grey arrows represent the collisional population transfer between the $n = 4$ levels.

from the level 3^1P^o to the ground state. In this sense no statement can be given at which point the model should be changed to fit the experimental result: both explanations as stated above are possible.

To resolve this problem, the value of the rate coefficient $\langle \sigma v \rangle_{3^1\text{D} \to 3^1\text{P}^\text{o}}$ could be measured by exciting the transition $2^1\text{P}^\text{o} \to 3^1\text{D}$ at $\lambda = 667.8\,\text{nm}$ and detecting the fluorescence at the laser wavelength and at $\lambda = 501.6\,\text{nm}$ from the level 3^1P^o. On the other hand, the 2^1S level population could be also measured by exciting atoms from this level to higher lying $n^1\text{P}^\text{o}$ levels. Such a measurement for the case of $n = 4$ has been undertaken and is described in the next section.

6.1.5 Transition $2^1\text{S} \to 4^1\text{P}^\text{o}$

The pumping scheme is shown in Figure 6.12. It is an analogue experiment to that presented in the Sec. 6.1.4 except for the principal quantum number $n = 4$ of the populated level (the corresponding laser wavelength is $\lambda_\text{L} = 396.5\,\text{nm}$). The plasma parameters at the observation point ($r = 47\,\text{cm}$) were $n_\text{e} = 3.8 \times 10^{12}\,\text{cm}^{-3}$ and $T_\text{e} = 42\,\text{eV}$. Only the collision-induced fluorescence signal from the level 4^1D at $\lambda = 492.2\,\text{nm}$ was detected. Signal detection at the laser wavelength here was prevented by difficulties similar to the case described in the previous section.

The time trace of the signal averaged over several resonant laser pulses is shown in Figure 6.13. Its relative shape is compared to the result of our model calculation (blue line) and fits it well. The measured signal amplitude amounts to 0.67 (0.38-1.14 including the error bars) of the model prediction, which lies within the error bars of the
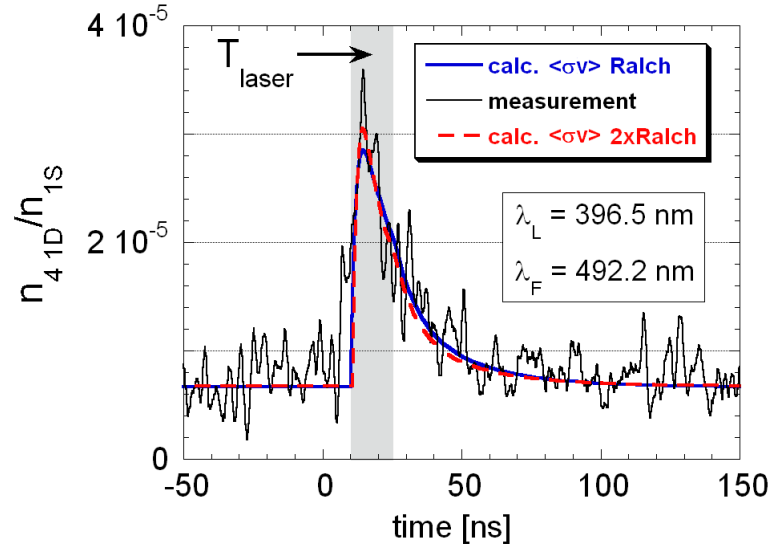
Figure 6.13: Time trace of fluorescence signal detected at the transition $4^1D \rightarrow 2^1P^o$ ($\lambda = 492.2$ nm) upon laser excitation the transition $2^1S \rightarrow 4^1P^o$ ($\lambda = 396.5$ nm). For comparison two calculated time traces are overlaid (the y axis scaling refers to the blue curve). The red curve is calculated after enlarging the rate coefficient $\langle \sigma v \rangle_{4^1D \rightarrow 4^1P^o}$ by factor two.

measurement. Similarly to the experiment described in the previous section, no signal at the laser wavelength was detected and hence there is no direct measurement of the absolute population of the lower level 2^1S. Therefore, since we have two measurements and three unknown values (2^1S population, $\langle \sigma v \rangle_{3^1D \rightarrow 3^1P^o}$ and $\langle \sigma v \rangle_{4^1D \rightarrow 4^1P^o}$), we deal with an under-determined system for which merely some possible solutions can be discussed.

For simplicity we will first treat the result of the fluorescence measurement from the level 4^1D as confirming the model prediction. To explain the too low model prediction of the signal at $\lambda = 667.8$ nm two simple variations of the model parameters can be suggested. First, the rate coefficient $\langle \sigma v \rangle_{3^1D \rightarrow 3^1P^o}$ could be enhanced by a factor ~ 1.9. This appropriately increases the predicted fluorescence from the level 3^1D having no impact on the model prediction of the fluorescence from the level 4^1D (constant model population of the common lower level 2^1S). On the other hand, one could keep the mentioned rate coefficient unchanged and force an increase of the fluorescence from the level 3^1D by changing some other model parameters (e.g. by dividing by two the rate coefficient between the level 2^1S and 2^1P^o) such as to obtain a higher 2^1S population. This, however, also entails an increase of the calculated fluorescence signal from the level 4^1D by 60%, which has to be balanced accordingly by lowering the rate coefficient $\langle \sigma v \rangle_{4^1D \rightarrow 4^1P^o}$ by a factor two. Appropriate combinations of both solutions are of course possible as well.

There are some arguments supporting the first ansatz. The rate coefficient $\langle \sigma v \rangle_{3^1D \rightarrow 3^1P^o}$ used in our calculation (recommended by Ralchenko et al. [2000]) increased by the factor 1.9 is equivalent to the rate coefficient used by Brix [1998] (calculation with the ATOM code based on the Born approximation, see Figure 6.11). Moreover, the
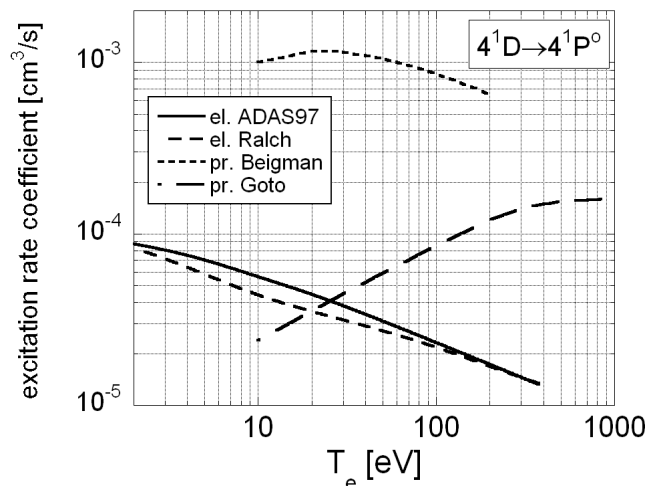
Figure 6.14: Comparison of the rate coefficients from the level 4^1D to 4^1P^o for electron excitation included in the Brix model (ADAS97 dataset) [Brix, 1998] and recommended by Ralchenko et al. [2000] as well as for the proton excitation by Beigman et al. [2003] and Goto and Fujimoto [1997].

population of the singlet metastable 2^1S does not have to be assumed to be higher than our model prediction. Measured absolute populations of the triplet levels 2^3S and 2^3P^o are lower than the model prediction (Sec. 6.1.1). This effect could be caused by loss of helium atoms in the beam due to charge exchange collisions of background plasma ions with excited helium [Brix, 2007]. If so, this mechanism can also affect the singlet metastable level, similarly lowering its population. Finally, in the second ansatz the rate coefficient $\langle \sigma v \rangle_{4^1D \to 4^1P^o}$ must be assumed to be lower than the values found in the compilation of Ralchenko and used by Brix (Figure 6.14). However, the impact of proton collisions on the population transfer between levels of the same n shell is supposed to be stronger with increasing n value. Born calculations by Beigman et al. [2003], shown also in Figure 6.14, which have to be considered as the upper limit provide rate coefficients for proton collisions for the transition $4^1D \to 4^1P^o$ over an order of magnitude larger than for electron collisions in the temperature range of interest. The simple energy scaling law proposed by Goto results in a rate coefficient, which exceeds the electron impact rate coefficient already for temperatures $T \gtrsim 30\,\mathrm{eV}$. Therefore, assuming an even lower collisional rate coefficient than the one due to the electron impact only seems to be an inadequate solution.

If we additionally take into account that the measured signal at 492 nm was lower by 30% than the model prediction, the first solution for the model corrections must be slightly changed: the population of the pumped level 2^1S in the model should be lowered (lowering by 30% of the predicted signal at $\lambda = 492\,\mathrm{nm}$ at unchanged value of $\langle \sigma v \rangle_{4^1D \to 4^1P^o}$) and, in order to keep the signal at $\lambda = 667.8\,\mathrm{nm}$ unchanged, the factor by which the electron impact rate coefficient $\langle \sigma v \rangle_{3^1D \to 3^1P^o}$ is enhanced must lie slightly above the value of 1.9, i.e. this rate coefficient exceeds the larger one of both provided from

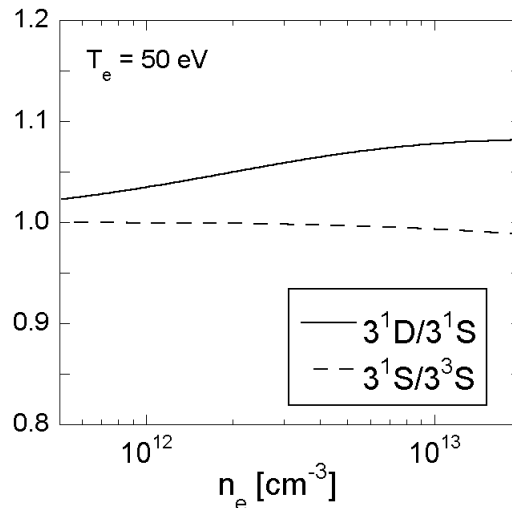Figure 6.15: Change of the line intensity ratios used for the n_e and T_e derivation resulting from enhancing the rate coefficient $\langle \sigma v \rangle_{3^1D \to 3^1P^\circ}$ by factor 1.9.

calculations (Figure 6.14). This could be explained with the proton impact excitation. However, since the proton excitation is expected to play a larger role with increasing value of n this process should be also visible in enhanced collisional population transfer between the levels 4^1D and 4^1P°, which is not included in the solution except if we assume that the rate coefficient $\langle \sigma v \rangle_{4^1D \to 4^1P^\circ}$ already partially consists of the proton impact excitation.

Even if **the first ansatz** (enhancing the rate coefficient $\langle \sigma v \rangle_{3^1D \to 3^1P^\circ}$) **seems to be a more probable way to explain the deviations** between the measured and calculated collision-induced fluorescence signals from the levels 3^1D and 4^1D, no definitive answer can be given to this problem. For this the population of the lower level 2^1S would have to be determined in a direct way by exciting it to one of the n^1P° levels and detecting the fluorescence at the laser wavelength. Similarly to the case described in the previous section no additional information about the rate coefficient $4^1D \to 4^1P^\circ$ is gained from the shape of the time trace of the measured signal either. This is visible in Figure 6.13. The red curve has been calculated under the assumption of a two times larger rate coefficient. It can still fit the measured curve well due to its noise level.

In Figure 6.15 the change of the line intensity ratios used for the derivation of the electron density and temperature in the plasma is calculated assuming an enhanced rate coefficient $\langle \sigma v \rangle_{3^1D \to 3^1P^\circ}$ by the factor of 1.9. An electron temperature of $T_e = 50$ eV (similar to the one at which our fluorescence measurements were performed) was assumed. While the T_e sensitive ratio remains nearly constant, the n_e sensitive ratio increases by up to 8% at higher densities. **This is approximately equivalent to an overestimation of the density by 10-20% depending on the particular density**.

6.2 Uncertainty estimation

In the following the uncertainties of the measurements presented above are quantified. First, all sources of uncertainties are listed, which apply to the derivation of the absolute population of the levels with $n = 2$ from the fluorescence light at the laser wavelengths. Some of the errors cancel in the derivation of rate coefficients from the ratios of collision-induced signals and the fluorescence at the laser wavelength. Further improved accuracy is given if obtaining ratios of rate coefficients by comparing collision-induced fluorescence signal maxima. Finally, the best accuracy is achieved when analysing the time traces of decaying collision-induced signals to obtain the rate coefficient for the transition responsible for the population transfer from the upper to the observed level.

The knowledge of the laser radiation properties is important for a correct signal simulation. The spectral width is here of concern, since the pumped fraction of atoms (the pumping efficiency) depends on it. The width is obtained from measurements on the glow discharge, if existent, and from the fit of the spectral fluorescence profiles measured in TEXTOR to the simulated spectra. The deviations between the spectral widths obtained from both measurements give rise to an uncertainty in this quantity, which results in an uncertainty in the pumping efficiency of up to 30%. However, it enlarges only the upper error bars in a case in which the pumping efficiency already reached its maximum. The pumping efficiency would also have to be enlarged by up to 20-50% in the extreme case of very rapid (on the time scale of the laser pulse length) collisional population redistribution between the magnetic sublevels of the upper level. However, this effect is counteracted by the drop in the effective polarisation factor of the fluorescence light at the laser wavelength (see Sec. 5.2). An increase of only collision-induced signals is expected affecting the rate coefficients obtained from the ratios of collision-induced signals and signals from the upper level.

The temporal profile of the laser pulse energy is not of great importance for the analysis of the maximum fluorescence signal at the laser wavelength (during the laser pulse) since the laser energy is chosen such as to ensure a strong saturation ($S \sim 100$). The disturbance of the decaying fluorescence, as visible in Figure 6.8 (b), is not observed (at least not indicated by the comparison with the modelled signal decay) in the interesting case of collision-induced fluorescence from the level 3^3D at the wavelength $\lambda = 587.6$ nm (Figure 6.7 (a)).

The scattered laser light posed a severe problem when detecting fluorescence at the laser wavelength as usual for 2-level LIF schemes. The fact that the laser beam hit the metallic nozzle for our geometry did not allow for a proper laser dump. The maximum fluorescence signals (during the laser pulse) were in many cases only a fraction of few percent of the total signal. Most probably this issue made it impossible to detect the fluorescence at the laser wavelength when exciting the 2^1S level at the laser wavelength $\lambda_L = 501.6$ nm (Figure 5.16 (b)). Moreover, the high signal amplitudes could result in an onset of the nonlinear response of the photomultiplier. Additionally to the scattered laser light, in few cases unresolved fluctuations of measured signals (from pulse to pulse) were observed enlarging the uncertainty of the maximum signal amplitude up to factor

two.

Another kind of uncertainties concerns the number of atoms in the level pumped by the laser. The ground state atoms abundance in the observation volume is derived from test gas puffs into the torus in absence of plasma (flow rate) and by Abel inversion of camera pictures, which provide information about the degree of the beam attenuation and divergence at the observation point. The accuracy of the flow rate is estimated to 20% and of the attenuation and divergence degree to 20-40% depending on the plasma radius of the observation point. Finally, uncertainties of the plasma parameters n_e (10%) and T_e (30%) have impact on the lower level population (up to 50%; part of this uncertainty is in some cases caused by the lack of population relaxation at lower electron densities) as well as on the collisional transfer rate (10%) from the upper level to other observed levels.

Finally, the absolute calibration of the observation system is characterised by some error level. An uncertainty of up to 50% is assumed for some measurements, which is connected to a drop of the system sensitivity due to progressive coating of the first, in-vessel mirror during plasma operation. A very low light intensity for the wavelengths $\lambda <$ 400 nm of the Ulbricht sphere used to obtain calibration signals results in an uncertainty of 20% of the calibration factors. This is due to the noise level of the calibration signals being only detectable at highest photomultiplier supply voltages of 1000 V whereas some measurements were performed at the voltages 500-700 V. Hence, accurate gain curves for the detectors are needed and their uncertainties influence the TEXTOR measurements. An additional uncertainty results from the fact that the radiation of the Ulbricht sphere collected during calibration measurements was uniform over the observed circular area of diameter 8 mm (1:1 image on the light guides with 8 mm diameter, see Sec. 4.4). This is different in the case of our TEXTOR measurements. The local helium density 4 mm away from the beam axis drops to around 65% at both outermost observation channels (see the local helium distribution profile around the beam axis in Figure 5.8). This can be neglected only under the assumption of uniform sensitivity of the observation system over the whole observed area (see Eq. (4.15) and the comments on that below). Since this was not checked, an estimated uncertainty of 10% is introduced.

All of the uncertainties described above can contribute, if relevant, to the absolute measurement of level populations. On the contrary, some of them are not of concern when analysing ratios of fluorescence signals. In the case of a ratio of a collision-induced signal to a signal from the upper level the uncertainty of the pumping efficiency (laser spectral width) applies approximately in the same way to both signals and therefore cancels. The same holds for the number of observed atoms (beam attenuation and divergence, helium flow through the nozzle) as well as for the sensitivity dependence across the observed area. When comparing two collision-induced signals the uncertainty connected with the collisional population redistribution between the magnetic sublevels cancels and, on the other hand, the laser stray light does not pose a problem. Finally, when deriving the rate coefficients from the time traces of collision-induced fluorescence, only relative signal intensity is of interest and the only remaining parameter, which considerably influences the derived value of the rate coefficient is the electron density if

the proton impact excitation is neglected.

6.3 Derivation of the electron density from laser- and collision-induced fluorescence signals

As can be seen in Figure 6.5 (c) a very pure time trace of the collision-induced fluorescence signal at the wavelength $\lambda = 587.6\,\text{nm}$, upon the laser excitation at the wavelength $\lambda_{\text{L}} = 388.9\,\text{nm}$, can be obtained. The decay shape of this signal depends mainly on the collisional transition rate between the upper level 3^3P° and the level 3^3D from which the collisional fluorescence is observed. The transition rate is given, provided only electron collisions play a role, by the product of electron density and the rate coefficient. Thus, at known electron density the collisional rate coefficient can be obtained for a given electron temperature with an accuracy of $\sim 15\%$. On the other hand, once the rate coefficient has been determined, the decaying fluorescence signal at $\lambda = 587.6\,\text{nm}$ can be used to derive the local electron density.

Measurements of electron densities in low temperature plasmas performed by use of similar pumping and observation schemes have been reported. Chall et al. [1985] measured $n_{\text{e}} \approx 5 \times 10^{12}\,\text{cm}^{-3}$ from the time decay rate of the fluorescence signal at the laser wavelength at $\lambda = 587.6\,\text{nm}$ in an argon arc plasma of $T_{\text{e}} \approx 0.4\,\text{eV}$ with small admixture of helium. Similarly to the way we obtained e.g. the rate coefficient $\langle \sigma v \rangle_{3^3\text{D} \to 3^3\text{P}^\circ}$ in Sec. 6.1.3 from fluorescence intensity ratio, the electron density in the range $n_{\text{e}} = 10^{11} - 10^{12}\,\text{cm}^{-3}$ in a helium plasma of $T_{\text{e}} \approx 5\,\text{eV}$ was determined by Tsuchida et al. [1983] from the ratio of time integrated collision- ($\lambda = 667.8\,\text{nm}$) and laser-induced fluorescence signals upon the laser excitation at $\lambda_{\text{L}} = 501.6\,\text{nm}$ (see Figure 5.16 rhs). Shcheglov et al. [2006] determined electron densities of $n_{\text{e}} \approx 5 \times 10^{11}\,\text{cm}^{-3}$ in an argon plasma ($T_{\text{e}} \approx 10\,\text{eV}$) with helium content using relative collision-induced signals $I_{388.9\,\text{nm}}/I_{706.5\,\text{nm}}$ upon laser excitation at $\lambda_{\text{L}} = 587.6\,\text{nm}$ (Figure 5.16 lhs).

For the case of higher temperatures and densities of edge fusion plasmas it is suggested to use the time trace of the collision-induced fluorescence signal at $\lambda = 587.6\,\text{nm}$ upon laser excitation at $\lambda_{\text{L}} = 388.9\,\text{nm}$. The high signal-to-noise ratio results from the relatively high population of the triplet metastable in our parameter range (see Figure 3.8) and a larger rate coefficient for the collisional transition to the observed level 3^3D than e.g. in the opposite direction (Eq. (2.25)). Moreover, thanks to the wavelength difference between the laser light and the observed fluorescence, the stray light of the laser does not blind the detectors.

In Figure 6.16 we see the time trace of the collision-induced fluorescence from the level 3^3D measured at the wavelength $\lambda = 587.6\,\text{nm}$ resulting from the laser excitation of the transition $2^3\text{S} \to 3^3\text{P}^\circ$ ($\lambda_{\text{L}} = 388.9\,\text{nm}$) as well as the best fit requiring lowered rate coefficient $\langle \sigma v \rangle_{3^3\text{P}^\circ \to 3^3\text{D}}$ by 35% (the electron density of $n_{\text{e}} = 3.5 \times 10^{12}\,\text{cm}^{-3}$ provided by the helium beam diagnostic was assumed). Two additional calculated time traces are added for a slightly increased and decreased value of the electron density. It is seen that the both curves are significantly different from the initial calculation. Hence, the
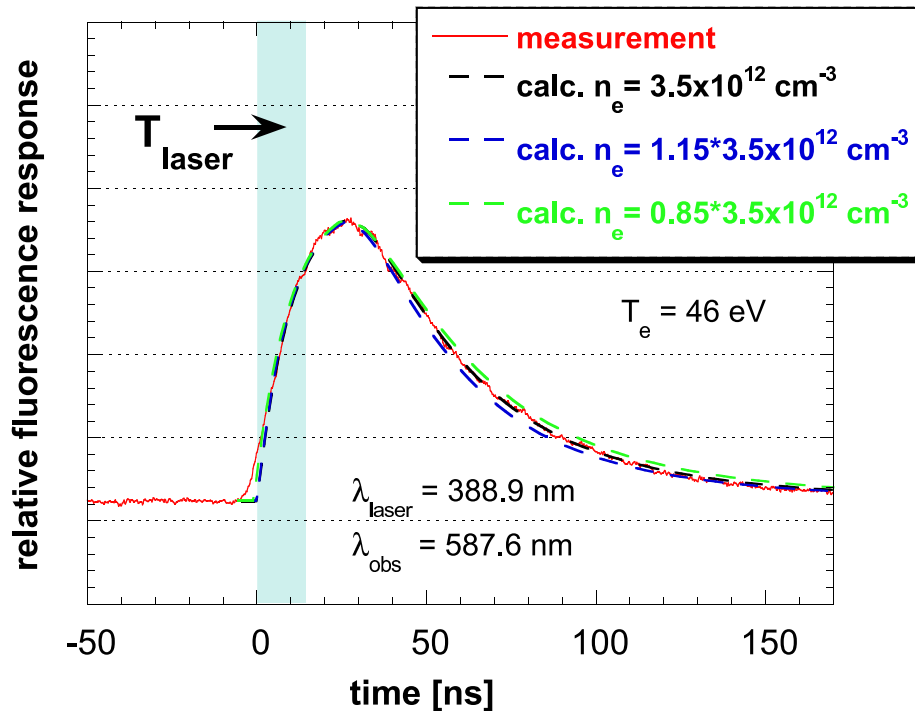
Figure 6.16: Best fit of the measured collision-induced fluorescence signal time trace originating from the level $3^3\mathrm{D}$ ($\lambda = 587.6\,\mathrm{nm}$) upon the laser excitation at $\lambda_\mathrm{L} = 388.9\,\mathrm{nm}$. Two additional fits are overlaid obtained by enhancing and lowering the electron density by 15%.

derivation of n_e with an accuracy of 15% should be possible in this way, provided the value of the mentioned rate coefficient is known with sufficient accuracy.

The sensitivity of the decay shape of the considered collision-induced signal to the change of electron density will of course depend on the density itself and on the temperature. In Figures 6.17 and 6.18 simulations of the time traces of the fluorescence signals at the laser wavelength $\lambda = 388.9\,\mathrm{nm}$ as well as at $\lambda = 587.6\,\mathrm{nm}$ for five different pairs of n_e and T_e are shown. In Figure 6.17 (a) the signals are rescaled to the maximum value and shifted in time such that the maximum signals appear at the same time point. It is done in this way in order to be able to compare the signal shapes starting approximately from the maximum (which is after the end of the laser pulse) since they are then independent from the temporal profile of the laser power. Considerable shortening of the decay times is visible with increasing parameter values (this is because the excessive upper population finds with increasing collisional transfer to the other $n = 3 - 4$ triplet levels additional decay channels to the levels of the $n = 2$ shell). The method becomes more sensitive when fitting the whole time traces including the rising edges. This can be done if the temporal profile of the laser saturation parameter (i.e. also the spatial distribution of the spectral laser power density at the observation volume) is known since it will influence the rising part of the fluorescence profile. However, this requires additional calibration and adjustment effort.

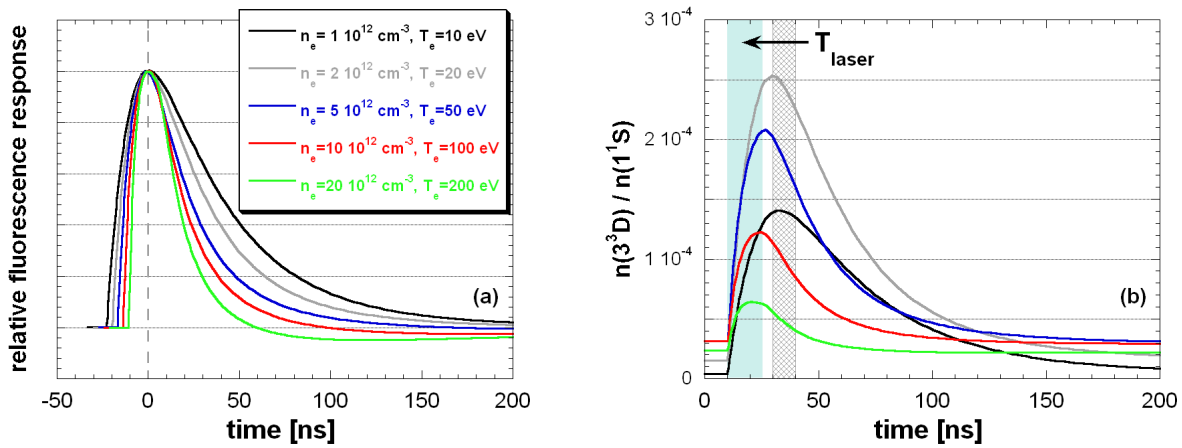The maximum signal amplitudes of both signals at the laser wavelength and the one

Figure 6.17: Simulation of the relative fluorescence response at $\lambda = 587.6\,\text{nm}$ as a result of a laser pulse at $\lambda = 388.9\,\text{nm}$ performed for five different pairs of (n_e, T_e). (a) Resulting curves rescaled in the amplitude and shifted in the time according to the maximum; (b) Resulting curves without rescaling and shift in time.

induced by collisions are strongly correlated to the initial population density of the lower level 2^3S, which has a maximum at electron temperatures of $T_e \cong 20 - 50\,\text{eV}$ depending on the value of n_e (see the quasi-steady state populations in Figure 3.8). This is demonstrated for the collision-induced signal in Figure 6.17 (b) and for the signal at the laser wavelength in Figure 6.18 (a) – the values of population densities relative to the ground state population are plotted without rescaling. The population increase is getting lower for $T_e > 20\,\text{eV}$. Hence, at higher temperatures the signals will become poorer and the fits less reliable. In this case additional analysis of the ratio of the time integrated laser- and collision-induced fluorescence signals can be applied [Tsuchida et al., 1983]. (From the experimental point of view this additional measurement would require a spatial separation of fluorescence photons at both wavelengths e.g. by a beam splitter and simultaneous recording of both signals by two relatively calibrated detectors; absolute signal measurement connected with severe experimental effort and additional uncertainties is not necessary). In Figure 6.18 (b) the time dependent ratios of the collisional- and the laser-induced fluorescence signals for the same pairs of n_e and T_e are plotted. The grey box indicates a possible integration time interval of the signal after the end of the laser pulse (including the signals during the laser pulse would increase the signal-to-noise ratio provided the laser stray light can be sufficiently surpressed). As we see in Figure 6.18 (b) the signal ratio reveals a pronounced dependence on the chosen plasma parameters.

However, there are some limitations to the derivation of the electron density as described above. The collisional transfer rate between the level 3^3P^o and 3^3D depends explicitly on the electron density and the rate coefficient, which is a weak function of electron temperature. It drops by a factor of two with a temperature change from 20 to 200 eV. Though a corresponding increase of the electron density by a factor of ten has a much stronger impact on the transfer rate – it increases by the same factor of ten,
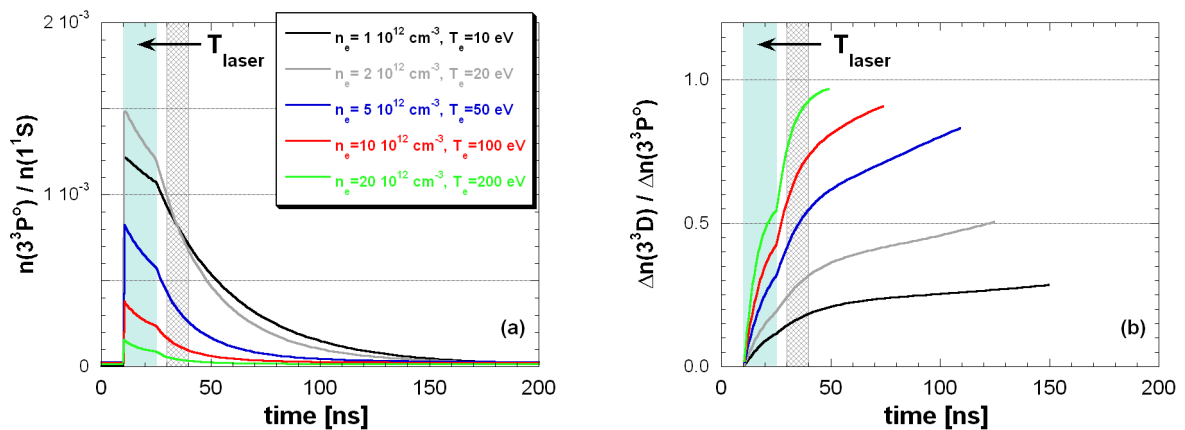
Figure 6.18: (a) Calculation of the relative fluorescence response at the laser wavelength as a result of a laser pulse at $\lambda = 388.9$ nm performed for five different pairs of (n_e, T_e); (b) Calculated ratio of the collisional- and laser-induced fluorescence signals upon the same laser pulse as in (a).

the consequence is that the electron density cannot be determined from the fluorescence signal without a certain knowledge of electron temperature. Additional simulations have shown that for a desired accuracy of the n_e measurement of 10%, T_e must be known with an accuracy of 30-40%, depending on n_e and T_e. For this reason this method makes sense only if accompanied by another diagnostics and the use of the passive radiation method of atomic helium based on the building of line intensity ratios naturally seems to be the first choice because of the intrinsic necessity for the existence of neutral helium in the observation volume of the LIF diagnostics.

Another limitation is the noise level of the fluorescence signals. When using a thermal or supersonic helium beam as neutral helium source the helium density will decrease along the beam path towards the plasma centre due to ionisation processes up to a complete vanishing of the beam. Hence, a similar intrinsic radial limitation of the measurement method appears as in the case of the n_e and T_e derivation from line intensity ratios on helium beams. A possible signal enhancement could be brought e.g. by the use of a laser with a larger spectral width covering the whole Zeeman structure or, better, by light collection over the whole toroidal extension of the diverging helium beam. On the other hand, the number of laser pulses for signal averaging can be increased. The time trace shown in Figure 6.16 was averaged over 20 pulses. At a laser repetition frequency of 150 Hz such a measurement takes 0.13 seconds. However, a single sample takes only few hundred nanoseconds. This is seen in Figures 6.17 (b) and 6.18 (a). After two hundred nanoseconds the laser-perturbed level populations are nearly relaxed i.e. their initial values are again established and the system is in principle ready for the next sample. The use of a dye laser provides very large saturation parameters of $S \gg 1000$ in the visible spectral range so that one laser pulse could be divided in several subpulses with still enough power density. The subpulses would additionally have to be delayed each one by a time interval of $t_{delay} \gtrsim 200$ ns. Averaging the fluorescence signals upon

the subpulses would preserve the signal-to-noise ratio of the case when using several undivided pulses and reduce the measurement time to a few microseconds.

6.4 Penetration depth of the beam

In order to compare the measured and modelled absolute populations of excited levels (or – by dividing them by the ground state population – the relative ones, as they were shown in Sec. 6.1.1) the abundance of ground state helium in the observation volume must be known. This quantity is provided by our model calculation, since ionisation processes are therein included (Sec. 3.2.1.1). However, the simulated absolute population densities rely of course on the accurate prediction of the beam attenuation. To avoid this additional source of uncertainty, we experimentally obtain the beam attenuation from 2D pictures of the beam emission recorded with a camera. The relation between the beam emission and its attenuation as well as example results are described in Sec. 5.1. In this section we compare the attenuation curve measured in this way with the result of our CR modelling.

In order to obtain the radial beam attenuation profile we use radial profiles of the beam emission derived by toroidal integration of the recorded light intensity at a given radial position (Sec. 5.1). This light intensity is a measure of the ionisation losses from the ground state $(\mathrm{d}n_1(r,t)/\mathrm{d}t)$. Thus, according to Eq. (5.4) the derived radial attenuation profile depends on the assumed radial profile of the beam velocity[2]. In Figure 6.19 (a) three attenuation profiles derived from one measurement upon various assumptions are shown with thin solid lines. The red and green lines were obtained under the assumption of a radially constant beam velocity. For the derivation of the green line in Figure (a) only the central radial range of the beam emission of $\pm 1.3\,\mathrm{mm}$ was considered. The resulting beam attenuation occurs considerably faster than the one in which the whole beam emission was considered (thin red line). This is because those beam atoms, which escape from the central range during plasma penetration do not contribute to the considered 'ionisation signal' at smaller radii and hence the apparent ionisation shifts towards the plasma edge. The thin blue profile was obtained under the assumption of a linearly increasing beam velocity towards the plasma centre. It results again in derivation of a faster beam attenuation.

Two calculated beam attenuation profiles are additionally indicated in Figure 6.19 (a) (Figure (b) depicts the radial profiles of n_e and T_e assumed in the calculations). In one calculation (red line) a constant beam velocity of the value as measured at the radial position $r = 47\,\mathrm{cm}$ was assumed. A deeper calculated beam penetration is obtained for increasing velocity with plasma penetration following from the measured shift of the maximum fluorescence (Sec. 4.3.2). In the calculation of the blue profile a linearly increasing beam velocity was assumed: the measured velocities of $v_\mathrm{beam} = 1.53\,\mathrm{km/s}$ and $1.91\,\mathrm{km/s}$ at the radial positions $r = 47\,\mathrm{cm}$ and $45.5\,\mathrm{cm}$, respectively, are fit by a

---

[2]Since thermal helium beams are not monoenergetic an increasing beam velocity towards the plasma centre is expected; this is also supported by our LIF measurements, see Sec. 4.3.2
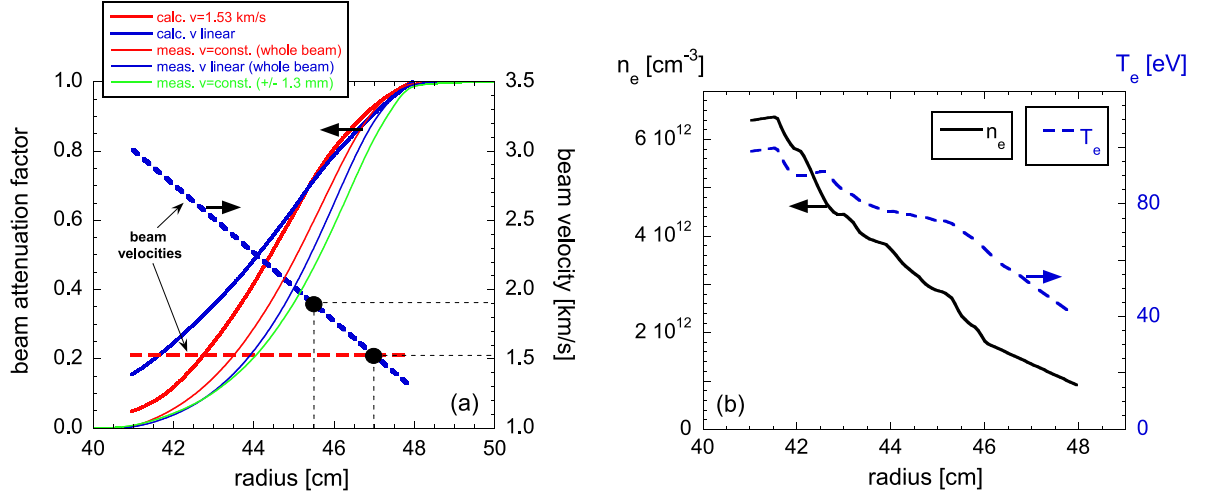
Figure 6.19: (a) Comparison of measured (thin lower solid lines) and calculated (thick solid lines) attenuation profiles. The dashed blue line shows the linear beam velocity assumed in deriving the calculated and measured curves (result indicated with solid blue lines) based on two measurement points indicated with two dots. In another case (solid red lines) the beam velocity was kept constant at the lower measured value of $v_{\mathrm{He}} = 1.53\,\mathrm{km/s}$ (dashed red line); (b) Profiles of electron density and temperature assumed in the calculation. See text for more details.

linear function (dashed blue line). Summarising, we obtain as a result calculated beam penetration, which is larger than the one derived from the measurement independently of the assumed beam velocity profile. The radial displacement reaches $\sim 20\,\mathrm{mm}$ in the case of the linear velocity profile (suggested by LIF measurements) and is smaller ($\sim 7\,\mathrm{mm}$) for the constant velocity. Owing to the velocity profile dependence of the simulated and measured beam attenuation a measurement on a (nearly) monoenergetic supersonic beam would be desirable for a reliable quantitative analysis.

Figure 6.20 shows the sensitivity of the calculated attenuation to changes of some further parameters. A linear velocity profile was used again for the calculations as well as for the derivation of the measured attenuation profile. Only slight influence on the calculated profile was observed after enhancing the n_e or T_e values to their upper error bars of 110% and 130% (shown in Figure (a)) as well as when changing the horizontal plasma shift by $\pm 2\,\mathrm{mm}$. Other calculation parameters, which effect the modelling of the beam attenuation are the ionisation rate coefficients assumed in the model. However, as already stated in Sec. 5.1, for the relatively large electron temperatures $T_e > 40\,\mathrm{eV}$ the main ionisation losses take place from the ground state (in Figure 6.21 for example we see that the cross sections for electron impact ionisation from the metastable levels are larger than the ones from the ground state only by factor < 30; quantitative comparison of ionisation losses from different n shells is given in [Brix, 1998]). Indeed, replacing all rate coefficients for the ionisation from the excited levels by the values recommended by Ralchenko et al. [2000], which are smaller by factor 2-3 than those used in our model, does not influence the calculation result at all. Therefore, a strong influence of the
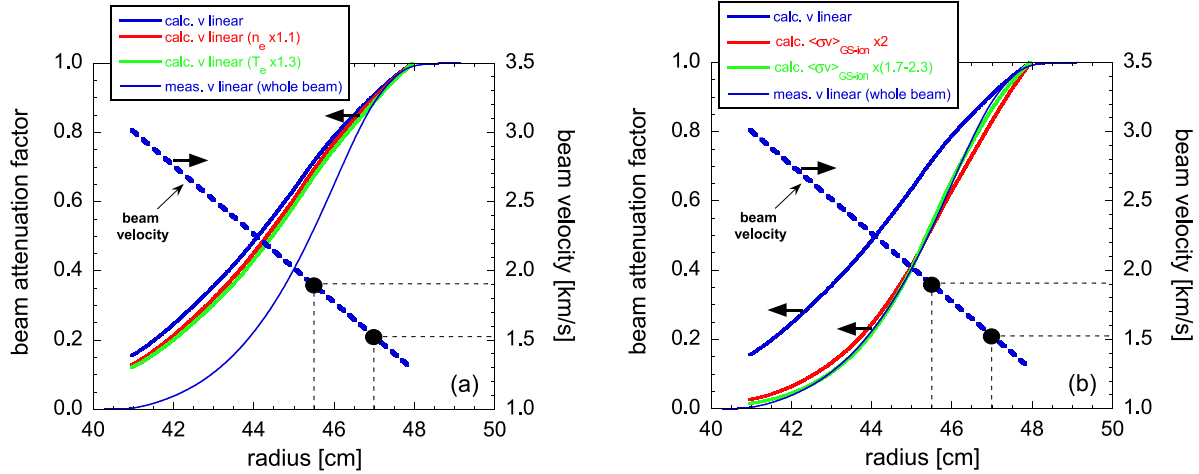
Figure 6.20: Modelling of the measured beam attenuation (thin blue line) assuming a linear beam velocity profile (dashed blue line); thick solid blue line-standard model; (a) red line-n_e enhanced by 10%, green line-T_e enhanced by 30%. (b): red line-$\langle\sigma v\rangle_{1^1S\to ion}$ doubled; green line-$\langle\sigma v\rangle_{1^1S\to ion}$ enhanced according to Figure 6.21.

ionisation from the ground state is expected. The enhancement of this rate coefficient by factor 2.0 was necessary to shift the calculated curve (red line in Figure 6.20 (b)) to the radial position of the measured one (thin blue line). (A smaller factor of 1.5 results if assuming a constant beam velocity of $v_{He} = 1.53 \, \text{km/s}$; this is, however, not supported by the measured increase of the beam velocity). A better fit was obtained by further enhancing the rate coefficient at larger temperatures ($T_e \sim 100 \, \text{eV}$) by the factor 2.3 and lowering it at $T_e \sim 50 \, \text{eV}$ by a factor 1.7 (green line). These factors lie far beyond the uncertainty of the used rate coefficient, which is estimated to $\sim 10\%$ based on the well coincidence of different measurements [Montague et al., 1984, Shah et al., 1988] and CCC calculations [Ralchenko et al., 2000] such that the considerably smaller penetration depth of the beam remains unclear. It is, however, consistent with earlier observations by Brix who reported a penetration depth of a supersonic beam into the TEXTOR plasma, which was lower by ~ 15 mm than the model prediction. Brix suggested momentum transfer collisions with the background plasma ions as possible explanation for the enhanced attenuation of the beam [Brix, 1998]. Hidalgo et al. [2005] observed an enhanced spread of a supersonic helium beam penetrating the plasma when comparing to a vacuum propagation, which is supposed to be caused by elastic collisions with H_2 molecules.

In spite of the discrepancy between the calculated and measured beam attenuation it is imperative to use the measured factors in derivation of population densities relative to the ground state population from our LIF signals. In this way the deficiency of the model in this respect is eliminated from the data analysis and only the uncertainty of the radial shape of the beam velocity profile to be assumed remains.
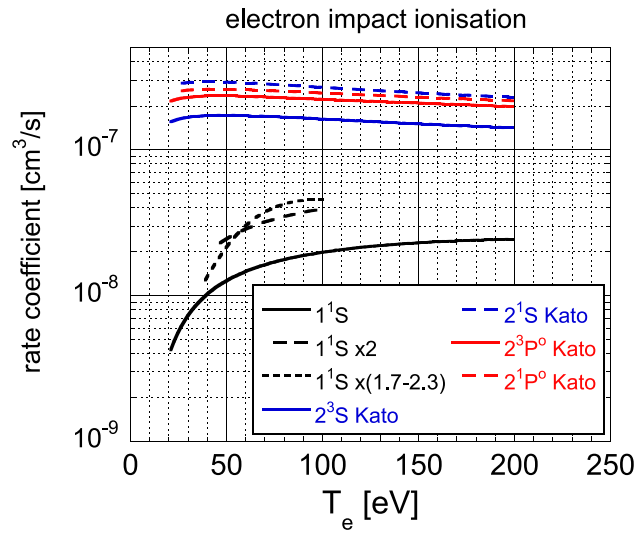
Figure 6.21: Rate coefficient for the electron impact ionisation from the ground state (solid black line) as well as enhanced values of this rate coefficient for $T_e = 40 - 100\,\mathrm{eV}$ (dashed black lines) used in the fitting of the measured ionisation attenuation profile (Figure 6.20). Rate coefficients for the electron impact ionisation from the $n = 2$ levels used in our CR model are added [Kato and Janev, 1992].

Chapter 7

Summary and conclusions

Reliable diagnosing of the parameters of a fusion edge plasma is of great importance for a better understanding of magnetically confined plasmas on the way to future nuclear fusion reactors. Helium beams are widely used to determine the electron density and temperature of the edge plasma in fusion experiments. They provide a means to determine n_e and T_e locally just from comparing intensity ratios of selected spectral lines of atomic helium with those calculated with a collisional-radiative model. This method is not only attractive due to the fact that it merely requires a relative calibration of the detection system but also because interference filter based detection systems with very high optical throughput can be used, which allow measurements to be taken with high temporal and spatial resolution. The accuracy of the derived plasma parameters relies strongly on the accuracy of the atomic data available for the collisional-radiative model and of course on the completeness of processes taken into account in the collisional-radiative model.

In this thesis the laser-induced fluorescence method is used to experimentally validate (some critical) predictions of the collisional radiative model, which are (mainly) not accessible by passive spectroscopic techniques. The experiments were performed on a thermal helium beam penetrating into the edge plasma of the TEXTOR tokamak at the Forschungszentrum-Jülich in Germany.

Original situation

There are various processes arising from the helium beam interaction with the surrounding plasma, which can affect the excitation population distribution of the beam atoms. Among these, electron impact excitation and ionisation are the most important ones. The cross sections (or rate coefficients) available from the literature, and which are based on various calculation methods, are reviewed with particular emphasis on their uncertainties. Only some of the data for transitions connected to the ground or metastable states are available with accuracies of about 10% while mostly the relative errors exceed 50%. We included in our collisional-radiative model the electron impact excitation data for transitions between the levels with $n = 1 - 4$ recommended by Ralchenko et al. [2000] based on recent convergent close coupling method calculations. The extension of our collisional-radiative model to the levels of the $n = 5$ shell is based on the data compiled by Brix [1998] just as the data for electron impact ionisation. It cannot be excluded that proton impact excitation might be of comparable size to electron impact excitation for transitions between levels with very small energy difference. However,

published rate coefficients calculated with different methods were found to differ by up to more than an order of magnitude. Because of these large uncertainties the inelastic collisions with protons are not included in our collisional-radiative model but only suggested as an explanation for an enhanced measured population transfer between excited levels. Charge exchange reactions between protons and excited helium could lead to an increase of particle losses from the beam. Due to the lack of data they were not included in our collisional-radiative model either. Collisions with impurity ions and other helium atoms were shown not to play a role at our experimental conditions. The effect of radiation trapping is estimated for our beam geometry. It results in a considerable population increase of some singlet levels, with the T_e sensitive line intensity ratio being at maximum affected by a few percent. The effect of beam relaxation was demonstrated to be very important for the modelling of the population of triplet levels with $n = 2$ for our outermost observation channel. Recombination does not have to be considered because the concentration of ionised helium in the plasma is very low.

The calculation of the population distribution by use of the collisional-radiative model is performed in two different ways. If the transport term connected to the beam movement can be neglected, the quasi-steady state distribution of populations relative to the ground state population is obtained by a simple solution of a system of linear inhomogeneous differential equations describing the population and depopulation rates for all excited levels. For the beam modelling at the outermost observation channel the beam relaxation is not given and a time dependent solution of the differential equation system for the absolute population densities must be solved. These calculations are also used to obtain the beam attenuation profiles which are compared to measured results. The time dependent solution at sufficiently high electron densities provides the same results as the quasi-steady state calculation. In order to simulate shapes of the time traces and the peak amplitudes of the fluorescence signals for different pumping schemes, the collisional-radiative code was extended by terms describing the impact of the resonant laser radiation on the level populations. The population distribution as resulting from the unextended collisional-radiative model for given plasma parameters is used to provide the start parameters for the simulation including the impact of the laser radiation.

Experimental

At the TEXTOR tokamak located in the Forschungszentrum Jülich an appropriate LIF experimental set-up was prepared. It consists of a two-stage pulsed laser system: an excimer-laser pumped dye laser. The laser beam – coming from a separate laboratory – was lead to the tokamak by use of folding mirrors. It was launched into the vacuum vessel from the top side and adjusted onto the helium gas nozzle at the bottom side of the torus. The nozzle was mounted within a radially movable vacuum lock system. This allowed to find the optimum nozzle position as well as to exchange the nozzle with calibration and adjustment light sources. The observation was made perpendicularly (in the poloidal direction) at three different radial positions by use of imaging optics and gated photomultipliers. Time traces of the fluorescence signals were recorded, with spectral selection obtained by use of interference filters. For the purpose of testing the laser's performance and its wavelength calibration a helium glow discharge was set up

in the laser laboratory to be able to perform fluorescence measurements. The precise wavelength calibration by making use of this chamber was utilised to perform the in-situ measurement of the helium beam velocity in the TEXTOR plasma.

Considerable effort was undertaken to measure the absolute populations of all four levels, which can be excited by the laser in the near ultraviolet and visible spectral range: these are the levels of the $n = 2$ shell of atomic helium. The absolute populations were derived in a direct way from the fluorescence at the laser wavelength during the laser pulse. The decaying part of the fluorescence time trace depends on the collisional population transfer rate from the upper level. In a similar way, the derivation of the population of the lower levels from collision-induced fluorescence at wavelengths other than the one of the laser light does not suffer from the laser stray light but their obtained populations depend on the accuracy of selected rate coefficients.

In order to infer the lower level population from the maximum fluorescence signal radiated from the upper level, the fraction of the atoms in the lower level, which was excited to the upper level, must be known. This fraction depends on the laser spectral profile and the laser intensity as well as on the absorption line profile. The spectral width of our laser system is smaller than the width of the absorption lines, which makes the analysis somewhat more complicated. An additional challenge arises from the splitting of the lines in the magnetic field (Zeeman and Paschen-Back effect) and due to the fine structure splitting in the case of the triplet transitions. To appropriately deal with these problems, the structure of the magnetic sublevels and of the pumping channels were studied in detail and implemented in a computer code. This allowed to simulate the fraction of the lower level population pumped to the upper level. The influence of the longitudinal modes in the spectrum of the laser light was also examined. The pumped fraction was calculated for a series of laser pulses with increasing central wavelength delivering simulated fluorescence spectra as they were obtained in the experiments. The simulated spectra of the pumped fraction were compared with the measured fluorescence spectra by additionally considering the polarisation of the fluorescence from the different magnetic sublevels. Good agreement was observed and the pumped fractions of the lower level populations at their maxima were used to derive the absolute populations of the lower levels from the maximum fluorescence signals.

To obtain the number of fluorescence photons emitted from the observation volume into the solid angle of the observation system, the sensitivity of the observation system must be absolutely calibrated. For this we used an Ulbricht sphere providing calibrated continuous radiation in the spectral region from near ultraviolet to near infrared covering all wavelengths of our interest. Special care was taken to minimise all sources of uncertainty including those connected to the transmission curves of the used interference filters. Additional problems arose due to the strong scattered laser light when measuring the fluorescence at the laser wavelength. Appropriate corrections in the electrical circuits of the detectors were undertaken in order to prevent the onset of the nonlinear sensitivity regime.

The collisional-radiative model provides a distribution of excited level populations relative to the ground state population. Hence, for comparing measured absolute pop-

ulations with the model calculations we need the number of ground state atoms in the observation volume to obtain relative populations. For this purpose 2D pictures of the helium line emission from the beam at $\lambda = 501.6$ nm were recorded by use of a camera with an image intensifier. It is shown that this emission is a measure of the loss of helium atoms from the beam by ionisation. By using this emission integrated in toroidal direction, radial profiles of the beam attenuation are derived, which depend on the assumed relative radial profile of the beam velocity (radial here means along the beam axis which is oriented along the plasma minor radius). The beam velocity has been determined at two radial positions in the TEXTOR plasma from the Doppler shift of the maximum fluorescence wavelength as derived at these two positions, compared to the unshifted maximum obtained from a laboratory measurement in a helium glow discharge. The beam velocity was observed to increase between the two radial positions in the TEXTOR plasma. To account for the beam divergence in the course of the plasma penetration as well as the fact that the observation line and the laser beam are of smaller diameter than the helium beam, the toroidal profiles of the beam emission recorded with the camera at a given plasma radius were Abel-inverted. The local ground state helium density distribution perpendicular to the beam propagation axis is derived in this way. Its integration up to the overlap region of the laser beam and the observation line finally provides the number of atoms in the observation volume.

Results

Experiments according to several pumping schemes were performed at the TEXTOR tokamak. The excitation in the near ultraviolet-visible spectral range is possible in the case of atomic helium only from the four levels of the $n = 2$ shell. All these levels were excited but only in the case of the triplet levels their absolute population could be obtained in a direct way by detecting the maximum fluorescence signal during the laser pulse at the laser wavelength. The resulting populations are roughly a factor of two lower than the model predictions. Analysis of the possible model corrections, which might explain these discrepancies shows that enhanced particle losses from both of these levels, such as ionisation losses, are the most probable reason. Since the cross section for the electron impact ionisation from the triplet metastable level is known with much higher accuracy than the factor of two, which is needed to explain the measured population, beam atom losses due to charge exchange reactions with the background plasma ions are considered to be the reason for the lowered population.

Analysis of the collision-induced fluorescence signals provides information about the rate coefficients for the transition between the upper level and the observed ones. These can be obtained e.g. from the ratio of the maximum of a collisional-induced signal to the maximum of the fluorescence from the upper level. Ratios of rate coefficients – for transitions from the upper level to two observed levels – are obtained from the corresponding ratios of the maximum of the collisional-induced signals of the observed levels. Finally, in case of fluorescence time traces with sufficiently high signal-to-noise ratio, the corresponding rate coefficient can be obtained from the shape of the decaying collision-induced signal. Several collision-induced signals were recorded and analysed. Enhanced rate coefficients between the triplet levels of the $n = 3$ shell were deduced

($\langle\sigma v\rangle_{3^3P^o \to 3^3S}$ by 30% and $\langle\sigma v\rangle_{3^3P^o \to 3^3D}$ by 50%). The rate coefficient between the levels 3^3P^o and 4^3D could be measured relatively to the rate coefficient $\langle\sigma v\rangle_{3^3P^o \to 3^3D}$ by analysing the collision-induced signals from the two levels 3^3D and 4^3D upon laser excitation to the level 3^3P^o at $\lambda_L = 388.9$ nm. The value of $\langle\sigma v\rangle_{3^3P^o \to 4^3D}$ assumed in our collisional-radiative model [Ralchenko et al., 2000] is reproduced by the measurement.

Measurements in the singlet helium indicate a 90% enhanced value of the rate coefficient $\langle\sigma v\rangle_{3^1D \to 3^1P^o}$ (relative to the value assumed in our collisional-radiative model [Ralchenko et al., 2000]) coinciding with the value used by Brix [1998]. However, for this result a correct model prediction of the 2^1S level must be assumed, since no direct measurement of its population was possible. With this assumption an approximately correct value of the rate coefficient $\langle\sigma v\rangle_{4^1D \to 4^1P^o}$ is confirmed by another measurement with the laser excitation to the $n = 4$ shell ($\lambda_L = 396.4$ nm).

The LIF measurements presented in this thesis are accompanied by relatively large uncertainties of typically a factor of two in the case of the absolute populations and of 30-50% for the remaining results except for the rate coefficient derivation from the time trace of the decaying collision-induced fluorescence, which only relies on the accuracy of the fit and of the local n_e value. However, some of the measurement points scatter by larger values than expected from the estimated uncertainties. The reason for this could lie in problems with the mapping of the n_e and T_e values used for the simulations, which were measured at another toroidal and poloidal position as well as in the discharge reproducibility. Therefore, it would be of interest to perform those measurements by in-situ measurement of n_e and T_e from the line emission of helium atoms in the LIF observation volume as well as by simultaneous recording of collision-induced fluorescence and fluorescence from the upper level during the same discharge by spatial separation of radiation at different wavelengths.

Not all pumping schemes in the visible were achievable with our laser system. The measurement in the triplet system at the laser wavelengths $\lambda_L = 706.5$ nm, 447.1 nm and 471.3 nm (the last one was tried but unexpectedly no signals were detected) would allow to cross-check the absolute 2^3P^o population and to measure some additional rate coefficients between the excited levels of the shells $n = 3 - 4$. In the singlet system with its lower population and the strong radiative transitions to the ground state a suppression of the laser scatter light would allow the direct measurement of the 2^1S and 2^1P^o populations from the fluorescence at the laser wavelength. For this purpose, the laser beam would have to be directed to the helium beam at a larger angle to its axis than 7° (as in our case) such as to hit a beam dump instead of the nozzle. The detection of fluorescence at the laser wavelength (e.g. at $\lambda_L = 501.6$ nm) would additionally give access to two rate coefficients $\langle\sigma v\rangle_{3^1S \to 3^1P^o}$ and $\langle\sigma v\rangle_{3^1D \to 3^1P^o}$, which are of high importance for the modelling of the line intensity ratios from which the value of n_e and T_e are typically derived. Finally, several transitions in the near ultraviolet and visible spectral range from the $n = 2$ shell to higher lying levels ($n > 4$) exist, which could be used to investigate the rate coefficients for transitions between those levels.

Comparison of the measured and modelled beam attenuation shows enhanced particle losses from the beam leading to a smaller penetration depth of the beam than predicted

by the model. In order to explain the measured profile an increase of the particle losses from the ground state by a factor of two is necessary. However, the accuracy of the measured electron impact ionisation cross section from the ground state assumed in the model calculation amounts to 10%. Elastic collisions with the background plasma ions could be the reason for the faster beam attenuation.

In the pumping scheme in which the laser at $\lambda_{\mathrm{L}} = 388.9\,\mathrm{nm}$ transfers the population to the level $3^3\mathrm{P}^{\mathrm{o}}$ the collision-induced signal from the level $3^3\mathrm{D}$ ($\lambda = 587.6\,\mathrm{nm}$) shows a good signal-to-noise ratio. Since the decaying part of its time trace mainly depends on the collisional transition rate between the levels $3^3\mathrm{P}^{\mathrm{o}}$ and $3^3\mathrm{D}$ it could be used for the derivation of the electron density in the plasma. Only the relative signal intensity is needed, neither an absolute calibration of the observation system nor an exact laser adjustment is required.

Conclusions

In the present study, thanks to the in-situ, performant LIF system installed on the TEXTOR tokamak a number of adjustments of rate coefficients are suggested and their influence on the n_{e} and T_{e} derivation is discussed. Measured populations of the $n = 2$ triplet levels with respect to the ground state population are lower than the model prediction by around a factor of two. Enhanced loss processes of beam atoms from these levels, which are a possible explanation, result in a lower predicted intensity of the triplet line at $\lambda = 706.5\,\mathrm{nm}$ by 30%. However, due to the lack of corresponding population measurements in singlet helium, no answer can be given in how far the enhanced loss processes influence the predicted line intensity ratios.

Analysis of collision-induced fluorescence signals suggests enhanced collisional transfer between the triplet levels $3^3\mathrm{S}$ and $3^3\mathrm{P}^{\mathrm{o}}$. Accounting for this in the model calculation results in lowering of the predicted $3^3\mathrm{S}$ population and hence in an increase of the calculated T_{e}-dependent line intensity ratio $I_{728.1}/I_{706.5}$. The corresponding overestimation of the T_{e} value amounts to up to 7%. This model correction has no effect on the n_{e} derivation from the singlet line intensities.

On the other hand, enhancement of the rate coefficient between the level $3^1\mathrm{P}^{\mathrm{o}}$ and $3^1\mathrm{D}$ – as following from the measurements – entails an increased value of the calculated n_{e}-dependent line intensity ratio $I_{667.8}/I_{728.1}$. This is equivalent to an overestimation of the n_{e} value by 10-20%. However, no experimental result could be obtained for another important rate coefficient $\langle \sigma v \rangle_{3^1\mathrm{S} \rightarrow 3^1\mathrm{P}^{\mathrm{o}}}$, which has impact on both line intensity ratios since no collision-induced fluorescence was detected from the level $3^1\mathrm{S}$ ($\lambda = 728.1\,\mathrm{nm}$).

Enhanced values of all measured rate coefficients for the collisional transfer between levels of the $n = 3$ shell may be an indication of inelastic proton collisions starting to play a role. Stronger beam attenuation in the course of plasma penetration than predicted by the model was observed. It shows that there are possibly additional important processes, which are not included in the model. Elastic proton collisions with ground state helium atoms are considered in this context.
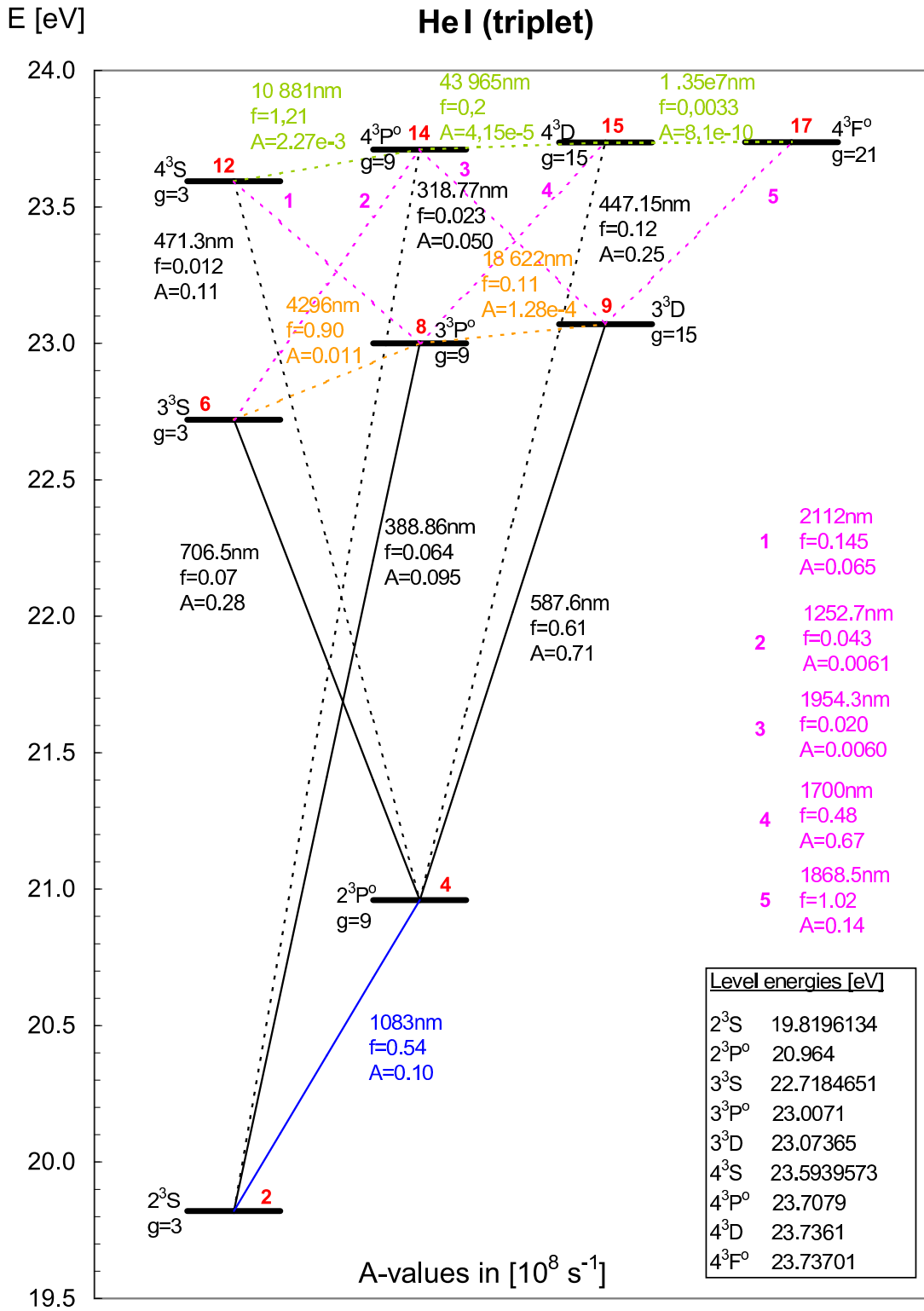
Appendix

List of discharge parameters for two radial points of observation. The line-averaged electron densities as well as the wavelengths of excitation and observation are indicated.

discharge number	$\overline{n}_{\mathrm e}$ $[10^{19}\,\mathrm{m}^{-2}]$	λ_{laser} [nm]	$\lambda_{\mathrm{observ.}}$ [nm]	$r = 45.5\,\mathrm{cm}$		$r = 47\,\mathrm{cm}$	
				$n_{\mathrm e}$ $[10^{12}\,\mathrm{cm}^{-3}]$	$T_{\mathrm e}$ [eV]	$n_{\mathrm e}$ $[10^{12}\,\mathrm{cm}^{-3}]$	$T_{\mathrm e}$ [eV]
99332	2.5	587.6	587.6	2.0	68	1.1	35
99333	3.25	587.6	587.6	3.55	60	1.5	45
99334	4.05	587.6	587.6	6.1	50	1.95	40
99335	4.1	587.6	388.9	5.9	52	2.55	40
99337	3.35	587.6	388.9			1.1	30
99343	2.55	587.6	388.9	2.2	70	1.25	50
100018	2.5	388.9	388.9	2.4	71	1.35	50
100020	2.5	388.9	587.6			1.35	50
100024	2.5	388.9	706.5			1.35	50
100036	4.1	388.9	388.9	5.9	52	2.55	40
100071	2.7	501.6	667.8			3.5	45
102435	2.9	388.9	587.6	6.2	54	3.5	46
102440	2.9	388.9	447.1	6.2	54	3.5	46
102442	2.95	396.5	492.2			3.8	42

Part of the Grotrian diagram of atomic helium (singlet). Levels of the shells n = 2-4 are included. In red the levels are numbered in the order of increasing excitation energy.
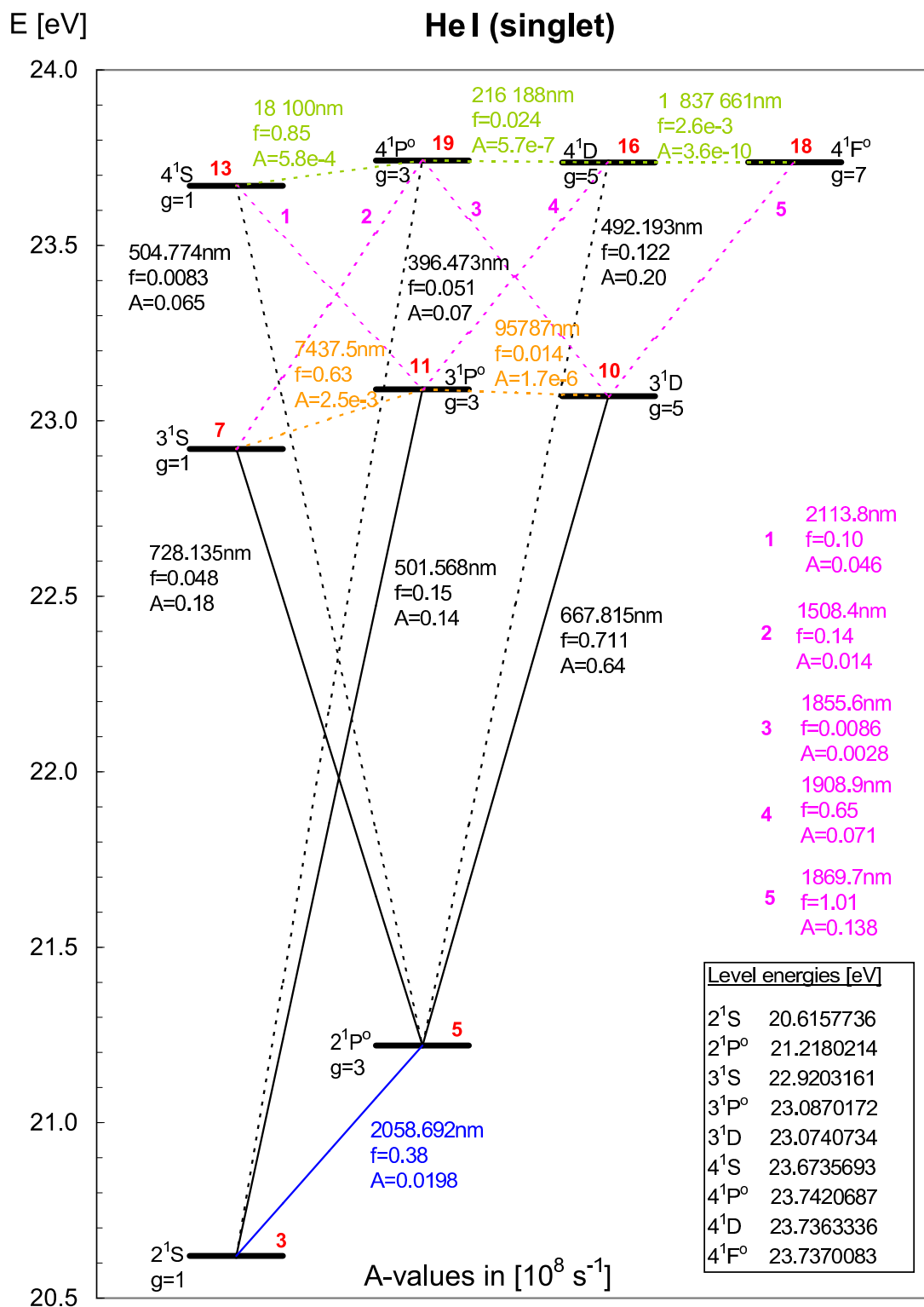
Part of the Grotrian diagram of atomic helium (triplet). Levels of the shells $n = 2\text{-}4$ are included (no fine structure).

E [eV]

HeI (triplet)

A-values in $[10^8 \text{ s}^{-1}]$

10 881nm
f=1,21
A=2.27e-3

43 965nm
f=0,2
A=4,15e-5

1.35e7nm
f=0,0033
A=8,1e-10

4^3P^o **14**
g=9

4^3D **15**
g=15

17 4^3F^o
g=21

4^3S **12**
g=3

3
318.77nm
f=0.023
A=0.050

1 **2** **4** **5**

471.3nm
f=0.012
A=0.11

447.15nm
f=0.12
A=0.25

4296nm
f=0.90
A=0.011

18 622nm
f=0.11
A=1.28e-4

8 3^3P^o
g=9

9 3^3D
g=15

3^3S **6**
g=3

388.86nm
f=0.064
A=0.095

587.6nm
f=0.61
A=0.71

706.5nm
f=0.07
A=0.28

2112nm
1 f=0.145
A=0.065

1252.7nm
2 f=0.043
A=0.0061

1954.3nm
3 f=0.020
A=0.0060

1700nm
4 f=0.48
A=0.67

1868.5nm
5 f=1.02
A=0.14

2^3P^o **4**
g=9

1083nm
f=0.54
A=0.10

Level energies [eV]	
2^3S	19.8196134
2^3P^o	20.964
3^3S	22.7184651
3^3P^o	23.0071
3^3D	23.07365
4^3S	23.5939573
4^3P^o	23.7079
4^3D	23.7361
4^3F^o	23.73701

2^3S **2**
g=3

Bibliography

ADAS manual. http://adas.phys.strath.ac.uk/manual.php, 2007.

V.A. Abramov, L.A. Vainstein, and G.I. Krotova. *Recommended Cross-Sections and Rates for Electron Inelastic Collisions with Helium Atoms.* I. V. Kurchatov Institute of Atomic Energy, Moskau, 1987.

D. Andruczyk, S. Namba, B.W. Jamesa, K. Takiyama, and T. Oda. A short-pulsed compact supersonic helium beam source for plasma diagnostics. *Plasma Devices and Operations*, 14:81–89, 2006.

M. Anton, D. Detleffsen, and K.-H. Schartner. Heavy ion impact excitation of helium: experimental total cross-sections. In R.K. Janev, editor, *Atomic and Plasma-Material Interaction Data for Fusion, Vol. 3.* IAEA, Vienna, 1992.

F.T. Arecchi and E.O. Schulz-Dubois, editors. *Laser Handbook.* Nortz-Holland Publishing Company, Amsterdam, 1972.

C.P. Ballance, D.C. Griffin, S.D. Loch, R.F. Boivin, and M.S. Pindzola. Collisional-radiative calculations of He line emission in low-temperature plasmas. *Phys. Rev. A*, 74:012719, 2006.

K. Bartschat. Electron-impact excitation of helium from the 1^1S and 2^3S states. *J. Phys. B: At. Mol. Opt. Phys.*, 31:L469–L476, 1998.

K. Bartschat, I. Bray, F.J. de Heer, W.C. Fon, and R.K. Janev. *Electron-Impact Excitation Cross Section Data for Helium.* IAEA, Vienna, 1995.

K. Bartschat, E.T. Hudson, M.P. Scott, P.G. Burke, and V.M. Burke. Differential cross sections and electron-impact coherence parameters for electron scattering from helium atoms. *J. Phys. B: At. Mol. Opt. Phys.*, 29:2875–2885, 1996a.

K. Bartschat, E.T. Hudson, M.P. Scott, P.G. Burke, and V.M. Burke. Convergent R matrix with pseudostates calculation for e^--He collisions. *Phys. Rev. A*, 54:R998–R1001, 1996b.

K. Behringer. *Escape Factors for Line Emission and Population Calculations, IPP-10-11.* Max-Planck-Institut fuer Plasmaphysik, Garching, 1998.

I.L. Beigman. private communication, 2007.

I.L. Beigman, L.A. Vainshtein, M. Brix, A. Pospieszczyk, I. Bray, and D.F. Fursa. *Excitation and ionization cross-sections for HeI excited states ($n = 2 - 4$, $\Delta S = 0$). Born and K-Matrix approaches.* Jülicher Report Jül-3479, 1997.

I.L. Beigman, L.A. Vainshtein, M. Brix, A. Pospieszczyk, I. Bray, D.V. Fursa, and Yu. V. Ralchenko. Excitation and Ionization Cross Sections for He I from Normalized Born and K-Matrix Calculations: $\Delta S = 0$ Transitions from $n = 2, 3$ Excited States. *At. Data Nucl. Data Tables*, 74:123–153, 2000.

I.L. Beigman, D.V. Borodin, and L.A. Vainshtein. Cross Sections and Rate Coefficients of Transitions in He and He-Like Ions Induced by Collisions with Heavy Particles. *Optics and Spectroscopy*, 95:493–506, 2003.

K.A. Berrington and A.E. Kingston. Electron excitation in helium: including the $n = 4$ levels in an R-matrix calculation. *J. Phys. B: At. Mol. Phys.*, 20:6631–6640, 1987.

K.A. Berrington, P.G. Burke, and A.L. Sinfailam. Low energy scattering of electrons by helium atoms. *J. Phys. B: Atom. Molec. Phys.*, 8:1459–1473, 1975.

H.A. Bethe and E.E. Salpeter. *Quantum Mechanics of One- and Two-Electron Atoms.* Plenum Publishing Corporation, New York, 1977.

J.B. Boffard, M.E. Lagus, L.W. Anderson, and C.C. Lin. Electron-impact-excitation cross sections out of the (2^3S) metastable level of helium at high energies. *Phys. Rev. A*, 59:4079–4082, 1999.

P. Bogen and E. Hintz. Plasma Edge Diagnostics using Optical Methods. In D.E. Post and R. Behrisch, editors, *Physics of Plasma-Wall Interactions in Controlled Fusion.* Plenum Press, New York, 1986.

P. Bogen, H. Hartwig, E. Hintz, K. Höthker, Y.T. Lie, A. Pospieszczyk, U. Samm, and W. Bieger. Properties of the TEXTOR boundary layer. *J. Nucl. Mater.*, 128-129: 157–162, 1984.

D. Borodin, I. Beigman, L. Vainshtein, and A. Pospieszczyk. Close coupling approach for heavy particle collisions with an excited atom: transitions between $n = 3$ states in He. *Phys. Scr.*, 74:464–471, 2006.

U. Brackmann. *Lambdachrome Laser Dyes.* Lambda Physik GmbH, 1997.

B.H. Bransden and C.J. Joachain. *Physics of Atoms and Molecules.* Longman Inc., New York, 1983.

I. Bray, A. Burgess, D.V. Fursa, and J.A. Tully. He(1^1S, 2^3S, 2^1S, 2^3P $\rightarrow n^{1,3}L$): Thermally averaged electron collision strengths for $n \leq 5$. *Astron. Astrophys. Suppl. Ser.*, 146:481–498, 2000.

S. Brezinsek. *Untersuchung von atomarem und molekularem Wasserstoff vor einer Graphitoberfläche in einem Hochtemperatur-Randschichtplasma.* Jülicher Report Jül-3962, 2002.

S. Brezinsek, Ph. Mertens, and A. Pospieszczyk. Laser-Induced Fluorescence at Lyman-α in the Plasma Edge of TEXTOR-94. *Contrib. Plasma Phys.*, 42:657–662, 2002.

J.S. Briggs and Yong-Ki Kim. Total Cross Sections for Inelastic Scattering of Charged Particles by Atoms and Molecules. VI. Metastable Helium. *Physical Review A*, 3: 1342–1348, 1971.

M. Brix. *Messung von Elektronentemperatur und -dichte mittels Heliumstrahldiagnostik im Randschichtplasma eines Tokamaks.* Jülicher Report Jül-3638, 1998.

M. Brix. private communication, 2007.

H.H. Brongersma, F.W.E. Knopp, and C. Backx. Total Electron-Impact Excitation Cross Sections of Helium. *Chemical Physics Letters*, 13:16–19, 1972.

B. Brosda. *Modellierung von Helium-Atomstrahlen und ihr Einsatz zur Plasmadiagnostik der Tokamakrandschicht.* Dissertation, Ruhr-Universität Bochum, 1993.

S. Büscher, S. Glenzer, Th. Wrubel, and H.-J. Kunze. Profiles of the He I 2^3P $- 3^3$D Line at High Densities. *J. Quant. Spectrosc. Radiat. Transfer*, 54:73–80, 1995.

V.S. Burakov, N.V. Tarasenko, and N.A. Cheptsova. Lasers for plasma diagnostics and laser methods of investigation (review). *Journal of Applied Spectroscopy*, 54:321–333, 1991.

P.G. Burke and K.A. Berrington, editors. *Atomic and Molecular Processes. An R-Matrix Approach.* IOP Publishing Ltd, London, 1993.

C.F. Burrell and H.-J. Kunze. Collisional transfer rates between excited levels in helium. *Phys. Rev. A*, 18:2081–2088, 1978.

S.S. Bychkov, R.S. Ivanov, and G.I. Stotskii. Determination of the local value of the effective charge of a hot plasma by resonant fluorescence. *Sov. J. Plasma Phys.*, 13: 769–774, 1987.

P. Chall, E.K. Souw, and J. Uhlenbusch. Laser diagnostics of a low-pressure hollow-cathode arc. *J. Quant. Spectrosc. Radiat. Transfer*, 34:309–320, 1985.

F.F. Chen. *Introduction to plasma physics and controlled fusion.* Plenum Press, New York, 1984.

E.U. Condon and G.H. Shortley. *The Theory of Atomic Spectra.* Cambridge University Press, Cambridge, 1991.

R.D. Cowan and K.L. Andrew. Coupling Considerations in Two-Electron Spectra. *J. Opt. Soc. Am.*, 55:502–516, 1965.

D. Cubric, D.J.L. Mercer, J.M. Channing, G.C. King, and F.H. Read. A study of inelastic electron scattering in He covering the complete angular range from 0° to 180°. *J. Phys. B: At. Mol. Opt. Phys.*, 32:L45–L50, 1999.

U. Czarnetzki, D. Luggenhölscher, and H.F. Döbele. Space and time resolved electric field measurements in helium and hydrogen RF-discharges. *Plasma Sources Sci. Technol.*, 8:230–248, 1999.

J.W. Daily. Saturation of fluorescence in flames with a Gaussian laser beam. *Applied Optics*, 17:225–229, 1978.

F.J. de Heer. *Critically Assessed Electron-Impact Excitation Cross Sections for He (1^1S)*. IAEA, Vienna, 1998.

F.J. de Heer, R. Hoekstra, A.E. Kingston, and H.P. Summers. Excitation of Neutral Helium by Electron Impact. In R.K. Janev, editor, *Atomic and Plasma-Material Interaction Data for Fusion, Vol. 3*. IAEA, Vienna, 1992.

F.J. de Heer, I. Bray, D.V. Fursa, F.W. Bliek, H.O. Folkerts, R. Hoekstra, and H.P. Summers. Excitation of He ($2^{1,3}$S) by electron impact. *At. Plasma-Mater. Int. Data Fusion*, 6, 1995.

W. Demtröder. *Laserspektroskopie*. Springer Verlag, Berlin, 2000.

R. Denkelmann, S. Maurmann, T. Lokajczyk, P. Drepper, and H.-J. Kunze. Measurement of rate coefficients for electron-atom collisions in a helium plasma by laser-induced fluorescence. *J. Phys. B: At. Mol. Opt. Phys.*, 32:4635–4646, 1999.

R. Denkelmann, S. Freund, and S. Maurmann. Measurement of Rate Coefficients for Atom-Atom Collisions in a Pulsed Helium Discharge by Laser-Induced Fluorescence. *Contrib. Plasma Phys.*, 40:91–95, 2000.

A. Dinklage. *Untersuchung der 2^3S-Population in einem energetischen Heliumstrahl*. Dissertation, Ruhr-Universität Bochum, 1995.

A.J. Dixon, M.F.A. Harrison, and A.C.H. Smith. A measurement of the electron impact ionization cross section of helium atoms in metastable states. *J. Phys. B: Atom. Molec. Phys.*, 9:2617–2631, 1976.

E. Dullni. *Fluoreszenzspektroskopische Bestimmung der Flußdichte von zerstäubtem Titan bei reinen und oxidierten Oberflächen*. Jülicher Report Jül-1936, 1984.

K. H. Finken, D. Reiter, T. Denner, K.H. Dippel, J. Hobirk, G. Mank, H. Kever, G.H. Wolf, N. Noda, A. Miyahara, T. Shoji, K.N. Sato, K. Akaishi, J.A. Boedo, J.N. Brooks, R.W. Conn, W.J. Corbett, R.P. Doerner, D. Goebel, D.S. Gray, D.L. Hillis, J. Hogan,

R.T. McGrath, M. Matsunaga, R. Moyer, R.E. Nygren, and J. Watkins. The Toroidal Pump Limiter ALT-II in TEXTOR. *Fus. Sci. Techn.*, 47:126–137, 2005a.

K.H. Finken, S.S. Abdullaev, M.F.M. De Bock, B. Giesen, M. Von Hellermann, G.M.D. Hogeweij, M. Jakubowski, R. Jaspers, M. Kobayashi, H.R. Koslowski, M. Lehnen, G. Matsunaga, O. Neubauer, A. Pospieszczyk, U. Samm, B. Schweer, and R. Wolf. Background and Initial Experiments with the Dynamic Ergodic Divertor on TEXTOR. *Fus. Sci. Techn.*, 47:87–96, 2005b.

L.C.G. Freitas, K.A. Berrington, P.G. Burke, A. Hibbert, A.E. Kingston, and A.L. Sinfailam. An eleven-state electron-helium scattering calculation. *J. Phys. B: At. Mol. Phys.*, 17:L303–L309, 1984.

W. Fritsch. Helium excitation in heavy particle collisions. In R.K. Janev, editor, *Atomic and Plasma-Material Interaction Data for Fusion, Vol. 3*. IAEA, Vienna, 1992.

T. Fujimoto. *Semi-empirical cross-sections and rate coefficients for excitation and ionization by electron collisions and photoionization of helium.* IPPJAM-8, Institute of Plasma Physics, Nagoya, Japan, 1978.

T. Fujimoto. A Collisional-Radiative Model for Helium and its Application to a Discharge Plasma. *J. Quant. Spectrosc. Radiat. Transfer*, 21:439–455, 1979.

T. Fujimoto. *Plasma Spectroscopy.* Clarendon Press, Oxford, 2004.

D.V. Fursa and I. Bray. Calculation of electron-helium scattering. *Phys. Rev. A*, 52: 1279–1297, 1995.

W.R. Gentry. Low-Energy Pulsed Beam. In G. Scoles, D. Bassi, U. Buck, and D. Lainé, editors, *Atomic and Molecular Beam Methods, Vol. 1*. Oxford University Press, New York, 1988.

M. Goto. Collisional-radiative model for neutral helium in plasma revisited. *J. Quant. Spectrosc. Radiat. Transfer*, 76:331–344, 2003.

M. Goto and T. Fujimoto. *Collisional-radiative Model for Neutral Helium in Plasma: Excitation Cross Section and Singlet-Triplet Wavefunction Mixing.* Rep. NIFS-DATA-43, NIFS, Nagoya, 1997.

M. Goto and S. Morita. Determination of the line emission locations in a large helical device on the basis of the Zeeman effect. *Phys. Rev. E*, 65:026401, 2002.

H.R. Griem. *Spectral Line Broadening by Plasmas.* Academic Press, New York, 1974.

H. Haken and H.C. Wolf. *Atom- und Quantenphysik.* Springer-Verlag, Berlin, 1990.

Hamamatsu. Photomultiplier tubes. Basics and applications, 1999.

P.H. Heckmann and E. Träbert. *Einführung in die Spektroskopie der Atomhülle.* Vieweg & Sohn, Braunschweig, 1980.

J.D. Hey, Y.T. Lie, D. Rusbüldt, and E. Hintz. Doppler Broadening and Magnetic Field Effects on Some Ion Impurity Spectra Emitted in the Boundary Layer of a Tokamak Plasma. *Contrib. Plasma Phys.*, 34:725–747, 1994.

J.D. Hey, M. Korten, Y.T. Lie, A. Pospieszczyk, D. Rusbüldt, B. Schweer, B. Unterberg, J. Wienbeck, and E. Hintz. Doppler Broadening and Magnetic Field Effects on the Balmer Lines Emitted at the Edge of a Tokamak Plasma. *Contrib. Plasma Phys.*, 36: 583–604, 1996.

J.D. Hey, C.C. Chu, and E. Hintz. Spectroscopic Studies of Cold Atomic Hydrogen and Deuterium Produced in a Tokamak Edge Plasma. *Contrib. Plasma Phys.*, 40:9–22, 2000.

J.D. Hey, C.C. Chu, and Ph. Mertens. Zeeman spectroscopy of tokamak edge plasmas. *'Spectral Line Shapes', Proceedings of the 16th International Conference on Spectral Line Shapes (Berkeley 2002), AIP Conference Proceedings No. 645*, 12:26–39, 2002.

A. Hidalgo, D. Tafalla, B. Brañas, and F.L. Tabarés. Multipulse supersonic helium beam diagnostic in the TJ-II stellarator. *Rev. Sci. Instr.*, 75:3478–3480, 2004.

A. Hidalgo, F.L. Tabarés, D. Tafalla, and B. Brañas. Self-consistent modelling of supersonic He beam attenuation in the TJ-II Edge Plasmas. *Proc. 32nd EPS Conf. on Plasma Physics (Tarragona)*, 29C:P–2.084, 2005.

A. Hidalgo, F.L. Tabarés, and D. Tafalla. Testing of the collisional-radiative model by laser-induced perturbation of a supersonic He beam in TJ-II plasmas. *Plasma Phys. Control. Fusion*, 48:527–536, 2006.

F.L. Hinton. Collisional Transport in Plasma. In M.N. Rosenbluth and R.Z. Sagdeev (eds.), editors, *Handbook of Plasma Physics, Vol. 1*. North-Holland Publishing Company, Amsterdam, 1983.

E. Hintz and B. Schweer. Plasma Edge Diagnostics by Atomic Beam Supported Emission Spectroscopy - Status and Perspectives. *Plasma Phys. Control. Fusion*, 37:A87–A101, 1995.

R. Hippler and K.-H. Schartner. Absolute cross sections for the excitation of n^1P-levels of helium by proton impact (150-1000 keV). *J. Phys. B: Atom. Molec. Phys.*, 7:618–625, 1974.

T. Holstein. Imprisonment of resonance radiation in gases. *Physical Review*, 72:1212–1233, 1947.

T. Holstein. Imprisonment of Resonance Radiation in Gases. II. *Physical Review*, 83: 1159–1168, 1951.

I.H. Hutchinson. *Principles of Plasma Diagnostics.* University Press, Cambridge, 2002.

F.E. Irons. The Escape Factor in Plasma Spectroscopy-I. The Escape Factor Defined and Evaluated. *J. Quant. Spectrosc. Radiat. Transfer*, 22:1–20, 1979.

R.K. Janev. Excitation of helium by protons and multiply charged ions: analytic form of scaled cross sections. In R.K. Janev, editor, *Atomic and Plasma-Material Interaction Data for Fusion, Vol. 6*. IAEA, Vienna, 1995.

R.K. Janev, W.D. Langer, K. Evans Jr., and D.E. Post Jr. *Elementary Processes in Hydrogen-Helium Plasmas, Cross Sections and Reaction Rate Coefficients.* Springer-Verlag, Berlin, 1987.

P.A. Jannson, editor. *Deconvolution of Images and Spectra.* Academic Press, San Diego, 1997.

T. Kato and R.K. Janev. Parametric Representation of Electron Impact Excitation and Ionization Cross-Sections for Helium Atoms. In R.K. Janev, editor, *Atomic and Plasma-Material Interaction Data for Fusion, Vol. 3.* IAEA, Vienna, 1992.

T. Kato, Y. Itikawa, and K. Sakimoto. *Compilation of Excitation Cross Sections for He Atoms by Electron Impact.* Rep. NIFS-DATA-15, NIFS, Nagoya, 1992.

Y.-K. Kim. Theory of Electron-Atom Collisions. In F. Brouillard and J.W. McGowan, editors, *Physics of Ion-Ion and Electron-Ion Collisions.* Plenum Press, New York, 1983.

P. Kornejew. *Bestimmung der Elektronenparameter in Randschichtplasmen unter Verwendung eines thermischen Heliumstrahls, IPP-8/10.* Max-Planck-Institut für Plasmaphysik, Garching, 1996.

J. Kramer. Saturated laser-induced fluorescence in a high-pressure metal halide discharge. *J. Appl. Phys.*, 67:2289–2297, 1990.

U. Kruezi. *Entwicklung einer Heliumstrahldiagnostik zur Messung der Elektronendichte und -temperatur mit hoher räumlicher und zeitlicher Auflösung*, volume 62. Jülicher Report Jül-4220, 2007.

H.-J. Kunze. *Physikalische Meßmethoden: eine Einführung in Prinzipien klassischer und moderner Verfahren.* Teubner, Stuttgart, 1986.

M. Lehnen. *Untersuchungen der Plasmarandschichtstruktur im Tokamak TEXTOR-94 mittels der Heliumstrahldiagnostik.* Jülicher Report Jül-3835, 2000.

W. Lochte-Holtgreven. Evaluation of Plasma Parameters. In W. Lochte-Holtgreven, editor, *Plasma Diagnostics.* North-Holland Publishing Company, Amsterdam, 1968.

D.R. Long and R. Geballe. Electron-Impact Ionization of He(2^3S). *Physical Review A*, 1:260–265, 1970.

W.C. Martin. Energy Levels of Neutral Helium (^{4}He I). *J. Phys. Chem. Ref. Data*, 2: 257–265, 1973.

W.C. Martin. New values for some ^{4}He I 1*snl* energy levels, ionization energies, and Lamb shifts. *Phys. Rev. A*, 29:1883–1888, 1984a.

W.C. Martin. Erratum: New values for some ^{4}He I 1*snl* energy levels, ionization energies, and Lamb shifts. *Phys. Rev. A*, 30:651, 1984b.

R.W.P. McWhirter. Spectral Intensities. In R.H. Huddlestone and S.L. Leonard, editors, *Plasma Diagnostic Techniques*. Academic Press, New York, 1965.

H. Meister, R. Dux, L.D. Horton, B. Kurzan, H. Zohm, the ASDEX Upgrade Team, and P.J. McCarth. An integrated system to measure the effective charge of fusion plasmas in the ASDEX Upgrade tokamak. *Rev. Sci. Instrum.*, 74:4625–4633, 2003.

H.C. Meng and H.-J. Kunze. Investigation of the diffusion of impurity atoms in plasmas by laser fluorescence. *Phys. Fluids*, 22:1082–1088, 1979.

H. Merabet, M. Bailey, R. Bruch, J. Hanni, S. Bliman, D.V. Fursa, I. Bray, K. Bartschat, H.C. Tseng, and C.D. Lin. Cross sections and collision dynamics of the excitation of $(1snp)$ $^1P^o$ levels of helium, $n = 2 - 5$, by intermediate- and high-velocity electron, proton, and molecular-ion (H_2^+ and H_3^+) impact. *Phys. Rev. A*, 64:012712, 2001.

Ph. Mertens and P. Bogen. Densities and Velocity Distributions of Atomic Hydrogen and Carbon, Measured by Laser-Induced Fluorescence with Frequency Tripling into the Vacuum UV. *Appl. Phys. A*, 43:197–204, 1987.

Ph. Mertens, P. Bogen, and B. Schweer. Study of sputtered Si-atoms in front of a TEXTOR-limiter by laser-induced fluorescence. *Proceedings of 20th Europ. Conf. on Controlled Fusion and Plasma Physics*, III:1123–1126, 1993.

R.G. Montague, M.F.A. Harrison, and A.C.H. Smith. A measurement of the cross section for ionisation of helium by electron impact using a fast crossed beam technique. *J. Phys. B: At. Mol. Phys.*, 17:3295–3310, 1984.

K. Muraoka and M. Maeda. Application of laser-induced fluorescence to high-temperature plasmas. *Plasma Phys. Control. Fusion*, 35:633–656, 1993.

K. Muraoka and M. Maeda. *Laser-Aided Diagnostics of Plasmas and Gases*. IOP Publishing Ltd, Bristol, 2001.

O. Neubauer, G. Czymek, B. Giesen, P.W. Hüttemann, M. Sauer, W. Schalt, and J. Schruff. Design Features of the Tokamak TEXTOR. *Fus. Sci. Techn.*, 47:76–86, 2005.

N. Omenetto, J. Bower, J. Bradshaw, C.A Van Duk, and J.D. Winefordner. A theoretical and experimental approach to laser saturation broadening in flames. *J. Quant. Spectrosc. Radiat. Transfer*, 24:147–158, 1980.

R.M. Parish and R.W. Mires. Singlet-Triplet Mixing in Excited Helium Atoms. *Phys. Rev. A*, 4:2145–2160, 1971.

I.D. Paton. *On the neutral gas puff as a tokamak edge diagnostic.* University of Strathclyde, 2005.

E.H. Piepmeier. Theory of laser saturated atomic resonance fluorescence. *Spectrochimica Acta*, 27B:431–443, 1972.

A. Pospieszczyk and G.G. Ross. Use of laser-ablated fast particle beams for the measurement of n_e and T_e profiles in the TEXTOR boundary layer. *Rev. Sci. Instr.*, 59: 1491–1493, 1988.

A. Pospieszczyk, P. Bogen, H. Hartwig, and Y.T. Lie. Determination of low surface coverages of H_2 and Co by vacuum UV-resonance fluorescence spectroscopy of laser desorbed particles. *J. of Nucl. Mat.*, 93 & 94:368–376, 1980.

W.H. Press, S.A. Teukolsky, W.T. Vetterling, and B.P. Flannery. *Numerical Recipes in C++. The Art of Scientific Computing.* Cambridge University Press, Cambridge, 2002.

Yu.V. Ralchenko, R.K. Janev, T. Kato, D.V. Fursa, I. Bray, and F.J. de Heer. *Cross Sections Database for Collision Processes of Helium Atom with Charged Particles. I. Electron Impact Processes.* Rep. NIFS-DATA-59, NIFS, Nagoya, 2000.

C.A. Sacchi and O. Svelto. Basic Principles of Lasers. In N. Omenetto, editor, *Analytical Laser Spectroscopy.* John Wiley & Sons, New York, 1978.

J.T. Salmon and N.M. Laurendeau. Analysis of probe volume effects associated with laser-saturated fluorescence measurements. *Applied Optics*, 24:1313–1321, 1985.

G. Sauerbrey. Linearitätsabweichungen bei Strahlungsmessungen mit Photovervielfachern. *Applied Optics*, 11:2576–2583, 1972.

P.M.J. Sawey and K.A. Berrington. Collision Strengths from a 29-State R-Matrix Calculation on Electron Excitation in Helium. *Atomic Data and Nuclear Data Tables*, 55:81–142, 1993.

P.M.J. Sawey, K.A. Berrington, P.G. Burke, and A.E. Kingston. Electron scattering in helium at low energies: a 29-state R-matrix calculation. *J. Phys. B: At. Mol. Opt. Phys.*, 23:4321–4329, 1990.

O. Schmitz. *Experimentelle Untersuchung der Plasmastruktur und Charakterisierung des Transportverhaltens in der laminaren Zone einer stochastisierten Plasmarandschicht.* Jülicher Report Jül-4220, 2006.

B. Schweer, M. Brix, and M. Lehnen. Measurement of edge parameters in TEXTOR-94 at the low and high field side with atomic beams. *J. of Nucl. Mater.*, 266-269:673–678, 1999.

B. Schweer, S. Brezinsek, H.G. Esser, A. Huber, Ph. Mertens, S. Musso, V. Philipps, A. Pospieszczyk, U. Samm, G. Sergienko, and P. Wienhold. Limiter Lock Systems at TEXTOR: Flexible Tools for Plasma-Wall Investigation. *Fus. Sci. Techn.*, 47:138–145, 2005.

M.B. Shah, D.S. Elliott, P. McCallion, and H.B. Gilbody. Single and double ionisation of helium by electron impact. *J. Phys. B: At. Mol. Phys.*, 21:2751–2761, 1988.

D.A. Shcheglov, S.I. Vetrov, I.V. Moskalenko, A.A. Skovoroda, and D.A. Shuvaev. Laser Spectroscopy for Measuring the Parameters of a Plasma Containing Helium and Argon. *Plasma Physics Reports*, 32:119–122, 2006.

V.P. Shevelko and L.A. Vainshtein. *Atomic Physics for Hot Plasmas.* Institute of Physics Publishing, Bristol, 1993.

Sirah Laser- und Plasmatechnik GmbH. Sirah Dye Laser Manual, 1999.

I.I. Sobelman. Über die Theorie der Linienbreite von Atomen. *Fortschritte der Physik*, 5:175–210, 1957.

I.I. Sobelman. *Atomic Spectra and Radiative Transisions.* Springer-Verlag, Berlin, 1979.

I.I. Sobelman, L.A. Vainshtein, and E.A. Yukov. *Excitation of Atoms and Broadening of Spectral Lines.* Springer-Verlag, Berlin, 1995.

H. Soltwisch, H.L. Bay, G. Bertschinger, P. Bogen, H. Conrads, K.H. Dippel, G. Fuchs, H. Gerhauser, B. Giesen, E. Graffmann, E. Hintz, F. Hcenen, A. Kaleck, L. Könen, M. Korten, M. Lochter, N. Noda, A. Pospieszczyk, U. Samm, J. Schlüter, B. Schweer, F. Waelbroeck, G. Waidmann, L.H. Wei, P. Wienhold, J. Winter, and G. Wolf. First Results from TEXTOR. *Plasma Phys. Control. Fusion*, 26:23–35, 1984.

R.F. Stebbings, F.B. Dunning, F.K. Tittel, and R.D. Rundel. Photoionization of Helium Metastable Atoms near Threshold. *Physical Review Letters*, 30:815–817, 1973.

S. Stenholm. Absorption and Gain Spectra. In G.W.F. Drake, editor, *Handbook of Atomic, Molecular, and Optical Physics.* Springer-Verlag, Berlin, 2006.

H.P. Summers and M.G. O'Mullane. The Atomic Data and Analysis Structure. In R.E.H. Clark and D.H. Reiter (eds.), editors, *Nuclear Fusion Research. Understanding Plasma-Surface Interactions.* Springer-Verlag, Berlin, 2005.

K. Takiyama, H. Sakai, M. Yamasaki, and T. Oda. Measurement of Density Distribution of Metastable He Atom in a Plane-Parallel Hollow Cathode He Plasma. *Jpn. J. Appl. Phys.*, 33:5038–5045, 1994.

K. Takiyama, T. Katsuta, M. Watanabe, S. Li, and T. Oda. Spectroscopic method to directly measure electric field distribution in tokamak plasma edge. *Rev. Sci. Instrum.*, 68:1028–1031, 1997.

C. Theodosiou. Transition Probabilities for the Helium Singly Excited States $1snl^{1,3}L$ with $n = 2 - 21$ and $l = 0 - 5$. *Atomic Data and Nuclear Data and Nuclear Data Tables*, 36:97–127, 1987.

G. Traving. *Über die Theorie der Druckverbreiterung von Spektrallinien.* Verlag G. Braun, Karlsruhe, 1960.

G. Traving. Interpretation of line broadening and line shift. In W. Lochte-Holtgreven, editor, *Plasma Diagnostics.* North-Holland Publishing Company, Amsterdam, 1968.

K. Tsuchida, S. Miyake, K. Kadota, and J. Fujita. Plasma electron density measurements by the laser- and collision-induced fluorescence method. *Plasma Physics*, 25:991–999, 1983.

A. Unsöld. *Physik der Sternatmosphären.* Springer Verlag, Berlin, 1968.

H.J. van der Meiden, T. Oyevaar, S.K. Varshney, E. Uzgel, M.Yu. Kantor, D.V. Kouprienko, A. Pospieszczyk, C.J. Barth, A.J.H. Donné, and the TEXTOR Team. Multipulse Thomson scattering system for TEXTOR. *Proceedings of the 12th International Conference on Laser Aided Plasma Diagnostics, LAPD12, Snowbird, USA*, 2005.

M. van Lessen, R. Schnabel, and M. Kock. Population densities of Fe I and Fe II levels in an atomic beam from partially saturated LIF signals. *J. Phys. B: At. Mol. Opt. Phys.*, 31:1931–1946, 1998.

H. van Regemorter. Rate of Collisional Excitation in Stellar Atmospheres. *Astrophysical Journal*, 136:906–915, 1962.

J. Wesson. *Tokamaks.* Oxford University Press, Oxford, 1997.

W.L. Wiese. Line broadening. In R.H. Huddlestone and S.L. Leonard, editors, *Plasma Diagnostic Techniques.* Academic Press, New York, 1965.

W.L. Wiese, M.W. Smith, and B.M. Glennon. *Atomic Transition Probabilities, Volume I: Hydrogen Through Neon.* NSRDS-NBS 4, Washington D.C., 1966.

M. Wutz, H. Adam, W. Walcher, and K. Jousten. *Handbuch Vakuumtechnik.* Vieweg Verlag, Braunschweig, 2000.

S. Zoletnik and S. Kálvin. A method for tomography using arbitrary expansions. *Rev. Sci. Instrum.*, 64:1208–1212, 1993.

H.R. Zwicker. Photoemissive Detectors. In R.J. Keyes, editor, *Optical and Infrared Detectors*. Springer-Verlag, Berlin, 1977.

Acknowledgments

Curriculum Vitae

Maciej Krychowiak

Geburtsdatum	29. März 1975
Geburtsort	Trzcianka (Polen)
Familienstand	verheiratet seit dem 26. April 2003
	mit Dorota Krychowiak, geb. Pokorska
	Geburt des Sohnes Pascal am 06. August 2004

Eltern

Edward Krychowiak, geboren am 24. Juli 1941
Mirosława Krychowiak, geboren am 05. Juli 1942

Geschwister

Paweł Krychowiak, geboren am 07. April 1972, Ingenieur (Telekommunikation)
Jarosław Krychowiak, geboren am 18. Mai 1965, Ingenieur (Industrieautomatik)

Lebenslauf

1981 - 1989	Besuch der Juliusz-Słowacki-Grundschule in Trzcianka
1989 - 1993	Besuch des Stanisław-Staszic-Lyzeums in Trzcianka, anschließend Abitur im Juni 1993
Oktober 1993 - Juli 1998	Studium der Betriebswirtschaftslehre (Diplom) an der Europa-Universität Viadrina in Frankfurt (Oder)
Juli 1998	Abschluß der Diplomarbeit: "Problembereiche der Konzernrechnungslegung in Polen"
Oktober 1998 - Oktober 2003	Studium der Physik (Diplom) an der Ernst-Moritz-Arndt-Universität in Greifswald
Oktober 2003	Abschluß der Diplomarbeit: "Dynamik von Verunreinigungen im Divertorbetrieb des Stellarators Wendelstein 7-AS"
Oktober 2003 - Juli 2007	Doktorarbeit am Max-Planck-Institut für Plasmaphysik, Teilinstitut Greifswald: "Laser-induced fluorescence of atomic helium beams in a fusion edge plasma"

Fellow of the
"International Max-Planck Research School on Bounded Plasmas"

Eidesstattliche Erklärung

Hiermit erkläre ich an Eides statt, dass diese Arbeit bisher von mir weder der Mathematisch-Naturwissenschaftlichen Fakultät der Ernst-Moritz-Arndt-Universität Greifswald noch einer anderen wissenschaftlichen Einrichtung zum Zwecke der Promotion eingereicht wurde.
Ferner erkläre ich, dass ich diese Arbeit selbstständig verfasst und keine anderen als die darin angegebenen Hilfsmittel benutzt habe.

Greifswald, im Juli 2007

_____
(Maciej Krychowiak)